

Photophysical Studies of
Multilayer Two-Dimensional
Covalent Organic Frameworks

Caroline Vanessa Nowicka-Dylag

Thesis submitted to University College London for
the degree of Doctor of Philosophy in Chemistry

2020

I, *Caroline Vanessa Nowicka-Dylag*, confirm that the work presented in this thesis is my own. Where information has been derived from other sources, I confirm that this has been indicated in the thesis.

Abstract

This thesis studies the photophysical properties of multilayer two-dimensional (2D) covalent organic frameworks (COFs). COFs are a type of crystalline porous polymer which allow the atomically precise incorporation of organic units to create structures with predesigned skeletons and nanopores. In all COFs the molecules are linked via covalent bonds within the single layers, which is an important characteristic that defines these materials. This leads to a variety of applications; for example, catalysis, gas storage, adsorption and optoelectronics. This thesis focuses on porphyrins to make COFs via a Schiff-base condensation reaction. Porphyrins have been studied for decades and have been shown to have interesting photophysical properties, such as the generation of triplet states and charge states. The synthesis of the COFs was mainly studied using scanning tunnelling microscopy (STM), and supported using Fourier transform infrared spectroscopy (FTIR) and X-ray photoelectron spectroscopy (XPS). The photophysical properties of the porphyrin COFs was studied using transient absorption spectroscopy (TAS). The STM results have shown a successful synthesis of 2D-COFs but the synthesis is not reliable nor reproducible which is a large stumbling block. The TAS results have shown a difference when comparing the porphyrins, and then COFs, in solution and as a multilayer film. In a solution the porphyrins exhibit triplet states. However, as a film the porphyrins and COFs exhibit charge states and subsequent bimolecular recombination. The generation of charge states was then compared between the porphyrin film precursor and subsequent COF film and the differences have been expanded upon in the thesis. Future work to improve the synthesis of the COF films and further photophysical studies have also been included.

Impact Statement

The transition to using more sustainable energy and lowering our carbon footprint has become one of the most important scientific endeavours in the 21st century. The research working towards this encompasses a number of fields, from how we harvest energy and energy storage, to the manufacture and materials that make our day-to-day items, and even to our food and agriculture. This thesis looks at a novel material that can be used to harvest solar energy, but in particular, it is looking at the use of an environmentally friendly material. Current materials tend to incorporate rare-earth metals or harsh synthesis techniques, which negates the environmentally beneficial technique of harnessing solar energy.

The material looked at in this thesis is a covalent organic framework (COF). COFs with optical properties can have the capacity to improve the way we harness and store energy with little to no impact on the environment. The key emphasis for using COFs in this research is the use of light elements and economical synthetic techniques. Specifically, the focus is on porphyrin-based COFs as porphyrins have been investigated for use in organic solar cells (OSCs) for decades.

The key outcome of this research is highlighting the pitfalls in using two-dimensional monolayer COFs, as the synthesis techniques are not precise enough to ensure accurate and repeat results. However, scanning tunnelling microscopy (STM) was successfully used to image some films that were synthesised, both freebase porphyrins as well as metallated analogues. Also, from using transient absorption spectroscopy (TAS) to investigate the charge dynamics of the COF films, it is clear to see the interesting optical behaviour of the films which is attributed to charge generation across multiple wavelengths. Charge generation is important if any solar energy harvesting application is one aim of the application. Differences were also seen between freebase porphyrin molecules and metallated analogues which builds an understanding in the optical characteristics of the COF films, opening the possibility of custom films for particular applications.

Acknowledgements

Firstly, I would like to thank both my supervisors, Dr. Tracey Clarke and Dr. Matthew Blunt, for their support, guidance and patience throughout the duration of my research. Also, a huge thanks goes to Prof. Claire Carmalt for her support at the end of my studies. I also want to thank UCL for the funding and opportunity to complete my PhD.

Also at UCL, I want to say a massive thank you to everyone in the 2nd floor office, especially Dr. Jose Marin Beloqui for always letting me bother him with questions, and Simran Dhaliwal for all the laughs and her support when I needed it most. A special thanks goes to Charles Willoughby, for all our 'tea, cake and trivia' catch-ups which I will undoubtedly miss.

My deepest thanks go to my family and friends. To name but a few, my Mum, Dad, Auntie Bogda, Natalia, James, Dan, Jake, Clara, Rupinder, Annie, Charlotte, Maya, Megan, Jenny, Rehana, Sara, and my friends at the National Portrait Gallery. Thank you for being there when I needed you most.

Contents

Abstract.....	3
Impact Statement.....	4
Acknowledgements.....	5
Contents.....	6
Abbreviations and Acronyms	10
List of Tables.....	12
List of Figures	12
1 Background and Motivation	28
1.1 Introduction	28
1.2 Motivation	29
1.3 COF Synthesis	30
1.4 STM of COFs	32
1.5 Photophysical Electron Transfer and Energy Transfer Processes	39
1.5.5 Singlet and Triplet States	39
1.5.1.1 Oxygen: Quenching Triplet States	41
1.5.2 Charge-Transfer (CT) States	42
1.6 Porphyrins	43
1.6.1 Ground State UV-Visible Absorption Spectra of Porphyrins	44
1.6.2 Emission Studies of Porphyrins	47
1.6.3 Flash Photolysis of Porphyrins showing Triplet Species	49
1.6.4 Porphyrin Studies Showing Charges	50
1.6.5 Porphyrin Applications	52

1.6.5.1	Dye-Sensitised Solar Cells	52
1.6.5.2	Organic Solar cells	54
1.6.6	TAS on Porphyrins	56
1.6.6.1	Previous TAS Studies of Porphyrins in Solution and Solid State	58
1.7	Thesis Aim and Structure	59
1.8	Bibliography	61
2	Experimental Procedures	67
2.1	Key Materials	67
2.2	COF Synthesis	68
2.2.1	Experimental Set-Up	68
2.2.2	Substrate	68
2.3	Scanning Tunnelling Microscopy	69
2.3.1	Using STM on COFs in this Thesis	72
2.3.2	Data Acquisition and Processing in Ambient STM	72
2.3.2.1	Experimental Set-Up	72
2.3.2.2	Tip Preparation	73
2.3.2.3	Drift Correction	73
2.4	Transient Absorption Spectroscopy	74
2.4.1	TAS with Microsecond Resolution Setup	75
2.4.2	TAS Sample Preparation	77
2.4.3	TAS Data Analysis	77
2.5	Fourier Transform Infrared (FT-IR) Spectroscopy	79
2.5.1	Experimental Setup	80
2.5.2	FTIR Sample Preparation	80
2.6	X-ray Photoelectron Spectroscopy (XPS)	80

2.6.1	Experimental Setup and Data Processing	81
2.6.2	XPS Sample Preparation	83
2.7	Bibliography	84
3	COF Film Synthesis	87
3.1	Introduction	87
3.1.1	Schiff-Base Reactions	87
3.1.2	Linker	89
3.1.3	Imine Bonded COFs	91
3.2	COF-366 Synthesis	92
3.3	STM of COFs	93
3.3.1	STM Results	93
3.3.2	COF Synthesis with Acetic Acid	100
3.3.3	Metallated COFs	102
3.4	Other Proof of COF Synthesis	105
3.4.1	Fourier-Transform Infrared Spectroscopy (FTIR)	105
3.4.2	X-ray Photoelectron Spectroscopy (XPS)	108
3.5	Conclusion	112
3.6	Bibliography	115
4	Laser Studies: TAPP and COF	118
4.1	TAPP Solution	120
4.1.1	TAPP and COF solution	125
4.2	TAPP Film	128
4.2.1	TAPP Film and Solution Comparison	137
4.3	COF Film	139
4.3.1	TAPP and COF Film Comparison	149
4.3.2	TAPP and COF Comparison of Kinetics	150

4.3.3	TAPP Film, Pump Wavelength = 680 nm	156
4.3.4	COF Film, Pump Wavelength = 652 nm	157
4.3.5	5 μ s Comparison of TAPP and COF films	158
4.4	Conclusion	161
4.5	Bibliography	163
5	Photophysical Properties of Zinc and Copper Metalloporphyrins	166
5.1	Introduction	166
5.1.1	Triplet or Charge State	168
5.2	Studies on ZnTAPP: Results and Discussion	170
5.2.1	ZnCOF	176
5.2.2	ZnTAPP and ZnCOF Comparison	182
5.3	Studies on CuTAPP: Results and Discussion	185
5.3.1	CuCOF	191
5.3.2	CuTAPP and CuCOF Comparison	197
5.4	Metal-TAPP comparison	201
5.5	Conclusion	203
5.6	Bibliography	205
6	Conclusion and Future Work	207
6.1	Bibliography	214
A1	Appendix 1	216
A2	Appendix 2	219
A3	Appendix 3	222
A4	Appendix 4	223

Abbreviations and Acronyms

2D	Two-Dimensional
3D	Three-Dimensional
A	Electron Acceptor
AFM	Atomic Force Microscopy
BDA	Benzene-1,4-dicarboxaldehyde
CB	Conduction Band
COF	Covalent Organic Framework
CS	Charge Separated
CT	Charge-Transfer
CuTAPP	Copper (II) -5,10,15,20-tetrakis-(4-aminophenyl) porphyrin
CV	Cyclic Voltammetry
D	Electron Donor
DCC	Dynamic Covalent Chemistry
DFT	Density Functional Theory
DOS	Density of States
DSSCs	Dye-Sensitized Solar Cells
FTIR	Fourier Transform Infrared
FWHM	Full Width Half Maximum
HOMO	Highest Occupied Molecular Orbital
HOPG	Highly ordered pyrolytic graphite
HOPG	Highly Ordered Pyrolytic Graphite
ISC	Intersystem Crossing
LUMO	Lowest Unoccupied Molecular Orbital
OD	Optical Density
OPO	Optical Parametric Oscillator
OSCs	Organic Solar Cells
pXRD	Powder X-Ray Diffraction
PPDA	p-Phenylenediamine

PTFE	Polytetrafluoroethylene
PZn	Zinc Porphyrin
RES	Renewable Energy Sources
SOC	Spin–Orbit Coupling
SM	Small-Molecule
SSA	Singlet–Singlet Annihilation
STM	Scanning Tunneling Microscopy
TAPB	1,3,5-tris(4-aminophenyl)benzene
TAPP	5,10,15,20-tetrakis-(4-aminophenyl) porphyrin
TAS	Transient Absorption Spectroscopy
TB	Through-Bond
TFB	1,3,5-triformyl-benzene
TPA	Terephthaldicarboxaldehyde
TS	Through-Space
UHV	Ultrahigh Vacuum
VB	Valence Band
XPS	X-ray Photoelectron Spectroscopy
ZnTAPP	Zinc (II) -5,10,15,20-tetrakis-(4-aminophenyl) porphyrin
ZnTPP	Zinc (II) -tetraphenylporphyrin

List of Tables

Table 3.1: Summary of IR stretching and bending bands for primary amines and imines. ³⁰	106
Table 3.2: XPS binding energy values of nitrogen species in ZnTAPP from literature and experimental results. ^{32,33}	109
Table 3.3: XPS binding energy values of nitrogen species in ZnCOF films from literature and experimental results.	111
Table 5.1: A list of peak shifts between ZnTAPP films and the resultant ZnCOF film for the Soret and Q-bands in the UV-vis spectra. The error reported is the population standard deviation.....	177

List of Figures

Figure 1.1: The combination of building blocks with different geometries to design 2D-COFs.	30
Figure 1.2: Scheme diagram for solid–vapour interface reaction. The red molecule begins as a film on the substrate and then, the blue linker is in the form of a vapour which can collide with the red molecules on the surface to react to form an extended structure i.e. a COF. ¹³	32
Figure 1.3: Reaction scheme of benzene-1,3,5-tricarbaldehyde and different aromatic diamines into hexagonal surface COFs. The organic backbones of aromatic diamines are symbolically represented by ellipses. ¹⁵	34
Figure 1.4: (a) STM image showing clearly the domain boundaries resulting from incomplete condensation. (b and c) Digital magnifications of the areas marked by the white and blue rectangles, respectively. White arrows indicate domain	

boundaries and, black and red arrows indicate defects. The tunneling conditions were $I = 0.05 \text{ nA}$, $V = 0.50 \text{ V}$.¹⁵ 34

Figure 1.5: Condensation of trigonal precursors 1,3,5-tris(4-aminophenyl)benzene (TAPB, 1) or 1,3,5-triformyl-benzene (TFB, 3) and linear precursors terephthalaldehyde (TPA, 2) or p-phenylenediamine (PPDA, 4) can form SCOF-IC1 or SCOF-LZU1, respectively. The expected lattice parameters are indicated.¹⁸ 36

Figure 1.6: STM images and a structural model for SCOF-IC1. (a) Large-scale STM image ($100 \times 100 \text{ nm}^2$) of SCOF-IC1 with the inset depicting the corresponding fast Fourier transform (FFT) spectrum of the STM image. (b) High resolution STM image ($20 \times 20 \text{ nm}^2$) of SCOF-IC1. (c) A structural model with the measured structural parameter for SCOF-IC1. Imaging conditions: (a) $V_{\text{bias}} = 700 \text{ mV}$, $I_t = 500 \text{ pA}$; (b) $V_{\text{bias}} = 693 \text{ mV}$, $I_t = 450 \text{ pA}$.¹⁸ 37

Figure 1.7: STM images and a structural model for SCOF-LZU1. (a) Large-scale STM image ($100 \times 100 \text{ nm}^2$) of SCOF-LZU1 with the inset depicting the corresponding FFT spectrum of the STM image. (b) High resolution STM image ($20 \times 20 \text{ nm}^2$) of SCOF-LZU1. (c) A structural model with the measured structural parameter for SCOF-LZU1. Imaging conditions: $V_{\text{bias}} = 620 \text{ mV}$, $I_t = 536 \text{ pA}$.¹⁸ 38

Figure 1.8: Diagram showing possible spin states after electronic excitation and their respective labels. Horizontal lines used to represent states at different quanta of energy. 40

Figure 1.9: A Jablonski diagram illustrating the electronic states of a molecule and the transitions between. The straight arrows indicate radiative processes, the curved arrows indicate non-radiative processes. 40

Figure 1.10: Structure of porphin, the simplest porphyrin. 44

Figure 1.11: Representation of the four Gouterman orbitals in porphyrins .. 45

Figure 1.12: The chemical structures for free-base and metallated forms of porphin are shown on the left. The ground state UV-visible spectra are shown on the right. Q_0 in metalloporphin is due to a pure electronic transition (no molecular vibrations) between the electronic ground state and the first electronic excited state; Q_1 is due to the same electronic transition but, in addition, molecular vibrations are involved. This band is called a vibronic band. The subscripts 0 and 1 for free base

porphin carry a similar interpretation. The x and y subscripts refer to the orientation (polarisation) of the vector of the absorbed light with respect to the axes shown on the chemical structure diagram for freebase porphin. ⁵⁶	46
Figure 1.13: Energy levels scheme of a DSSC.	53
Figure 1.14: Organic solar cell set-up.	54
Figure 2.1: a) 5,10,15,20-tetrakis-(4-aminophenyl) porphyrin (TAPP); b) zinc (II) -5,10,15,20-tetrakis-(4-aminophenyl) porphyrin (ZnTAPP); c) copper (II) -5,10,15,20-tetrakis-(4-aminophenyl) porphyrin (CuTAPP).	67
Figure 2.2: Linker: benzene-1,4-dicarboxaldehyde (BDA)	67
Figure 2.3: Synthetic set-up for 2D-COF synthesis, using TAPP and BDA.	68
Figure 2.4: Schematic demonstrating electron tunnelling between STM tip and sample. The tip surface separation (d), the Fermi levels of both the tip (E _{FT}) and substrate (E _{FS}), and the vacuum energy level (E _{vac}) are labeled. The movement of electrons occurs from the sample to the tip.	70
Figure 2.5: A block diagram representing a nanosecond-microsecond transient absorption experimental setup. The change in the optical density relative to the ground state absorbance after excitation may be plotted as a function of probe wavelength, λ , yielding a transient absorption spectrum.	75
Figure 3.1: Simplified Schiff-base mechanism	88
Figure 3.2: Thermodynamic control in the dynamic covalent chemistry of COFs. ⁵	88
Figure 3.3: Benzene-1,4-dicarboxaldehyde (BDA)	90
Figure 3.4: COF-366 Reaction Scheme using 5,10,15,20-tetrakis-(4-aminophenyl) porphyrin (TAPP) which are linked together via a Schiff-base condensation reaction with benzene-1,4-dicarboxaldehyde (BDA).	92
Figure 3.5: 0.15 g CuSO ₄ ·5H ₂ O, 60 μ L (2 mg/mL BDA), 40 μ L of 0.123 mg/mL TAPP in anisole spin coated: 1000 rpm, accelerated 12,000 rps, 2 minutes, 130 °C for 18.5 hours. a) and b) imaging parameters: V _s = -0.55 V and I _t = 5 pA. c) Line profile indicated in Figure 3.5 b) which has been drift corrected.	94
Figure 3.6: Section taken from Figure 3.5 b) with the COF-366 structure overlaid.	95

Figure 3.7: 0.15 g CuSO ₄ ·5H ₂ O, 60 μL (2 mg/mL BDA), 40 μL of 0.123 mg/mL TAPP in anisole spin coated: 1000 rpm, 12, 000 rps, 2 minutes, 130 °C for 18.5 hours. Imaging parameters: V _s = -0.55 V and I _t = 5 pA.....	95
Figure 3.8: 0.15 g CuSO ₄ ·5H ₂ O, 60 μL (2 mg/mL BDA), 40 μL of 0.041 mg/mL TAPP in anisole spin coated: 1000 rpm, 12, 000 rps, 2 minutes, 130 °C for 19 hours. a) Imaging parameters: V _s = -0.55 V and I _t = 5 pA. b) and c) Imaging parameters: V _s = -0.55 V and I _t = 10 pA. d) Line profile indicated in Figure 3.8 c).	97
Figure 3.9: 0.15 g CuSO ₄ ·5H ₂ O, 60 μL (2 mg/mL BDA), 40 μL of 0.041 mg/mL TAPP in anisole spin coated: 1000 rpm, 12, 000 rps, 2 minutes, 130 °C for 65 hours. Imaging parameters: V _s = -0.55 V and I _t = 5 pA.....	100
Figure 3.10: 0.16 g CuSO ₄ ·5H ₂ O, 60 μL (2 mg/mL BDA), 50 μL of 0.35 mg/mL TAPP in anisole spin coated: 1000 rpm, 500 rps, 2 minutes, 20 μL acetic acid, 130 °C for 52 hours. Imaging parameters: V _s = -0.55 V and I _t = 10 pA.....	101
Figure 3.11: 0.15 g CuSO ₄ ·5H ₂ O, 60 μL (2 mg/mL BDA), 50 μL of 0.26 mg/mL TAPP in anisole spin coated: 2000 rpm, 1500 rps, 2 min, 5 μL acetic acid, 130 °C for 16 hours. a) and b) imaging parameters: V _s = -0.50 V and I _t = 5 pA.	102
Figure 3.12: 0.15 g CuSO ₄ ·5H ₂ O, 65 μL (2 mg/mL BDA), 75 μL of 0.30 mg/mL ZnTAPP in THF spin coated: 1000 rpm, 500 rps, 2 minutes, 130 °C for 20 hours. Imaging parameters: V _s = -0.55 V and I _t = 10 pA.....	104
Figure 3.13: 0.15 g CuSO ₄ ·5H ₂ O, 65 μL (2 mg/mL BDA), 75 μL of 0.30 mg/mL ZnTAPP in THF spin coated: 1000 rpm, 500 rps, 2 minutes, 130 °C for 20 hours. Imaging parameters: V _s = -0.55 V and I _t = 10 pA. Drift corrected.....	104
Figure 3.14: 0.15 g CuSO ₄ ·5H ₂ O, 30 μL (4 mg/mL BDA), 50 μL of 0.10 mg/mL CuTAPP in THF spin coated: 800 rpm, 10, 000 rps, 2 minutes, 130 °C for 3 hours. Imaging parameters: V _s = -0.55 V and I _t = 10 pA.....	105
Figure 3.15: FT-IR spectrum of TAPP, 18.18 mg/mL in chloroform spin coated (10, 000 rps; 800 rpm; 2 min) on calcium fluoride substrate.	106
Figure 3.16: FT-IR spectrum of COF made from TAPP 18.18 mg/mL in chloroform spin coated (10, 000 rps; 800 rpm; 2 min) on calcium fluoride substrate; 0.15 g CuSO ₄ ·5H ₂ O, 30 μL of 2 mg/mL BDA, argon purged and 16 hours at 130 °C.	107

Figure 3.17: N1s XPS spectra for unreacted ZnTAPP and ZnCOF. The synthesis procedure is detailed in Figure 3.12. The black lines represent experimental data after background subtraction. The coloured components correspond to Gaussian–Lorentzian functions used to fit the data. The graph legends show the binding energy associated with each component. The schematic at the bottom of the figure shows the molecular configurations of the different N species. The orange area is the satellite peak. 108

Figure 3.18: Modified diagram of Figure 2.3 showing an additional pressure release valve incorporated into the steel autoclave to prevent condensation of BDA linker..... 113

Figure 4.1: Ground state absorbance spectrum of TAPP (0.006575 mg/mL in chlorobenzene). 2 mm path length quartz cuvette. 121

Figure 4.2: Microsecond transient absorption (TA) spectrum of TAPP (0.006575 mg/mL in chlorobenzene). 2mm path length quartz cuvette. Excited with a pump wavelength of 427 nm and excitation density of $45 \mu\text{J cm}^{-2}$ 122

Figure 4.3: Kinetics of TAPP (0.006575 mg/mL in chlorobenzene). 2mm path length quartz cuvette. Excited with a pump wavelength of 427 nm, probe wavelength of 750 nm and excitation density of $40 \mu\text{J cm}^{-2}$. The red dashed line indicates the monoexponential fit with the lifetime of the species $\tau_1 = 3.42 \times 10^{-5} \text{ s}$ 123

Figure 4.4: Oxygen dependent kinetics of TAPP (0.006575 mg/mL in chlorobenzene). 2mm path length quartz cuvette. Excited with a pump wavelength of 427 nm and a probe wavelength of 750 nm..... 124

Figure 4.5: Ground state absorbance spectrum of TAPP (0.006575 mg/mL in chlorobenzene); and a COF solution (1.5 mL of 0.01315 mg/mL TAPP + 1.5 mL of 0.2973 mg/mL BDA in chlorobenzene + 10 μL acetic acid). 2 mm path length quartz cuvette. 125

Figure 4.6: Microsecond transient absorption spectrum of COF solution (1.5 mL of 0.01315 mg/mL TAPP + 1.5 mL of 0.2973 mg/mL BDA in chlorobenzene + 10 μL acetic acid). 2mm path length quartz cuvette. Excited with a pump wavelength of 427 nm and excitation density of $33 \mu\text{J cm}^{-2}$ 126

Figure 4.7: Microsecond transient absorption spectrum of TAPP (0.006575 mg/mL in chlorobenzene) and COF solution (1.5 mL of 0.01315 mg/mL TAPP + 1.5 mL

of 0.2973 mg/mL BDA in chlorobenzene + 10 μ L acetic acid). 2mm path length quartz cuvette. Excited with a pump wavelength of 427 nm and excitation density of 45 μ J cm^{-2} and 33 μ J cm^{-2} respectively.	127
Figure 4.8: Ground state absorption of TAPP film (9.56 mg/mL in anisole spin coated: 10, 000 rps; 800 rpm; 2 min).....	128
Figure 4.9: Microsecond transient absorption spectrum of TAPP film (9.56 mg/mL in anisole spin coated: 10, 000 rps; 800 rpm; 2 min). Excited with a pump wavelength of 450 nm and excitation density of 42 μ J cm^{-2}	129
Figure 4.10: Oxygen dependent kinetics of TAPP (20.86 mg/mL in anisole spin coated: 10, 000 rps; 800 rpm; 2 min). Excited with a pump wavelength of 450 nm, probe wavelength of a) 850 nm, b) 1250 nm, and excitation density of 42-43 μ J cm^{-2}	129
Figure 4.11: Kinetics of TAPP film (1.1 mg/mL in anisole spin coated: 10,000 rps; 800 rpm; 2 min). Excited with a pump wavelength of 450 nm and probe wavelength of 850 nm.	131
Figure 4.12: Kinetics of TAPP film (1.1 mg/mL in anisole spin coated: 10,000 rps; 800 rpm; 2 min). Excited with a pump wavelength of 450 nm and probe wavelength of 1250 nm.	131
Figure 4.13: Normalised to 1 Δ OD measured at 10 μ s as a function of laser excitation density. The slope to the plateau, which is an average of both data plots, is plotted as a blue line with a gradient, x, of 0.017.	132
Figure 4.14: Comparison of kinetics of TAPP film (1.1 mg/mL in anisole spin coated: 10,000 rps; 800 rpm; 2 min). Excited with a pump wavelength of 450 nm and different probe wavelengths.	133
Figure 4.15: Kinetics of TAPP (20.86 mg/mL in anisole spin coated: 10, 000 rps; 800 rpm; 2 min). Excited with a pump wavelength of 450 nm and probed at 650 nm.	136
Figure 4.16: Kinetics of TAPP (20.86 mg/mL in anisole spin coated: 10, 000 rps; 800 rpm; 2 min). Excited with a pump wavelength of 450 nm and probed at 800 nm.	136

Figure 4.17: Kinetics of TAPP (20.86 mg/mL in anisole spin coated: 10, 000 rps; 800 rpm; 2 min). Excited with a pump wavelength of 450 nm and probed at 850 nm.	136
Figure 4.18: Kinetics of TAPP (20.86 mg/mL in anisole spin coated: 10, 000 rps; 800 rpm; 2 min). Excited with a pump wavelength of 450 nm and probed at 1250 nm.	136
Figure 4.19: Normalised ground state absorption spectrum of a solution of TAPP (0.006575 mg/mL in chlorobenzene), and a TAPP film (8.06mg/mL spin coated: 12,000 rps; 800 rpm; 2 mins).	137
Figure 4.20: Normalised microsecond transient absorption spectrum of TAPP film (8.06mg/mL spin coated: 12,000 rps; 800 rpm; 2 mins), excited with a pump wavelength of 450 nm and excitation density of $40 \mu\text{J cm}^{-2}$, compared to a solution of TAPP (0.006575 mg/mL in chlorobenzene), 2mm path length quartz cuvette, excited with a pump wavelength of 427 nm and excitation density of $45 \mu\text{J cm}^{-2}$	138
Figure 4.21: Ground state absorption of TAPP film (9.56 mg/mL in anisole spin coated: 10, 000 rps; 800 rpm; 2 min) and COF synthesised from mentioned TAPP film.	140
Figure 4.22: Microsecond transient absorption spectrum of a COF film made from TAPP film (9.56 mg/mL in anisole spin coated: 10, 000 rps; 800 rpm; 2 min). Excited with a pump wavelength of 450 nm and excitation density of $53 \mu\text{J cm}^{-2}$	141
Figure 4.23: Oxygen dependent kinetics of COF film. Excited with a pump wavelength of 450 nm, probe wavelength of 765 nm and excitation density of $48 \mu\text{J cm}^{-2}$	142
Figure 4.24: Kinetics of a COF film. Excited with a pump wavelength of 450 nm and probe wavelength of 765 nm.	143
Figure 4.25: Kinetics of a COF film. Excited with a pump wavelength of 450 nm and probe wavelength of 800 nm.	143
Figure 4.26: Kinetics of COF. Excited with a pump wavelength of 450 nm and probe wavelength of 1250 nm.	144
Figure 4.27: Normalised ΔOD measured at $10 \mu\text{s}$ as a function of laser excitation density. The slope to the plateau, which is averaged amongst the different probe wavelengths, is plotted as a green line with a gradient, x , of 0.016.	144

Figure 4.28: Comparison of COF kinetics at probe wavelengths of 765, 800 and 1250 nm. Excited with a pump wavelength of 450 nm. Excitation density is 53 -56 $\mu\text{J cm}^{-2}$	146
Figure 4.29: Kinetics of COF film. Excited with a pump wavelength of 450 nm and probed at 650 nm.....	147
Figure 4.30: Kinetics of COF film. Excited with a pump wavelength of 450 nm and probed at 765 nm.....	147
Figure 4.31: Kinetics of COF film. Excited with a pump wavelength of 450 nm and probed at 800 nm.....	147
Figure 4.32: Kinetics of COF film. Excited with a pump wavelength of 450 nm and probed at 1250 nm.....	147
Figure 4.33: Normalised microsecond transient absorption spectrum of TAPP film (9.56 mg/mL in anisole spin coated: 10, 000 rps; 800 rpm; 2 min), excited with a pump wavelength of 450 nm and excitation density of 42 $\mu\text{J cm}^{-2}$, compared to a COF made from the aforementioned TAPP film, excited with a pump wavelength of 450 nm and excitation density of 53 $\mu\text{J cm}^{-2}$. Ground state absorbance overlaid.	149
Figure 4.34: Kinetics of TAPP (20.86 mg/mL in anisole spin coated: 10, 000 rps; 800 rpm; 2 min) and COF film. Both films excited with a pump wavelength of 450 nm and probed at 650 nm. TAPP film at an excitation density of 43 $\mu\text{J cm}^{-2}$ and COF film at 48 $\mu\text{J cm}^{-2}$	151
Figure 4.35: Kinetics of TAPP (20.86 mg/mL in anisole spin coated: 10, 000 rps; 800 rpm; 2 min) and COF film. Both films excited with a pump wavelength of 450 nm. TAPP film probed at 850 nm and at an excitation density of 43 $\mu\text{J cm}^{-2}$ and COF film probed at 765 nm and at an excitation density of 48 $\mu\text{J cm}^{-2}$	151
Figure 4.36: Kinetics of TAPP (20.86 mg/mL in anisole spin coated: 10, 000 rps; 800 rpm; 2 min) and COF film. Both films excited with a pump wavelength of 450 nm and probed at 800 nm. TAPP film measured at an excitation density of 43 $\mu\text{J cm}^{-2}$ and COF film measured at an excitation density of 48 $\mu\text{J cm}^{-2}$	151
Figure 4.37: Kinetics of TAPP (20.86 mg/mL in anisole spin coated: 10, 000 rps; 800 rpm; 2 min) and COF film. Both films excited with a pump wavelength of 450 nm and probed at 1250 nm. TAPP film measured at an excitation density of 43 $\mu\text{J cm}^{-2}$ and COF film measured at an excitation density of 48 $\mu\text{J cm}^{-2}$	151

Figure 4.38: A plot of the change in α value against the change in transient peak between TAPP and COF films (nm). All films were made in exactly the same way, as detailed in Chapter 2.	153
Figure 4.39: Ground state absorption of TAPP film (9.56 mg/mL in anisole spin coated: 10, 000 rps; 800 rpm; 2 min) and COF synthesised from mentioned TAPP film.	155
Figure 4.40: Ground state absorption of TAPP film (9.56 mg/mL in anisole spin coated: 10, 000 rps; 800 rpm; 2 min) and COF synthesised from mentioned TAPP film. Straight dashed lines at 652 and 680 nm showing different pump wavelengths that will be used.	155
Figure 4.41: Microsecond transient absorption spectrum of TAPP film (9.56 mg/mL in anisole spin coated: 10, 000 rps; 800 rpm; 2 min). Excited with a pump wavelength of 680 nm and excitation density of $48 \mu\text{J cm}^{-2}$	156
Figure 4.42: Microsecond transient absorption spectrum of a COF film made from TAPP film (9.56 mg/mL in anisole spin coated: 10, 000 rps; 800 rpm; 2 min). Excited with a pump wavelength of 652 nm and excitation density of $45 \mu\text{J cm}^{-2}$	157
Figure 4.43: Normalised microsecond transient absorption spectrum of TAPP film (9.56 mg/mL in anisole spin coated: 10, 000 rps; 800 rpm; 2 min), excited with a pump wavelength of 680 nm and excitation density of $48 \mu\text{J cm}^{-2}$, compared to COF made from aforementioned film, excited with a pump wavelength of 652 nm and excitation density of $45 \mu\text{J cm}^{-2}$. Ground state absorbance overlaid.	158
Figure 4.44: Normalised to 1 microsecond transient absorption spectrum of TAPP film, excited with a pump wavelength of 450 nm and excitation density of $43 \mu\text{J cm}^{-2}$, compared to a TAPP film excited with a pump wavelength of 680 nm and excitation density of $43 \mu\text{J cm}^{-2}$	160
Figure 4.45: Normalised microsecond transient absorption spectrum of TAPP film, excited with a pump wavelength of 450 nm and excitation density of $43 \mu\text{J cm}^{-2}$, compared to a TAPP film excited with a pump wavelength of 680 nm and excitation density of $43 \mu\text{J cm}^{-2}$	160
Figure 4.46: Normalised microsecond transient absorption spectrum of a COF made from a TAPP film excited with a pump wavelength of 652 nm and excitation	

density of $45 \mu\text{J cm}^{-2}$, compared to a COF film excited with a pump wavelength of 450 nm and excitation density of $52 \mu\text{J cm}^{-2}$	160
Figure 4.47: Normalised to 1 microsecond transient absorption spectrum of a COF made from a TAPP film excited with a pump wavelength of 652 nm and excitation density of $45 \mu\text{J cm}^{-2}$, compared to a COF film excited with a pump wavelength of 450 nm and excitation density of $52 \mu\text{J cm}^{-2}$	160
Figure 5.1: Molecular orbital diagram for metalloporphyrins showing orbital mixing between the π^* and metal d-orbitals.	167
Figure 5.2: The $d\pi$ metal orbital overlap with the π system of the porphyrin ring.	167
Figure 5.3: Ground state absorption of ZnTAPP film (ZnTAPP in THF spin coated: 10, 000 rps; 800 rpm; 2 min).....	170
Figure 5.4: Microsecond transient absorption spectrum of ZnTAPP film (ZnTAPP in THF spin coated: 10, 000 rps; 800 rpm; 2 min). Excited with a pump wavelength of 450 nm and excitation density of $32 \mu\text{J cm}^{-2}$	170
Figure 5.5: Oxygen dependent kinetics of ZnTAPP film (2.95 mg/mL in THF spin coated: 10, 000 rps; 800 rpm; 2 min). Excited with a pump wavelength of 450 nm, probe wavelength of a) 750 nm, b) 1125 nm, and excitation density of $32 \mu\text{J cm}^{-2}$	171
Figure 5.6: Kinetics of ZnTAPP film (ZnTAPP in THF spin coated: 10, 000 rps; 800 rpm; 2 min). Excited with a pump wavelength of 450 nm and probed at 750 nm.	172
Figure 5.7: Kinetics of ZnTAPP film (ZnTAPP in THF spin coated: 10, 000 rps; 800 rpm; 2 min). Excited with a pump wavelength of 450 nm and probed at 875 nm.	172
Figure 5.8: Kinetics of ZnTAPP film (ZnTAPP in THF spin coated: 10, 000 rps; 800 rpm; 2 min). Excited with a pump wavelength of 450 nm and probed at 1125 nm.	173
Figure 5.9: Normalised ΔOD measured at $10 \mu\text{s}$ as a function of laser excitation density. The slope to the plateau is averaged amongst the three data plots and is a green line with a gradient, x , of 0.032.	174

Figure 5.10: Kinetics of ZnTAPP film (ZnTAPP in THF spin coated: 10, 000 rps; 800 rpm; 2 min). Excited with a pump wavelength of 450 nm and excitation density of $30 \mu\text{J cm}^{-2}$, with varying probe wavelengths.	174
Figure 5.11: Comparison of alpha values at the three sampling wavelengths for ZnTAPP with error bars showing standard deviation.....	175
Figure 5.12: Ground state absorption of ZnTAPP film (ZnTAPP in THF spin coated: 10, 000 rps; 800 rpm; 2 min) and ZnCOF made from said ZnTAPP film.	176
Figure 5.13: Microsecond transient absorption spectrum of ZnCOF film. Excited with a pump wavelength of 450 nm and excitation density of $32 \mu\text{J cm}^{-2}$	177
Figure 5.14: Oxygen dependent kinetics of ZnCOF film. Excited with a pump wavelength of 450 nm and probe wavelength of a) 750 nm and b) 1125 nm.....	178
Figure 5.15: Kinetics of ZnCOF film. Excited with a pump wavelength of 450 nm and probed at 750 nm.	178
Figure 5.16: Kinetics of ZnCOF film. Excited with a pump wavelength of 450 nm and probed at 875 nm.	179
Figure 5.17: Kinetics of ZnCOF film. Excited with a pump wavelength of 450 nm and probed at 1125 nm.	179
Figure 5.18: Normalised ZnCOF ΔOD measured at $10 \mu\text{s}$ as a function of laser excitation density. The slope to the plateau is an average of the three probe plot and is shown as a green line with a gradient, x , of 0.025.	181
Figure 5.19: Kinetics of ZnCOF film. Excited with a pump wavelength of 450 nm and excitation density of $32 \mu\text{J cm}^{-2}$, with varying probe wavelengths.	181
Figure 5.20: Microsecond transient absorption spectrum of ZnTAPP film (ZnTAPP in THF spin coated: 10, 000 rps; 800 rpm; 2 min) and ZnCOF film made from said ZnTAPP film. Excited with a pump wavelength of 450 nm and excitation density of $32 \mu\text{J cm}^{-2}$	182
Figure 5.21: Normalised microsecond transient absorption spectrum of ZnTAPP film (ZnTAPP in THF spin coated: 10, 000 rps; 800 rpm; 2 min) and ZnCOF film made from said ZnTAPP film. Excited with a pump wavelength of 450 nm and excitation density of $32 \mu\text{J cm}^{-2}$. Ground state absorption overlaid.	183
Figure 5.22: Kinetics of ZnTAPP film (ZnTAPP in THF spin coated: 10, 000 rps; 800 rpm; 2 min) and ZnCOF film made from said ZnTAPP film. Excited with a pump	

wavelength of 450 nm, probe wavelength of 750 nm and excitation density of 30 and 32 $\mu\text{J cm}^{-2}$ respectively.	184
Figure 5.23: Kinetics of ZnTAPP film (ZnTAPP in THF spin coated: 10, 000 rps; 800 rpm; 2 min) and ZnCOF film made from said ZnTAPP film. Excited with a pump wavelength of 450 nm, probe wavelength of 875 nm and excitation density of 30 and 32 $\mu\text{J cm}^{-2}$ respectively.	184
Figure 5.24: Kinetics of ZnTAPP film (ZnTAPP in THF spin coated: 10, 000 rps; 800 rpm; 2 min) and ZnCOF film made from said ZnTAPP film. Excited with a pump wavelength of 450 nm, probe wavelength of 1125 nm and excitation density of 30 and 32 $\mu\text{J cm}^{-2}$ respectively.	184
Figure 5.25: Ground state absorption of CuTAPP film (10.01 mg/mL in anisole spin coated: 10, 000 rps; 800 rpm; 2 min).	185
Figure 5.26: Microsecond transient absorption spectrum of CuTAPP film (10.01 mg/mL in anisole spin coated: 10, 000 rps; 800 rpm; 2 min) excited with a pump wavelength of 450 nm and excitation density of 67 $\mu\text{J cm}^{-2}$	186
Figure 5.27: Oxygen dependent kinetics of CuTAPP film (10.01 mg/mL in anisole spin coated: 10, 000 rps; 800 rpm; 2 min). Excited with a pump wavelength of 450 nm and probe wavelength of a) 725 nm and b) 1050 nm.	187
Figure 5.28: Kinetics of CuTAPP film (10.01 mg/mL in anisole spin coated: 10, 000 rps; 800 rpm; 2 min). Excited with a pump wavelength of 450 nm and probe wavelength of 475 nm.	188
Figure 5.29: Kinetics of CuTAPP film (10.01 mg/mL in anisole spin coated: 10, 000 rps; 800 rpm; 2 min). Excited with a pump wavelength of 450 nm and probe wavelength of 725 nm.	188
Figure 5.30: Kinetics of CuTAPP film (10.01 mg/mL in anisole spin coated: 10, 000 rps; 800 rpm; 2 min). Excited with a pump wavelength of 450 nm and probe wavelength of 1050 nm.	189
Figure 5.31: Normalised CuTAPP ΔOD measured at 10 μs as a function of laser excitation density.	189
Figure 5.32: Kinetics of CuTAPP film (10.01 mg/mL in anisole spin coated: 10, 000 rps; 800 rpm; 2 min). Excited with a pump wavelength of 450 nm and varying probe wavelengths.	190

Figure 5.33: Ground state absorption of CuTAPP film (10.01 mg/mL in anisole spin coated: 10, 000 rps; 800 rpm; 2 min) and CuCOF made from said CuTAPP film.	191
Figure 5.34: Microsecond transient absorption spectrum of CuCOF film. Excited with a pump wavelength of 450 nm and excitation density of 70 $\mu\text{J cm}^{-2}$	192
Figure 5.35: Oxygen dependent kinetics of CuCOF film. Excited with a pump wavelength of 450 nm and probe wavelength of a) 725 nm and b) 1050 nm.	193
Figure 5.36: Kinetics of CuCOF film. Excited with a pump wavelength of 450 nm and probed at 515 nm.	194
Figure 5.37: Kinetics of CuCOF film. Excited with a pump wavelength of 450 nm and probed at 725 nm.	194
Figure 5.38: Kinetics of CuCOF film. Excited with a pump wavelength of 450 nm and probed at 1050 nm.	195
Figure 5.39: Normalised CuTAPP ΔOD measured at 10 μs as a function of laser excitation density.	195
Figure 5.40: Kinetics of CuCOF film. Excited with a pump wavelength of 450 nm and excitation density of 75 $\mu\text{J cm}^{-2}$, with varying probe wavelengths.	196
Figure 5.41: Microsecond transient absorption spectrum of CuTAPP film (10.01 mg/mL in anisole spin coated: 10, 000 rps; 800 rpm; 2 min) and CuCOF film made from said CuTAPP film. Excited with a pump wavelength of 450 nm and excitation density of 67 $\mu\text{J cm}^{-2}$ and 70 $\mu\text{J cm}^{-2}$ respectively.	197
Figure 5.42: Normalised microsecond transient absorption spectrum of CuTAPP film (10.01 mg/mL in anisole spin coated: 10, 000 rps; 800 rpm; 2 min) and CuCOF film made from said CuTAPP film. Excited with a pump wavelength of 450 nm and excitation density of 67 $\mu\text{J cm}^{-2}$ and 70 $\mu\text{J cm}^{-2}$ respectively. Ground state absorption overlaid.	197
Figure 5.43: Kinetics of CuTAPP film (10.01 mg/mL in anisole spin coated: 10, 000 rps; 800 rpm; 2 min) and CuCOF film made from said CuTAPP film. Excited with a pump wavelength of 450 nm, probe wavelength of 475 and 515 nm, and excitation density of 70 $\mu\text{J cm}^{-2}$ and 75 $\mu\text{J cm}^{-2}$ respectively.	199
Figure 5.44: Kinetics of CuTAPP film (10.01 mg/mL in anisole spin coated: 10, 000 rps; 800 rpm; 2 min) and CuCOF film made from said CuTAPP film. Excited with a	

pump wavelength of 450 nm, probe wavelength of 725 nm, and excitation density of $79 \mu\text{J cm}^{-2}$ and $75 \mu\text{J cm}^{-2}$ respectively..... 199

Figure 5.45: Kinetics of CuTAPP film (10.01 mg/mL in anisole spin coated: 10,000 rps; 800 rpm; 2 min) and CuCOF film made from said CuTAPP film. Excited with a pump wavelength of 450 nm, probe wavelength of 1050 nm, and excitation density of $71 \mu\text{J cm}^{-2}$ and $75 \mu\text{J cm}^{-2}$ respectively..... 199

Figure 5.46: A plot of the change in α value against the change in transient peak between CuTAPP and CuCOF films (nm)..... 200

Figure 5.47: Microsecond transient absorption spectrum of TAPP film (7.67 mg/mL in anisole spin coated: 10,000 rps; 800 rpm; 2 min) excited with a pump wavelength of 450 nm and excitation density of $42 \mu\text{J cm}^{-2}$; compared to a ZnTAPP film (2.95 mg/mL in THF spin coated: 10,000 rps; 800 rpm; 2 min) excited with a pump wavelength of 450 nm and excitation density of $32 \mu\text{J cm}^{-2}$; and CuTAPP film (10.01 mg/mL in anisole spin coated: 10,000 rps; 800 rpm; 2 min) excited with a pump wavelength of 450 nm and excitation density of $67 \mu\text{J cm}^{-2}$ 201

Figure 5.48: Normalised microsecond transient absorption spectrum of TAPP film (7.67 mg/mL in anisole spin coated: 10,000 rps; 800 rpm; 2 min) excited with a pump wavelength of 450 nm and excitation density of $42 \mu\text{J cm}^{-2}$; compared to a ZnTAPP film (2.95 mg/mL in THF spin coated: 10,000 rps; 800 rpm; 2 min) excited with a pump wavelength of 450 nm and excitation density of $32 \mu\text{J cm}^{-2}$; and CuTAPP film (10.01 mg/mL in anisole spin coated: 10,000 rps; 800 rpm; 2 min) excited with a pump wavelength of 450 nm and excitation density of $67 \mu\text{J cm}^{-2}$. Ground state absorbance overlaid..... 201

Figure 5.49: Normalised to per photon absorbed, microsecond transient absorption spectrum of TAPP film (7.67 mg/mL in anisole spin coated: 10,000 rps; 800 rpm; 2 min) excited with a pump wavelength of 450 nm and excitation density of $42 \mu\text{J cm}^{-2}$; compared to a ZnTAPP film (2.95 mg/mL in THF spin coated: 10,000 rps; 800 rpm; 2 min) excited with a pump wavelength of 450 nm and excitation density of $32 \mu\text{J cm}^{-2}$; and CuTAPP film (10.01 mg/mL in anisole spin coated: 10,000 rps; 800 rpm; 2 min) excited with a pump wavelength of 450 nm and excitation density of $67 \mu\text{J cm}^{-2}$. All traces are normalised from the $5 \mu\text{s}$ original traces from Figure 5.45... 202

Figure A.1: Oxygen dependent kinetics of TAPP (20.86 mg/mL in anisole spin coated: 10, 000 rps; 800 rpm; 2 min). Excited with a pump wavelength of 450 nm, probe wavelength of 800 nm and excitation density of 42-43 $\mu\text{J cm}^{-2}$	216
Figure A.2: Oxygen dependent kinetics of TAPP (20.86 mg/mL in anisole spin coated: 10, 000 rps; 800 rpm; 2 min). Excited with a pump wavelength of 450 nm, probe wavelength of 650 nm and excitation density of 42-43 $\mu\text{J cm}^{-2}$	216
Figure A.3: Oxygen dependent kinetics of COF film. Excited with a pump wavelength of 450 nm, probe wavelength of 1250 nm and excitation density of 48 $\mu\text{J cm}^{-2}$	217
Figure A.4: Oxygen dependent kinetics of COF film. Excited with a pump wavelength of 450 nm, probe wavelength of 800 nm and excitation density of 48 $\mu\text{J cm}^{-2}$	217
Figure A.5: Oxygen dependent kinetics of COF film. Excited with a pump wavelength of 450 nm, probe wavelength of 650 nm and excitation density of 48 $\mu\text{J cm}^{-2}$	218
Figure A.6: Oxygen dependent kinetics of TAPP (20.86 mg/mL in anisole spin coated: 10, 000 rps; 800 rpm; 2 min). Excited with a pump wavelength of 680 nm, probe wavelength of 1250 nm and excitation density of 44-45 $\mu\text{J cm}^{-2}$	219
Figure A.7: Oxygen dependent kinetics of TAPP (20.86 mg/mL in anisole spin coated: 10, 000 rps; 800 rpm; 2 min). Excited with a pump wavelength of 680 nm, probe wavelength of 850 nm and excitation density of 44-45 $\mu\text{J cm}^{-2}$	219
Figure A.8: Oxygen dependent kinetics of TAPP (20.86 mg/mL in anisole spin coated: 10, 000 rps; 800 rpm; 2 min). Excited with a pump wavelength of 680 nm, probe wavelength of 800 nm and excitation density of 44-45 $\mu\text{J cm}^{-2}$	220
Figure A.9: Oxygen dependent kinetics of COF film. Excited with a pump wavelength of 652 nm, probe wavelength of 1250 nm and excitation density of 44-45 $\mu\text{J cm}^{-2}$	220
Figure A.10: Oxygen dependent kinetics of COF film. Excited with a pump wavelength of 652 nm, probe wavelength of 800 nm and excitation density of 44-45 $\mu\text{J cm}^{-2}$	221

Figure A.11: Oxygen dependent kinetics of COF film. Excited with a pump wavelength of 652 nm, probe wavelength of 765 nm and excitation density of 44-45 $\mu\text{J cm}^{-2}$	221
Figure A.12: Oxygen dependent kinetics of ZnTAPP film (2.95 mg/mL in THF spin coated: 10, 000 rps; 800 rpm; 2 min). Excited with a pump wavelength of 450 nm and probe wavelength of 750 nm.....	222
Figure A.13: Oxygen dependent kinetics of ZnCOF film. Excited with a pump wavelength of 450 nm and probe wavelength of 875 nm.....	222
Figure A.14: Oxygen dependent kinetics of CuTAPP film (10.01 mg/mL in anisole spin coated: 10, 000 rps; 800 rpm; 2 min). Excited with a pump wavelength of 450 nm and probe wavelength of 475 nm.....	223
Figure A.15: Oxygen dependent kinetics of CuCOF film. Excited with a pump wavelength of 450 nm and probe wavelength of 515 nm.....	223

1 Background and Motivation

1.1 Introduction

Covalent organic frameworks (COFs) are a type of crystalline porous polymers which allow the atomically precise incorporation of organic units to create structures with predesigned skeletons and nanopores.¹ By constructing the frameworks using strong covalent bonds, well-defined crystalline porous structures, with the possibility to introduce different functionalities, can be achieved. The advantages of COFs are their innate porosity, ordered channel structure, defined pore size, and large surface area. This leads to a variety of applications; for example, catalysis, gas storage, adsorption and optoelectronics.¹

With regards to gas storage, one example is the potential use of COFs to store hydrogen. Hydrogen is a promising alternative energy carrier due to its clean combustion and high chemical energy density.² For commercial use of hydrogen as a power source, efficient and safe storage of hydrogen is one of the main bottlenecks. Consequently, a large number of studies have focused on hydrogen storage with porous materials.^{2,3} The US Department of Energy has set a target for hydrogen storage of 5.5 wt% at an operating temperature of -40 to 60 °C and under a maximum pressure of 100 atm before 2025.⁴ So far, three-dimensional (3D) COFs have shown potential for hydrogen storage due to their high surface areas. Most notably, Furukawa *et al.* have synthesised “COF-102” which shows hydrogen uptake of 7.24 wt% at saturation (~ 35 atm, 0°C).⁵

Porous solids with large surface areas for heterogeneous catalysis have been known for several decades.⁶ Suitable COF candidates for catalytic applications should incorporate robust catalytic sites and possess a high stability to thermal treatments, water, and most organic solvents. Furthermore, the easy accessibility to the catalytic

sites and the efficient mass transport inside the porous catalyst should also be guaranteed for the ideal catalytic performance. Ding *et al.* have taken advantage of the regular structure of COFs and have synthesised “COF-LZU1” which has a two-dimensional (2D) eclipsed layered-sheet structure and the distance of nitrogen atoms is 3.7 Å in the adjacent layers.⁷ They have been able to find precise applications in which this distance is suitable for strong coordination of metal ions, specifically lead. “Pd/COF-LZU1” was then tested for catalysing the Suzuki–Miyaura coupling reaction.⁷ (Further information about the Suzuki–Miyaura coupling reaction can be found in Reference [7].) The excellent catalytic performance was shown by excellent yields (96–98%) of the reaction products, together with the high stability and easy recyclability of the catalyst.

This thesis focuses on the optical properties 2D-COFs possess synthesised using porphyrins. The reasoning will be explained in this chapter. Firstly, the motivation to use 2D-COFs will be outlined, then the synthesis will be briefly outlined to show the variety of 2D-COFs that have been synthesised, and the imaging technique used to monitor the synthesis of 2D-COFs. After which, the porphyrin precursors used in this research will be elaborated on i.e. their properties and applications.

1.2 Motivation

Finding sustainable energy sources is one of the biggest challenges we face in the 21st century. With a growing population, the demand for fossil fuels to drive industries, and fuel day-to-day life has increased exponentially. An alternative energy source that is renewable, sustainable and environmentally friendly is needed in order to replace fossil fuels. Renewable energy sources (RES) such as solar, tidal, geothermal, biofuels and wind provide appealing alternatives to fossil fuels. Solar energy is the most abundant of the different RES available.⁸ However, it is not always easy to store and transport this solar energy and many technologies are being researched in order to use solar energy more efficiently.

One solution is COFs with optical properties which can have the capacity to improve the way we harness and store energy with little to no impact on the environment. In general, a great deal of solar energy harvesting and energy storage technology uses heavy metals and harsh manufacturing techniques. The key emphasis for using COFs in this research is the use of light elements and economical synthetic techniques. Specifically, the focus is on porphyrin-based COFs as porphyrins have been investigated for use in organic solar cells (OSCs) for decades.

1.3 COF Synthesis

COFs are constructed from organic building blocks using reticular chemistry and display periodic architectures.⁹ COFs can be synthesised in various forms, including 3D-COFs, bulk 2D-COFs and monolayer 2D-COFs. A 3D-COF is a covalently interlinked molecular crystal. Bulk 2D-COFs consist of 2D covalent molecular layers stacked on top of each other held together by van der Waals interactions. Monolayer 2D-COFs are simply the single layers and can be studied as such, and are analogous to other 2D materials like graphene. In all these materials the molecules are linked via covalent bonds within the single layers, which is an important characteristic that defines these materials.

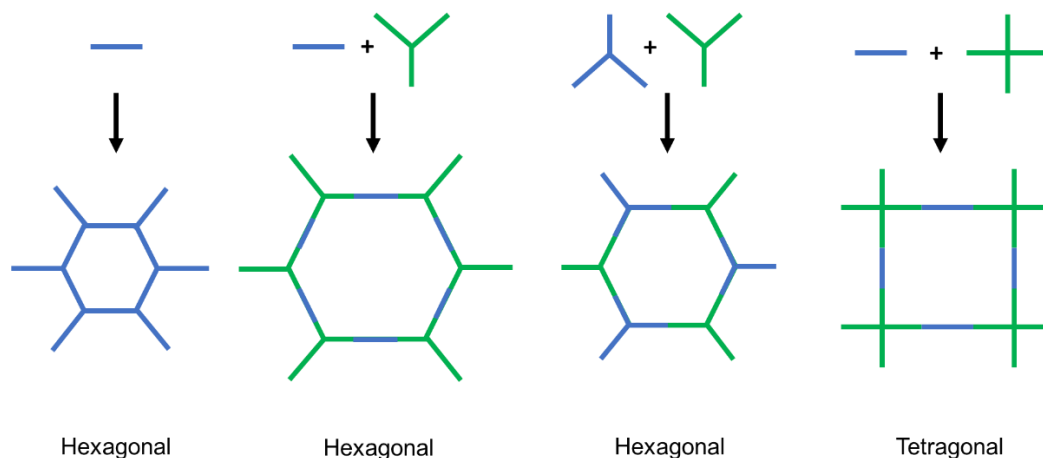


Figure 1.1: The combination of building blocks with different geometries to design 2D-COFs.

Figure 1.1 is a simple schematic to represent the beginnings of a vast library of 2D architectures that can be assembled, as well as the geometry of the pores that can be synthesised i.e. hexagonal and tetragonal. Monolayer 2D-COFs can be synthesised with a range of techniques, the most common being top-down exfoliation of bulk 2D-COFs or a bottom-up formation directly on a substrate from molecular building blocks. The size and morphology of the resulting 2D-COFs are highly tuneable and can be changed by varying the size, shape and chemical structure of the molecular building blocks used.¹⁰ The different building blocks can also give rise to different physical and chemical properties of the final 2D-COF. A bottom-up approach has been chosen as it gives more synthetic freedom with the final product because more structures can be achieved by simply changing what is deposited on a substrate, be it a change in functional group or size of a pore in a ring structure. With regards to a top-down approach, the synthesis of bulk 2D-COFs is not simple, especially with large molecules with large pore sizes, and then the exfoliation technique must be sensitive enough not to break the individual 2D-layers.

In order to form a monolayer 2D-COF on a surface via an on-surface bottom-up approach, a suitable chemical reaction mechanism needs to be chosen.¹¹ In order to be suitable, several factors need to be taken into consideration:

- 1) The molecular building blocks used must have specific desired locations where they can react to form covalent bonds, otherwise undesired side reactions may occur.
- 2) The reaction should be reversible in suitable synthesis conditions so that the formation of highly ordered 2D-COFs is more likely.
- 3) The structural integrity of the building blocks must be maintained during framework construction, respecting reticular synthesis rules.¹²

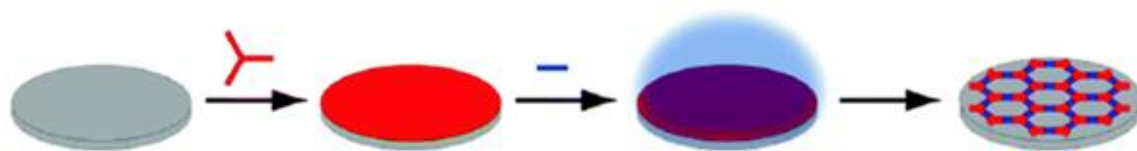


Figure 1.2: Scheme diagram for solid–vapour interface reaction. The red molecule begins as a film on the substrate and then, the blue linker is in the form of a vapour which can collide with the red molecules on the surface to react to form an extended structure i.e. a COF.¹³

Figure 1.2 shows the technique used in this thesis to synthesise 2D-COFs: an on-surface bottom-up approach, with the reaction of two precursors occurring at a solid-vapour interface. A precursor is deposited on a substrate, and the other precursor is in a vapour phase which can collide with the surface to react with the precursor on the surface. This synthesis is detailed in Chapters 2 and 3 which outlines the precursors used and the reaction occurring in the solid-vapour interface.

In order to determine the success of reactions and the morphology of the 2D-COF formed, an imaging technique is needed to study the characteristics of 2D-COFs on surfaces. One such technique is scanning tunnelling microscopy (STM), which can image surfaces at the atomic level and will be used in this thesis.

1.4 STM of COFs

Scanning tunnelling microscopy (STM) is an important experimental technique for studying molecular nanostructures adsorbed on solid surfaces. Specifically, by studying STM images of COFs, the morphology of the product, the crystallinity of the layers and the coverage on the substrate surface (i.e. domain size) can be elucidated and used as a measure of success of the synthetic procedure.

Details of the STM technique are discussed in Chapter 2. In brief, when electrons tunnel through a molecule adsorbed on a solid surface, the produced image is a result of the complex interaction of the surface, molecule and tip electronic states.¹⁴ To interpret the STM image, all three factors need to be taken into account.

The tunnelling current through a tip-molecule-substrate junction depends on the energy of the highest occupied molecular orbital (HOMO) and the lowest unoccupied molecular orbital (LUMO) of the adsorbed molecule relative to the tip and Fermi levels of both the tip and substrate. The Fermi level is the total chemical potential of electrons. The Fermi level in a metal is the highest occupied orbital in the conduction band and determines the direction of flow of electrons. The tunnelling current is also dependent on the mixing of the molecular orbitals of the adsorbed molecule with the surface electronic states. Molecules that strongly interact with the surface will show a local density of states that is a mix of both molecule and surface electronic states and will be less defined. The image produced is a topographic map of the surface, dependent on the density of states at different areas.

The following two examples show how STM has been used to learn about the success of synthesis and uses of COFs. The first is a study by Xu *et al.*, which used STM as an important tool to visually monitor the COF formed and provide information about the pore sizes and defects etc.¹⁵ Xu *et al.* studied the formation between benzene-1,3,5-tricarbaldehyde and different aromatic diamines into hexagonal surface COFs, using a Schiff-base condensation reaction on highly ordered pyrolytic graphite (HOPG). A general reaction scheme is illustrated in Figure 1.3. Through elimination of one water molecule, -CHO and -NH₂ undergo a condensation reaction and form a Schiff-base framework.¹⁶ Xu *et al.* have used four different aromatic diamines to synthesise different COF frameworks, all of which have an extended honeycomb network with hexagonal pores resulting in a surface-confined framework with a tunable pore size. Then STM was used to determine the surface coverage of the COF on HOPG and to characterise the crystallinity of the COFs.

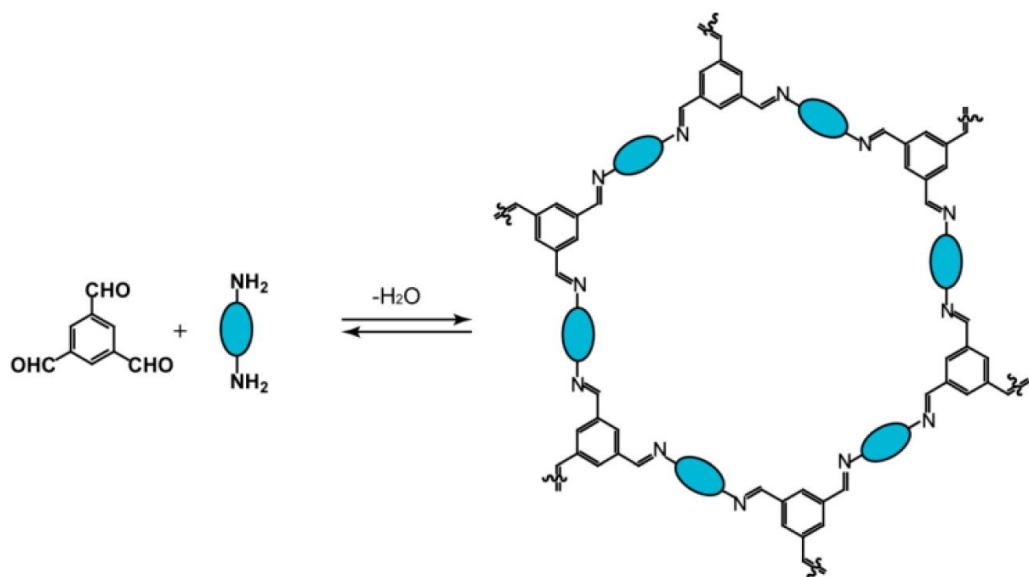


Figure 1.3: Reaction scheme of benzene-1,3,5-tricarbaldehyde and different aromatic diamines into hexagonal surface COFs. The organic backbones of aromatic diamines are symbolically represented by ellipses.¹⁵

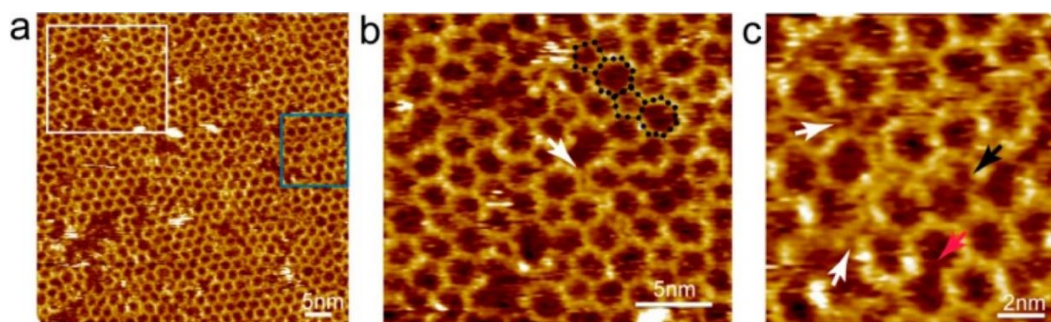


Figure 1.4: (a) STM image showing clearly the domain boundaries resulting from incomplete condensation. (b and c) Digital magnifications of the areas marked by the white and blue rectangles, respectively. White arrows indicate domain boundaries and, black and red arrows indicate defects. The tunneling conditions were $I = 0.05 \text{ nA}$, $V = 0.50 \text{ V}$.¹⁵

Figure 1.4 is an example of some of the STM images Xu *et al.* have collected.¹⁵ Using these images and others they were able to conclude several points:

- 1) STM revealed perfect single crystalline domains more than 1000 nm x 1000 nm in size;
- 2) The COFs are predominantly monolayer, the formation of a bilayer was also detected in some areas where the contrast of the image showed a

layer beneath, and the high resolution STM images confirmed that the bilayers are stacked in an eclipsed manner;

- 3) Most of the pores are hexagons, highlighting the completeness of the reaction.
- 4) The misorientated domains in the COF shown in Figure 1.4 may indicate the growth at the solid/liquid interface happens simultaneously at different sites.

Focusing on point 4, evidence supporting this hypothesis is the observation of domain boundaries resulting from incomplete reaction due to space confinement which will only happen when there are different nucleation sites rather than a fixed origin of reaction.¹⁷ Referring to Figure 1.4, the white arrows indicate such boundaries where only two out of the three aldehyde groups reacted with the amines. Due to the limited space, the third aldehyde group was not able to approach the amine monomers. This kind of domain boundary is possible only where the growth happens simultaneously at different sites and two or more growing domains meet together, which was evidenced through research by Chang *et al.* who studied perovskite crystal growth.¹⁷ The black and red arrows in Figure 1.4 indicate the other two defects, where one aldehyde and one amine building block was missing, respectively.

The following research by Liu *et al.* shows how STM has been used to study the morphology of COF structures and using previous research, find appropriate uses.¹⁸ Figure 1.5 shows two possible reactions using precursors with either amine or aldehyde functional groups studied by Liu *et al.*¹⁸ The expected pore size as predicted by density functional theory (DFT) calculations is labelled in Figure 1.5. In order to confirm the pore size *in situ* STM was used. Figures 1.6 and 1.7 were collected by Liu *et al.* and the pore size taken from the STM image was compared to the pore sizes predicted by DFT calculations.

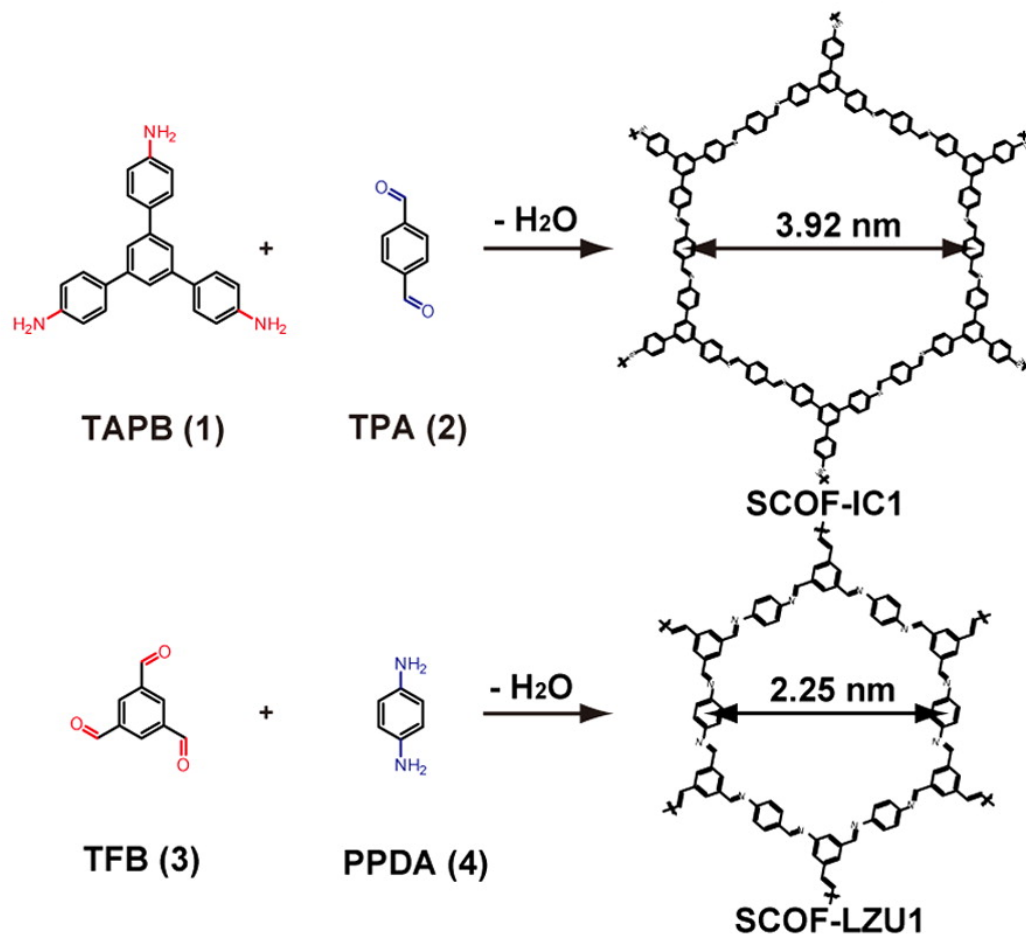


Figure 1.5: Condensation of trigonal precursors 1,3,5-tris(4-aminophenyl)benzene (TAPB, 1) or 1,3,5-triformylbenzene (TFB, 3) and linear precursors terephthalaldehyde (TPA, 2) or p-phenylenediamine (PPDA, 4) can form SCOF-IC1 or SCOF-LZU1, respectively. The expected lattice parameters are indicated.¹⁸

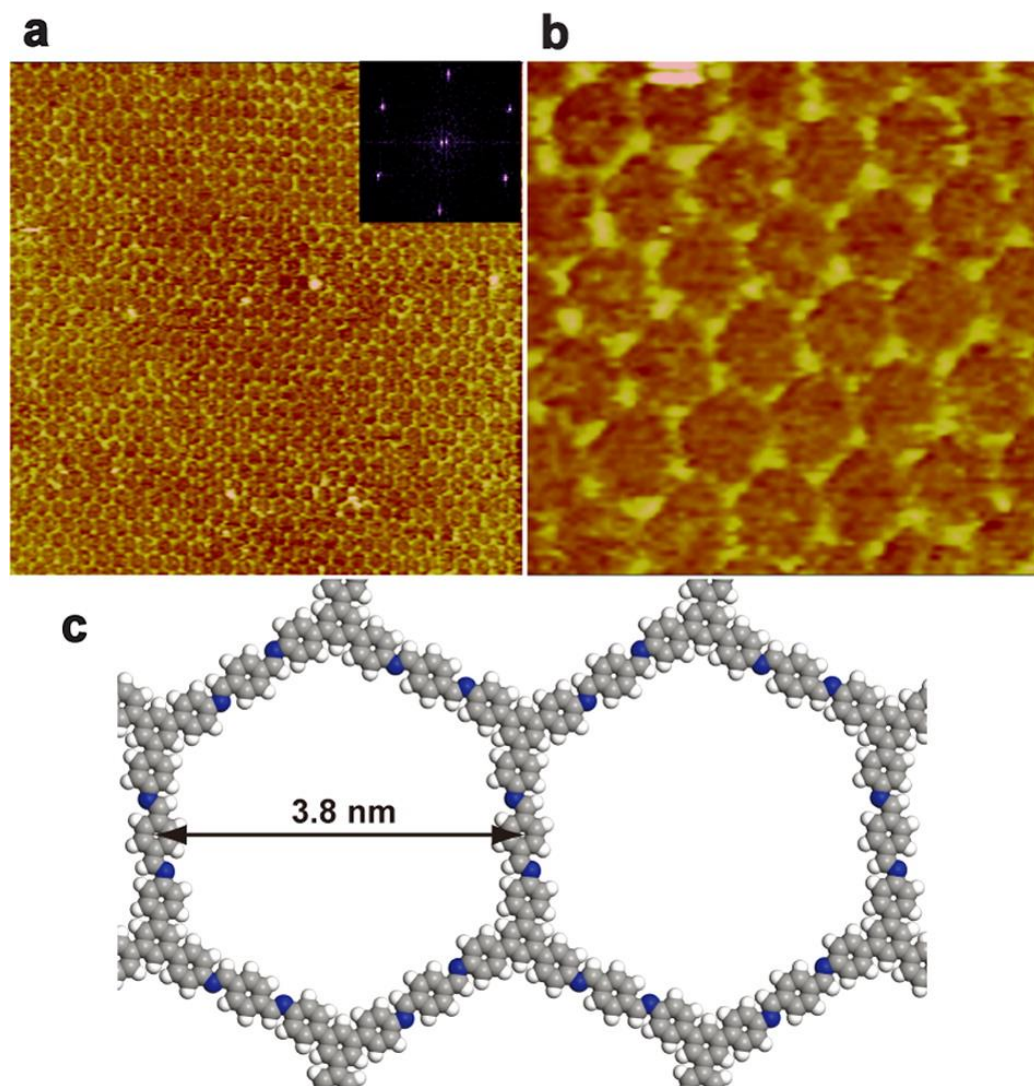


Figure 1.6: STM images and a structural model for SCOF-IC1. (a) Large-scale STM image ($100 \times 100 \text{ nm}^2$) of SCOF-IC1 with the inset depicting the corresponding fast Fourier transform (FFT) spectrum of the STM image. (b) High resolution STM image ($20 \times 20 \text{ nm}^2$) of SCOF-IC1. (c) A structural model with the measured structural parameter for SCOF-IC1. Imaging conditions: (a) $V_{bias} = 700 \text{ mV}$, $I_t = 500 \text{ pA}$; (b) $V_{bias} = 693 \text{ mV}$, $I_t = 450 \text{ pA}$.¹⁸

The lattice parameter of the structure in Figure 1.6a is measured to be $3.8 \pm 0.2 \text{ nm}$, which agrees well with the expected size of 3.92 nm by DFT calculation, and thus confirms the covalent formation of the imine-linked SCOF-IC1. Structural analysis of the SCOF-LZU1 network in Figure 1.7a shows the pore size is $2.2 \pm 0.2 \text{ nm}$ which is in excellent agreement with the 2.25 nm size predicted by the DFT calculation. After confirming the pore size, it is possible to determine the applications of gas storage or

adsorption for example. Two research groups have studied the effects of pore size on hydrogen storage, introduced at the beginning of this chapter.^{19,20} Research led by Han *et al.* and Pang *et al.* have determined that a pore size of 2.7 nm is ideal for hydrogen storage which eliminates the uses of SCOF-IC1 and SCOF-LZU1. However, Yang *et al.* have studied ammonia capture using COFs and using a pore size of 2.2 nm is ideal, opening possibilities of SCOF-LZU1 being used for ammonia storage, which was not addressed by Liu *et al.*²¹

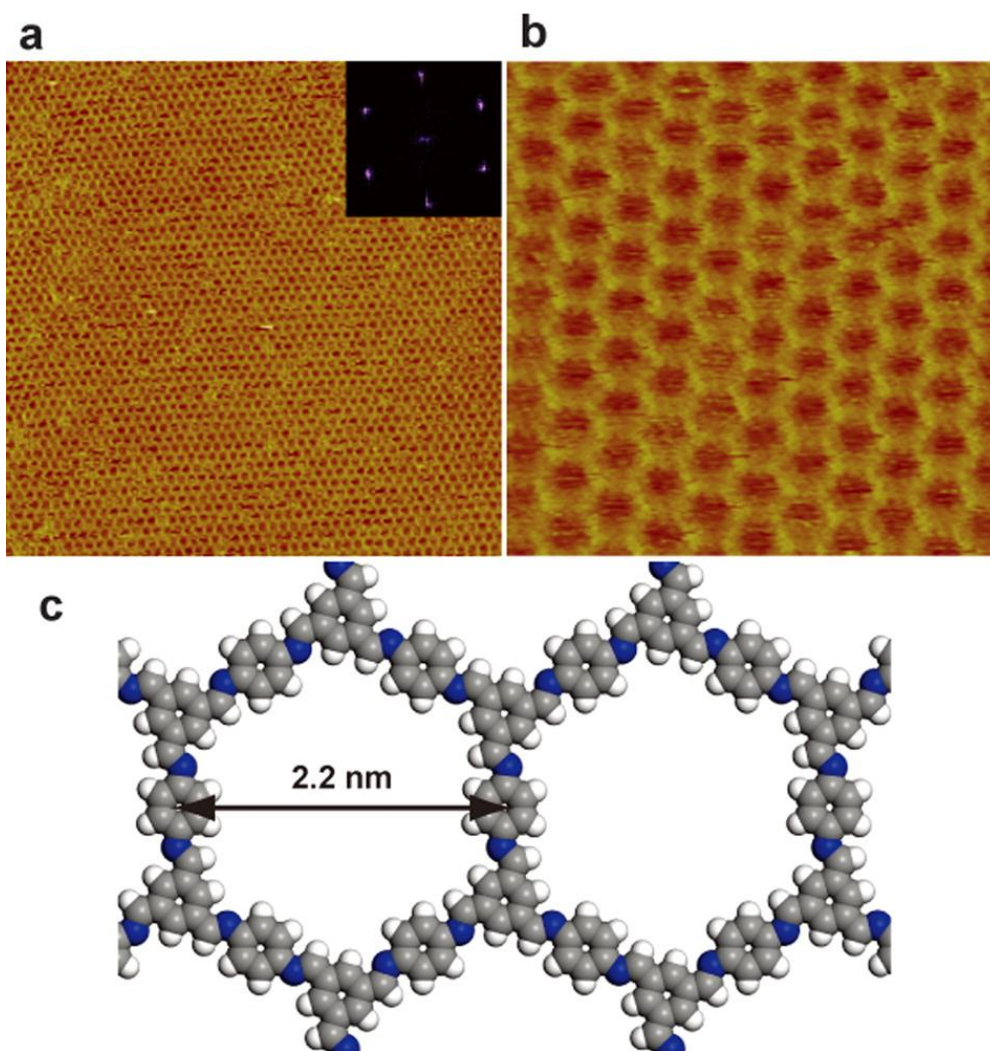


Figure 1.7: STM images and a structural model for SCOF-LZU1. (a) Large-scale STM image ($100 \times 100 \text{ nm}^2$) of SCOF-LZU1 with the inset depicting the corresponding FFT spectrum of the STM image. (b) High resolution STM image ($20 \times 20 \text{ nm}^2$) of SCOF-LZU1. (c) A structural model with the measured structural parameter for SCOF-LZU1. Imaging conditions: $V_{\text{bias}} = 620 \text{ mV}$, $I_t = 536 \text{ pA}$.¹⁸

It is clear to see the broad scope that COFs have regarding synthesis and applications. This thesis focuses on COFs made using porphyrin precursors and their optoelectronic properties. In order to understand the properties, the next section will begin with an explanation of photophysical electron transfer and energy transfer processes. Then, an explanation about why porphyrins have been chosen as the precursor and previous studies on porphyrins, highlighting their important photophysical properties that makes them ideal candidates for COFs with optoelectronic applications. Finally, previous and current applications of porphyrins will be explained and how this thesis aims to study the use of COFs in these applications as an improved alternative.

1.5 Photophysical Electron Transfer and Energy Transfer Processes

1.5.1 Singlet and Triplet States

To understand the photophysical properties of the studied porphyrins and COFs, it is important to address what photophysical pathways can occur. Excited states occur when an electron in a molecule is promoted to a higher energy level by absorbing a sufficient quantum of radiation. Shown in Figure 1.8, a singlet excited state is one in which the excited electron's spin is paired to the ground state electron spin with opposing spin. In a triplet state, the excited electron's spin is not paired with the spin of the ground state electron, i.e. they have the same spin.

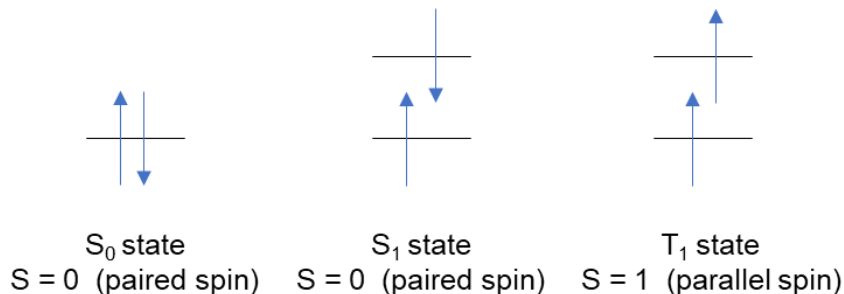


Figure 1.8: Diagram showing possible spin states after electronic excitation and their respective labels. Horizontal lines used to represent states at different quanta of energy.

Transitions between states with different spin multiplicity is “spin-forbidden”, according to the Pauli Exclusion Principle (no two electrons can have the same quantum number), because of a required change between two different spin states and therefore, is less likely to occur compared to transitions with no change in spin multiplicity.^{22,23} Electrons with the same spin tend to be well separated, minimising the Coulombic repulsion between them and lowering the overall energy of the system.²⁴

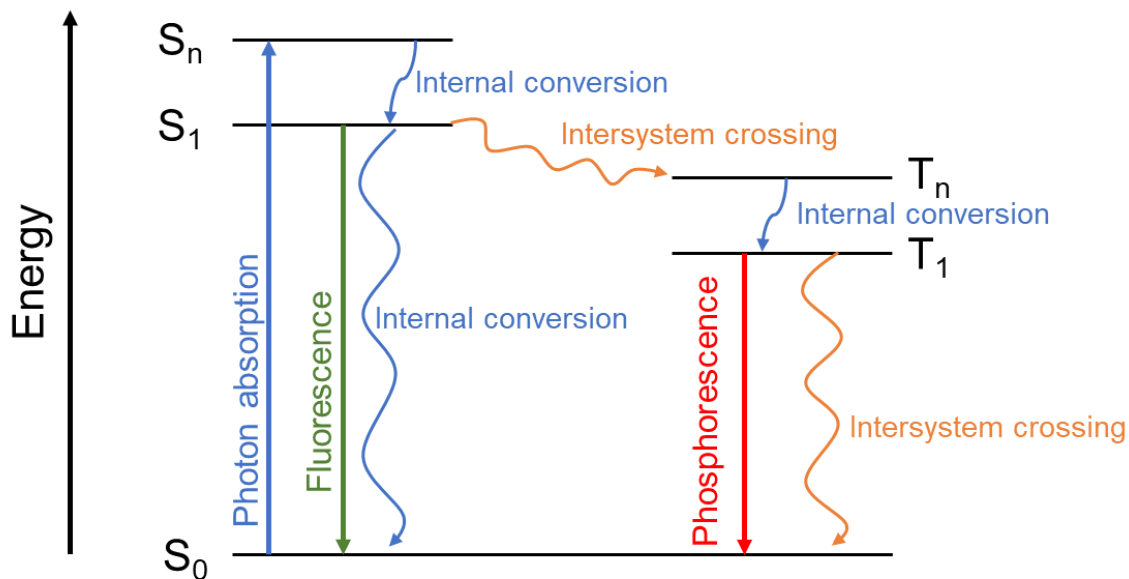


Figure 1.9: A Jablonski diagram illustrating the electronic states of a molecule and the transitions between. The straight arrows indicate radiative processes, the curved arrows indicate non-radiative processes.

After excitation, there are relaxation processes that can occur. Figure 1.9 illustrates some electronic states of a molecule and the transitions between them. After absorption of photons of a particular wavelength to an S_n energy level, the electrons have additional energy to lose. Some of the energy can be lost as vibrational energy. Once some of the energy is lost, the molecule returns to the lowest vibrational level of the S_1 excited state, this is called internal conversion. Once this point is reached, to return to the ground state, the molecule can relax via fluorescence. For fluorescence, the excited electron in the S_1 state returns to the ground state by ejecting the extra energy as a photon. The spin multiplicity of the electrons is also preserved in fluorescence. Internal conversion is also possible between the S_1 and ground state because for some molecules, the vibrational levels of the ground state overlap with the S_1 state, which leads to fast deactivation.²⁵

However, it is possible to transition between two electronic states with different spin multiplicities *via* intersystem crossing (ISC), illustrated in Figure 1.9. ISC is a non-radiative process and a singlet state can non-radiatively pass to a triplet state, or *vice versa*, and principally the spin of the excited electron is changed. ISC is more common in molecules containing heavy-atoms due to enhanced spin-orbit coupling.²⁶ The radiative decay from an excited triplet state back to the singlet ground state is known as phosphorescence. Although transitions between states of different spin multiplicity are spin forbidden, singlet states occasionally have some triplet character due to mixing of the singlet and triplet wavefunctions, thus relaxing this selection rule. Nevertheless, the probability for such a transition remains small, and as a consequence, the triplet–singlet transition is very long-lived and can result in phosphorescence lifetimes on the order of milliseconds to a few seconds.²⁷

1.5.1.1 Oxygen: Quenching Triplet States

Oxygen readily quenches triplet states.²⁸ The mechanism of oxygen quenching of triplet states is complex and beyond the scope of this thesis. The mechanism has been extensively studied, and a detailed mechanism can be found from References [28-32].²⁸⁻³²

In brief, oxygen (O_2) is a biradical: a molecular system with two unpaired electrons. The ground state electronic structure of oxygen is a triplet, 3O_2 , and the unpaired electrons each occupy a degenerate anti-bonding π^* -orbital. The S_1 excited state of oxygen is when the two electrons pair up in one π^* -orbital: this is now singlet oxygen, 1O_2 with the term symbol $^1\Sigma^+_g$. Excitation will prompt the electronic transition from 3O_2 to 1O_2 . After a triplet excited state of a molecule is formed, the excited electron will undergo a relaxation process but because it is a spin-forbidden process the lifetime is longer than non-spin-forbidden processes. However, if the triplet excited state meets an oxygen molecule and the energy supplied is greater than the $0.98\text{ eV } T_0 \rightarrow S_1$ energy gap, then the interaction of the two triplet species provides a mechanism for the excited triplet state of the molecule to relax to its singlet ground state without breaking any fundamental principles. The triplet excited state of the molecule transfers its excitation energy on to the triplet ground state of the oxygen, so that the molecule returns to its singlet ground state while the oxygen is converted to a singlet excited state.

1.5.2 Charge-Transfer (CT) States

The following description of CT states is used as COF assemblies are analogous to donor-acceptor systems, as recently studied by Duvva *et al.* who looked at the intramolecular electron transfer in porphyrin-anthraquinone donor-acceptor systems.³³

A charge-transfer (CT) state is an association of two or more molecules, or of different parts of one large molecule, in which electronic charge is transferred between the molecular moieties.^{34,35} For example, Humphrey and Kuciauskas determine a CT state can be described as involving electron transfer from the porphyrin macrocycle to the metal d orbitals.^{36,37} The source molecule from which the charge is transferred is called the electron donor (D) and the receiving species is called the electron acceptor (A). An exciton is a bound state of an electron and an electron hole which are attracted to each other by the electrostatic Coulomb force.

When the exciton is localised on the donor material, the charge separation involves charge transfer between the lowest unoccupied molecular orbitals (LUMO) of D and A. This process, usually referred to as electron transfer, is driven by the $LUMO_D - LUMO_A$ energy difference. When the exciton is localised on the acceptor, hole transfer is driven by the difference in energy of the highest occupied molecular orbitals (HOMO) of A-D: $HOMO_A - HOMO_D$.^{38,39} In either case, charge transfer leads to an intermolecular charge-transfer (CT) state consisting of an electron and a hole that are located on the A and D respectively. Considering a material which is a blend of electron donor and acceptor moieties, upon excitation, the incident photons are absorbed by the material and generate an exciton that can subsequently dissociate into a pair of spatially separated charges at the D-A interface.⁴⁰ In the CT state, the charges still interact with each other as a result of the Coulomb forces acting across the D-A interface. For charge photogeneration, the creation of charge transfer states represents the intermediate step between exciton and fully separated charges. Recombination of free charges to the ground state is via the bound charge transfer state before being lost to the ground state. Bound charges are likely to recombine.⁴¹ If an electron and hole recombine with the same electron or hole they originated from then this is called geminate recombination. If the electron and hole and recombine with any other hole or electron, then this is called bimolecular recombination. Modern organic solar cells (OSCs) demonstrate ultrafast formation of CT states from excitons, and efficient dissociation of CT states into charge under short circuit conditions.⁴²

1.6 Porphyrins

This thesis focuses on porphyrins to make COFs because they have been studied for decades and have been shown to generate triplet states and charge states, which will be elaborated upon in following sections.⁴³⁻⁵¹

Porphyrins are large macrocycles with an 18-electron π system and are useful for the synthesis of porous materials like COFs. Porphyrins are a class of molecules

containing a flat ring of four linked heterocyclic pyrrole subunits, connected at their α -carbon atoms via methine bridges. The α -carbon positions are displayed in Figure 1.10.

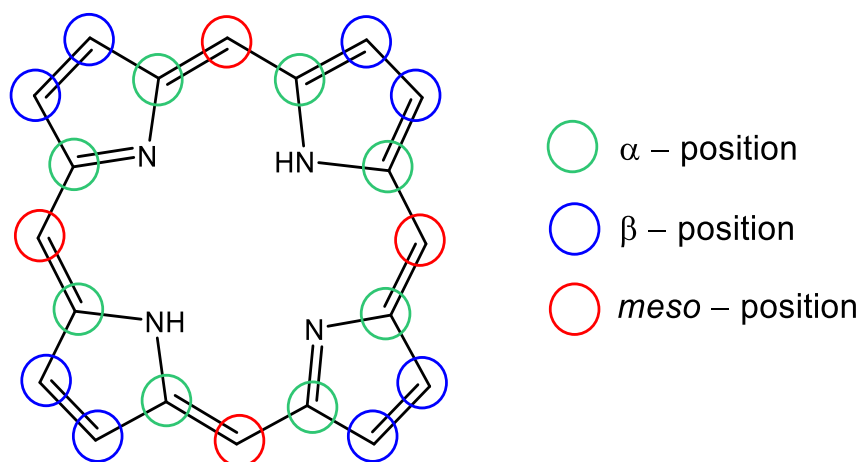


Figure 1.10: Structure of porphin, the simplest porphyrin.

The four nitrogen atoms in the porphyrin core can coordinate to a range of different metal atoms. A porphyrin's ground state optical characteristics and excited state properties (energy, lifetime, emission yield) can be tuned by changing the coordinated metal atom as well as the substituents at the peripheral *meso*- or β -positions, shown in Figure 1.10. To probe these changes, the ground state absorption UV-visible spectra are useful tools to compare porphyrin structures.

1.6.1 Ground State UV-Visible Absorption Spectra of Porphyrins

Porphyrins have characteristic ground state UV-visible absorption spectra that consist of two distinct regions: in the near ultraviolet and in the visible/near-IR region. It has been well documented that changes in the conjugation and symmetry of a porphyrin can affect its UV-visible absorption spectrum.^{44,52,53}

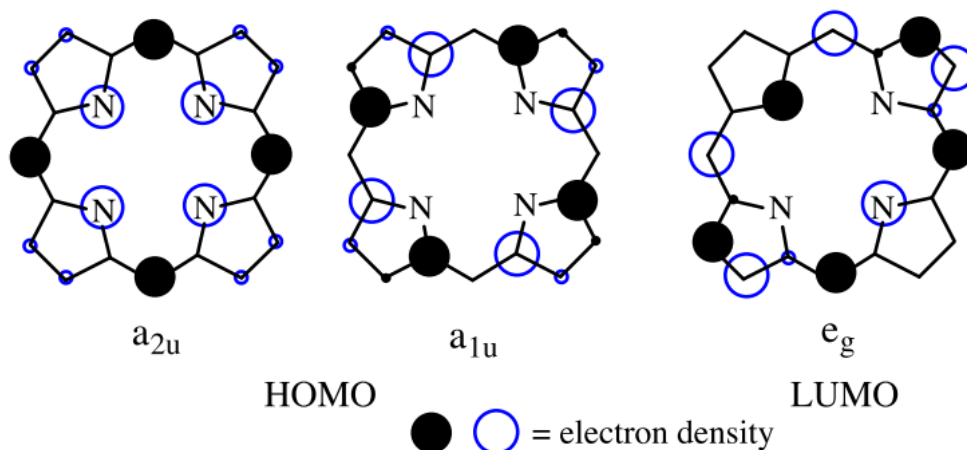


Figure 1.11: Representation of the four Gouterman orbitals in porphyrins.⁵⁴

The absorption spectra of porphyrins have long been described by the “four-orbital” (two highest occupied π orbitals and two lowest unoccupied π^* orbitals) model.⁴⁴ According to this model, the absorption bands in porphyrin systems arise from transitions between two HOMOs and two LUMOs, and it is the identities of the metal centre and the substituents on the ring that affect the relative energies of these transitions. The HOMOs were calculated by Gouterman to be an a_{1u} and an a_{2u} orbital, while the LUMOs were calculated to be a degenerate set of e_g orbitals, shown in Figure 1.11.⁴⁴ (The terms a_{1u} , a_{2u} and e_g refer to the symmetry notation of the molecular orbitals.⁵⁵) Transitions between these orbitals gives rise to two excited states. Orbital mixing splits these two states in energy, creating a higher energy state and a lower energy state. Therefore, the UV-visible spectrum of a typical porphyrin consists of two distinct regions shown in Figure 1.12. The first involves the transition from the ground state to the second excited state ($S_0 \rightarrow S_2$) and the corresponding band is called the Soret band. The range of absorption is between 380-500 nm depending on whether the porphyrin is β - or *meso*-substituted. The second region consists of a weak transition to the first excited state ($S_0 \rightarrow S_1$) corresponding to the Q bands, and these appear in the range between 500-750 nm.

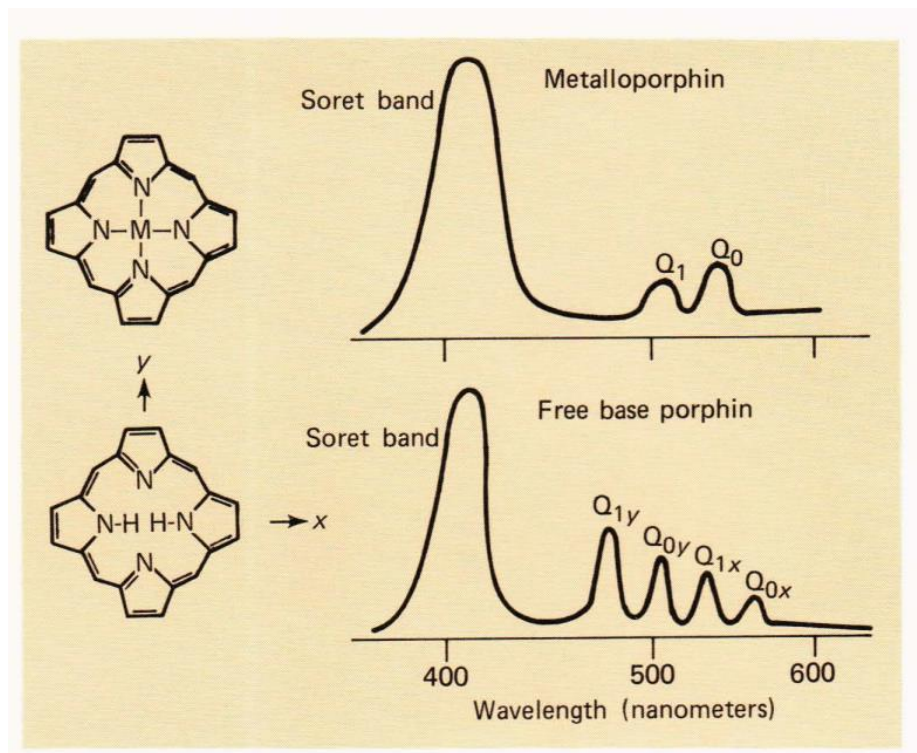


Figure 1.12: The chemical structures for free-base and metallated forms of porphyrin are shown on the left. The ground state UV-visible spectra are shown on the right. Q_0 in metalloporphyrin is due to a pure electronic transition (no molecular vibrations) between the electronic ground state and the first electronic excited state; Q_1 is due to the same electronic transition but, in addition, molecular vibrations are involved. This band is called a vibronic band. The subscripts 0 and 1 for free base porphyrin carry a similar interpretation. The x and y subscripts refer to the orientation (polarisation) of the vector of the absorbed light with respect to the axes shown on the chemical structure diagram for freebase porphyrin.⁵⁶

The relative intensity of Q bands is due to the type and position of substituents on the macrocycle ring.⁵⁷ In addition, a porphyrin macrocycle can exist freebase (in D_{2h} symmetry) or metallated (in D_{4h} symmetry). Q_0 in metalloporphyrin is due to a pure electronic transition (no molecular vibrations) between the electronic ground state and the first electronic excited state. Q_1 is due to the same electronic transition but, in addition, molecular vibrations are involved. This band is called a vibronic band. The subscripts 0 and 1 for freebase porphyrin carry a similar interpretation. The x and y subscripts refer to the orientation (polarisation) of the vector of the absorbed light with respect to the axes shown on the chemical structure diagram for freebase porphyrin. So, when the porphyrin macrocycle is coordinated with a metal, the macrocycle has

increased symmetry than in the porphyrin free base and this produces a simplification of Q bands pattern for the formation of two Q bands. Therefore, free base porphyrins display four Q bands, but, metallated porphyrins show two Q bands.⁴⁴

1.6.2 Emission Studies of Porphyrins

The ground state UV-visible absorption spectra of porphyrins are unique but it does not explain why porphyrins have been extensively studied for their photophysical properties and why they can be used in optoelectronics for example. The application of porphyrins in optoelectronics is inspired by natural photosynthetic systems performing effective light harvesting and electron transfer, specifically chlorophylls, the basic structure of which is a porphyrin ring.⁵⁸ Studies of the photophysical dynamics of porphyrins and their multi-chromophoric derivatives has paid particular attention to the behaviour of higher electronic states accessed by photoexcitation in the strong Soret absorption band.⁵⁹ Then by studying the emission from the higher electronic states (wavelengths of photons emitted during their transition from an excited state to the ground state), the intensity and timescales of emission of porphyrins have shown they can be used as key components harvesting solar radiation and converting it into electric current.^{60,61} Panda *et al.* have studied natural porphyrin-synthetic systems and believe that porphyrins, being abundant in most natural pigments, are an important element for designing artificial molecular assemblies for solar photoconversion.⁶¹

The first studies of the emission spectra of porphyrins occurred in the 1960s and set a basis for future emission studies of porphyrins.⁶²⁻⁶⁴ Photophysical processes (such as fluorescence, phosphorescence, and their respective lifetimes) are important tools for the elucidation of the mechanism of excited state interactions. As previously stated, porphyrins encompass a wide range of macrocyclic molecules, with or without coordinated metal centres. Therefore, some porphyrins are known to fluoresce rather than phosphoresce, *vice versa*, or both. For example, zinc-tetraphenylporphyrin (ZnTPP) is widely studied because it exhibits both fluorescence and phosphorescence.⁶⁵ The emission studies of porphyrins have collected information determining why certain

molecules preferentially undergo fluorescence rather than phosphorescence, *vice versa*, and other factors that affect these competing processes.

Phosphorescence is common of transition-metal porphyrins.⁶⁶ Explained in Section 4.1, electronic transitions associated with a change of spin are prohibited by the spin-selection rule. However, transition-metal ions that have a high atomic number and a large spin-orbit coupling (SOC) usually leads to more efficient spin-orbit coupling which can relax the spin selection rule. Fast intersystem crossing in the sub-picosecond to picosecond time scale leads to rapid depletion of a singlet excited state to a triplet excited state instead of fluorescence as fluorescence radiative lifetime is typically in the nanosecond range.⁶⁶ Thus, in transition-metal complexes, phosphorescence normally prevails in their emission spectra.

However, free-base porphyrins are still known to phosphoresce. Harriman has studied free-base, zinc-, nickel-, and manganese-porphyrins.⁶⁷ The results published by Harriman show that the geometry and tautomerism of the porphyrin can also affect the rate constants for ISC. Harriman proposed that the enhanced rate of ISC for free-base porphyrins is associated with the pyrrole N-H bonds. Perun *et al.* have further investigated the rates of ISC in free-base porphyrins to show that opening of an unprotonated pyrrole ring as well as excited-state single and double proton transfer inside the porphyrin cavity leads to crossings of the potential energy curves of the lowest singlet and triplet excited states.⁴⁶ This leads to efficient radiationless deactivation of the lowest singlet excited states of free-base porphyrin via ISC. By tuning the geometry of the porphyrin, fluorescence can be enhanced. Liu *et al.* have induced long-lived fluorescence by intercalating free-base porphyrin molecules with DNA, introducing rigidity in the porphyrin core.⁶⁸

So far, the photophysical processes, such as electron transfer, have been explained, as well as unique properties of porphyrins which give these molecules interesting ground state UV-visible and emission spectra. In the next sections, previous studies of porphyrins investigating the aforementioned electron transfer mechanisms

will be described. Then the historical and modern applications using porphyrins' unique photophysical properties, for example, dye-sensitized solar cells (DSSCs) and organic solar cells (OSCs) will be explained.

1.6.3 Flash Photolysis of Porphyrins showing Triplet Species

Previous studies of porphyrins, mainly chlorophyll and its derivatives, have used a flash photolysis technique, also known as a pump-probe technique. Flash photolysis is a technique in which a sample is first excited by a strong pulse of light from a laser (the "pump"). This first pulse leads to an increased population of energy levels other than the ground state within the sample. The absorption of light by the sample is recorded within short time intervals by a "probe" pulse to monitor relaxation processes initiated by the pump pulse.⁶⁹

The existence of a triplet state in chlorophylls is well established.⁷⁰⁻⁷⁵ Pekkarinen *et al.* have used the evidence of triplets in chlorophylls to study tetraphenylporphine, zinc-tetraphenylporphine and bacteriochlorophyll.⁷¹ Collecting the triplet absorption spectra of these compounds in solution using flash photolysis, Pekkarinen *et al.* have been able to discern many features of triplets like those the chlorophylls exhibit in flash photolysis. For example, in every case, the strongest triplet absorption band lies just to the red of the main Soret peak. This feature seems to be as typical of these compounds as the Soret band itself. All the spectra also show a second peak lying on the high-energy side of the Soret absorption, and the spectra show a peculiarly broad absorption, extending into the infrared. These same general aspects also have been found by Livingston and Fujimori in studying triplets using photographic flash experiments on various porphyrins, chlorins and phthalocyanines and may be regarded now as well established.^{74,75}

Another example is porphin, in Figure 1.10, which has been studied and it is believed that after excitation in the Soret band, higher excited states internally convert to the lowest singlet excited state, S_1 . After, ~ 5 % of the molecules relax to the ground state *via* fluorescence, while $S_1 \rightarrow T_1$ intersystem crossing transfers ~ 90 % of the

molecules to the lowest triplet state.⁴⁶ The depopulation of the triplet state to the ground state results in phosphorescence which, in the case of porphin, is a very low quantum yield. Most triplet states relax to the ground state via intersystem crossing in the case of porphin.

1.6.4 Porphyrin Studies Showing Charges

Even though porphyrins are known to produce excited triplet states, research has also shown that porphyrin systems can favour long-lived charge separated (CS) states.⁷⁶ Flamigni *et al.* have studied a metallated porphyrin triad film which shows a charge-separated state (free charges) in the microsecond range.⁷⁶ Evidence for the formation of free charges was obtained by a flash photolysis technique called transient absorption spectroscopy (TAS). A previous study by Flamigni *et al.* using a free-base porphyrin showed a fast charge recombination (~ 3.5 ns) due to the presence of a low-lying triplet state localised on a free-base porphyrin.⁷⁷ However, substitution of the free-base porphyrin unit with zinc porphyrin in the triad is expected to result in an increase in the triplet energy level; this should leave the CS state as the lowest state with the only possibility to deactivate to the ground state. So, using the zinc porphyrin Flamigni *et al.* measured a CS state with a lifetime of 450 ns. An estimate of the efficiency of the charge separation process with respect to the photons absorbed by the zinc porphyrin moiety was calculated on the basis of the molar absorption coefficient. High efficiency in the charge separation process requires a very fast electron transfer, so to prevent competition with luminescence. The detected quenching of the luminescence is faster than 20 ps in agreement with this requirement, but this is specifically in this zinc porphyrin system. Griffith *et al.* have studied porphyrins as the light harvesting component of dye-sensitised nanocrystalline TiO₂ solar cells and determine a nanosecond range (0.5 – 100 ns) charge recombination between photo-injected electrons and porphyrin cations.⁷⁸ Griffith *et al.* express that charge recombination is an important limitation of most porphyrin-sensitised solar cells but there nanosecond range is greatly different from the 450 ns CS state lifetime reported by Flamigni *et al.*. It is important to note that the porphyrin studied by

Flamingi *et al.* is a zinc porphyrin in a triad system whereas the Griffith *et al.* porphyrin is in a DSSC, showing how versatile the applications of porphyrins can be and the extent to which they can behave differently in different systems. As shown in Section 5.1.1, geometry of porphyrins plays an important role in electron transfer. It is the same case for energy transfer as Flamingi *et al.* state that it is essential that the multicomponent systems be rigid to ensure good geometrical control to favour long-lived CS states.⁷⁶

Geometrical control is emphasised by Qi *et al.*, who have studied charges present in porphyrin films.⁷⁹ UV-visible absorption spectra and infrared spectra were used to determine the formation of ordered porphyrin films. The charge transfer characteristics were studied using cyclic voltammetry (CV). The results showed that the structural order of the porphyrin films has an effect on the charge transfer characteristics. The amount of charges and the diffusion coefficient of charges change regularly with the degree of order of the porphyrin films and the number of layers of the porphyrin films. A set of films was made at varying degrees of order, and CV measurements undertaken. As the order of the film increased, the current value increased significantly. Therefore, with increased order of porphyrin molecules, the charge of the film enhances.⁸⁰ Research by Yoshizawa on electron transport in π -conjugated molecules states the symmetry and regular spatial distribution of frontier orbitals is an important factor governing electron transport properties within and between molecules.⁸⁰ The phase and amplitude of the HOMO and LUMO of π -conjugated molecules determine the essential properties of their electron transport. Thus, when the molecules are more ordered; the phase, amplitude, and spatial distribution of the frontier orbitals facilitates improved electron transfer, which is more efficient in applications.

Brédas *et al.* have studied organic semiconductors and the basic parameters that govern charge transport, one important parameter is the amplitude of the electronic transfer integrals between adjacent oligomer or polymer chains.⁸¹ This amplitude is extremely sensitive to the molecular packing of the system; and in fully π -

conjugated systems, the largest splitting of the HOMO and LUMO levels was consistently found for perfectly cofacial configurations (two faces parallel and π -orbitals overlapping). Therefore, when multi-layered systems are used, efficient and fast electron transport will occur when the molecules and/or films are well ordered.

1.6.5 Porphyrin Applications

1.6.5.1 Dye-Sensitised Solar Cells

Dye-sensitised solar cells (DSSCs) are photovoltaic devices that are used to convert light energy into electrical energy by the use of organic dyes (photosensitisers) and semiconductors.⁸² DSSCs were invented in the 1980s by M. Grätzel and the publication of the first high efficiency (the conversion of incident photons to electrical current is more than 80%) DSSC was in 1991 by B. O'Regan and M. Grätzel.⁸³ An in-depth explanation of a DSSC can be found from Reference [84].⁸⁴ For the purposes of this thesis, the following is a brief description and illustrated in Figure 1.13.

A typical DSSC is a sandwich structure device having four major parts:^{85,86}

- 1) A photoanode composed of a nanocrystalline semiconductor film such as TiO_2 on a conducting glass substrate.
- 2) Monolayer of a sensitiser, normally a dye, adsorbed on the TiO_2 surface.
- 3) An electrolyte containing a redox couple such as I^-/I_3^- .
- 4) A cathode.

The cell is illuminated through the TiO_2 side. Upon illumination:

- 1) Light absorbed by the sensitiser that is adsorbed on the surface of TiO_2 excites an electron.
- 2) An electron from the excited dye injects into the conduction band (CB) of TiO_2 . The dye molecules lose an electron (oxidised).
- 3) The free electron travels through the layer of TiO_2 and flow through the external circuit to arrive at the counter electrode.
- 4) The electrode converts I_3^- to I^- .

5) Then, the oxidised dye is reduced back to its neutral state by electron donation from the electrolyte. The electrolyte usually is an organic solvent or ionic liquid solvent containing an I_3^-/I^- redox system. I^- is regenerated by reduction of I_3^- at the counter electrode.

Through the above steps (1 – 5) the circuit is completed and the process can continue without permanent chemical change. Step 5) is completed by recombination of the injected electrons, either with the oxidised dye or the electron acceptor of the redox couple (I_3^-), and by relaxation of the excited dye to its ground state by a non-radiative decay process.

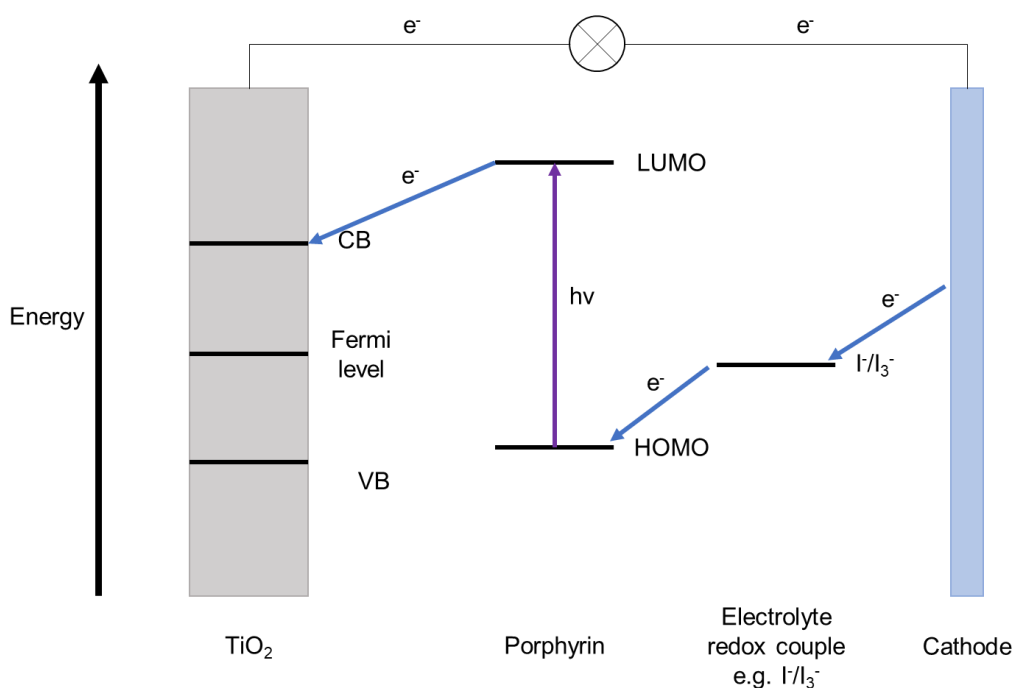


Figure 1.13: Energy levels scheme of a DSSC.

In this section the focus is on the dye, specifically an organic dye containing porphyrins. The dye acts as an electron donor in DSSC by absorbing visible light, generating excited electrons and injecting them into the semiconductor. Porphyrins have been focused on because of their modest cost, large molar absorption coefficients and stability.⁸⁵ The extended π macrocycle of porphyrins is beneficial to adsorb on the TiO_2 surface because it promotes strong electronic coupling of energy levels of the

excited porphyrin sensitiser and the TiO₂, which results in fast and efficient electron transfer. As shown in Figure 1.13, the energy of the LUMO orbitals of porphyrins are above the conduction band of TiO₂ while the HOMO level is below the redox couple of the electrolyte solution.⁵⁴ Also, porphyrins absorb light in the visible and near infrared (NIR) spectrum and the properties of porphyrin sensitisers can be modified by changing the functional groups at the β- and *meso*- positions and changing the metal centre.

With respect to porphyrin DSSCs, the highest power conversion efficiency of 13 % has been achieved by Mathew *et al* in 2014.⁸⁷ They used a molecularly engineered porphyrin dye, coded SM315, which features the prototypical structure of a donor–π-bridge–acceptor, and maximises electrolyte compatibility and improves light-harvesting properties. Rather than using a I⁻/I₃⁻ redox couple, a [Co(bpy)₃]^{2+/3+} redox couple was used with SM315. Many properties and materials can be changed for DSSCs, the literature is extensive, and this includes the wide variety of porphyrin DSSCs.

1.6.5.2 Organic Solar cells

Porphyrins have more commonly been used in DSSCs but are now appearing more frequently in organic solar cells (OSCs). OSCs have been one of the many key research areas into renewable energy sources. This is because of their unique characteristics such as low-cost, easy manufacturing, light-weight and flexibility.⁸⁸ Most OSCs are made of an organic active layer between an anode and cathode. The organic active layer contains a p-type material as the electron-donor and an n-type material as the electron-acceptor, which could be fabricated as a bilayer or bulk heterojunction (BHJ) blend, as shown in Figure 1.14.

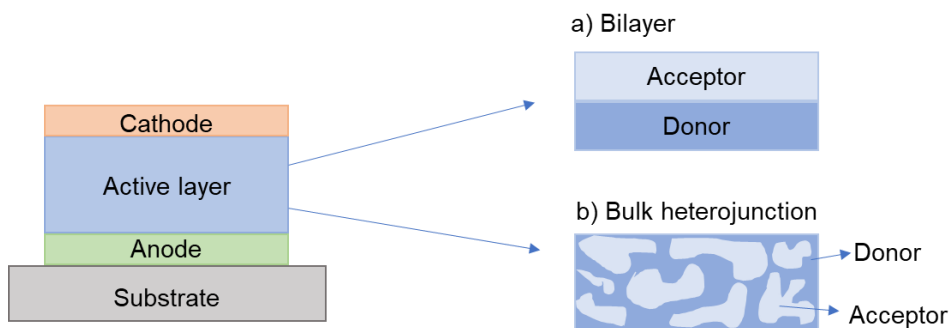


Figure 1.14: Organic solar cell set-up.

The BHJ blend arrangement has been shown to represent the most effective configuration to increase the internal donor-acceptor area, allowing for efficient charge separation and a bicontinuous network for both electron and hole transport.⁸⁸ There has been increased research into creating the materials used for the electron-donor and electron-acceptor materials for photovoltaics. Porphyrins have been extensively researched because of a number of features:

- 1) They are excellent light-harvesters because of their high molar absorptivity coefficients in both the blue and red part of the visible spectrum.
- 2) Exhibit efficient electron transfer.
- 3) Their optical and electronic properties can be easily fine-tuned by straightforward synthetic modifications at the β - and *meso*-positions and variations of the metal centre.
- 4) They are robust, air stable and have good thermal stability.

Looking at nature, many studies into OSCs are looking towards porphyrins because porphyrin analogues with extensive π -conjugated systems show high efficiency in photosynthesis. Gao *et al.* have used pyrrole units linked to porphyrin cores to extend the π -conjugation via an ethynylene bridge. This is for two reasons; (1) introducing sp^1 carbon hybridisation can lower, with respect to the vacuum level, the HOMO energy level of the target materials since there are more s-orbital components; and (2) its continual cylinder-like π -electron density is more adaptable to conformational and steric constraints, thus enhancing intermolecular π - π stacking and facilitating intramolecular charge transport.⁸⁹ In 2016 Nian *et al.* have reported a three-component OSC with 11 % efficiency, using the porphyrin studied by Gao *et al.* for near-IR sensitisation.⁹⁰ By incorporating the porphyrin, the composite film showed absorption beyond 900 nm, a first for a three-component OSC.

Fullerenes are commonly used in OSCs but Hadmojo *et al.* have studied fullerene-free, all-small-molecule (SM) OSCs based on porphyrin donors.⁹¹ Fullerene-

free all-small-molecule OSCs have attracted attention because of extremely high efficiencies and well-defined molecular structures with low batch-to-batch variation; and by removing the fullerene, the band gap of the electron-acceptor is more tunable.⁹² Porphyrin derivatives have recently emerged as one of the promising conjugated building blocks for the SM donors. Three zinc porphyrin (PZn)-based SM donors, which have strong absorption in the visible region and near-infrared region, were synthesised. Constructing bulk-heterojunction active layers using the PZn donors and a SM acceptor achieved panchromatic photon-to-current-conversion from 400 to 900 nm. The manipulation of side chains in the PZn donors considerably influenced the molecular ordering and morphology of the BHJ active layers. PZn based fullerene-free SM-OSC devices with promising power conversion efficiency of 6.13 % were achieved, setting a standard for developing fullerene-free OSCs using porphyrin derivatives. The highest power conversion efficiency of 15.7 % for non-porphyrin non-fullerene OSCs was recently published by Yuan *et al.* in 2019. However, the reason there is a focus on porphyrins is because some other organic donors possess limited absorption in the NIR. Therefore, development of organic donors with a broader absorption range is highly important for the harvesting of lower energy photons. Even though porphyrins have this broad optical absorption, further work needs to be done to improve the overall power conversion efficiency.

1.6.6 TAS on Porphyrins

This thesis will investigate the properties of porphyrins using transient absorption spectroscopy (TAS), which is explained in detail in Chapter 2.

TAS allows the investigation of photophysical processes and photochemical reactions in real time.⁹³ This research has been possible because of the advent of ultrafast tunable laser systems in the mid-1900s; the first being a dye laser discovered by Sorokin and Lankard and, Schäfer *et al.* in 1966.^{94,95} Further developments such as the continuous wave dye laser and the introduction of telescope-grating oscillators for high-power pulsed dye lasers, have led to the tunable lasers used today.^{96,97}

Transient absorption spectroscopy measures absorption spectra and kinetic behaviour of transient species: chemical species that have very short lifetimes and cannot be observed with classical experimental methods that require long detection times.⁹⁸ The key is to use an intense light pulse with a short duration to unsettle the energetic equilibrium of a system and then the generation and evolution of any transient species formed is followed spectroscopically. To do this, the change in absorbance is measured:

$$\Delta OD = OD_{excited} - OD_{initial} \quad (\text{Equation 1})$$

Where $OD_{excited}$ is the absorbance of the excited sample, $OD_{initial}$ is the absorbance of the sample before excitation and ΔOD is the change in absorbance. The duration of the excitation pulse can determine the time resolution of the measurement and the excitation pulse must be intense enough to create a detectable concentration of transient species.

The following methods could be employed (other methods are not relevant to this thesis):

- 1) The absorption spectrum of the transient species is recorded at a single delay time after the excitation pulse.
- 2) To measure the kinetics, the absorption of the sample is observed at a single probe wavelength as a function of time.

$\Delta OD(\lambda, t)$ gives information on the dynamic processes that occur in the system being studied, for example, excited-state energy migration, electron and/or proton transfer processes, isomerisation and intersystem crossing.⁹⁸ Microsecond systems cover a window of time from 10^{-7} to 10^{-2} seconds whereas femtosecond systems can measure as short a time as 10^{-15} seconds.

The lifetimes of triplet states are in the range from 10^{-4} to about 10 seconds.⁹⁹ The lifetime of charge separation then recombination is not easy to define, but with respect to porphyrins, it has been found that charge separated products are relatively

long-lived i.e. several microseconds.¹⁰⁰ By using microsecond TAS, the optical absorption and therefore any photogenerated charges of porphyrins can directly be monitored. Nanosecond and femtosecond TAS systems can be used to monitor a wide range of systems too, but with regards to this project on porphyrins and COFs, microsecond TAS is an appropriate technique because triplets and charges in porphyrins are long-lived.

1.6.6.1 Previous TAS Studies of Porphyrins in Solution and Solid State

So far, reported TAS studies have largely focused on ultrafast TAS on porphyrins in solution.^{43,101–103} In solution molecular photochemistry, a considerable degree of rationalization and understanding on the photophysical and photochemical events has been gained by applying TAS to the detection of electronic excited states and reactive intermediates generated photochemically. A previous study of TAS on porphyrins shows that there is a strong disparity between the molecules in solution and in a solid.¹⁰⁴ Li *et al.* have investigated the relaxation processes of zinc tetraphenyl porphyrin (ZnTPP). Ultrafast laser spectroscopy was applied to study excited state properties of ZnTPP films compared with monomers in solution. In solution strong quenching of the excited states S_2 and S_1 was observed as a result of intramolecular S_1-S_1 and S_2-S_2 Förster energy transfer (energy transfer through dipole coupling between molecules).¹⁰⁵ The Förster energy transfer is followed by fluorescence to the ground state. When compared with porphyrin films, their results showed ultrafast S_2-S_1 internal conversion followed by quenching of both the S_2 and S_1 states due to the efficient energy transfer between adjacent ZnTPP moieties, where both S_2 and S_1 excited states are involved. The strong quenching is a result of the significant spectral overlap of absorption and steady-state fluorescence spectra in the film.

Tran-Thi *et al.* have also used TAS to study porphyrin solutions and films. After studying the kinetic decays of a zinc-porphyrin/phthalocyanine complex in solution, they conclude that the time decay shows a long-lived triplet state. However, in a film, the transient decay kinetics were attributed to a transient charge transfer (CT) state. The difference is because of the relative energy levels of the triplet and CT states; in

solution the energy level of the CT state is higher than that of the triplet, and *vice versa* in the solid state. Tran-Thi *et al.* propose the change in energy levels is a result of the aggregation and well-ordered stacking of the porphyrins. When the porphyrins in films are well-ordered then the conjugated network is extended, facilitating the transfer of charges and the energy of the CT state lowers. In solution, the porphyrins are disordered, more solvated, and the porphyrins are not in close proximity so there is less conjugation and the triplet energy level is lower and leads to faster deactivation to the ground state.

The solvation effect on the energy of the triplet state was investigated by Barbosa Neto *et al.*⁴³ The group studied the solvent effects of excited state absorption spectra of porphyrins and their results show that the triplet state transitions $T_1 \rightarrow T_n$ are affected not only by the solvent dipole moment, but also by hydrogen bonds established between the porphyrin and solvent molecules.⁴³ In general, they observed that the energy level of triplet excited states change greatly from the environment: the triplet energy level lowers when the dipole moment of the solvent increases. They theorise that it is due to the larger solvation sphere being able to redistribute electronic density, thus, lowering the energy of the triplet state.

It is clear to see from previous research studies that small changes in the structure or moieties of porphyrins can have effects on their photophysical properties. Depending on whether the porphyrin is in a solution or film will also have an effect on the photophysical properties of the porphyrin. This thesis looks at porphyrin and COF solutions and films. The next section will outline the aims of this thesis and explain what steps will be done in order to accomplish these aims.

1.7 Thesis Aim and Structure

It is important to note that a large majority of the initial aim of this project was to investigate thin films, moving towards TAS studies of monolayer porphyrins and COFs. A thin film was arbitrarily considered a film that has a Soret peak in the ground state absorption spectrum equal to or less than 0.1 abs. This part of the project never

came to fruition because of the difficulties of adapting the TAS setup to measure thin films with a weak signal. The signal to noise ratio was overpowered by the noise of the system that no data collected was deemed trustworthy or distinguishable between porphyrin and COF.

So, the aim of this project became more to ascertain the photophysical properties of multilayer porphyrin-based COFs and understand how they may apply in optoelectronic applications. Throughout the introduction, many examples have been given on the properties of porphyrins and several of the applications of COFs. However, there have been few incongruent investigations into the photophysical properties of porphyrin-based COFs. In addition, this thesis will primarily focus on films rather than solutions. So firstly, how the COF films are made and then studied by STM will be explained.

In Chapter 4, the photophysical properties of the porphyrin in solution will be outlined but a larger focus will be on porphyrin and COF films. In Chapter 5, the focus will be on metallated porphyrins and the COFs made from them. The metallated porphyrins/COFs will be compared to the freebase porphyrin derivative.

In the conclusion, the significance of the results from this thesis will be summarised and further work will be proposed.

1.8 Bibliography

- 1 S.-Y. Ding and W. Wang, *Chem. Soc. Rev.*, 2013, **42**, 548–568.
- 2 J. Graetz, *Chem. Soc. Rev.*, 2009, **38**, 73–82.
- 3 J. Germain, J. M. J. Fréchet and F. Svec, *Small*, 2009, **5**, 1098–1111.
- 4 Hydrogen Storage | Department of Energy,
<https://www.energy.gov/eere/fuelcells/hydrogen-storage>, (accessed 10 June 2019).
- 5 H. Furukawa and O. M. Yaghi, *J. Am. Chem. Soc.*, 2009, **131**, 8875–8883.
- 6 F. Schüth, K. S. W. Sing and J. (Jens) Weitkamp, *Handbook of porous solids*, Wiley-VCH, Weinheim Germany, 2002.
- 7 S.-Y. Ding, J. Gao, Q. Wang, Y. Zhang, W.-G. Song, C.-Y. Su and W. Wang, *J. Am. Chem. Soc.*, 2011, **133**, 19816–19822.
- 8 J. Ryan, *Org. Hybrid Optoelectron. Devices Underst. Key Loss Mech.*, 2015, **Thesis**, 2013.
- 9 Y. Zhi, P. Shao, X. Feng, H. Xia, Y. Zhang, Z. Shi, Y. Mu and X. Liu, *J. Mater. Chem. A*, 2018, **6**, 374–382.
- 10 X. Feng, X. Ding and D. Jiang, *Chem. Soc. Rev.*, 2012, **41**, 6010.
- 11 X. Zhang, Q. Zeng and C. Wang, *Nanoscale*, 2013, **5**, 8269.
- 12 O. M. Yaghi, M. O’Keeffe, N. W. Ockwig, H. K. Chae, M. Eddaoudi and J. Kim, *Nature*, 2003, **423**, 705–714.
- 13 J. L. Segura, M. J. Mancheño and F. Zamora, *Chem. Soc. Rev.*, 2016, **45**, 5635–5671.
- 14 G. Binnig and H. Rohrer, *Surf. Sci.*, 1983, **126**, 236–244.
- 15 L. Xu, X. Zhou, Y. Yu, W. Q. Tian, J. Ma and S. Lei, *ACS Nano*, 2013, **7**, 8066–8073.
- 16 R. Tanoue, R. Higuchi, N. Enoki, Y. Miyasato, S. Uemura, N. Kimizuka, A. Z. Stieg, J. K. Gimzewski and M. Kunitake, *ACS Nano*, 2011, **5**, 3923–3929.
- 17 C. Liu, Y. B. Cheng and Z. Ge, *Chem. Soc. Rev.*, 2020, **49**, 1653–1687.
- 18 X.-H. Liu, C.-Z. Guan, S.-Y. Ding, W. Wang, H.-J. Yan, D. Wang and L.-J. Wan, *J. Am.*

- Chem. Soc.*, 2013, **135**, 10470–10474.
- 19 S. S. Han, H. Furukawa, O. M. Yaghi and W. A. Goddard, *J. Am. Chem. Soc.*, 2008, **130**, 11580–11581.
 - 20 Z.-F. Pang, S.-Q. Xu, T.-Y. Zhou, R.-R. Liang, T.-G. Zhan and X. Zhao, *J. Am. Chem. Soc.*, 2016, **138**, 4710–4713.
 - 21 Y. Yang, M. Faheem, L. Wang, Q. Meng, H. Sha, N. Yang, Y. Yuan and G. Zhu, *ACS Cent. Sci.*, 2018, **4**, 748–754.
 - 22 W. Pauli, *Z. Phys.*, 1925, **31**, 765.
 - 23 M. A. El-Sayed, *Acc. Chem. Res.*, 1968, **1**, 8–16.
 - 24 N. J. Turro, V. Ramamurthy and J. C. Scaiano, *Photochem. Photobiol.*, 2012, **88**, 57–63.
 - 25 D. C. Harris and M. D. Bertolucci, *Symmetry and spectroscopy : an introduction to vibrational and electronic spectroscopy*, Dover Publications, 1989.
 - 26 C. M. Marian, *Wiley Interdiscip. Rev. Comput. Mol. Sci.*, 2012, **2**, 187–203.
 - 27 A. Jain, C. Blum and V. Subramaniam, *Adv. Biomed. Eng.*, 2009, 147–176.
 - 28 H. Linschitz and L. Pekkarinen, *J. Am. Chem. Soc.*, 1960, **82**, 2411–2416.
 - 29 O. L. J. Gijzeman, F. Kaufman and G. Porter, *J. Chem. Soc. Faraday Trans. 2*, 1973, **69**, 708.
 - 30 W. R. Ware, *J. Phys. Chem.*, 1962, **66**, 455–458.
 - 31 C. Grewer and H.-D. Brauer, *J. Phys. Chem.*, 1994, **98**, 4230–4235.
 - 32 F. Wilkinson and A. A. Abdel-Shafi, *J. Phys. Chem. A*, 1999, **103**, 5425–5435.
 - 33 N. Duvva, A. R. Ramya, G. Reddy and L. Giribabu, *J. Porphyr. Phthalocyanines*, 2019, **23**, 628–638.
 - 34 J.-L. Brédas, J. E. Norton, J. Cornil and V. Coropceanu, *Acc. Chem. Res.*, 2009, **42**, 1691–1699.
 - 35 C. Deibel, T. Strobel and V. Dyakonov, *Adv. Mater.*, 2010, **22**, 4097–4111.
 - 36 M. Gouterman, *J. Chem. Phys.*, 1959, **30**, 1139–1161.
 - 37 J. Humphrey and D. Kuciauskas, *J. Phys. Chem. B*, 2004, **108**, 12016–12023.

- 38 M. M. Wienk, J. M. Kroon, W. J. H. Verhees, J. Knol, J. C. Hummelen, P. A. van Hal and R. A. J. Janssen, *Angew. Chemie Int. Ed.*, 2003, **42**, 3371–3375.
- 39 J. J. M. Halls, K. Pichler, R. H. Friend, S. C. Moratti and A. B. Holmes, *Appl. Phys. Lett.*, 1996, **68**, 3120–3122.
- 40 T. M. Clarke and J. R. Durrant, *Chem. Rev.*, 2010, **110**, 6736–6767.
- 41 J. D. Servaites, B. M. Savoie, J. B. Brink, T. J. Marks and M. A. Ratner, *Energy Environ. Sci.*, 2012, **5**, 8343–8350.
- 42 W. Chang, D. N. Congreve, E. Hontz, M. E. Bahlke, D. P. McMahon, S. Reineke, T. C. Wu, V. Bulović, T. Van Voorhis and M. A. Baldo, *Nat. Commun.*, 2015, **6**, 6415.
- 43 N. M. Barbosa Neto, D. S. Correa, L. De Boni, G. G. Parra, L. Misoguti, C. R. Mendonça, I. E. Borissevitch, S. C. Zílio and P. J. Gonçalves, *Chem. Phys. Lett.*, 2013, **587**, 118–123.
- 44 M. Gouterman, *J. Mol. Spectrosc.*, 1961, **6**, 138–163.
- 45 A. T. Gradyushko and M. P. Tsvirko, *Opt. Spektrosk.*, 1971, **31**, 548–556.
- 46 S. Perun, J. Tatchen and C. M. Marian, *ChemPhysChem*, 2008, **9**, 282–292.
- 47 H. Gratz and A. Penzkofer, *Chem. Phys.*, 2000, **254**, 363–374.
- 48 Bahr, Kuciauskas, Liddell, Moore, Moore and Gust, *Photochem. Photobiol.*, 2000, **72**, 598–611.
- 49 C.-W. Chang, L. Luo, C.-K. Chou, C.-F. Lo, C.-Y. Lin, C.-S. Hung, Y.-P. Lee and E. W.-G. Diau, *J. Phys. Chem. C*, 2009, **113**, 11524–11531.
- 50 X. Feng, L. Chen, Y. Dong and D. Jiang, *Chem. Commun.*, 2011, **47**, 1979.
- 51 X. Feng, L. Liu, Y. Honsho, A. Saeki, S. Seki, S. Irle, Y. Dong, A. Nagai and D. Jiang, *Angew. Chemie Int. Ed.*, 2012, **51**, 2618–2622.
- 52 A. H. Corwin, A. B. Chivvis, R. W. Poor, D. G. Whitten and E. W. Baker, *J. Am. Chem. Soc.*, 1968, **90**, 6577–6583.
- 53 D. David and D. Dolphin, *Acad. New York*, 1978, 740.
- 54 K. Sirithip, S. Morada, S. Namuangruk, T. Keawin, S. Jungsuttiwong, T. Sudyoadsuk and V. Promarak, *Tetrahedron Lett.*, 2013, **54**, 2435–2439.
- 55 A. Zhang, L. Kwan and M. J. Stillman, *Org. Biomol. Chem.*, 2017, **15**, 9081–9094.

- 56 B. F. Kim and J. Bohandy, *Johns Hopkins APL Tech. Dig. (Applied Phys. Lab., 1981, 2, 153–163.*
- 57 H. Z. Gök, *Turkish J. Chem., 2015, 39, 750–763.*
- 58 W. Khlbrandt and D. N. Wang, *Nature, 1991, 350, 130–134.*
- 59 J. Karolczak, D. Kowalska, A. Lukaszewicz, A. Maciejewski and R. P. Steer, *J. Phys. Chem. A, 2004, 108, 4570–4575.*
- 60 W. M. Campbell, A. K. Burrell, D. L. Officer and K. W. Jolley, *Coord. Chem. Rev., 2004, 248, 1363–1379.*
- 61 M. K. Panda, K. Ladomenou and A. G. Coutsolelos, *Coord. Chem. Rev., 2012, 256, 2601–2627.*
- 62 J. B. Allison and R. S. Becker, *J. Chem. Phys., 1960, 32, 1410–1417.*
- 63 R. S. Becker and J. B. Allison, *J. Phys. Chem., 1963, 67, 2662–2669.*
- 64 H. Kobayashi, *J. Chem. Phys., 1959, 30, 1362–1363.*
- 65 S. M. B. Costa, M. M. Velázquez, N. Tamai and I. Yamazaki, *J. Lumin., 1991, 48–49, 341–351.*
- 66 K. T. Chan, G. S. M. Tong, W.-P. To, C. Yang, L. Du, D. L. Phillips and C.-M. Che, *Chem. Sci., 2017, 8, 2352–2364.*
- 67 A. Harriman, *J. Chem. Soc. Faraday Trans. 1 Phys. Chem. Condens. Phases, 1980, 76, 1978–1985.*
- 68 Y. Liu, J. A. Koningstein and Y. Yevdokimov, *Can. J. Chem., 2006, 69, 1791–1795.*
- 69 G. Porter, *Proc. R. Soc. London. Ser. A. Math. Phys. Sci., 1950, 200, 284–300.*
- 70 H. Linschitz and K. Sarkanen, *J. Am. Chem. Soc., 1958, 80, 4826–4832.*
- 71 L. Pekkarinen and H. Linschitz, *J. Am. Chem. Soc., 1960, 82, 2407–2411.*
- 72 A. K. Chibisov, *Photochem. Photobiol., 1969, 10, 331–347.*
- 73 J. S. Connolly, D. S. Gorman and G. R. Seely, *Ann. N. Y. Acad. Sci., 1973, 206, 649–69.*
- 74 E. Fujimori and R. Livingston, *Nature, 1957, 180, 1036–1038.*
- 75 R. Livingston and E. Fujimori, *J. Am. Chem. Soc., 1958, 80, 5610–5613.*

- 76 L. Flamigni, I. M. Dixon, J. P. Collin and J. P. Sauvage, *Chem. Commun.*, 2000, **0**, 2479–2480.
- 77 I. M. Dixon, J. P. Collin, J. P. Sauvage, F. Barigelletti and L. Flamigni, *Angew. Chemie - Int. Ed.*, 2000, **39**, 1292–1295.
- 78 M. J. Griffith, K. Sunahara, P. Wagner, K. Wagner, G. G. Wallace, D. L. Officer, A. Furube, R. Katoh, S. Mori and A. J. Mozer, *Chem. Commun.*, 2012, **48**, 4145–4162.
- 79 P. Qi, Z. H. Li, Y. Zhou, F. Wang, Y. Du, L. Q. Zhang, G. Li and H. Z. Zhang, *Appl. Surf. Sci.*, 2013, **279**, 349–352.
- 80 K. Yoshizawa, *Acc. Chem. Res.*, 2012, **45**, 1612–1621.
- 81 J. L. Brédas, J. P. Calbert, D. A. Da Silva Filho and J. Cornil, *Proc. Natl. Acad. Sci. U. S. A.*, 2002, **99**, 5804–5809.
- 82 J. L. Varanasi, R. Veerubhotla, S. Pandit and D. Das, in *Microbial Electrochemical Technology*, Elsevier, 2018, pp. 843–869.
- 83 B. O'Regan and M. Grätzel, *Nature*, 1991, **353**, 737–740.
- 84 M. Grätzel, *J. Photochem. Photobiol. C Photochem. Rev.*, 2003, **4**, 145–153.
- 85 Ö. Birel, S. Nadeem and H. Duman, *J. Fluoresc.*, 2017, **27**, 1075–1085.
- 86 Nwanya, A. C., Ezema, F. I., Ejikeme and P. M., *Int. J. Phys. Sci.*, 2011, **6**, 5190–5201.
- 87 S. Mathew, A. Yella, P. Gao, R. Humphry-Baker, B. F. E. Curchod, N. Ashari-Astani, I. Tavernelli, U. Rothlisberger, M. K. Nazeeruddin and M. Grätzel, *Nat. Chem.*, 2014, **6**, 242–247.
- 88 A. Mahmood, J.-Y. Hu, B. Xiao, A. Tang, X. Wang and E. Zhou, *J. Mater. Chem. A*, 2018, **6**, 16769–16797.
- 89 K. Gao, L. Li, T. Lai, L. Xiao, Y. Huang, F. Huang, J. Peng, Y. Cao, F. Liu, T. P. Russell, R. A. J. Janssen and X. Peng, *J. Am. Chem. Soc.*, 2015, **137**, 7282–7285.
- 90 L. Nian, K. Gao, F. Liu, Y. Kan, X. Jiang, L. Liu, Z. Xie, X. Peng, T. P. Russell and Y. Ma, *Adv. Mater.*, 2016, **28**, 8184–8190.
- 91 W. T. Hadmojo, D. Yim, S. Sinaga, W. Lee, D. Y. Ryu, W.-D. Jang, I. H. Jung and S.-Y. Jang, *ACS Sustain. Chem. Eng.*, 2018, **6**, 5306–5313.
- 92 S. Li, L. Zhan, C. Sun, H. Zhu, G. Zhou, W. Yang, M. Shi, C. Z. Li, J. Hou, Y. Li and H.

- Chen, *J. Am. Chem. Soc.*, 2019, **141**, 3073–3082.
- 93 R. Berera, R. van Grondelle and J. T. M. Kennis, *Photosynth. Res.*, 2009, **101**, 105–118.
- 94 P. P. Sorokin and J. R. Lankard, *IBM J. Res. Dev.*, 1966, **10**, 162–163.
- 95 F. P. Schäfer, W. Schmidt and J. Volze, *Appl. Phys. Lett.*, 1966, **9**, 306–309.
- 96 O. G. Peterson, S. A. Tuccio and B. B. Snavely, *Appl. Phys. Lett.*, 1970, **17**, 245–247.
- 97 T. W. Hänsch, *Appl. Opt.*, 1972, **11**, 895.
- 98 V. Balzani, P. Ceroni and A. Juris, *Photochemistry and photophysics : concepts, research, applications*, WILEY-VCH Verlag GmbH, 2014.
- 99 D. S. McClure, *J. Chem. Phys.*, 1949, **17**, 905–913.
- 100 J. D. Batteas, A. Harriman, Y. Kanda, N. Mataga and A. K. Nowak, *J. Am. Chem. Soc.*, 1990, **112**, 126–133.
- 101 H. Z. Yu, J. S. Baskin and A. H. Zewail, *J. Phys. Chem. A*, 2002, **106**, 9845–9854.
- 102 A. Marcelli, P. Foggi, L. Moroni, C. Gellini and P. R. Salvi, *J. Phys. Chem. A*, 2008, **112**, 1864–1872.
- 103 D. Gao, S. M. Aly, P. L. Karsenti, G. Brisard and P. D. Harvey, *Phys. Chem. Chem. Phys.*, 2017, **19**, 2926–2939.
- 104 X. Li, C. Gong, G. G. Gurzadyan, M. F. Gelin, J. Liu and L. Sun, *J. Phys. Chem. C*, 2018, **122**, 50–61.
- 105 G. A. Jones and D. S. Bradshaw, *Front. Phys.*, 2019, **7**, 100.

2 Experimental Procedures

In this chapter, the materials used are listed as well as the synthesis to prepare the COF samples used. Also described are the main microscopy and spectroscopy experimental techniques used for characterisation and data processing employed.

2.1 Key Materials

Figures 2.1 and 2.2 show the three porphyrins used in this thesis and the only linker used.

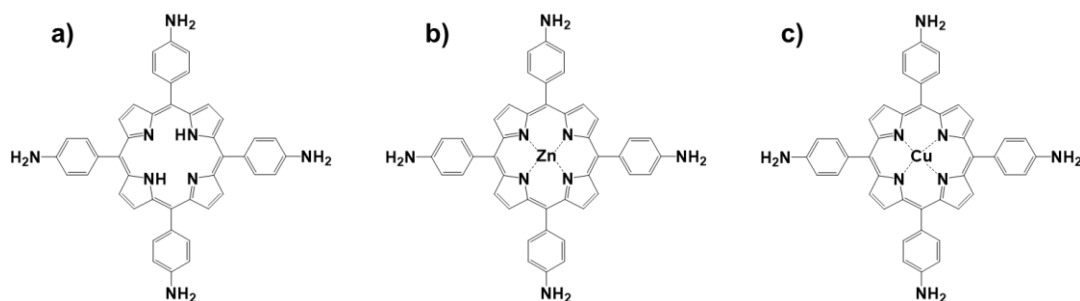


Figure 2.1: a) 5,10,15,20-tetrakis-(4-aminophenyl) porphyrin (TAPP); b) zinc (II) -5,10,15,20-tetrakis-(4-aminophenyl) porphyrin (ZnTAPP); c) copper (II) -5,10,15,20-tetrakis-(4-aminophenyl) porphyrin (CuTAPP).

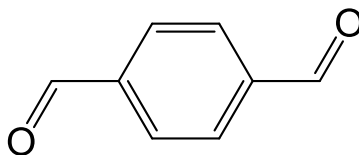


Figure 2.2: Linker: benzene-1,4-dicarboxaldehyde (BDA)

2.2 COF Synthesis

2.2.1 Experimental Set-Up

Figure 2.3 shows the experimental setup used to synthesise COFs which consists of a polytetrafluoroethylene (PTFE) liner in a stainless-steel autoclave. It is essential to have a good seal to maintain the equilibrium inside the PTFE reaction vessel. All the reactants are sealed inside the PTFE liner. The benzene-1,4-dicarboxaldehyde (BDA) linker is deposited by evaporating a solution of BDA in chloroform on the PTFE liner. Copper sulphate ($\text{CuSO}_4 \cdot 5\text{H}_2\text{O}$) solid is placed at the bottom of the PTFE liner. A substrate (highly oriented pyrolytic graphite [HOPG] or quartz coated glass), with the porphyrin spin coated on one side, is placed in a PTFE holder to prevent it coming into contact with the copper sulphate. Finally, the PTFE liner is purged with argon. The pressure of the sealed autoclaves was not monitored.

The exact parameters of each synthesis are detailed in the figure legends for direct reference.

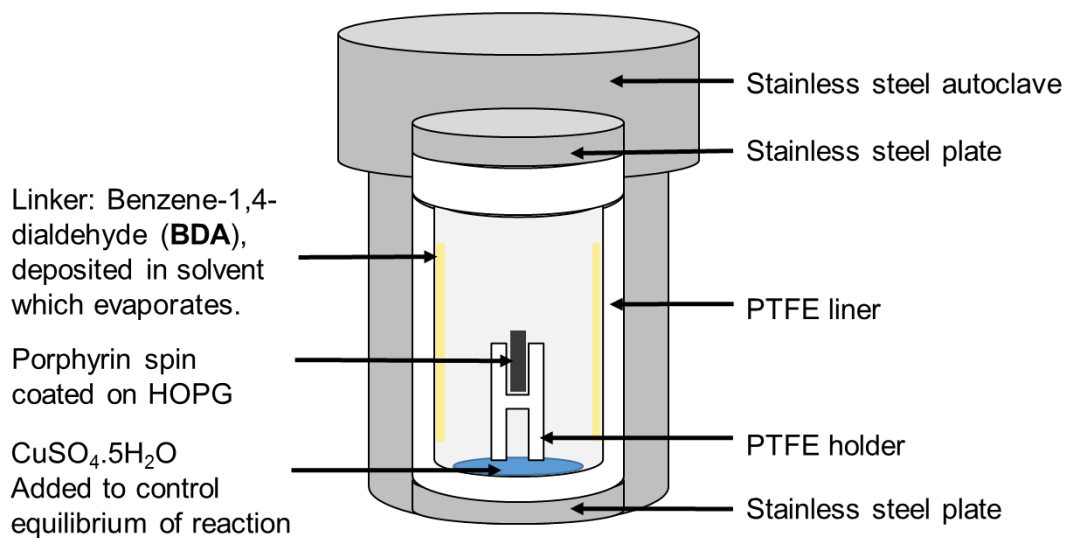


Figure 2.3: Synthetic set-up for 2D-COF synthesis, using TAPP and BDA.

2.2.2 Substrate

All the 2D-COFs in this report used for microscopy analysis were synthesised on highly oriented pyrolytic graphite (HOPG) substrates. HOPG provides atomically flat

areas that do not hinder the diffusion of the compounds on the surface. It is relatively economical and can be reused multiple times after cleaving the surface clean.

2.3 Scanning Tunnelling Microscopy

A scanning tunnelling microscope (STM) is an instrument for imaging surfaces with atomic resolution. It is valuable in understanding what material surfaces look like with high spatial resolution. Many COF studies have used STM to characterise the COF structures being formed.¹ In this thesis, regarding characterisation of COFs, STM provides an insight into whether or not the synthetic procedure described in Section 2.1 has worked and, if so, the morphology of the product, the crystallinity of the layers, and the coverage on the HOPG surface (i.e. domain size).

An STM probes the local electron density of states (DOS) and topography on an atomic scale.² The DOS is the number of allowed electron (or hole) states at a given energy.³ In principle, an STM creates a topology of a conductive sample by scanning a tip over the surface of the sample; the tip and the surface act as electrodes and the change in tunnelling current is measured and used to represent the surface topography. The tip is typically made of tungsten or platinum/iridium and is ideally 1 atom sharp at its tip. The geometry and chemical nature of the tip has a strong influence on the quality of the images obtained and a considerable amount of time can be spent attempting to prepare an appropriate tip. The tip is brought within 10 Å of the surface to image it. At these distances, an overlap of the tip and substrate wavefunctions occurs.⁴ This allows for transport of electrons via tunnelling (pass through the potential barrier) from one to the other, which generates a current. This current is exponentially dependent on the tip surface separation (d), the Fermi levels of both the tip (E_F^T) and substrate (E_F^S), the density of states of the tip (ρ_T) and substrate (ρ_S), the energy interval (ε), and is described in Equation 1.

$$I = \frac{4\pi e}{h} \int_0^{eV} \rho_T(E_F^T - eV + \varepsilon) \rho_S(E_F^S + \varepsilon) e^{-2kd} d\varepsilon \quad (\text{Equation 1})$$

The Fermi level describes the chemical potential of electrons. The Fermi level is the energy level with 50% probability of being occupied at a finite temperature.⁵ The Fermi level determines the direction of flow of electrons, schematically shown in Figure 2.4.⁶

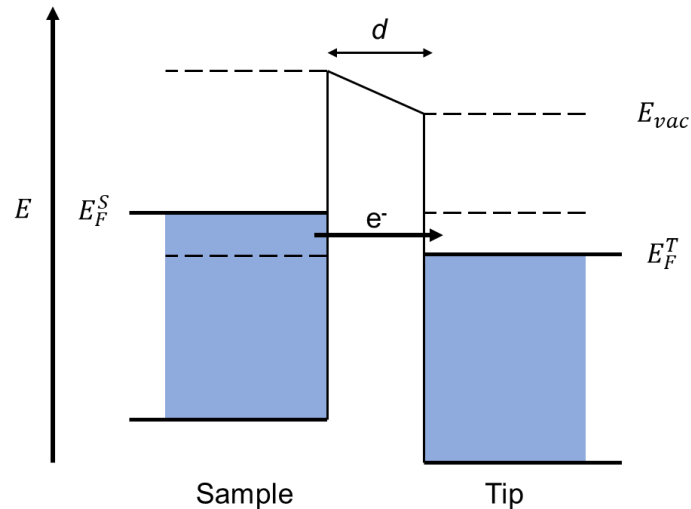


Figure 2.4: Schematic demonstrating electron tunnelling between STM tip and sample. The tip surface separation (d), the Fermi levels of both the tip (E_F^T) and substrate (E_F^S), and the vacuum energy level (E_{vac}) are labeled. The movement of electrons occurs from the sample to the tip.

A bias is applied between the tip and substrate to ensure current flow in one direction dominates. The tip is raster scanned across the surface using the tip-substrate current as a feedback mechanism.

The imaging method used in this study is constant current mode: the tip is brought close enough to the surface that a sufficient tunnelling current can be measured.⁷ The tip raster scans over the surface and the current between the tip and surface is measured, a feedback loop changes the height of the tip to keep the current constant. The movement of the tip is controlled by piezoelectrics which are able to move the tip distances on the scale of 0.1 nm.⁸ Before the millennium, a good lateral resolution was 1 nm and now, with improvements of the piezoelectric design, a good lateral resolution is considered to be 0.1 nm.⁹ It is the record of the movement of these

piezoelectrics that can be used to determine the topography of the substrate. An image consists of a map $z(x,y)$, of tip height z versus lateral position x,y .

Alternatively, in constant height mode, the tip is scanned across the surface at constant height and the current is recorded. Therefore, the changes in current as a result of the tip moving over the surface is plotted versus lateral position x,y . Both modes have their advantages. For example, the constant current mode is advantageous when studying surfaces that are not atomically flat, whereas the constant height mode allows for faster imaging of atomically flat surfaces because only the electronics, and not the z *piezo* translator, must respond to the atoms passing under the tip. Fast scan rates are important for studying processes in real time and faster imaging reduces image distortion (refer to Section 2.3.2.3 on drift correction). In order to scan in constant height mode however, the lateral movement of the tip must be perfectly parallel to the surface of the substrate. If the substrate is tilted with respect to the x,y piezo movement, there is a risk of the tip crashing into the surface. This requirement of being parallel at this scale is only ever satisfied for sample sizes which are less than a few nanometres in size. As such, constant height mode is only ever regularly used for single molecule studies in ultra-high vacuum at liquid helium cooled temperatures.¹⁰

As seen in Equation 1, the tunnelling current is not only a result of the tip sample separation but also the local DOS of the tip and sample. Therefore, a scan of a surface also reveals the local DOS of the surface. Unless the DOS are fully occupied; a higher local DOS results in a higher probability of tunnelling and, as such, a higher current. The image obtained is a result of both changes in topography and local DOS. This must be taken into account when looking solely for one of the two contributions as the two cannot be easily deconvoluted.

Initially, the key purpose of an STM was to image a structure and measure electrical properties of insulating layers thin enough to allow electron tunnelling.¹¹ Now STMs are capable of diverse applications: local modifications and processing, for example, mechanical or electrical deformations.

2.3.1 Using STM on COFs in this Thesis

When electrons tunnel through an organic molecule adsorbed on a solid surface, the image is a result of the complex interaction of the surface, molecule and tip electronic states. To interpret the STM image, all three factors need to be taken into account. The tunnelling current through a tip-molecule-substrate junction depends on the energy of the highest occupied molecular orbital (HOMO) and the lowest unoccupied molecular orbital (LUMO) of the adsorbed molecule. As previously mentioned, the tunnelling current is also dependent on the mixing of the molecular orbitals with the surface electronic states. Molecules that strongly interact with the surface will show a local DOS that is a mix of both molecule and surface electronic states and will be less defined. Porphyrins do not interact strongly with the substrate. In general, porphyrins are a class of molecules that have been extensively studied by STM because of their distinguished electronic properties, their preference to lie planar on a HOPG substrate and their stability in ambient conditions.¹²

This project focusses on the use of ambient STM conditions. STM investigations can be carried out in a variety of environmental conditions. The benefit of using ambient-STM is that the equipment setup is much less complex than UHV-STM where expensive UHV chambers and pumping is required. Also, ambient STM will probe the surface under realistic environmental conditions i.e. if such surface has a practical application, then it is more important to visualise this surface in “real-life”. However, ambient STMs will show less image stability, higher noise levels and even a potential for contamination compared to UHV-STM systems. This is an accepted compromise for the ease of using ambient STMs compared to UHV systems.

2.3.2 Data Acquisition and Processing in Ambient STM

2.3.2.1 Experimental Set-Up

An Agilent 5500 SPM system was used to acquire all the STM images in this thesis. The Agilent 5500 system uses a tube piezoelectric scanner arrangement. To reduce noise from vibrations there is an anti-vibration system which works by cancelling out vibrations

sensed by piezo-electric actuators. The sample plate on which the sample sits and makes electrical contact is attached to the microscope by magnetic posts. The magnetic posts are connected to stepper motors that allow vertical positioning of the sample plate with respect to the tip. The lateral position of the sample plate can be adjusted using micrometre screws built into the STM stand.

2.3.2.2 Tip Preparation

The fabrication of an atomically sharp tip is important to collect STM images with atomic resolution. For ambient STM a platinum-iridium (Pt/Ir) alloy is widely used and simply cutting the Pt/Ir wire will produce a tip that can image a molecule on substrate with no problems.

2.3.2.3 Drift Correction

During the acquisition of an STM image, there is a possibility that the image can be distorted due to *drift*. During the imaging, neither the tip nor the sample necessarily stay fixed in the exact same position. The drift of an STM tip with respect to the sample surface is the reason why the structure observed in the resulting STM images might not be the real structure of the surface at that instance. Drift effects can be due to different rates of thermal expansion of the STM scanner and sample surface from changes in temperature, this is called thermal drift. Thermal drift is both the displacement of molecules on the surface as well as the expansion of the sample substrate itself or STM device material when there is a slight increase in temperature. The sample substrate and the materials making the STM device will have different coefficients of thermal expansion.¹³ So, whilst the scanning device consists of piezoceramics, the sample holder and device housing is mainly made of metals, and the sample and substrate can be any material.

As well as temperature effects, drift may occur because the area of the sample being scanned is not parallel to the STM scanning plane, depending on how the sample slopes on the sample plate. Piezoelectric creep is the displacement of the piezo when there is a constant applied electric field.¹⁴ The creep of piezo-electric materials in the

STM scanners can cause distortions during STM scanning. Unlike the variable distortions associated with temperature and sample orientation, these scanner induced distortions remain constant for a specific piece of STM equipment so can be reduced by choosing adequate scanning parameters as well as scanning the same area several times so the creep can become constant.¹³ Drift can be corrected using the lattice dimensions of the substrate (HOPG in this case) as a form of calibration. When collecting an image, the image of the HOPG surface on which the molecule sits can be collected by changing the set-point and sample bias parameters. All other scanning parameters must remain the same, e.g. scan size, scan direction, scan angle etc. The two images collected, one of the molecule and the other of the HOPG surface, will both have the same level of drift and so the images would have been distorted by the same amount.

Using a software package (SPIP software, Image Metrology, Denmark) to analyse the unit cells of both images, a correction parameter can be applied to the image of the molecule. These correction parameters are found by using known parameters of the HOPG lattice. The extent to which the collected HOPG image differs from the known parameters will be the same as that of the image of the molecule to a true image of the molecule.

All images in this report that have been drift corrected are indicated in this thesis. All images have been processed using WSxM or Gwyddion software.

2.4 Transient Absorption Spectroscopy

Transient absorption spectroscopy (TAS) measures absorption spectra and kinetic behaviour of transient species: chemical species that have very short lifetimes and cannot be observed with classical experimental methods that require long detection times.¹⁵ Refer to Section 1.6.6 for a discussion on TAS.

This thesis only used microsecond-TAS because the transient species being studied occur in the microsecond timescale.

2.4.1 TAS with Microsecond Resolution Setup

In a microsecond TAS setup a pulsed laser (pump) is used to excite the sample (film or solution), and at the same time a continuous white light source (probe) is passed through the sample and into a monochromator where it hits a photodiode and records a voltage that has been amplified on an oscilloscope, seen in Figure 2.5.

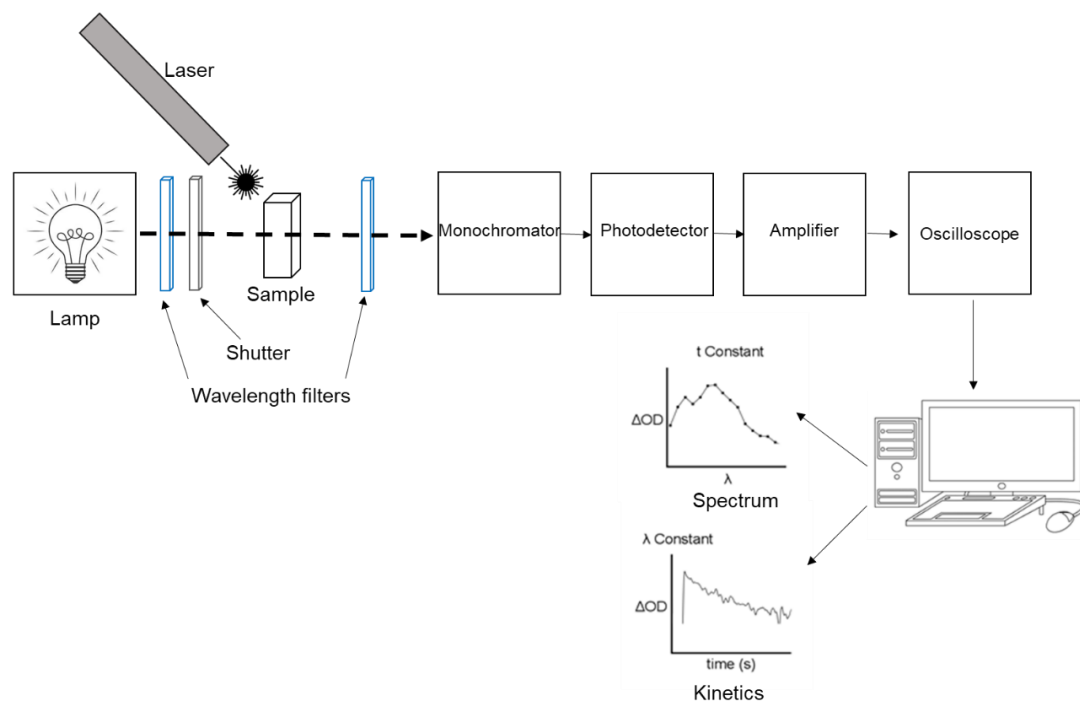


Figure 2.5: A block diagram representing a nanosecond-microsecond transient absorption experimental setup. The change in the optical density relative to the ground state absorbance after excitation may be plotted as a function of probe wavelength, λ , yielding a transient absorption spectrum; or collecting ΔOD as a function of time to yield the kinetics.

The “pump” excitation source used is a Quanta-Ray INDI pulsed ND:YAG (neodymium-doped yttrium aluminium garnet) which emits light with a wavelength of 1064 nm. The wavelength is halved to acquire laser light at 532 nm, which is mixed with the laser light at 1064 nm to yield higher harmonics at 355 nm.

The 355 nm output laser beam is directed into a GWU versaScan β -barium borate optical parametric oscillator (OPO). An OPO is an optical cavity resonator that uses parametric amplification, a non-linear optical phenomenon, that generates two beams that cover a wide range of wavelengths. The OPO converts an input pump laser beam

into two output beams: a higher energy 'signal' beam in the range of 410 nm – 709 nm, and a lower energy 'idler' beam in the range of 710 -2630 nm. The signal output is used as the excitation source, and its excitation density is varied *via* means of neutral density filters.¹⁶ The beams used in this setup cover wavelengths from near UV to near IR, therefore it is possible to perform experiments with different excitation wavelengths.

The duration of the laser pulse is 6 ns and the repetition rate is 10 Hz. This gives a time window large enough to monitor processes of triplet formation or charge recombination that occur within these timescales. The repetition rate of the exciting pump laser beam must be long enough to allow for relaxation to the ground state.

The probe beam is generated from a Bentham IL1 quartz halogen lamp with a stabilised power source. The probe light is passed through the sample, located in a quartz cuvette, and into a Cornerstone™ 130 monochromator. The monochromator isolates a narrow wavelength range from the emission spectrum of a light source so permitting the selection of a single probe wavelength.

The probe light is then focused onto either a visible or infrared optical transient detector preamplifier, connected to a main amplifier which converts the signal into a difference in voltage. The visible detector comprised of a silicon PIN photodiode (Hamamatsu S3071 low noise photodiode) with a spectral detection range of 320-1060 nm, while the infrared detector is comprised of an indium gallium arsenide (InGaAs) PIN photodiode with a spectral detection range of 700-1700 nm.¹⁶

The main amplifier displays the overall probe light level that reaches the detector and is connected to a multichannel Tetronix (DPO 4034B, 350 Mhz, 2.5 GS/s) oscilloscope which displays the change in voltage. A 'trigger' is used to set time zero for the experiments. The trigger is connected to the oscilloscope.¹⁶ The trigger used for the system is scattered laser light from the laser source so upon starting a measurement, the trigger will set a laser pulse as time zero and communicate to the oscilloscope when the measurement began. The oscilloscope is connected to a computer which completes the data acquisition via commercial software (TEKAVEUSB, Costronics Electronics).

It should be noted that to reduce any background signals affecting the measurements, two sets of data are measured. The first is the sample being probed and pumped simultaneously, and the second is when the probe is blocked to give on the pump measurement. The latter is subtracted from the former to give only the probe measurement.

Background signals from light in the laboratory environment can also be avoided by using wavelength filters in front of the white light probe and in front of the monochromator aperture. The filters also help to remove stray light from the monochromator, or light passed from the monochromator which is second or third order of the selected probe wavelength. These filters can be long pass or band pass filters. Long pass filters allow wavelengths longer than what the filter absorbs to pass through and band pass filters only allow a specific range of wavelengths.

Note that the measurements are typically carried out in an inert atmosphere, such as nitrogen or argon. The sample is placed in a quartz cuvette for the measurement and the cuvette has a seal that is connected to two tubes, one is an inlet connected to a gas cylinder and the other is an outlet so there is no pressure build up. Even though the flow rate is very low (<100 ml/min), the lab area should be well ventilated. Purging the sample helps to prevent oxygen quenching the triplet species that may be forming during the measurement. Equally, if a species is thought to be a triplet then kinetic measurements are carried out in a pure oxygen atmosphere which should reduce the lifetime of the species, indicated by the transient decay.¹⁷

2.4.2 TAS Sample Preparation

All samples used for TAS investigations were carried out on quartz coated glass substrates. The porphyrin was spin coated on to the quartz/glass substrate. The COF was synthesised as described in Section 2.2.

2.4.3 TAS Data Analysis

As previously mentioned, to measure the kinetics the ΔOD of a sample is observed at a single probe wavelength as a function of time. The plot of this data can

help to provide an understanding of the photophysical relaxation processes occurring and fitting parameters have been extensively studied.¹⁸⁻²⁵ The following equations have been applied to polymer systems but have been applied to this porphyrin and COF study because of the disperse, disordered nature of the TAPP and COF films. It is important to note that the STM studies carried out on the COF films in Chapter 3 were focused on making monolayer COF. So, when spin coating the TAPP on the HOPG substrate, the TAPP in solution was a very low concentration. However, in order to get a signal on the TAS, the COF films made were multilayer, with a 0.4 a.u. ground state absorbance being around 100 layers. The bulk multilayers used in the TAS studies enables the use of the equations for disperse, disordered regions. If only a 2D monolayer is studied then another data analysis will need to be used.

The kinetic decay trace is the rate of change in the number of the transient species over time. In the following equation n signifies the number of transient species which can be charges or triplets for example.¹⁸

$$n = \frac{\Delta OD \times N_A}{\epsilon \times l \times 1000} \quad (\text{Equation 2})$$

ΔOD is the change in absorbance, N_A is Avogadro's number, ϵ is the molar extinction coefficient in $\text{L mol}^{-1} \text{cm}^{-1}$, and l is the thickness in cm.

In a first order equation, a plot of the natural logarithm of the ΔOD versus time is a straight line. Singlet and triplet excited state decay kinetics generally show a monoexponential first order decay in diluted molecular systems.²⁶ Yet, the possibility of non-radiative internal conversion and intersystem crossing processes can change the decay dynamics to a non-exponential decay. With respect to a monoexponential decay, the rate of change of n over time is defined by the following equation.

$$\frac{dn}{dt} = \beta n \quad (\text{Equation 3})$$

β is the rate coefficient.

With regards to higher order reactions, the rate of change of n over time is defined by the following equation.¹⁹

$$\frac{dn}{dt} = \beta n^{\gamma+1} \quad \text{where} \quad \gamma = \frac{1}{\alpha} \quad (\text{Equation 4})$$

For a second order reaction, γ is equal to 1 and this can represent pure bimolecular recombination. However, in a disperse system without defined order this is not always the case. Therefore, if α is less than 1, γ is greater than 1 and the rate coefficient is not discrete and so a power law is applied which is defined by Equation 5.^{24,25}

$$\Delta OD \propto t^{-\alpha} \quad (\text{Equation 5})$$

For a power law decay, a plot of the natural logarithm of the ΔOD versus the natural logarithm of time is a straight line with a gradient of $-\alpha$. A power law decay is applied in this thesis results from bimolecular recombination of dissociated charges in the presence of an exponential distribution of localised (trapped) states.^{24,27} The value of the gradient α is an indication of the energetic distribution of charge trap states. Organic photovoltaic materials are described as disordered semiconductors with a continuous distribution of both energetically shallow and deep trap bands.²⁸ The gradient α can be any value 0-1. An α value nearer to 1 are shallower trap states, and this facilitates faster recombination of charges.²⁷

2.5 Fourier Transform Infrared (FT-IR) Spectroscopy

Fourier transform infrared spectroscopy (FTIR) is a commonly used technique to study the chemical structure of molecules and compounds. When IR radiation is passed through a sample, some radiation is absorbed by the sample and some is transmitted. The sample molecules selectively absorb radiation of a specific wavelength which excites molecules into a higher vibrational state. As a result, a chemical functional group, or where there is a change in the molecular dipole, will absorb infrared radiation in a specific wavenumber range. FTIR detects this change of vibration characteristics of chemical functional groups in a sample. Other parts of the molecule can also absorb

infrared radiation and will appear in the fingerprint region where all bending vibrations within the molecule are recorded; but these are difficult to disentangle whereas functional groups have been well studied and appear spread out in the FTIR spectrum.

An FTIR spectrometer obtains infrared spectra by first collecting an interferogram of a sample signal with an interferometer, which measures all infrared frequencies simultaneously. An FTIR spectrometer acquires and plots the interferogram, performs the FT function, and outputs the spectrum. More detailed information about FTIR can be found from a variety of sources (References [29-31]).²⁹⁻³¹ For the purpose of this thesis, FTIR has been used to determine the success of a chemical reaction. Before and after spectra can be compared to see if a functional group has been converted to another, and this will show the success of the synthetic procedure. This will be discussed in Chapter 3.

2.5.1 Experimental Setup

An FTIR Shimadzu Tracer-100 was used with a Michelson interferometer (30° incident angle) and equipped with an Advanced Dynamic Alignment system. The beam splitter is a Germanium-coated KBr for middle IR as standard. The light source is a high-energy ceramic for middle/far IR as standard. The detector is a DLATGS detector with temperature control for middle/far IR as standard. The wavenumber range is 7,800 to 350 cm⁻¹.

2.5.2 FTIR Sample Preparation

All samples used for FTIR investigations were carried out on calcium fluoride (CaF₂) substrates. The porphyrin was spin coated on to the CaF₂ substrate. The COF was synthesised as described in Section 2.2.

2.6 X-ray Photoelectron Spectroscopy (XPS)

X-ray photoelectron spectroscopy (XPS) is a widely used surface analysis tool that provides quantitative information on the elemental composition of a sample surface irradiated with X-rays (200 – 2000 eV). XPS can measure the elemental composition, empirical formula, chemical state and electronic state of the elements within a material.

XPS spectra are obtained by irradiating a solid surface with a beam of X-rays while simultaneously measuring the kinetic energy and number of electrons that are emitted from the top 1-10 nm of the sample being analysed. A photoelectron spectrum is recorded by counting ejected electrons over a range of electron kinetic energies. Peaks appear in the spectrum from atoms emitting electrons of a particular characteristic energy. The energies and intensities of the photoelectron peaks enable identification and quantification of all surface elements (except hydrogen as hydrogen has no core electrons). More detailed information about XPS can be found from a variety of sources (References [32-34]).³²⁻³⁴ For the purpose of this thesis, XPS has been used to determine the success of a chemical reaction. This will be discussed in Chapter 3.

2.6.1 Experimental Setup and Data Processing

XPS measurements were undertaken on a Thermo Scientific K-Alpha XPS system. The XPS system consists of an analysis chamber that is maintained at UHV conditions with pressures typically of 1×10^{-9} mbar or lower. The vacuum environment ensures samples loaded into the system are free from contamination and helps prevent losses in electron kinetic energy. The Thermo Scientific K-Alpha XPS system is equipped with a monochromated Al K α X-ray source (1486.6 eV), generated by electron bombardment of an aluminium target. Spot sizes of the X-ray beam can be adjusted within the range of 30 – 400 μm . Photoelectrons emitted from the target area are collected by a lens system and directed into a hemispherical kinetic energy analyser. The analyser acts as an energy filter allowing electrons with a kinetic energy equal to the pass energy to reach the detector. By varying the pass energy in steps, electrons from a range of kinetic energies are detected. The detector counts the intensity of photoelectrons at a certain kinetic energy. The collected data is used to produce the final XPS spectrum.

Once the data is collected, there is a peak fitting process in which a sensible interpretation of the data and mathematical model is used to determine what species are indicated by the peaks. The peak fitting process relies on certain factors:

- 1) The expected elemental and chemical composition of the surface based on the preparation procedures.
- 2) The presence of potential contaminants.
- 3) The binding energies of atomic species expected on the surface.

The exact binding of a peak in an XPS spectrum varies depending on the chemical environment of the species in question. If the sample contains the same atoms in different chemical environments, the XPS peak will be a summation of the different species and deciphering the different species is complex. In order to fit the peaks correctly, an understanding of the chemical species in the sample is required when analysing XPS data.

To begin the peak fitting process, a background measurement is subtracted from the XPS data. The background measurement is from inelastically scattered electrons after absorption of photons. After subtraction, peaks are fitted based on the prior understanding of the physical and chemical properties of the samples. The preliminary positions of the peaks are decided according to binding energy values reported in literature. The choice of peak shape should be made by considering the structure of the materials being analysed and the computational ability of the software package used for peak fitting. In order to obtain an accurate fit to an XPS peak, the fit needs to be both mathematically valid, and chemically valid. Peak shapes commonly used for XPS peak fitting are: Doniach – Sunjic, Gelius, Gaussian – Lorentzian, and Voigt and pseudo-Voigt line shapes.³² To optimise the fitting results, constraints, such as peak position, full width at half maximum (FWHM) and line shape parameters (Gaussian/Lorentzian ratio and asymmetry factors), are adjusted in a step-by-step process.

In this thesis, when peak fitting for the N1s peak spectra, the positions of the nitrogen peaks listed in Chapter 3 were restrained to be ± 0.3 eV either side of the positions recorded in literature. A wider set of constraints was adopted for the satellite peak. Satellite peaks are due to a sudden change in Coulombic potential as the photo ejected electron passes through the valence band. The starting position of the satellite

peak was set to be 402 ± 0.5 eV. The FWHM obtained by fitting to the intense C1s carbon peak was 1.0 eV. This value was used as a standard for all XPS scans.³⁵ Restraints set for the FWHMs of the N1s XPS peaks were set to be between 0.8 and 1.2 eV. The restraint for the FWHM of the satellite peak was set to be between 1 and 2 eV.

2.6.2 XPS Sample Preparation

All samples used for XPS investigations were carried out on HOPG substrates. The porphyrin was spin coated on to the HOPG substrate. The COF was synthesised as described in Section 2.2.

2.7 Bibliography

- 1 J. F. Dienstmaier, A. M. Gigler, A. J. Goetz, P. Knochel, T. Bein, A. Lyapin, S. Reichmaier, W. M. Heckl and M. Lackinger, *ACS Nano*, 2011, **5**, 9737–9745.
- 2 G. Binnig and H. Rohrer, *Surf. Sci.*, 1983, **126**, 236–244.
- 3 K. Joulain, R. Carminati, J.-P. Mulet and J.-J. Greffet, *Phys. Rev. B*, 2003, **68**, 245405.
- 4 L. D. Landau and E. M. Lifshitz, *Quantum mechanics : non-relativistic theory*, Pergamon Press, Oxford, 1977.
- 5 A. Kahn, *Mater. Horizons*, 2016, **3**, 7–10.
- 6 S. Halas and T. Durakiewicz, *J. Phys. Condens. Matter*, 1998, **10**, 10815–10826.
- 7 P. K. Hansma and J. Tersoff, *J. Appl. Phys.*, 1987, **61**, R1–R24.
- 8 M. Liu, in *Controlled Synthesis and Scanning Tunneling Microscopy Study of Graphene and Graphene-Based Heterostructures*, Springer, Singapore, 2018, pp. 37–54.
- 9 J. T. Woodward IV and J. A. Zasadzinski, *Biophys. J.*, 1997, **72**, 964–976.
- 10 L. Gross, F. Mohn, N. Moll, G. Meyer, R. Ebel, W. M. Abdel-Mageed and M. Jaspars, *Nat. Chem.*, 2010, **2**, 821–825.
- 11 G. Binnig and H. Rohrer, *IBM J. Res. Dev.*, **30**, 4.
- 12 J. Otsuki, *Coord. Chem. Rev.*, 2010, **254**, 2311–2341.
- 13 P. Rahe, R. Bechstein and A. Kühnle, *J. Vac. Sci. Technol. B, Nanotechnol. Microelectron. Mater. Process. Meas. Phenom.*, 2010, **28**, C4E31-C4E38.
- 14 H. Jung and D. G. Gweon, *Rev. Sci. Instrum.*, 2000, **71**, 1896–1900.
- 15 V. Balzani, P. Ceroni and A. Juris, *Photochemistry and photophysics : concepts, research, applications*, WILEY-VCH Verlag GmbH, 2014.
- 16 J. Shaikh, *Exploring Triplet Energy Levels in Organic Solar Cells*, Thesis, 2017.

- 17 W. R. Ware, *J. Phys. Chem.*, 1962, **66**, 455–458.
- 18 J. Nelson, *Phys. Rev. B*, 2003, **67**, 155209.
- 19 C. G. Shuttle, B. O'Regan, A. M. Ballantyne, J. Nelson, D. D. C. Bradley and J. R. Durrant, *Phys. Rev. B*, 2008, **78**, 113201.
- 20 R. C. I. MacKenzie, T. Kirchartz, G. F. A. Dibb and J. Nelson, *J. Phys. Chem. C*, 2011, **115**, 9806–9813.
- 21 T. Kirchartz and J. Nelson, *Phys. Rev. B*, 2012, **86**, 165201.
- 22 A. V. Barzykin and M. Tachiya, *J. Phys. Chem. B*, 2002, **106**, 4356–4363.
- 23 M. Tachiya and K. Seki, *Phys. Rev. B*, 2010, **82**, 085201.
- 24 T. M. Clarke, F. C. Jamieson and J. R. Durrant, *J. Phys. Chem. C*, 2009, **113**, 20934–20941.
- 25 I. Montanari, A. F. Nogueira, J. Nelson, J. R. Durrant, C. Winder, M. A. Loi, N. S. Sariciftci and C. Brabec, *Appl. Phys. Lett.*, 2002, **81**, 3001–3003.
- 26 O. A. El Seoud, W. J. Baader and E. L. Bastos, in *Encyclopedia of Physical Organic Chemistry, 5 Volume Set*, 2016, pp. 1–68.
- 27 J. Wang, L. Xu, K. Xue and E. Wang, *Chem. Phys. Lett.*, 2008, **463**, 405–409.
- 28 J. A. Carr, Iowa State University, Digital Repository, 2014.
- 29 B. C. Smith, *Fundamentals of Fourier Transform Infrared Spectroscopy*, CRC Press, 2011.
- 30 A. Dutta, in *Spectroscopic Methods for Nanomaterials Characterization*, Elsevier, 2017, vol. 2, pp. 73–93.
- 31 B. Stuart, in *Kirk-Othmer Encyclopedia of Chemical Technology*, John Wiley & Sons, Inc., Hoboken, NJ, USA, 2015, pp. 1–18.
- 32 H. von D. Briggs, *Phys. unserer Zeit*, 1979, **10**, 30–30.

- 33 C. S. Fadley, R. J. Baird, W. Siekhaus, T. Novakov and S. Å. L. Bergström, *J. Electron Spectros. Relat. Phenomena*, 1974, **4**, 93–137.
- 34 C. S. Fadley, *Prog. Surf. Sci.*, 1984, **16**, 275–388.
- 35 Y. Niwa, H. Kobayashi and T. Tsuchiya, *J. Chem. Phys.*, 1974, **60**, 799–807.

3 COF Film Synthesis

3.1 Introduction

Monolayer 2D-COFs can be synthesised with a range of techniques, the most common being top-down exfoliation of bulk 2D-COFs or a bottom-up formation directly on a substrate from molecular building blocks.¹ The size and morphology of the resulting 2D-COFs are highly tuneable and can be changed by varying the size, shape and chemical structure of the molecular building blocks used. The different building blocks can also give rise to different physical and chemical properties of the final 2D-COF. The Schiff-base condensation reaction is one of the most common techniques used to grow monolayer 2D-COFs. The benefit of condensation reactions is that the equilibrium position of the reaction can be controlled with the presence of water in a closed reaction vessel. Control over the equilibrium position of the reaction allows for reversibility of the framework during the growth phase. This reversibility allows for defects to be rejected during growth and so larger, ordered domain sizes are achievable, i.e. “self-healing”. On the other hand, the disadvantage of condensation reactions is that the stability of the COF is limited in water rich environments because covalent links can undergo hydrolysis. Finding the correct window in the shifting equilibrium is essential.

3.1.1 Schiff-Base Reactions

Schiff base reactions are a generic term used for the formation of an imine bond: $R_2C=NR'$ ($R' \neq H$).² Firstly, a hemiaminal, $-C(OH)(NR_2)-$, is formed from a nucleophilic addition between a carbonyl and an aliphatic or aromatic amine group shown in Figure 3.1, then, dehydration to generate an imine.

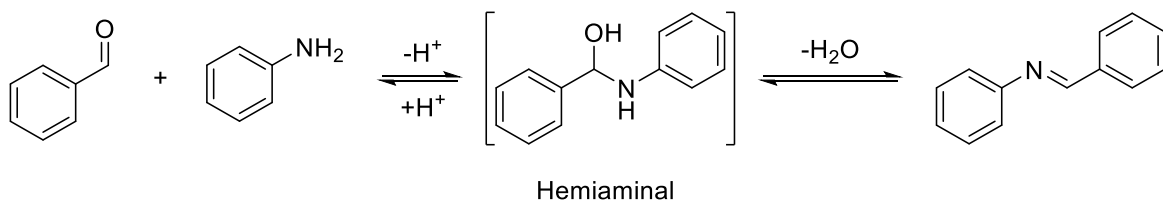


Figure 3.1: Simplified Schiff-base mechanism

Polymeric material synthesis is dominated by kinetically controlled reactions which irreversibly form covalent bonds.³ Therefore, it is difficult to crystallise linked organic polymers by irreversible reactions. Dynamic covalent chemistry (DCC) defines chemical reactions carried out reversibly under conditions of equilibrium control.⁴ This allows “error checking” synthetic processes and since the formation of products takes place under thermodynamic control, product yield depends only on the relative stabilities of the final product. In kinetically controlled reactions, it is the free energy differences between the transition states leading to the products that determines their relative proportions.

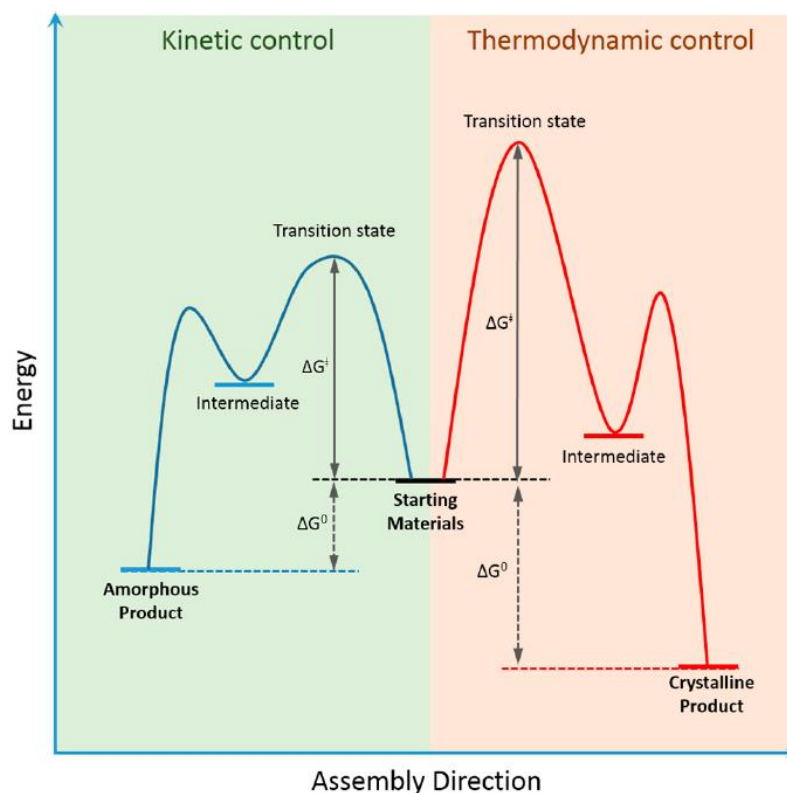


Figure 3.2: Thermodynamic control in the dynamic covalent chemistry of COFs.⁵

With regards to Figure 3.2, due to the lower barrier of activation (ΔG^\ddagger), kinetic intermediates have a fast rate of formation and initially dominate so can be trapped during quenching of the reaction and form amorphous products with an increase of entropy from their disordered arrangement.⁵ The thermodynamic products have the lowest overall Gibb's free energy (ΔG^0), so that given the opportunity, the reaction will re-equilibrate towards the global minimum to form the most stable and probably crystalline products. However, this is a simplistic analogy and there are cases in which the different transition states will be different and the activation barriers for these transition states can lead to the formation of a kinetic product rather than thermodynamic. With regards to a COF layer, it is not simply two reactants to make a single product as in Figure 3.1, there is a framework forming and statistically, there are more ways to arrange the molecules in an amorphous structure than in an ordered structure so this is where difficulties arise when synthesising pristine layers. Yet, in using DCC principles for the assembly of COFs, the "self-healing" feedback (error-checking) reduces the structural defects and promotes formation of an ordered structure.⁶ Therefore, the final COF can possess an ordered crystalline structure with high thermodynamic stability.

There are five main growth methods in which COF monolayers, bilayers and thin films may be synthesised: (1) solvothermal; (2) liquid-solid; (3) liquid-liquid; (4) liquid-vapour; and finally (5) solid-vapour interface growth which is used in this thesis.⁷

3.1.2 Linker

One way in which to synthesise a COF, which is the focus of this thesis, is using a linker molecule to form a bridge between porphyrin units. Especially for multi-porphyrin arrays that exhibit light harvesting properties, careful selection of the linker is important as the linker serves both a mechanical function and an electronic function.⁸ The mechanical function is to join the porphyrins together and build a stable network and the electronic function is to provide a way in which the porphyrins can communicate with each other to enhance the rate of excited-state energy transfer.⁹ This energy transfer can be described as through-bond (TB) or through-space (TS) energy transfer,

with TB being as much as 25 faster than TS in covalently linked multiporphyrin arrays.⁹ It is important to note that the efficiency of the TB or TS energy transfer can be changed in different chemical structures, for example, TS energy transfer dominates in isostructural zirconium and hafnium-based metal–organic layers.¹⁰ However, in the porphyrin-linker system studied in this thesis, the porphyrins are clearly separated in space and Clayton *et al.* state that in the absence of direct orbital overlap, TB interaction is found to significantly enhance the transfer integrals for electron transfer and triplet–triplet energy transfer.¹¹

Ideally the linker should provide efficient TB electronic communication between the porphyrins without participating in any harmful excited state quenching processes, be stable to oxidation and reduction and react readily with the porphyrins to produce the product framework with a high yield.

The linker focused on in this report is benzene-1,4-dicarboxaldehyde (BDA), a simple aromatic molecule with 2 aldehydes groups, as shown in Figure 3.3.

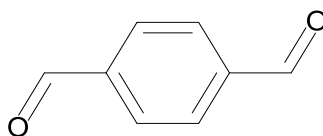


Figure 3.3: Benzene-1,4-dicarboxaldehyde (BDA)

Holten *et al.* investigated the ways in which linkers affect the electronic communication in covalently linked multiporphyrin arrays.⁹ They concluded that ultrafast excited state energy transfer occurs predominantly via a TB linker-mediated mechanism. This mechanism can be controlled by (1) the steric interactions between linker and porphyrin, (2) the characteristics of the frontier molecular orbitals of the porphyrin, and (3) the site on the porphyrin where the linker is bonded.⁹

The linker can affect a vast number of properties in COFs. BDA has been chosen as a linker because firstly, it is a relatively simple molecule and thus reduces the number of properties that can be affected. Secondly, BDA has been shown to readily act as an electron acceptor for porphyrins.¹² Thirdly, in order to use a Schiff-base condensation

reaction to create an imine bond, aldehyde substituents are vital to react with amino functionalised porphyrins which are used in this research. Finally, the ease of synthesis with the solid-vapour phase growth method as larger dialdehyde molecules would not vaporise as easily and this would make the synthesis of the COFs significantly more difficult.

3.1.3 Imine Bonded COFs

Even though many COFs are made from the condensation reaction between boronic acids and diol groups to form hexagonal boroxine rings and boronic esters, imine bonds feature a significantly higher hydrolytic stability than the boronic esters; hence making the resulting imine-linked COFs usable in a broader range of applications.¹³ Furthermore, by reacting an aromatic amine with an aromatic aldehyde, a conjugation of the π -systems of both molecular building blocks can be achieved, enabling conjugation over whole 2D-COF layers. The first imine-bonded monolayer 2D-COF was reported by Wang *et al.*, who used 1,3,5-triformylbenzene (TFB) and 1,4-phenylenediamine (PDA) in a liquid-liquid interface reaction to create a 2D-COF with hexagonal channels.¹⁴ Due to the large number of aromatic amines and aldehydes available, there is a possibility to construct conjugated π -systems throughout whole COF layers using different precursors. As a result, imine formation has become the most common synthesis technique used for COFs.

3.2 COF-366 Synthesis

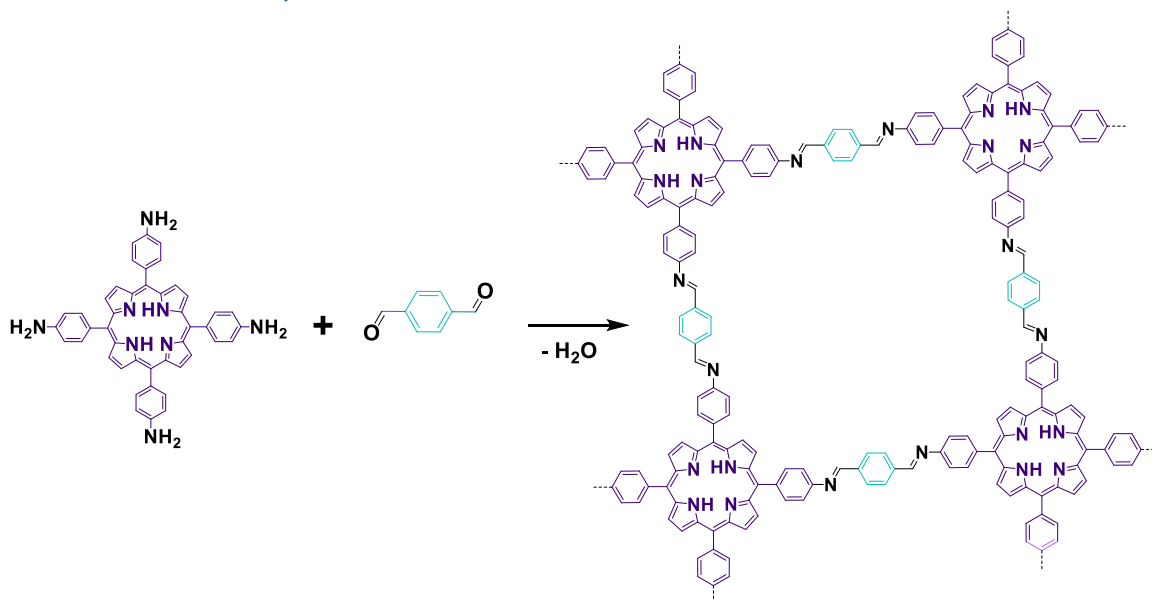


Figure 3.4: COF-366 Reaction Scheme using 5,10,15,20-tetrakis-(4-aminophenyl) porphyrin (TAPP) which are linked together via a Schiff-base condensation reaction with benzene-1,4-dicarboxaldehyde (BDA).

This report focusses on 5,10,15,20-tetrakis-(4-aminophenyl) porphyrin (TAPP) which is linked together via a Schiff-base condensation reaction with benzene-1,4-dicarboxaldehyde (BDA) shown in Figure 3.4. Hydrated copper sulphate is added to the reaction vessel in order to promote a self-healing reaction as shown in Figure 3.1. Adding water to the reaction vessel promotes the reverse reaction and has been shown to be effective by Guan *et al.*¹⁵ Rather than using water, hydrated copper sulphate is used because on the knowledge that it releases its waters of hydration at high temperatures and then reabsorbs them on cooling to prevent hydrolytic decomposition of the COF layers.^{16,17} TAPP and BDA were chosen because of the aforementioned benefits of imine bond formation and the extensive π -conjugation. Additionally, TAPP and BDA have previously shown to form COF-366 successfully and the aim of this thesis is to study the photophysics so a successful synthesis is essential.¹⁸

The experimental set-up has been detailed in Chapter 2. All the monolayer 2D-COFs that were studied using an STM in this report were synthesised on highly oriented pyrolytic graphite (HOPG) substrates. The main reason HOPG is used is because it is

electrically conductive which is a prerequisite for using STM to analyse structures and HOPG provides an atomically flat surface that does not hinder the diffusion of the compounds on the surface. Also, it is relatively economical and can be reused multiple times after cleaving the surface clean.

3.3 STM of COFs

3.3.1 STM Results

A variety of reactants, concentrations and reaction conditions have been studied and STM completed on each of them. Full details of each synthesis are written in the figure captions. From the images in this section, what is interesting to see is that slight changes in the synthetic procedure have led to a huge variety of morphologies and domain sizes. This purports that the reaction is very sensitive and any minor change in variable can lead to varied COF films. Not only is the reaction very sensitive but the ideal, guaranteed reaction parameters have not yet been found that will ensure a reproducible growth. Nguyen and Grünwald have studied the poor crystallinity of COFs and they emphasise the need for control over the relative strength of binding and stacking to tune the morphology of COF crystals.¹⁹ This is further explored alongside the results and in the conclusion in Section 3.5.

It is essential to address the reproducibility and reliability of the synthesis technique. The results reported in this section are a section of the positive results from the synthesis. Many films that were synthesised using the same conditions would not always guarantee a COF visible when scanned using the STM. The reasons behind the lack of reproducibility can be due to small changes in the synthesis procedure arising from human or environmental error, for example, changes in temperature of the laboratory, as this will affect the cooling of the steel autoclaves. Another reason can be that there has been a successful COF synthesis but the areas of HOPG imaged using STM have not landed on areas where the synthesis has been successful. This addresses issues with the uniformity of the films which in turn addresses problems with the spin coating technique used to deposit the TAPP on the HOPG. Other techniques will be discussed in

concluding Chapter 6. There is also the possibility that the STM imaging process itself disrupts the network as it is being imaged. This would lead to the belief that there is no COF layer present when in fact there was.

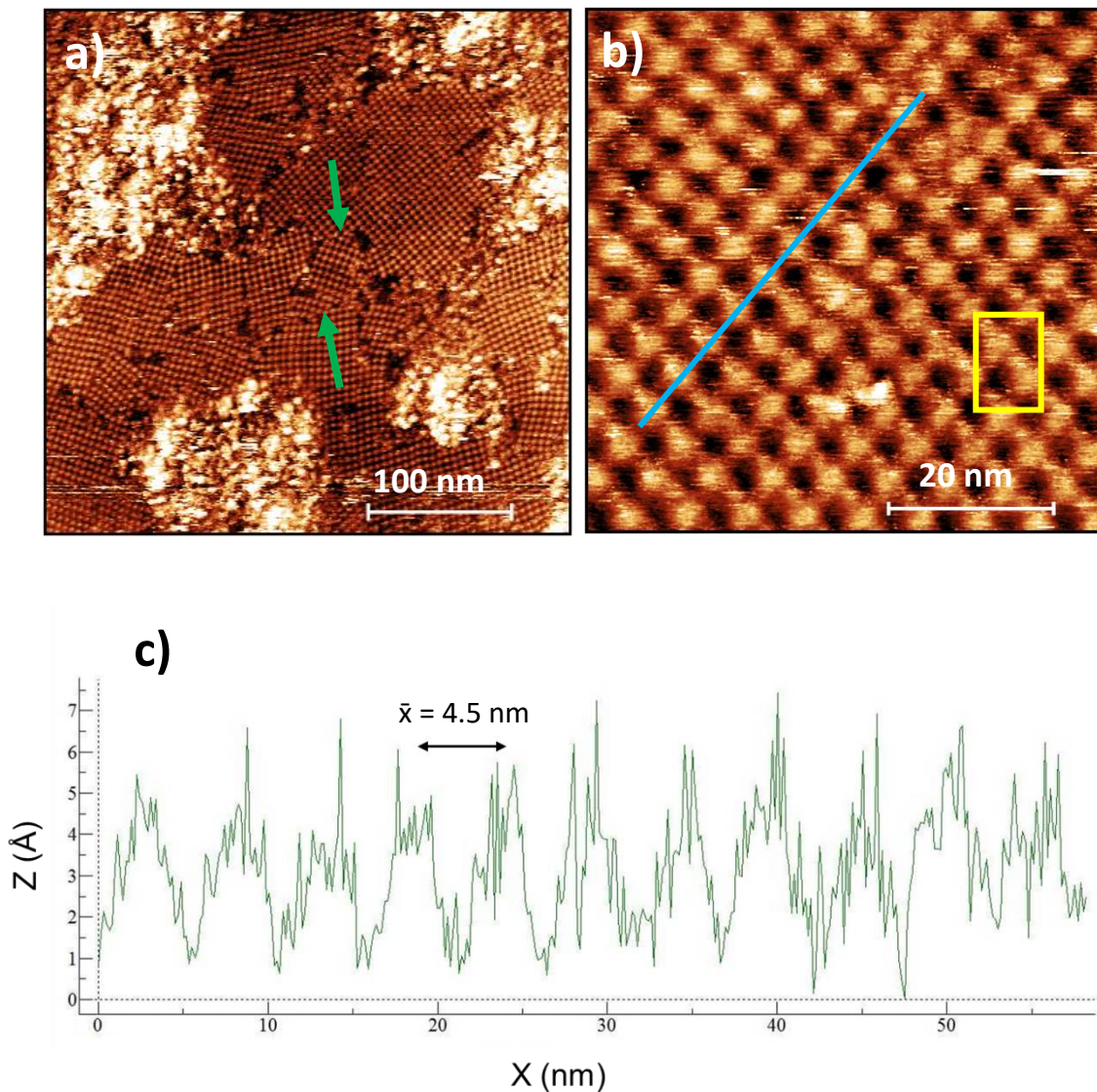


Figure 3.5: 0.15 g $\text{CuSO}_4 \cdot 5\text{H}_2\text{O}$, 60 μL (2 mg/mL BDA), 40 μL of 0.123 mg/mL TAPP in anisole spin coated: 1000 rpm, accelerated 12, 000 rps, 2 minutes, 130 °C for 18.5 hours. a) and b) imaging parameters: $V_s = -0.55$ V and $I_t = 5$ pA. c) Line profile indicated in Figure 3.5 b) which has been drift corrected. The two green arrows in Figure 3.5 a) indicate the domain boundaries between regions of COF. The yellow box highlights the electron density of the linker between the porphyrin cores.

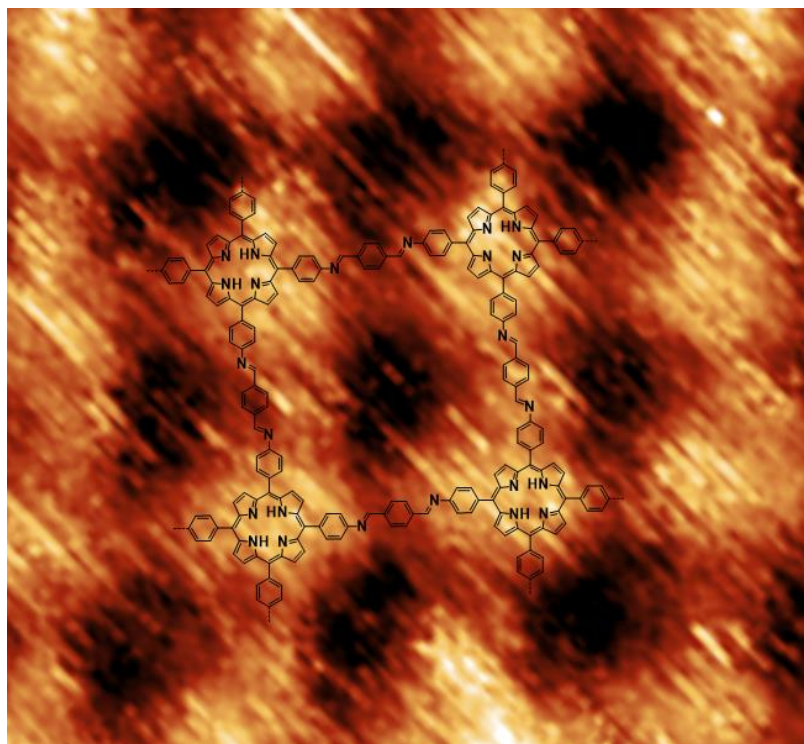


Figure 3.6: Section taken from Figure 3.5 b) with the COF-366 structure overlaid.

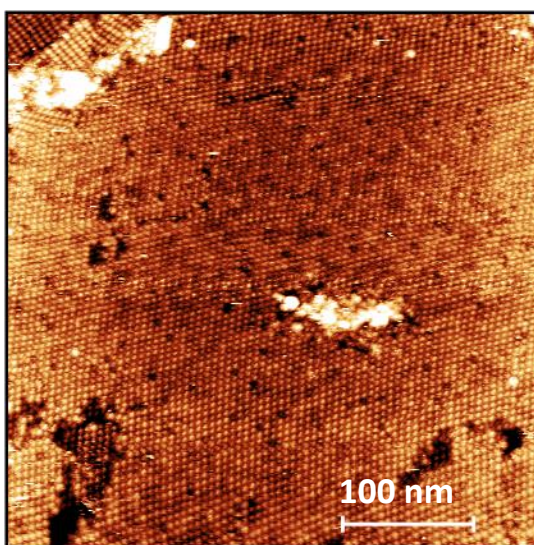


Figure 3.7: 0.15 g $\text{CuSO}_4 \cdot 5\text{H}_2\text{O}$, 60 μL (2 mg/mL BDA), 40 μL of 0.123 mg/mL TAPP in anisole spin coated: 1000 rpm, 12, 000 rps, 2 minutes, 130 $^\circ\text{C}$ for 18.5 hours. Imaging parameters: $V_s = -0.55$ V and $I_t = 5$ pA.

The STM images in Figures 3.5 and 3.7 both show COF-366 synthesised using the same standardised method. Well defined domains of different sizes can be seen and the image with a smaller scale (Figure 3.5 b) shows the regular crystallinity of said domains. This is emphasised in Figure 3.6 where the molecular structure has been overlaid on the STM image, making it clearer to see the areas of locally high density of states around the Fermi level where the porphyrin is bonded via the linker. On the other hand, you can also see regions that have no order in Figure 3.5 a). These regions appear to have an excess of material on the surface.

It is interesting to look at the crystalline domains and the boundaries at where they meet. Two examples are shown with green arrows in Figure 3.5 a). A defect domain boundary occurs because each domain began growing from a different nucleation site and when the domains meet, it is difficult to bond in a seamless manner as each domain already has a direction in which it is growing and may have already attached a linker/porphyrin which does not correspond to the molecule that it meets in the next domain. This will create a defect domain boundary.²⁰ Defects in domain boundaries has been studied by Xu *et al.* and Nguyen and Grünwald, who suggest that by reducing the number of nucleation sites then a film with larger domains can be achieved. One way this will be attempted will be to reduce the amount of TAPP on the surface, which will prevent aggregation. A second method will be to increase the time that the system is annealed for during synthesis. The second method aims to deal more with the defects that will form rather than preventing them i.e. it will give the self-healing aspect of the synthesis more time to come into effect and “repair” the domain boundaries to create larger domains.

To clarify, to improve on results presented in Figures 3.5 and 3.7, two approaches have been investigated; 1) reduce the amount of TAPP on the substrate; and 2) increase the time that the system is annealed so, the more ordered the crystal formed will be. Both possibilities are explored below.

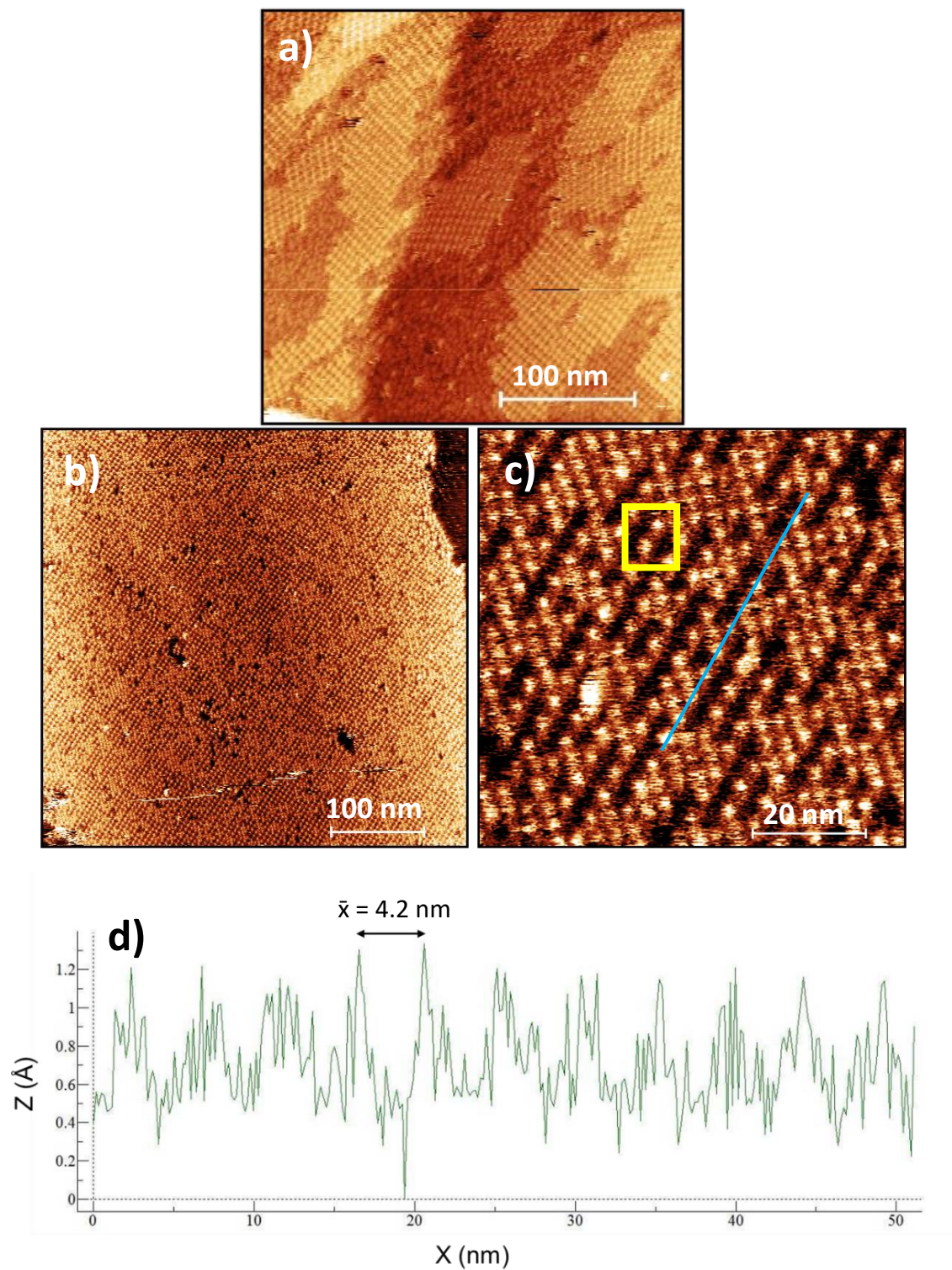


Figure 3.8: 0.15 g $\text{CuSO}_4 \cdot 5\text{H}_2\text{O}$, 60 μL (2 mg/mL BDA), 40 μL of 0.041 mg/mL TAPP in anisole spin coated: 1000 rpm, 12, 000 rps, 2 minutes, 130 $^\circ\text{C}$ for 19 hours. a) Imaging parameters: $V_s = -0.55$ V and $I_t = 5$ pA. b) and c) Imaging parameters: $V_s = -0.55$ V and $I_t = 10$ pA. d) Line profile indicated in Figure 3.8 c). The yellow box highlights the absence of electron density of the linker between the porphyrin cores.

The STM images in Figure 3.8 show what can happen when the concentration of TAPP is reduced by 66%. This does not mean that after spin-coating this translates to a reduction in amount of TAPP on the surface by 66%, the physical reduction of TAPP on the surface is assumed to be 66% because the same spin coating conditions have been used. Regions of different sizes have formed but interestingly, it seems as if these regions have formed on another film, as seen in Figure 3.8 a), which can be discerned from regions of order with a background of disordered TAPP molecules. It is unlikely that the ordered regions of COF are forming on top of a disordered layer underneath, so it is more likely that they are regions of bilayer COF and the disordered regions are monolayers. To prove this, height profiles are needed. Measuring height profiles requires a blank region next to the layers that need to be measured, but this was not possible with the images in Figure 3.8 as it was too difficult to etch away a small section with the STM tip. When this was tried, the tip became damaged and needed to be changed and then the same area could not be found again, or as was previously mentioned, maybe it was being damaged as the tip was imaging the framework and the same area could not be imaged again.

Also, from the same sample, the images in Figure 3.8 b) and 3.8 c) show TAPP molecules rather than a COF product. It is probable that there is an ordered COF structure which has some of its square pores occupied by unbound TAPP molecules as guests. This is clearer to see when comparing images 3.5 b) and 3.8 c), the former shows areas of strong electron density linked (*via* imine link) whereas the latter shows the cross-like structure of the TAPP molecule with higher electron density at the benzene rings. This is shown in the yellow boxes in Figures 3.5 b) and 3.8 c).

By measuring the line profiles, presented in Figures 3.5 c) and 3.8 d), then dividing by the number of subunits measured across, the porphyrin-porphyrin distance is measured. To improve the accuracy, the line profiles were measured five times across the same film and then averaged. For Figure 3.5 c) the value is 4.5 ± 0.9 nm and for Figure 3.8 d) it is 4.2 ± 0.2 nm. The error reported is the population standard deviation. The reported pore size for a COF-366 structure is 2 nm.²¹ There is an incredibly large

discrepancy between the result published by Wan *et al.* and the results shown here, even taking into account the standard deviation. Note that the piezoelectric scanner is regularly calibrated to the HOPG substrate, which rules out an issue with the scanner being calibrated incorrectly. One reason can be the errors in the drift correction that was performed on the image in Figure 3.5 b), whereas it was not possible to do the same for Figure 3.8 because an image of the underlying HOPG was not collected. But this still does not fully explain the large difference in pore size. Another reason could be that the peak to peak measurements are performed by eye here whereas Wan *et al.* have used powder X-Ray diffraction (pXRD) to measure the crystallinity and then a software package to calculate the pore size. The method used here is very basic and probably why the results differ so much. As other papers have reported the COF-366 pore size to be around 2.3 nm, the results in this research will not be justified or attempted to be proven correct.²² However, the result that the pore size for the COF in Figure 3.5 is larger than in Figure 3.8 will be looked into. This is because the fact that the separation increases for the bonded assembly in Figure 3.5 c) shows something else has been incorporated into the assembly. This supports the belief that Figure 3.5 shows a bonded COF with porphyrins further apart because of the additional incorporation of the linker molecules. Dogru *et al.* show that by adding and changing linker molecules with different lengths, the pore size will change.²³ The most likely reason for the distance measured in the line profile in Figure 3.8 c) is that Figures 3.8 a) - c) show a COF network filled with TAPP molecules in the pores.²⁴ Even though the amount of TAPP has been reduced, there can still be areas where TAPP can agglomerate and then coincidentally be imaged as the whole HOPG surface is 1.2 cm² and the STM will only image sections of several hundred nanometres at a time. Dipole-dipole interactions are holding the TAPP molecules in position and so the STM has been able to image them quite clearly. It can be supposed that the underlying network is very ordered as the layer formed on top is ordered. Figure 3.8 b) shows on a larger scale the extent of the overlay. In the same figure, small areas appear to be a bonded network, as those seen in Figure 3.5.

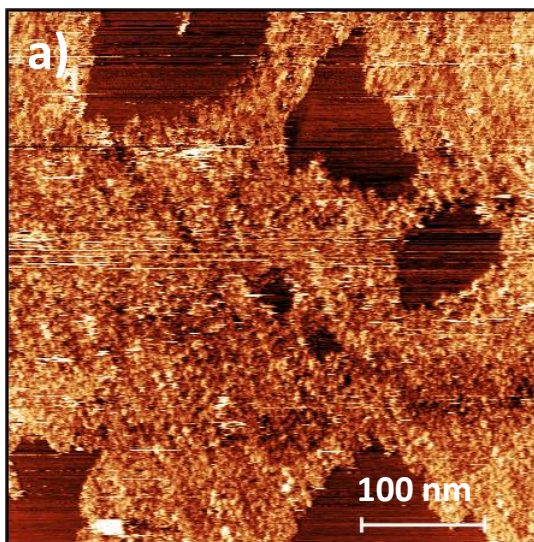


Figure 3.9: 0.15 g $\text{CuSO}_4 \cdot 5\text{H}_2\text{O}$, 60 μL (2 mg/mL BDA), 40 μL of 0.041 mg/mL TAPP in anisole spin coated: 1000 rpm, 12, 000 rps, 2 minutes, 130 $^\circ\text{C}$ for 65 hours. Imaging parameters: $V_s = -0.55$ V and $I_t = 5$ pA.

The STM image in Figure 3.9 shows what happened when increasing the reaction time from 18.5 to 65 hours. The experiments with an increased reaction time were only repeated 3 times, with the other sample showing zero success. The image is not easy to decipher because of the lack of order in the structure. This could mean that there is a side-reaction occurring with excess time which prevents the formation of the ordered COF. The type of side-reaction occurring is not possible to define as any intermediates formed may evaporate when the steel autoclave is opened or may deteriorate to other species that are not possible to image using STM. Potentially, there is an intermediate time between samples in Figure 3.5 (18.5 hours) and Figure 3.9 (65 hours) that is better suited to forming crystalline COF before any side-reactions take hold. There is a lot of potential for future work by studying other time scales. More details will be elaborated on in Chapter 6.

3.3.2 COF Synthesis with Acetic Acid

Using the conventional synthetic procedure outlined in Chapter 2 Section 2.2, it was decided to try adding a small amount of acetic acid to the system. When synthesising bulk three-dimensional (3D) COF it is essential to add acetic acid at a high concentration (6 M) in order to “push” the reaction back to its constituents to make the Schiff-based

reaction more reversible and to promote “self-healing”.²¹ Water is already added to the system in the form of $\text{CuSO}_4 \cdot 5\text{H}_2\text{O}$, so by adding acid, the hemiaminal intermediate is converted to the initial aldehyde and amine reactant (shown in Figure 3.1). This error checking system reduces the structural defects and promotes formation of an ordered structure.⁶ Therefore, the final COF possesses an ordered crystalline structure with high thermodynamic stability.

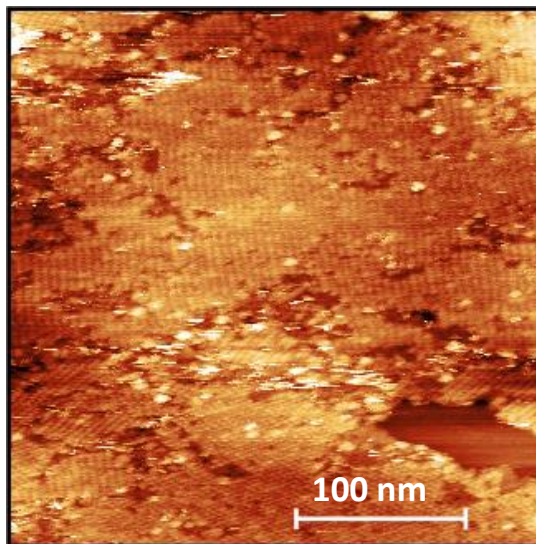


Figure 3.10: 0.16 g $\text{CuSO}_4 \cdot 5\text{H}_2\text{O}$, 60 μL (2 mg/mL BDA), 50 μL of 0.35 mg/mL TAPP in anisole spin coated: 1000 rpm, 500 rps, 2 minutes, 20 μL acetic acid, 130 °C for 52 hours. Imaging parameters: $V_s = -0.55$ V and $I_t = 10$ pA.

Figure 3.10 shows one of the first attempts to grow a COF with the addition of acetic acid. A COF layer has formed across greater than half of the surface that displays an ordered structure. However, there are also extensive patches of highly disordered structure which appear as vacancies in the film or where regions forming separately do not join to continue the crystallinity, and results in a significant number of defects. These structures are far from the pristine films that are desired.

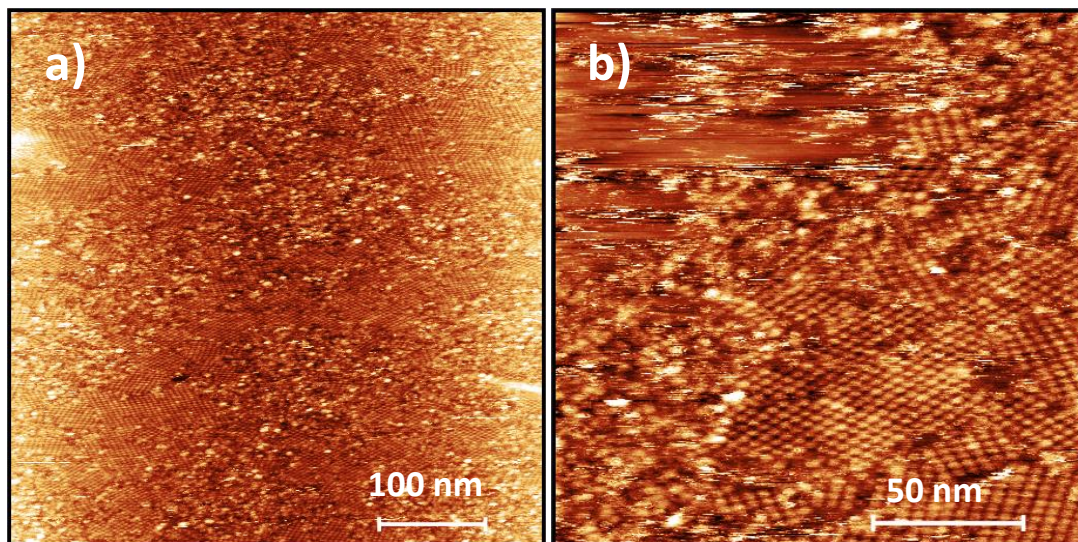


Figure 3.11: 0.15 g $\text{CuSO}_4 \cdot 5\text{H}_2\text{O}$, 60 μL (2 mg/mL BDA), 50 μL of 0.26 mg/mL TAPP in anisole spin coated: 2000 rpm, 1500 rps, 2 min, 5 μL acetic acid, 130 $^\circ\text{C}$ for 16 hours. a) and b) imaging parameters: $V_s = -0.50$ V and $I_t = 5$ pA.

After repeating the synthesis and changing several parameters, such as reducing the length of time of the synthesis by 36 hours, it was still uncertain whether the acid in the reaction system was helping or hindering. Better COF films had been made prior to the ones with the acetic acid (seen in Section 2.1). Even by reducing the amount of acid and shortening the synthesis time (to avoid side reactions), the COF films (Figure 3.11) had not improved in comparison to those made without acetic acid. For example, in Figures 3.5 and 3.8, the film looks more ordered and the coverage better and no acetic acid was included in the synthesis procedure. It was decided to set aside the idea of adding acid to the system. It is possible that the acid made the reaction too reversible and that even smaller amounts of acid are needed, or even that it was aiding side reactions that prohibited the formation of crystalline COF films.

3.3.3 Metallated COFs

So far, the focus has been on freebase TAPP to synthesise COFs. Experiments were also carried out on metallated TAPP; zinc (II) -5,10,15,20-tetrakis-(4-aminophenyl) porphyrin (ZnTAPP) and copper (II) -5,10,15,20-tetrakis-(4-aminophenyl) porphyrin (CuTAPP). The synthesis of freebase and metallated TAPP COFs is identical. It was decided to try to synthesise metallated COFs because the coordinated metal-ligand bond

changes the properties of the porphyrin, and subsequently the COF. For example, this can directly be seen in comparing the solubility of ZnTAPP to CuTAPP. Tetrahydrofuran (THF) is used to dissolve ZnTAPP because the THF can coordinate to the slightly ionic zinc in the porphyrin core, which reduces the possibility of oxidising the zinc.²⁵ CuTAPP does not dissolve in either THF or chloroform at the concentrations needed in this synthesis.

Zinc and copper TAPP derivatives were chosen because they are easy to acquire because of the ease of the synthesis as both zinc and copper atoms are the correct size to coordinate within the TAPP core, and because past research has shown that there is longer-lived charge separation in Zn-porphyrin compared to the freebase porphyrin.^{26,27} This is further elaborated on in Chapter 5 which studies the electronic properties of the metallated-TAPP and then COFs.

With regards to comparing the metallated-TAPP COFs to freebase TAPP COFs using STM, it is rather difficult to discern a difference in the STM images. The reason is because both zinc and copper are closed-shell metal ions with d^{10} configuration, and this means they do not contribute significantly to the density of states around the Fermi level of the systems.^{28,29} Therefore, there will not be an increase in current in the metal region and so they will not appear brighter in the STM image. Nonetheless, the STM images can show the successful synthesis of metallated COFs and further analysis will be undertaken using transient absorption spectroscopy, which is detailed in Chapter 5.

Figure 3.12 shows a monolayer ZnCOF but it is clear to see the coverage does not extend across the whole substrate. However, in comparison to Figure 3.5 a) of a freebase TAPP, Figure 3.12 does not show areas of unreacted ZnTAPP which is positive and so it can be assumed that the coverage is more likely to be ZnCOF rather than ZnTAPP. Figure 3.13 is a smaller section imaged from Figure 3.12 and shows the regular order within the individual domains.

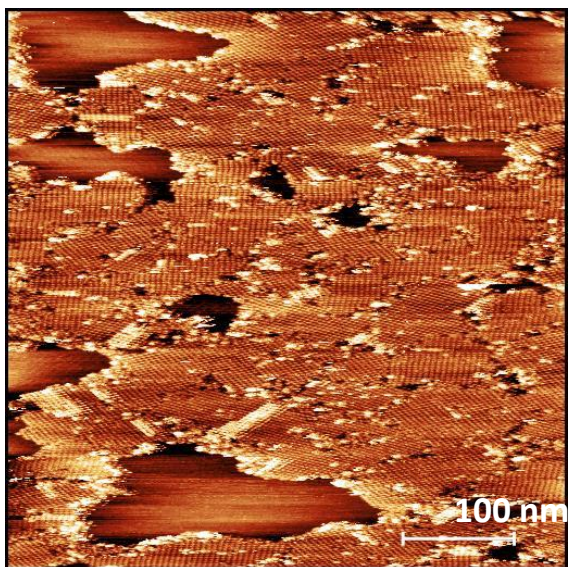


Figure 3.12: 0.15 g $\text{CuSO}_4 \cdot 5\text{H}_2\text{O}$, 65 μL (2 mg/mL BDA), 75 μL of 0.30 mg/mL ZnTAPP in THF spin coated: 1000 rpm, 500 rps, 2 minutes, 130 $^\circ\text{C}$ for 20 hours. Imaging parameters: $V_s = -0.55$ V and $I_t = 10$ pA.

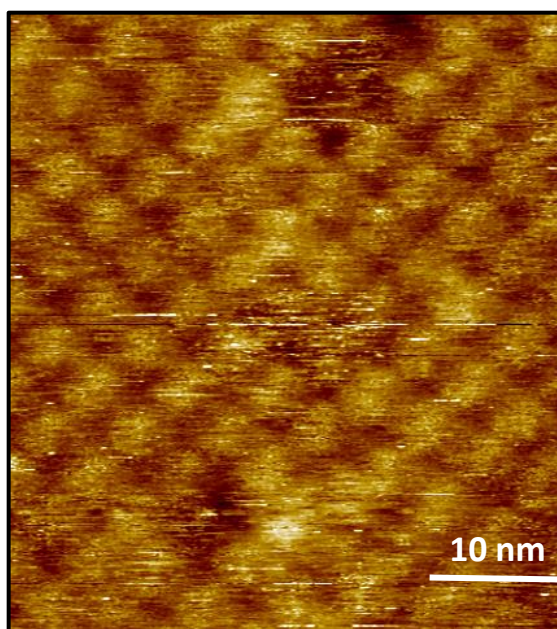


Figure 3.13: 0.15 g $\text{CuSO}_4 \cdot 5\text{H}_2\text{O}$, 65 μL (2 mg/mL BDA), 75 μL of 0.30 mg/mL ZnTAPP in THF spin coated: 1000 rpm, 500 rps, 2 minutes, 130 $^\circ\text{C}$ for 20 hours. Imaging parameters: $V_s = -0.55$ V and $I_t = 10$ pA. Drift corrected.

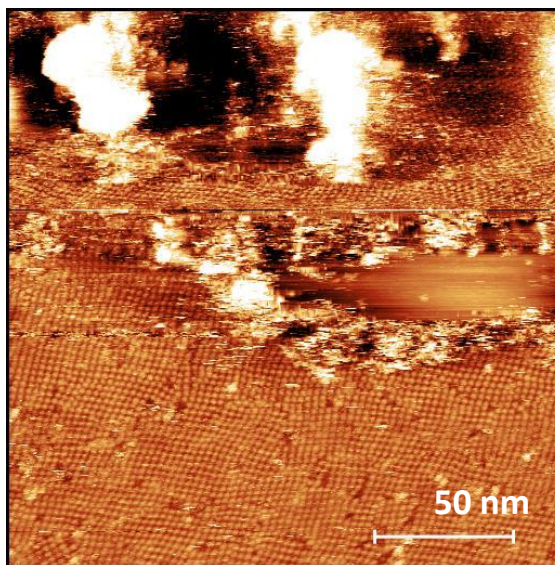


Figure 3.14: 0.15 g $\text{CuSO}_4 \cdot 5\text{H}_2\text{O}$, 30 μL (4 mg/mL BDA), 50 μL of 0.10 mg/mL CuTAPP in THF spin coated: 800 rpm, 10, 000 rps, 2 minutes, 130 $^\circ\text{C}$ for 3 hours. Imaging parameters: $V_s = -0.55$ V and $I_t = 10$ pA.

Figure 3.14 shows a CuCOF with half the image showing monolayer coverage and the upper half showing disordered reactants. As with previous STM images in this section, a large focus on future work needs to be on improving the synthesis to reduce the defects and disorder, and increase monolayer coverage.

3.4 Other Proof of COF Synthesis

3.4.1 Fourier-Transform Infrared Spectroscopy (FTIR)

Another way in which samples were determined to have successfully synthesised into COF films was using Fourier-transform infrared spectroscopy (FTIR). In an unreacted porphyrin sample, amine bands should appear in the FTIR spectra. After addition of an aldehyde linker, the aldehyde and amine will react via a Schiff-base reaction to form an imine bond, so in the FTIR spectra there will be a reduction in the amine band and the appearance of an imine band. With regards to the amine, there will be peaks showing the amine N-H stretching vibrations and the amine N-H bending vibrations.³⁰ As solids or liquids, the stretching vibrations of primary amines absorb in the general region 3450 – 3160 cm^{-1} .³⁰ Two bands will occur, one will be a broad band of medium intensity, in the region 3330 – 3250 cm^{-1} ; and the second will be a less intense band in the region 3400 –

3300 cm^{-1} . The amine N-H bending vibrations for primary amines have a medium-strong absorption in the region 1650 – 1580 cm^{-1} . For imines, the C=N stretching band occurs in the region 1690 – 1620 cm^{-1} . This is summarised in Table 3.1.

	Region (cm^{-1})
Primary amine N-H stretch	3400 – 3300
	3330 – 3250
Primary amine N-H bend	1650 – 1580
Imine C=N stretch	1690 – 1620

Table 3.1: Summary of IR stretching and bending bands for primary amines and imines.³⁰

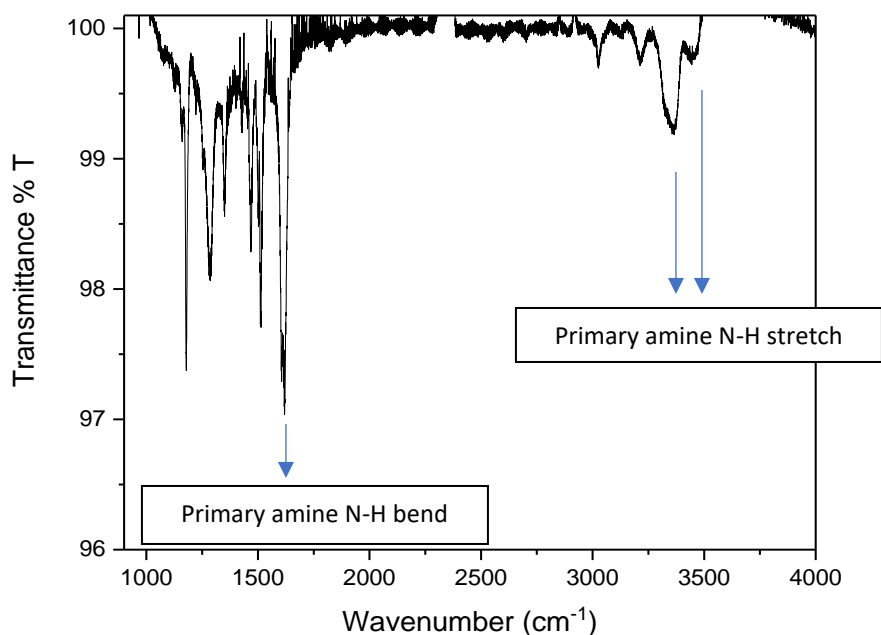


Figure 3.15: FT-IR spectrum of TAPP, 18.18 mg/mL in chloroform spin coated (10, 000 rps; 800 rpm; 2 min) on calcium fluoride substrate.

Figure 3.15 shows the FTIR spectrum of TAPP, the primary amine bands have been indicated. The concentration of the TAPP solution used is significantly larger than for monolayer synthesis used for the STM investigations. This is to get a measurable signal from the FTIR. The bands at 1610, 3350 and 3390 cm^{-1} occur in the amine regions as indicated by reference values highlighted in Table 3.1.³⁰ As the primary amine N-H

bend and imine C=N stretch have an overlap in the region they can appear, it is important to note that in the TAPP film used, no synthesis has been carried out and no BDA has been added so there is no chance for a C=N bond to form. Therefore, the bands must be attributed to a primary N-H amine band.

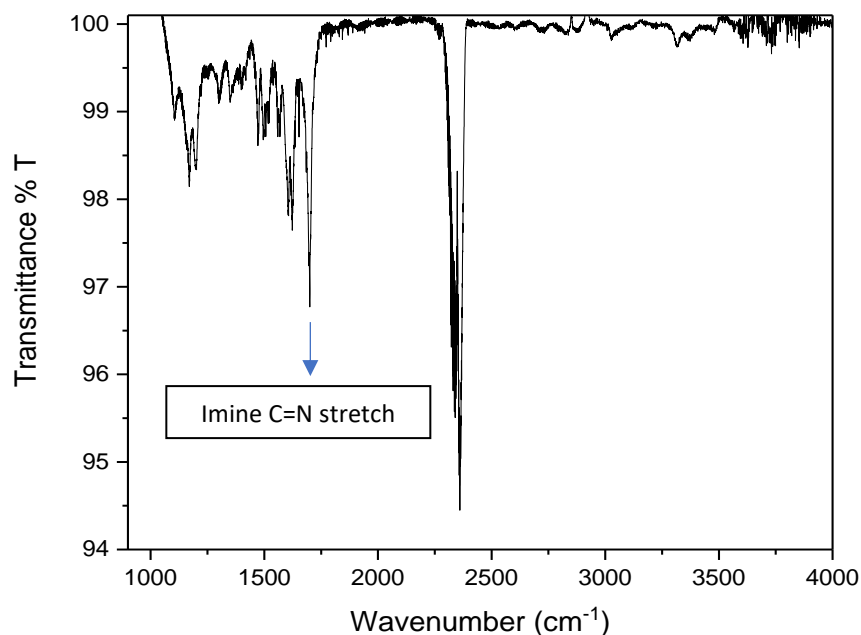


Figure 3.16: FT-IR spectrum of COF made from TAPP 18.18 mg/mL in chloroform spin coated (10,000 rps; 800 rpm; 2 min) on calcium fluoride substrate; 0.15 g CuSO₄·5H₂O, 30 μL of 2 mg/mL BDA, argon purged and 16 hours at 130 °C.

Figure 3.16 shows the FTIR spectrum of a COF, note the absence of the primary amine stretching bands in the region 3450 – 3160 cm⁻¹. Also, the band at 1680 cm⁻¹ shows the imine stretch. This is outside of the region where a primary amine N-H bend will appear so with confidence, it can be attributed to an imine stretch. No remnant of the amine N-H is clear to see in Figure 3.16 but the intensity of the peaks are not strong so it is not possible to say that no unreacted TAPP providing the N-H bands is present. It is important to note that the strong band at ~2350 cm⁻¹ is from background carbon dioxide.³¹ The peak also exists in Figure 3.15 but during the data processing it has been omitted. The FTIR spectra show the reaction of the amine to an imine, indicating the

successful reaction to form a COF. This result is extrapolated to COF films synthesised for other experimental techniques, mainly transient absorption spectroscopy.

3.4.2 X-ray Photoelectron Spectroscopy (XPS)

Another way in which samples were determined to have successfully synthesised into COF films was using X-ray photoelectron spectroscopy (XPS).

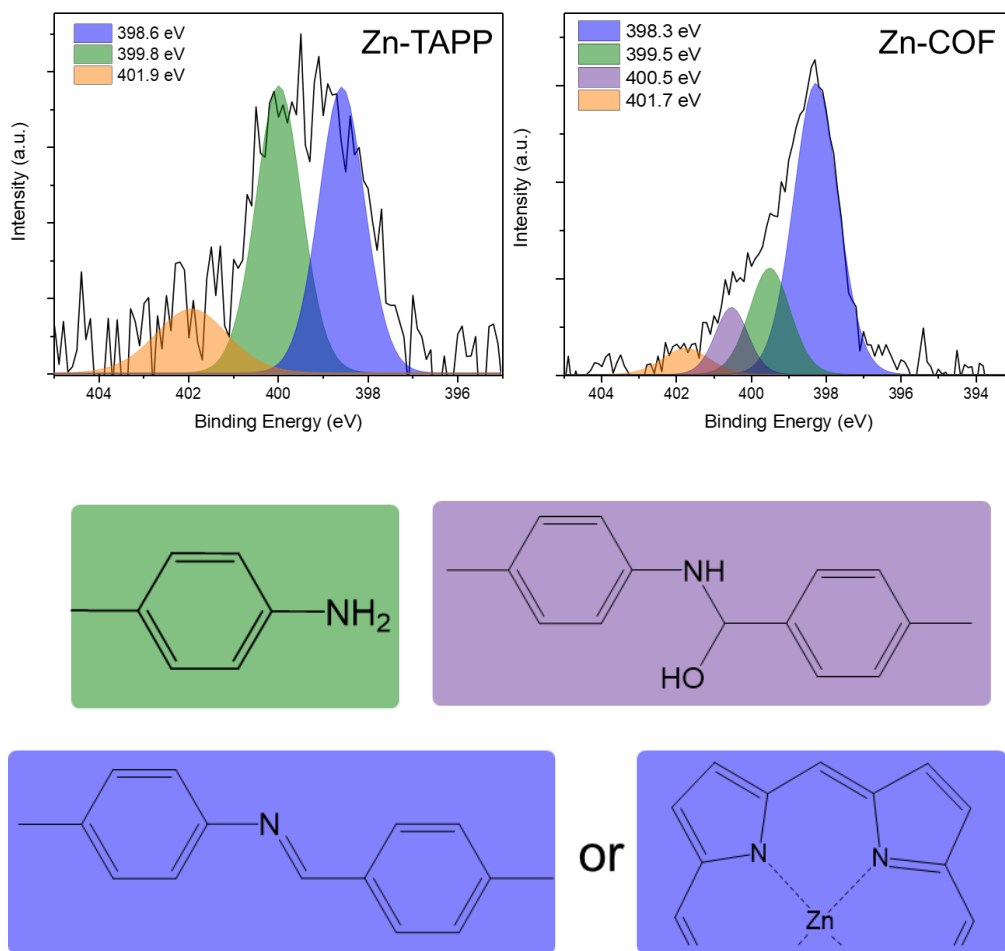


Figure 3.17: N1s XPS spectra for unreacted ZnTAPP and ZnCOF. The synthesis procedure is detailed in Figure 3.12. The black lines represent experimental data after background subtraction. The coloured components correspond to Gaussian–Lorentzian functions used to fit the data. The graph legends show the binding energy associated with each component. The schematic at the bottom of the figure shows the molecular configurations of the different N species. The orange area is the satellite peak.

The results in this section will focus on the COF synthesis from ZnTAPP. The chemical structure of the bonds before and after synthesis via the Schiff-base condensation reaction was investigated using XPS. Figure 3.17 shows the XPS spectra

before and after synthesis and the coloured schematics indicate which XPS peaks have been assigned to different nitrogen environments. N1s XPS spectra were used to study the chemical composition of the unreacted ZnTAPP and then the ZnCOF. For a ZnTAPP molecule, there are two nitrogen species: nitrogen in amine groups on the outer phenyl rings, and nitrogen coordinated to the Zn in the porphyrin core. This is shown in Table 3.2. Conventionally, XPS peak values are reported with respect to a reference peak. This is normally an intense peak in the survey spectra that is used as a fixed point. This process helps remove the possibility of charging of the substrate affecting the results by arbitrarily shifting the peak positions. In most cases the C1s peak is used (with a binding energy of ~285 eV) because even samples that are not supposed to have carbon present have it as adventitious carbon contamination. This peak is particularly easy to use in this research as all molecules are mostly carbon and the HOPG substrate is entirely carbon. The amine on the phenyl ring was measured to have a binding energy of 399.8 eV which is within the literature data of 399.4 ± 0.4 eV. The experimental values are in accordance with the literature values. The nitrogen coordinated to the Zn is also accurate with respect to the literature value as the experimental binding energy is 398.6 eV and literature value is 398.5 ± 0.3 eV.

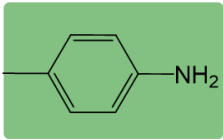
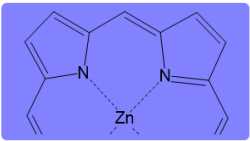
Nitrogen Species	Chemical Structure	Binding Energy in Literature (eV)	Experimental Binding Energy (eV)	Percentage of Total Fit Area
Amine on phenyl ring		$\sim 399.4 \pm 0.4$	399.8 ± 0.1	50.4 %
Nitrogen coordinated to zinc inside porphyrin core		$\sim 398.5 \pm 0.3$	398.6 ± 0.1	49.6 %

Table 3.2: XPS binding energy values of nitrogen species in ZnTAPP from literature and experimental results.^{32,33}

In addition to the N1s peaks for the unreacted ZnTAPP, an additional satellite peak was observed. The satellite peak is reported in literature in the binding energy range 401 – 402 eV for N1s XPS spectra of porphyrins.^{34,35} The satellite peak is a result from electron interactions within the aromatic porphyrin core which is an extended delocalised electron system.³⁶ This means there are a significant density of states (both occupied and unoccupied) around the Fermi level. The outgoing photoelectron can lose some energy by exciting one of these delocalised electrons into a slightly higher energy state within the delocalised system. This results in the emitted photoelectron having lower kinetic energy than expected and therefore it is measured as having an initially higher binding energy – hence the satellite peak at higher binding energy values. Details of the peak fitting and constraints applied can be found in Chapter 2. The N1s spectrum is an average taken from three identical N1s scans. The percentage of each nitrogen species is expected to be 50 % because of the molecular structure, which is shown to be in good accordance with the experimental data factoring in experimental error (50.4 and 49.6 %).

When fitting the N1s spectrum for the ZnCOF sample, the number of nitrogen species has changed. A proportion of amine groups on the phenyl ring will react via the Schiff-base condensation reaction between ZnTAPP and BDA. Four nitrogen species are expected to be present: the amine on the phenyl ring, nitrogen coordinated to Zn inside the porphyrin core, nitrogen imine bonds and nitrogen hemiaminal bonds. However, the binding energy of the N1s peaks for the nitrogen coordinated to the Zn and the nitrogen imine bond are so similar that their individual contributions to the XPS spectrum cannot be separated.³³ The binding energies are summarised in Table 3.3 for ZnCOF.

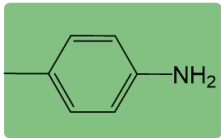
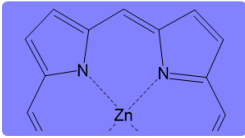
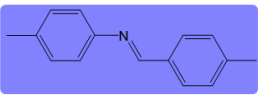
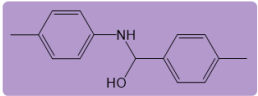
Nitrogen Species	Chemical Structure	Binding Energy in Literature (eV)	Experimental Binding Energy (eV)	Percentage of Total Fit Area
Amine on phenyl ring		$\sim 399.4 \pm 0.4$	399.5 ± 0.1	13.6 %
Nitrogen coordinated to zinc inside porphyrin core		$\sim 398.5 \pm 0.3$	398.3 ± 0.1	65.5 %
Nitrogen imine bond				
Nitrogen hemiaminal bond		400.7	400.5 ± 0.1	20.9 %

Table 3.3: XPS binding energy values of nitrogen species in ZnCOF films from literature and experimental results.

The XPS results show that percentage of amine nitrogen on phenyl rings has decreased from 50.4 % to 13.6 % as the amine is converted to an imine or hemiaminal bond. The percentage of the coordinated nitrogen to Zn species is assumed to be constant as these nitrogen atoms are not involved in the reaction. Therefore, the percentage of nitrogen in imine bonds is estimated to be 15.5 % (65.5 – 50%) as there are no imine bonds before reaction. The results in Table 3.3 show that there is a higher percentage of nitrogen hemiaminal species. This is due to several factors, for example, the addition of water in the synthetic procedure may facilitate the production of hemiaminal bonds. Also, the percentage of nitrogen atoms coordinated to Zn is assumed

to be 50 % whereas this may not be exact due to statistical fluctuations from the peak fitting. In conclusion, the XPS does show that a reaction is occurring but the success of the reaction, formation of imine bonds rather than hemiaminal, is not truly successful and further experiments can be carried out to investigate the reaction further.

3.5 Conclusion

In conclusion, 2D-COFs were grown using the Schiff-base condensation reaction between TAPP, ZnTAPP and CuTAPP with the BDA linker.

The crystallinity and morphology of the COF films could be determined by different experimental parameters and in this thesis, several parameters were changed in order to improve the crystallinity and domain sizes of the COF films; for example: amount of TAPP deposited on substrate, reaction time and addition of acetic acid.

STM, FTIR and XPS has shown that the COF synthesis technique used in this thesis is reliable in making a COF but STM images show that the crystallinity, domain sizes and defects of the COF need to be improved. Efforts were made to change parameters, as mentioned above, but the list of affected parameters is extensive giving a large scope for future work. Nguyen and Grünwald have studied the poor crystallinity in the synthesis of COFs and they emphasise the need for control over the relative strength of binding and stacking which can be used to tune the morphology of the COF crystals.¹⁹ If there is a strong interaction between the planar 2D-COF layers then the system will tend towards ordered stacking. To avoid this, Nguyen and Grünwald propose that the way the nucleation begins is an important property that can dictate the rest of the synthesis and so rather than allow a nucleation stage, use a solution at low supersaturation with a small concentration of the COF already synthesised to avoid defective aggregation of large numbers of small crystallites.¹⁹ In addition, Ascherl *et al.*, who studied 3D-COFs with the remit that COFs are promising materials for optoelectronic applications, state that long-range order within the framework remains a major challenge.³⁷ To overcome this, Ascherl *et al.* developed a concept that by utilising building blocks that are 3D propeller-shaped, they create well defined docking sites for consecutive COF sheets and this

promotes long range order. Trying to replicate a system that favours a certain conformation could hold possibilities that the self-healing reaction will always tend towards a certain product.

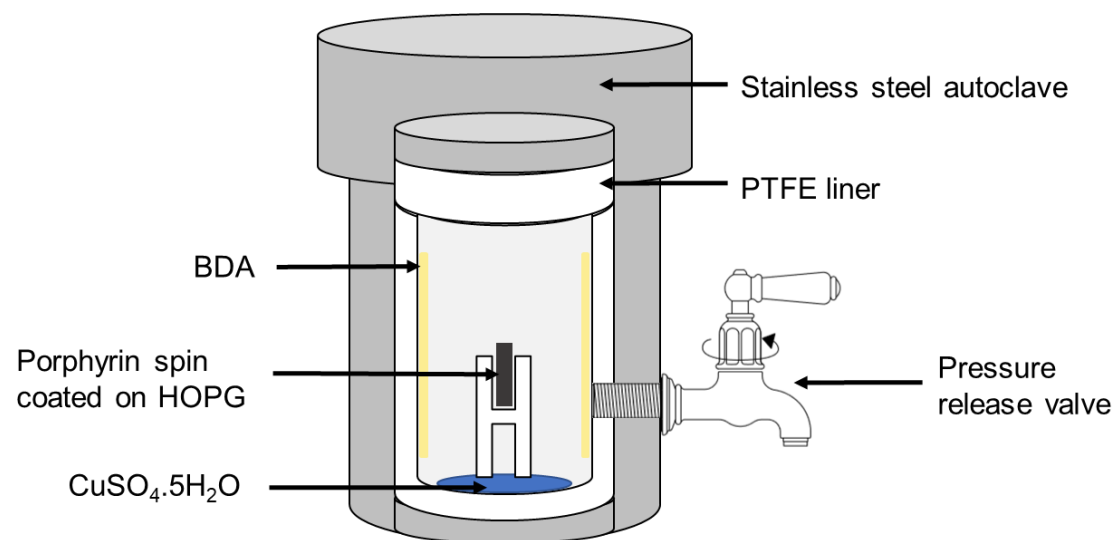


Figure 3.18: Modified diagram of Figure 2.3 showing an additional pressure release valve incorporated into the steel autoclave to prevent condensation of BDA linker.

Figure 3.18 is a proposed design for an improved steel autoclave. As a stumbling block was the condensation of the BDA linker during the cool down of the sample, it would be beneficial to incorporate a pressure release valve so that even though the autoclave is at a high temperature, it will still be possible to open the system to allow the BDA and water vapour to escape rather than condensate on the HOPG surface and effect the COF formation. It will be important to take into consideration that the valve does not add a potential leak to the sealed system, so the valve would need to be incorporated into the autoclave body rather than a separate alteration.

The XPS results showed that the chemical composition of the covalent bonds formed between the amine functionalised porphyrins and aldehyde linker changed to a mixture of imine and hemiaminal groups. This change in chemical composition is a reliable way in which to confirm a reaction has taken place over a larger area as the XPS

can measure an area of up to 400 μm , whereas the STM will scan areas of $\sim 1 \mu\text{m}$ until the sample area is manually moved.

With regards to comparing the freebase TAPP to metallated TAPP synthesis, it is not definitive to determine whether one forms a COF film more readily than the other. More samples were made using the freebase TAPP but this was mainly to improve on the reliability of the synthesis as a whole. The metallated TAPP COF synthesis was then carried out as improvements to the synthesis technique were made, for example, determining which spin coating parameters led to more uniform films.

The results collected in this chapter will help to advance the improvement of a more controllable and tuneable COF synthesis. There is a large scope for future work in improving the growth, morphology and chemical functionalisation of the COF films. Chapter 6 will describe in further detail the scope for future work.

3.6 Bibliography

- 1 R. K. Sharma, P. Yadav, M. Yadav, R. Gupta, P. Rana, A. Srivastava, R. Zbořil, R. S. Varma, M. Antonietti and M. B. Gawande, *Mater. Horizons*, 2020, **7**, 411–454.
- 2 C. D. Meyer, C. S. Joiner and J. F. Stoddart, *Chem. Soc. Rev.*, 2007, **36**, 1705.
- 3 G. Zhu and H. Ren, *Principles for the Synthesis of Porous Organic Frameworks*, Springer Berlin Heidelberg, 2015.
- 4 S. J. Rowan, S. J. Cantrill, G. R. L. Cousins, J. K. M. Sanders and J. F. Stoddart, *Angew. Chemie Int. Ed.*, 2002, **41**, 898–952.
- 5 L. Zhu and Y.-B. Zhang, *Molecules*, 2017, **22**, 1149.
- 6 X. Feng, X. Ding and D. Jiang, *Chem. Soc. Rev.*, 2012, **41**, 6010.
- 7 H. Wang, Z. Zeng, P. Xu, L. Li, G. Zeng, R. Xiao, Z. Tang, D. Huang, L. Tang, C. Lai, D. Jiang, Y. Liu, H. Yi, L. Qin, S. Ye, X. Ren and W. Tang, *Chem. Soc. Rev.*, 2019, **48**, 488–516.
- 8 I. V. Sazanovich, A. Balakumar, K. Muthukumaran, E. Hindin, C. Kirmaier, J. R. Diers, J. S. Lindsey, D. F. Bocian and D. Holten, *Inorg. Chem.*, 2003, **42**, 6616–6628.
- 9 D. Holten, D. F. Bocian and J. S. Lindsey, *Acc. Chem. Res.*, 2002, **35**, 57–69.
- 10 Z. Wang, Y. Liu, Z. Wang, L. Cao, Y. Zhao, C. Wang and W. Lin, *Chem. Commun.*, 2017, **53**, 9356–9359.
- 11 A. H. A. Clayton, G. D. Scholes, K. P. Ghiggino and M. N. Paddon-Row, *J. Phys. Chem.*, 1996, **100**, 10912–10918.
- 12 H. Yamaguchi, M. Kamachi and A. Harada, *Angew. Chemie*, 2000, **112**, 3987–3989.
- 13 M. S. Lohse and T. Bein, *Adv. Funct. Mater.*, 2018, **28**, 1705553.
- 14 S.-Y. Ding, J. Gao, Q. Wang, Y. Zhang, W.-G. Song, C.-Y. Su and W. Wang, *J. Am. Chem. Soc.*, 2011, **133**, 19816–19822.

- 15 C.-Z. Guan, D. Wang and L.-J. Wan, *Chem. Commun.*, 2012, **48**, 2943.
- 16 M. E. Galwey, A.K. ; Brown, *Thermal Decomposition of Ionic Solids: Chemical Properties and Reactivities of Ionic Crystalline Phases*, Elsevier, 1999, vol. 86.
- 17 E. Wiberg, N. Wiberg and A. F. Holleman, *Inorganic chemistry*, Academic Press, 2001.
- 18 Y. Hu, N. Goodeal, Y. Chen, A. M. Ganose, R. G. Palgrave, H. Bronstein and M. O. Blunt, *Chem. Commun.*, 2016, **52**, 9941–9944.
- 19 V. Nguyen and M. Grünwald, *J. Am. Chem. Soc.*, 2018, **140**, 3306–3311.
- 20 L. Xu, X. Zhou, Y. Yu, W. Q. Tian, J. Ma and S. Lei, *ACS Nano*, 2013, **7**, 8066–8073.
- 21 S. Wan, F. Gándara, A. Asano, H. Furukawa, A. Saeki, S. K. Dey, L. Liao, M. W. Ambrogio, Y. Y. Botros, X. Duan, S. Seki, J. F. Stoddart and O. M. Yaghi, *Chem. Mater.*, 2011, **23**, 4094–4097.
- 22 S. Lin, C. S. Diercks, Y.-B. Zhang, N. Kornienko, E. M. Nichols, Y. Zhao, A. R. Paris, D. Kim, P. Yang, O. M. Yaghi and C. J. Chang, *Science (80-.)*, 2015, **349**, 1208–1213.
- 23 M. Dogru, A. Sonnaier, A. Gavryushin, P. Knochel and T. Bein, *Chem. Commun.*, 2011, **47**, 1707–1709.
- 24 K. Wandelt, *Encyclopedia of interfacial chemistry: Surface science and electrochemistry*, 2018.
- 25 D. McKearney, S. Choua, W. Zhou, Y. Ganga-Sah, R. Ruppert, J. A. Wytko, J. Weiss and D. B. Leznoff, *Inorg. Chem.*, 2018, **57**, 9644–9655.
- 26 F. Hernández-Fernández, M. Pavanello and L. Visscher, *Phys. Chem. Chem. Phys.*, 2016, **18**, 21122–21132.
- 27 Bahr, Kuciauskas, Liddell, Moore, Moore and Gust, *Photochem. Photobiol.*, 2000, **72**, 598–611.
- 28 X. Lu and K. W. Hipps, *J. Phys. Chem. B*, 2002, **101**, 5391–5396.

- 29 L. Scudiero, D. E. Barlow and K. W. Hipps, *J. Phys. Chem. B*, 2000, **104**, 11899–11905.
- 30 G. Socrates, *Infrared and raman characteristic group frequencies : tables and charts.*, John Wiley & Sons, 2007.
- 31 M. Falk and A. G. Miller, *Vib. Spectrosc.*, 1992, **4**, 105–108.
- 32 P. G. Gassman, A. Ghosh and J. Almlöf, *J. Am. Chem. Soc.*, 1992, **114**, 9990–10000.
- 33 M. Di Giovannantonio, T. Kosmala, B. Bonanni, G. Serrano, N. Zema, S. Turchini, D. Catone, K. Wandelt, D. Pasini, G. Contini and C. Goletti, *J. Phys. Chem. C*, 2015, **119**, 19228–19235.
- 34 V. N. Nemykin, P. Galloni, B. Floris, C. D. Barrett, R. G. Hadt, R. I. Subbotin, A. G. Marrani, R. Zanoni and N. M. Loim, *J. Chem. Soc. Dalton Trans.*, 2008, **32**, 4233–4246.
- 35 Y. Niwa, H. Kobayashi and T. Tsuchiya, *J. Chem. Phys.*, 1974, **60**, 799–807.
- 36 D. H. Karweik and N. Winograd, *Inorg. Chem.*, 1976, **15**, 2336–2342.
- 37 L. Ascherl, T. Sick, J. T. Margraf, S. H. Lapidus, M. Calik, C. Hettstedt, K. Karaghiosoff, M. Döblinger, T. Clark, K. W. Chapman, F. Auras and T. Bein, *Nat. Chem.*, 2016, **8**, 310–316.

4 Laser Studies: TAPP and COF

This chapter begins to look at the photophysical properties of porphyrins and covalent organic frameworks (COFs). It has already been discussed in Chapter 1 the number of reasons why porphyrins are being extensively studied because of their unique properties. The technique that will be used, transient absorption spectroscopy (TAS), has been detailed in Chapter 2 with a discussion into how the data is processed.

There have been many studies recently of the photophysical properties of porphyrin-based COFs. A study by Jakowetz *et al.* looked at the ultrafast excited-state dynamics of a series of fully conjugated 2D-COFs in which different molecular subunits are connected through imine bonds, using TAS.¹ Although the COFs feature different topologies and chromophores, the excited states behave similarly across the series synthesised by Jakowetz *et al.* The proposed mechanism of the excited-state dynamics shows charges are generated through rapid singlet–singlet annihilation and show lifetimes of several tens of microseconds. Singlet–singlet annihilation (SSA) is a mechanism of fluorescence quenching induced by Förster-type energy transfer between two fluorophores while they are both in their first excited singlet states (S_1S_1).² The Förster energy transfer is the phenomenon that an excited donor transfers energy (not an electron) to an acceptor group through a non-radiative process.³ However, Jakowetz *et al.* speculate that there must be another process generating charges because it seems unlikely that SSA alone will yield a significant amount of charges. Their system was not set-up to study these processes at longer time scales and therefore they focus of the SSA process. Jakowetz *et al.* note that for potential applications in optoelectronics, it is essential to have a well-ordered, π -stacked framework as this architecture yields potentially well-defined electron- and hole-conducting channels.⁴ In their study they used vertically oriented thin films (stacked 2D films) of tetrafunctionalised 1,1,2,2-tetrakis(4-aminophenyl)ethane ($4PE(NH_2)_4$) and tridentate 1,3,5-tris(4-

aminophenyl)benzene ($3\text{PB}(\text{NH}_2)_3$) connected by linear dialdehyde linkers. Jakowetz *et al.* conclude that the high rate of SSA suggests that the initially generated charges might be significantly delocalised, leading to fast bimolecular recombination processes. They note that the singlets do not necessarily have to reside on the same COF sheet but can also interact across the different sheets. The free charges can eventually get “trapped” by either real molecular traps or across different COF sheets, isolating the charges and spatially hindering their recombination. This gives rise to the long-lived nature of these charges compared to pristine films of the precursor materials. This “long-lived” nature is the reason microsecond-TAS is used in this research.

The porphyrin that will be studied is TAPP, and the COF studied will be synthesised using TAPP and BDA. The synthesis is detailed in Chapter 2. Firstly, this chapter will look at the TAPP in solution and then as a film spin coated on a substrate. It is important to note that this film is classed as a “thick” film. This has been arbitrarily defined as a film with a Soret band in the ground state UV-visible absorption having an absorption greater than 0.4 a.u. [It is important to note that a thickness dependence study was carried out to be able to plot a line of best fit between ground state absorption and film thickness in nm. However, the method employed was not a reliable method. Firstly, a profilometer was used but this could not measure below 100 nm. Then an atomic force microscope (AFM) was used after manually scratching the films with a scalpel to create a profile. The profile will show the porphyrin material and then a “trench” where the material has been removed. It was not clear to see if all the material had been removed or if the glass substrate was being damaged from the scalpel scratch. Hence, further testing was stopped.] The aim was to use all films with a ground state absorption of 0.4 a.u. This is more reproducible than number of monolayers as the ground state absorption can be directly measured. After analysis of TAPP films, a COF film will be investigated with comparisons being made against the TAPP film.

4.1 TAPP Solution

In solution molecular photochemistry, a considerable degree of rationalisation and understanding of the photophysical and photochemical processes has been gained by applying transient absorption spectroscopy to the detection of electronic excited states and reactive intermediates generated photochemically. For this study in solution, the ideal is to study the individual porphyrin molecules compared to films in which the molecules can orientate and stack on top of each other, changing the crystallinity, morphology and electron delocalisation. However, porphyrins are known to self-aggregate in solution which is facilitated by a flat, wide, and electron-rich surface, creating van der Waals, π - π stacking and charge-transfer interactions.⁵ A variety of factors can influence the extent of self-aggregation including the nature of the porphyrin itself (metal ion, number and nature of peripheral groups) as well as external changes such as ionic strength, pH, solvent nature, temperature, etc. To address the large number of factors that can influence the study of TAPP in solution, it was essential to maintain conditions in all experiments so that further studies could be reproducible. Therefore, the same concentration, solvent and inert atmosphere was used but it became apparent that factors that could not be controlled will still affect the results. For example, when purging with nitrogen, the concentration of the solution can change as some solvent will evaporate but adding more solvent will mean that the solution needs to be purged for a longer period of time and the concentration will still not be a stable value. That being the case, all care and attention was used to control the factors that would lead to stable values.

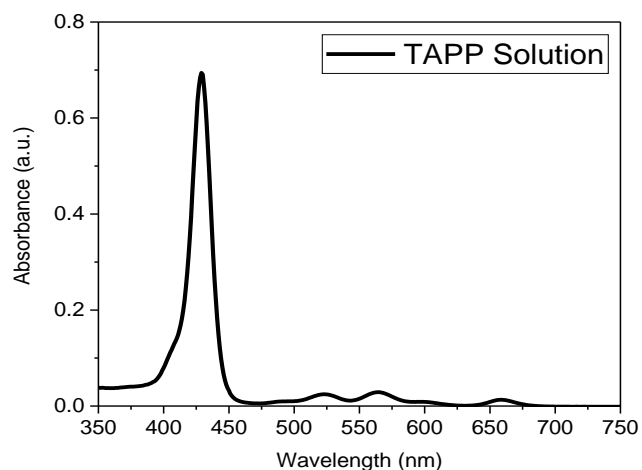


Figure 4.1: Ground state absorbance spectrum of TAPP (0.006575 mg/mL in chlorobenzene). 2 mm path length quartz cuvette.

To begin with, the ground state UV-visible absorption spectrum is collected to identify the wavelength of the Soret and Q bands so that the TAS pump wavelength can be chosen. Figure 4.1 shows the ground state absorption spectrum of a TAPP in a chlorobenzene solution. The Soret band peak is at 427 nm and the Q-bands are found at 660, 600, 565 and 525 nm. The TAS pump wavelength was chosen to be 427 nm as this wavelength will facilitate greater population of excited states which is beneficial for the purpose of this experiment as the signal to noise ratio will be improved. If the absorbance is too high, other photophysical processes may occur, e.g. annihilation processes, which is not what is being studied.

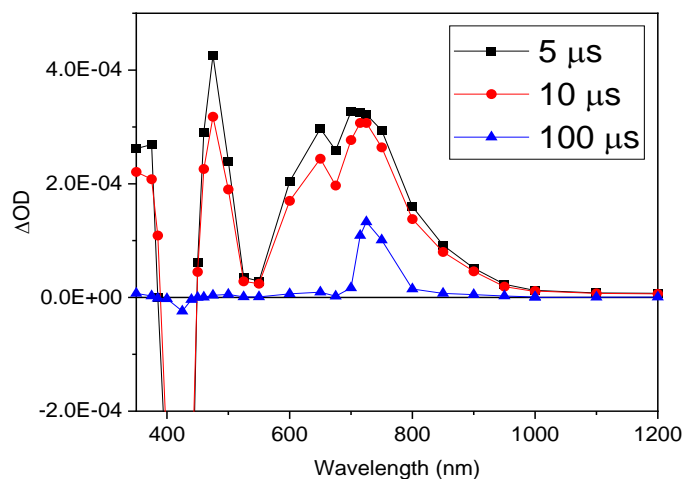


Figure 4.2: Microsecond transient absorption (TA) spectrum of TAPP (0.006575 mg/mL in chlorobenzene). 2mm path length quartz cuvette. Excited with a pump wavelength of 427 nm and excitation density of $45 \mu\text{J cm}^{-2}$.

Figure 4.2 is a microsecond transient absorption (TA) spectrum which gives some understanding into the photophysical properties of the TAPP solution. The negative signal at 425 nm shows the ground state bleach of the TAPP solution; this corresponds to the Soret band in the ground state absorbance at 425 nm, shown in Figure 4.1. As a percentage of the molecules have been promoted to the excited state, the number of molecules in the ground state has decreased.⁶ Hence, the ground state absorption in the excited sample is less than that in the non-excited sample. Consequently, a negative signal in the ΔOD spectrum is observed in the wavelength region of ground state absorption. There appear to be peaks at 475 nm and 750 nm that show the transient species of the solution. However, it is possible that it is one broad peak showing one transient species which is being overwhelmed by a negative ΔOD signal from the ground state bleach at 525 nm (Figure 4.1). Measuring the kinetic decay in this wavelength region will help to understand what kind of transient species is forming, be it a triplet state or charge state. This ultimately leads to future uses and efficiencies of porphyrin COFs as light-harvesting methods.⁷

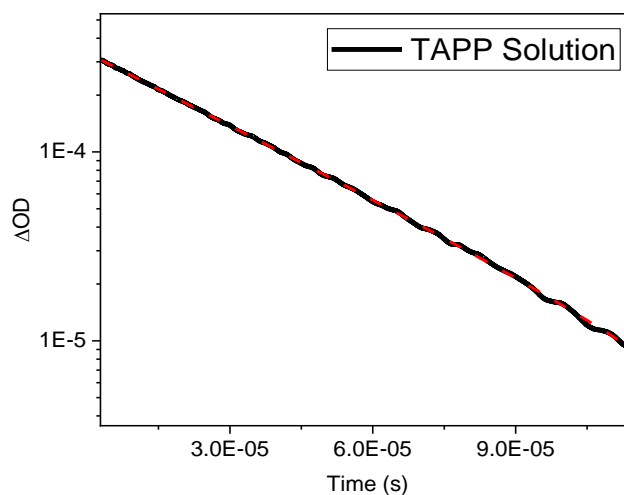


Figure 4.3: Kinetics of TAPP (0.006575 mg/mL in chlorobenzene). 2mm path length quartz cuvette. Excited with a pump wavelength of 427 nm, probe wavelength of 750 nm and excitation density of $40 \mu\text{J cm}^{-2}$. The red dashed line indicates the monoexponential fit with the lifetime of the species $\tau_1 = 3.42 \times 10^{-5}$ s.

Figure 4.3 shows the kinetic decay of the TAPP solution, pumped at 427 nm and probed at 750 nm. The plot of the kinetic decay and subsequent fitting can suggest the type of species being monitored. This is elaborated on in Chapter 2 Section 2.4.3 and is essential in understanding why fittings have been applied to the kinetic decays. The kinetic decay plotted is the ‘natural log of the ΔOD vs. time’ using OriginLab (data analysis and graphing software) exponential decay fitting. As the kinetic decay in Figure 4.3 is linear on a log-linear scale, a monoexponential decay, this suggests a triplet state at 750 nm, with the lifetime of the species $\tau_1 = 3.42 \times 10^{-5}$ s.^{8,9} In order to confirm if a triplet state is present at probe 750 nm then the next step is to study the kinetic decays in the presence of oxygen. Oxygen can quench triplet states so oxygen dependent measurements are a useful tool to determine if a triplet state is present.

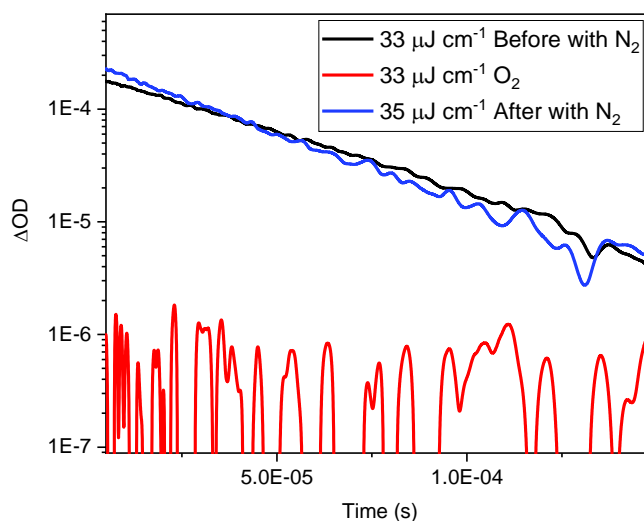


Figure 4.4: Oxygen dependent kinetics of TAPP (0.006575 mg/mL in chlorobenzene). 2mm path length quartz cuvette. Excited with a pump wavelength of 427 nm and a probe wavelength of 750 nm.

Figure 4.4 shows the oxygen dependent measurements undertaken on the TAPP solution. The solution is purged with nitrogen again after having been purged with oxygen. This is important because it will verify if the oxygen has permanently altered or damaged the TAPP. It is clear to see from Figure 4.4 that in the presence of nitrogen, an inert atmosphere, the decay remains as a monoexponential decay before and after oxygen dependent measurements. Whereas in the presence of oxygen, there is no signal and the trace is electronic noise from background light. On the basis of the monoexponential decay shown in both Figures 4.3 and 4.4 and the oxygen dependence shown in Figure 4.4, it can be concluded that triplet states exist in the solution.

Due to the sensitivity of the TAPP solution to oxygen quenching, it was unfeasible to measure kinetics at longer time scales or at more than one point as the signal deteriorated rapidly. The solution needed constant purging with an inert atmosphere which was not feasible with time constraints. To collect enough kinetic decays to plot an excitation dependence graph then a minimum of 5 kinetic measurements are needed at different excitation energies. Between each measurement the TAPP solution needed to be purged for minimum 2 hours and as explained previously, the purging with an inert

atmosphere will change the concentration of the solution and therefore collecting the kinetic decays becomes increasingly moot. It was decided to do one experiment with a COF solution to see if it was the same occurrence. One solution would be to change the design of the quartz cuvette used for the measurements. The one used had a screw top with an inert rubber centre through which a needle could be inserted. Where the needle was inserted could cause a leak of the inert gas and air to enter the cuvette. So, it is possible for the cuvette containing the sample solution to be placed inside another quartz cuvette, then a freeze-pump-thaw process (see Ref [10]) to de-gass the larger cuvette which is then heat sealed by melting the quartz for an hermetic seal.¹⁰

4.1.1 TAPP and COF solution

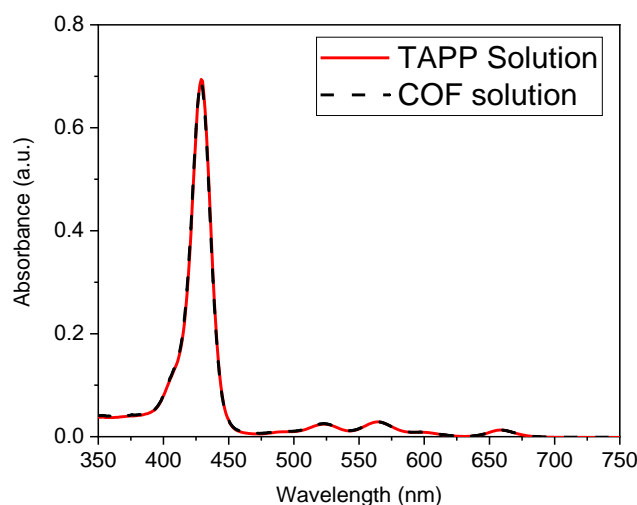


Figure 4.5: Ground state absorbance spectrum of TAPP (0.006575 mg/mL in chlorobenzene); and a COF solution (1.5 mL of 0.01315 mg/mL TAPP + 1.5 mL of 0.2973 mg/mL BDA in chlorobenzene + 10 μ L acetic acid). 2 mm path length quartz cuvette.

The COF solution was made by mixing 1.5 mL of 0.01315 mg/mL TAPP, and 1.5 mL of 0.2973 mg/mL BDA in chlorobenzene with 10 μ L acetic acid. Acetic acid is added as this facilitates the reaction and is elaborated on in Chapter 3. Even though adding acetic acid was not successful for the vapour-phase thin film COF synthesis, in solution COF synthesis, acetic acid is essential for enabling the reverse self-healing reaction to

form large crystals.¹¹ Concentrations were chosen so that the initial ground state absorbance would be the same for both the TAPP and COF solution in chlorobenzene. The ground state absorption spectrum in Figure 4.5 shows a comparison of the TAPP solution and the initial ground state absorption spectrum of what was synthesised to be a COF solution. The ground state traces are near-identical. The following TA spectra look into the similarity between the solutions further, as the TA spectra could be different, but not in this case.

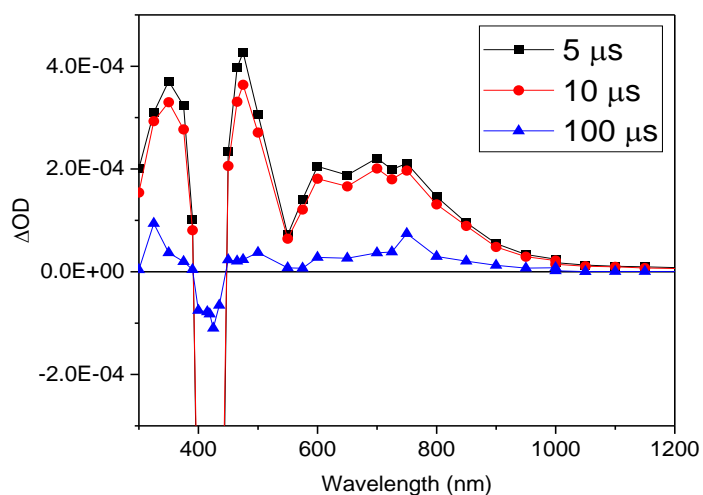


Figure 4.6: Microsecond transient absorption spectrum of COF solution (1.5 mL of 0.01315 mg/mL TAPP + 1.5 mL of 0.2973 mg/mL BDA in chlorobenzene + 10 μL acetic acid). 2mm path length quartz cuvette. Excited with a pump wavelength of 427 nm and excitation density of 33 $\mu J cm^{-2}$.

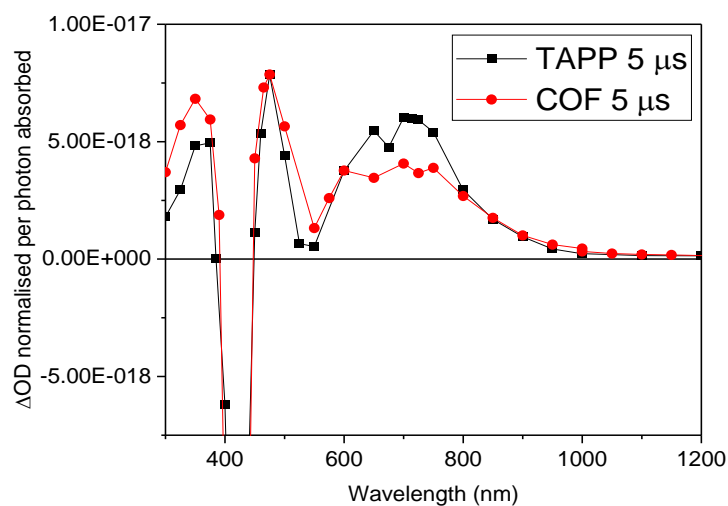


Figure 4.7: Microsecond transient absorption spectrum of TAPP (0.006575 mg/mL in chlorobenzene) and COF solution (1.5 mL of 0.01315 mg/mL TAPP + 1.5 mL of 0.2973 mg/mL BDA in chlorobenzene + 10 μ L acetic acid). 2mm path length quartz cuvette. Excited with a pump wavelength of 427 nm and excitation density of 45 μ J cm^{-2} and 33 μ J cm^{-2} respectively.

The transient absorption spectrum of the lone TAPP in Figure 4.2 was compared to the COF solution spectrum in Figure 4.6, with the plots for 5 μ s collated in Figure 4.7. The spectra are very similar and most probably the unreacted TAPP is dominating the spectrum – any COF is presumably lower in concentration, but there is a possibility that there is no COF as well. The most likely hypothesis is that there was an insufficient amount of linker to react with porphyrin or the ambient conditions were not favourable to the Schiff-base reaction in order for large networks to form that may have changed the TAS spectrum. After repeating the test with an even greater excess of linker molecule, there was still no change in the TA spectrum. Another variable may also have been the addition or absence of acetic acid that is typically added during 3D-COF synthesis.¹² The reason for adding the acetic acid to the COF solutions is to make the reaction described in Chapter 3 more “self-healing”. In the small amount that was synthesised in this report, the acetic acid may have hindered the reaction process by making it too reversible and the final COF product was not forming. It was not realistic

to investigate the effects of the amount of acetic acid in solution when the main aim is to look at films so this idea was abandoned.

4.2 TAPP Film

The following set of results are from one TAPP film. The same experiment was carried out on 19 other TAPP films (some identical, some with different ground state absorbances) but the following set of results has been chosen because they were the most representative of the collection.

This section will focus on the transient absorption data of TAPP films and then a comparison will be made between TAPP solutions and films.

Figure 4.8 shows a ground state absorption spectrum of a TAPP film which has been spin coated. The Soret band is found at 450 nm and the Q-bands are found at 675, 580, and 540 nm.

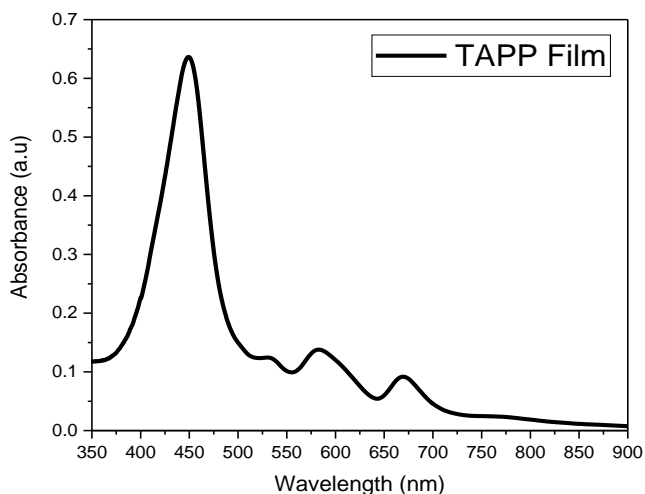


Figure 4.8: Ground state absorption of TAPP film (9.56 mg/mL in anisole spin coated: 10, 000 rps; 800 rpm; 2 min).

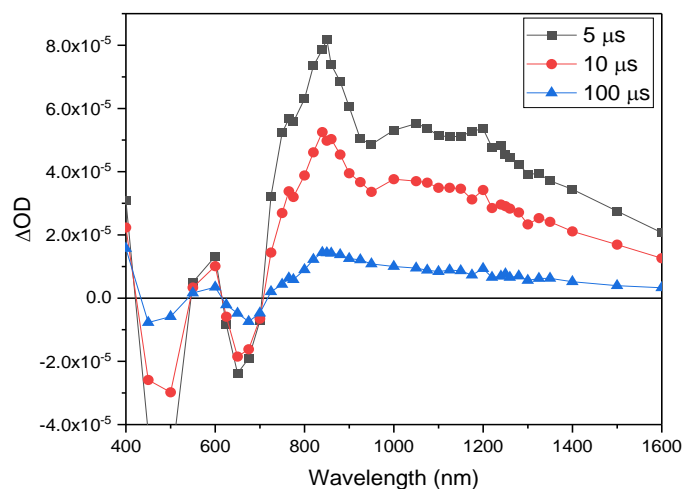


Figure 4.9: Microsecond transient absorption spectrum of TAPP film (9.56 mg/mL in anisole spin coated: 10, 000 rps; 800 rpm; 2 min). Excited with a pump wavelength of 450 nm and excitation density of $42 \mu\text{J cm}^{-2}$.

Figure 4.9 is the TA spectrum of the same TAPP film from Figure 4.8. The two negative signals at 450 and 650 nm show the ground state bleach of the TAPP film. The peak at 850 nm and broad peak at 1250 nm show the transient species of the film. Oxygen dependence measurements are taken to determine the presence or lack of triplet states. Figure 4.10 shows the oxygen dependence measurements at a pump wavelength of 450 nm and probe wavelength of 850 and 1250 nm.

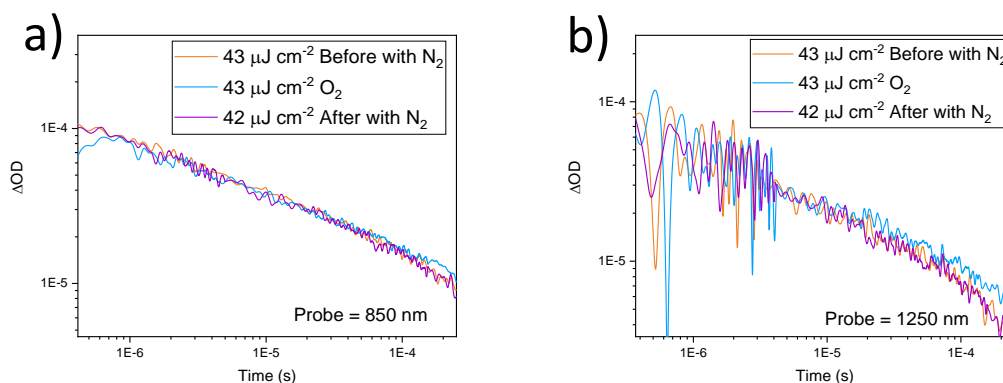


Figure 4.10: Oxygen dependent kinetics of TAPP (20.86 mg/mL in anisole spin coated: 10, 000 rps; 800 rpm; 2 min). Excited with a pump wavelength of 450 nm, probe wavelength of a) 850 nm, b) 1250 nm, and excitation density of 42-43 $\mu\text{J cm}^{-2}$.

Figure 4.10 shows that the kinetic decay remains the same when in an inert atmosphere as well as when the film is purged with oxygen. Measurements were also taken at a pump wavelength of 450 nm and probe wavelength of 650 and 800 nm, and these can be seen in Appendix 1. All the oxygen dependence measurements eliminate the presence of triplet states and could suggest charges. However, the probe wavelengths shown in Figure 4.10, 850 and 1250 nm, show a dissimilar trend when using the natural logarithm of the x- and y- axis. A linear decay is seen at probe 850 nm and in an oxygen atmosphere at 1250 nm, but in an inert nitrogen atmosphere at probe 1250 nm the decays are not linear but start to arch. The kinetic decays shown in Figure 4.10 b, purple and orange plots, will still be assigned to charges because they are not exponential decays and have not reacted with oxygen so can still be considered as charges like the other kinetic decay measurement for TAPP and COF films. As the majority of kinetic decays exhibit a clear power law decay, this will be investigated by the excitation energy dependence kinetic measurements where a power law will be fit. Excitation energy dependence will provide evidence on whether bimolecular recombination or geminate recombination is occurring. At higher excitation density the concentration of charges increases. By comparing the decay rates at different concentration of charges, the recombination processes can be determined.

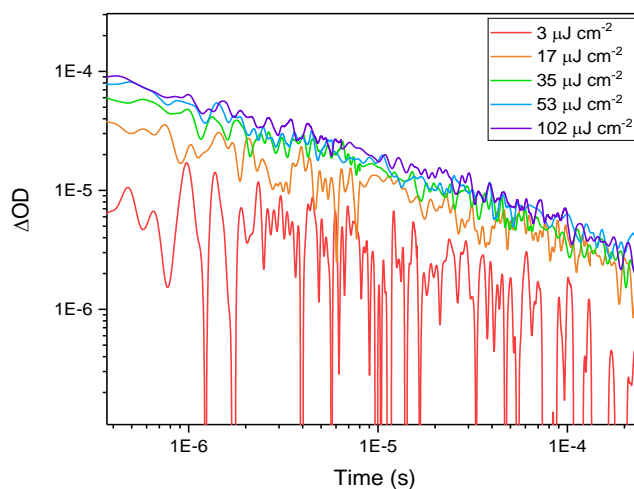


Figure 4.11: Kinetics of TAPP film (1.1 mg/mL in anisole spin coated: 10,000 rps; 800 rpm; 2 min). Excited with a pump wavelength of 450 nm and probe wavelength of 850 nm.

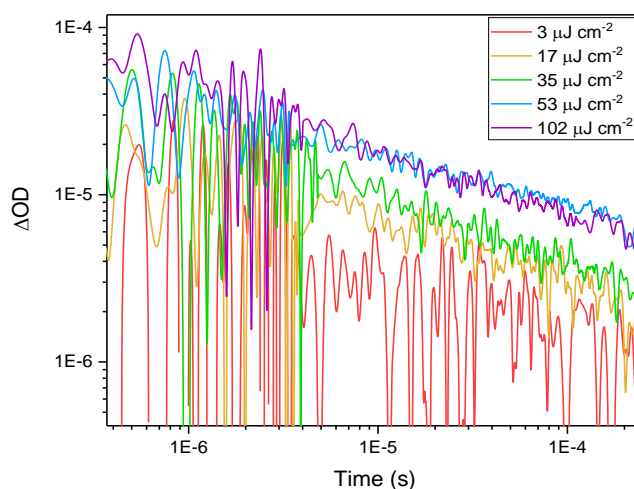


Figure 4.12: Kinetics of TAPP film (1.1 mg/mL in anisole spin coated: 10,000 rps; 800 rpm; 2 min). Excited with a pump wavelength of 450 nm and probe wavelength of 1250 nm.

Figures 4.11 and 4.12 are the kinetic measurements taken of the TAPP film at probe wavelengths of 850 and 1250 nm. The traces measured at different laser energies show a power law decay and that the ΔOD plateaus from $\sim 53 \mu\text{J cm}^{-2}$. (The fitting of the $53 \mu\text{J cm}^{-2}$ decay is described in Figure 4.14.) This has been seen from other kinetic measurements taken during this research using the same TAPP molecule: even with

energies nearing $160 \mu\text{J cm}^{-2}$, the trace is no different to those measured around $50 \mu\text{J cm}^{-2}$. The energy level is being saturated.

The purpose of Figure 4.13 is to show the dependence of excitation density, which is consistent with bimolecular recombination rather than geminate recombination: as the excitation density has increased, the ΔOD plateaus.¹³ [The ΔOD has been normalised to 1; this is done by normalising the highest signal to 1 and then scaling all other signal intensities by the same factor.] With regards to geminate recombination, there would be a flat line parallel to the x-axis as there is no strong dependence. Neither loss mechanism is better or worse than the other, it all depends on the material and the system, but the duration of charge dissociation for the charge to “do work” in a specific application is important.¹⁴ For porphyrin systems, the kinetic decays follow a power law which also suggests bimolecular recombination. More information will be discerned from studying the kinetic decays and quantifying the kinetics using a power law.

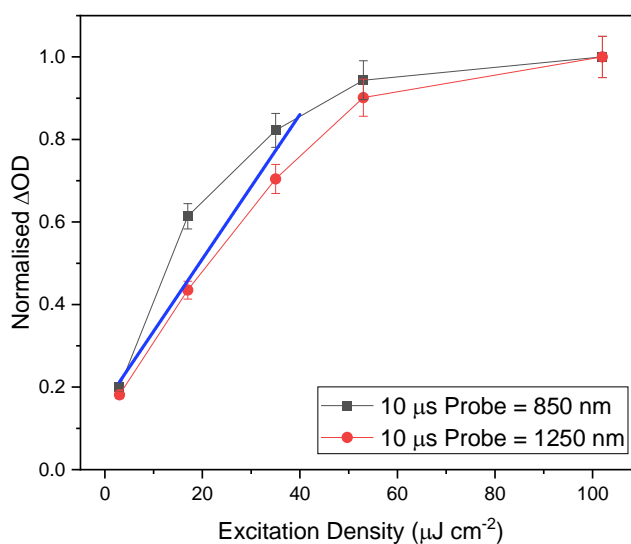


Figure 4.13: Normalised to 1 ΔOD measured at $10 \mu\text{s}$ as a function of laser excitation density. The slope to the plateau, which is an average of both data plots, is plotted as a blue line with a gradient, x , of 0.017.

Albrecht *et al.* have focused on quantifying charge extraction in organic solar cells and have compared the effects of geminate recombination and nongeminate recombination, the nongeminate recombination being bimolecular recombination in this case.¹⁵ It is widely recognised that nongeminate recombination in organic solar cells is dominated by bimolecular recombination.¹⁵ Nongeminate losses will become dominant for slow extraction, as it causes a large steady-state carrier density in the bulk of the active medium. Therefore, the rate at which the bimolecular recombination occurs, will affect the efficiency and performance during charge extraction. Figure 4.13 can help to understand how the TAPP (and later COF) films will perform when the charges generated need to be extracted. This can be done by calculating the gradient of the slope at low excitation intensity where the signal rise is still linear. As the plateau is being approached, so as the slope decreases, the smaller the density of unoccupied states and so bimolecular recombination is achieved faster, and this will contribute to the performance of the charge extraction. The gradient plotted in Figure 4.13 is shown by the blue line with gradient, x , being 0.017. This gradient will be compared to the excitation density plots for the COF films and then the metallated analogues in Chapter 5.

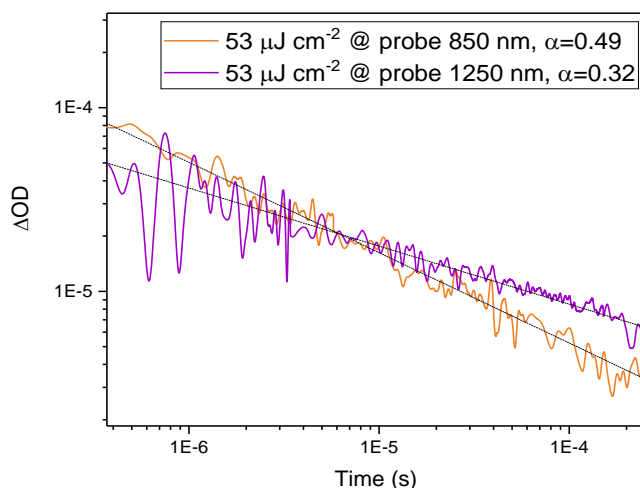


Figure 4.14: Comparison of kinetics of TAPP film (1.1 mg/mL in anisole spin coated: 10,000 rps; 800 rpm; 2 min). Excited with a pump wavelength of 450 nm and different probe wavelengths. The black lines are the power law fitting ($\Delta OD \propto t^{-\alpha}$) to each decay.

As explained in Chapter 2, the power law decay used is $\Delta OD \propto t^{-\alpha}$.¹⁷ The value of α , the gradient of the power law, expresses the energetic distribution of charge trap states. The gradient is linear on a log-log scale. Organic photovoltaic materials are described as disordered semiconductors with a continuous distribution of both energetically shallow and deep trap bands. An α value near to 1 indicates shallower trap states, and this facilitates faster detrapping of charges. The extent of the depth of the traps is the rate limiting process. The power law fit in Figure 4.14 provides an α value of 0.49 when measuring the kinetics at a probe wavelength of 850 nm but an α value of 0.32 at 1250 nm. The value of α is different for both kinetic decays so each probe wavelength has different trap distribution energies. Even though the same film has been used at both probe wavelengths, the variety of the morphology across the film, e.g. different domain sizes or number of aggregated layers, can give different spectroscopic signatures because the properties will change the trap energies at different areas of the film. So it could be that at different probe wavelengths, different charges are being detected in different morphologies of the film; one which will recombine faster than the other and this could be linked to the spatial distribution of the charges.

The spatial distribution is not possible to ascertain from the kinetic decays unfortunately. However, the results in Figure 4.14 show, that after excitation at 850 nm there will be faster detrapping of charges which can be “put to work” rather than excitation at 1250 nm.

The kinetic decays were measured at 850 and 1250nm, but also at 650 and 800 nm. Kinetic measurements at probe 650 and 800 nm will be used to compare to the COF transient species because at 650 and 800 nm there are peaks in the COF TA spectrum. So, to have a TAPP to COF comparison, kinetic decays at these wavelengths were collected for the TAPP films, which will be further discussed in Section 4.3.2. The following Figures 4.15-4.18 were created to compare the α values at the same pump and probe wavelength but at different excitation densities. Typically for processes undergoing bimolecular recombination there will be a consistent α value for different

excitation densities as the model used assumes an energetically homogeneous system at each transient species wavelength.¹⁸ However, at different excitation densities the following figures show a change in the α value, and said change is inconsistent between the different probe wavelengths. The main stumbling block was the amount of error and lack of reproducibility there are in thin film samples. One reason for the lack of reproducibility and trend seen in the alpha values is that at slower time scales (100 ns - 10 ms) there is a different recombination pathway than at the faster decay times (<20 ns), which is also presented by Montanari *et al.* who performed TAS studies on polymer/fullerene composites at room temperature.¹⁹ At slower time scales a power law independent upon excitation density is attributed to the recombination dynamics of the localised polarons while the fast decay component is dependent upon excitation density and does not follow a power law decay.¹⁹ Maybe the same can be applied to the TAPP and COF films, that only slower time scales follow a power law but “slow time scales” for TAPP films are not yet known, as the time scales reported by Montanari *et al.* are for polymer/fullerene composites which behave differently to porphyrins. Therefore, the α gradient fitted in the kinetic decays in this thesis may be inappropriate and not fully grasping the possible charge recombination channels due to the limited time interval probed by the instrument. However, for consistency, a power law is fitted between the same time interval for a better comparison (1E-6 - 1E-4). Another reason for the changes in the slopes between samples can be changes in morphology of the film which could also include defects in the film which hinder the charge carrier mobility.²⁰ When applying the fitting in Figures 4.15-4.18, the line of best fit has been created by using the same range of data points i.e. the same range with respect to the x-axis. This range has been used for all kinetic fitting in this thesis. On average across Figures 4.15-4.18 there is a change in α of 0.13 which is a large difference given that the results range is [0, 1]. There is scope for a lot of future work in confirming the data which will be elaborated on after presenting comparisons between the TAPP film and solution, and COF results, in the following sections and discussed in Chapter 6.

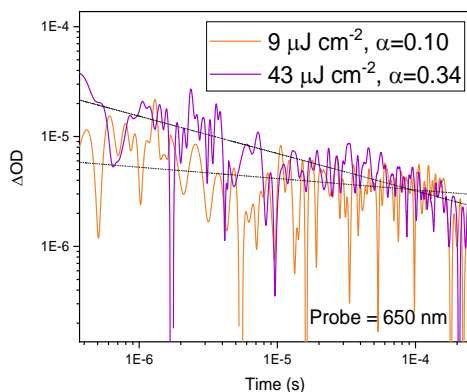


Figure 4.15: Kinetics of TAPP (20.86 mg/mL in anisole spin coated: 10,000 rps; 800 rpm; 2 min). Excited with a pump wavelength of 450 nm and probed at 650 nm. The black lines are the power law fitting ($\Delta OD \propto t^{-\alpha}$) to each decay.

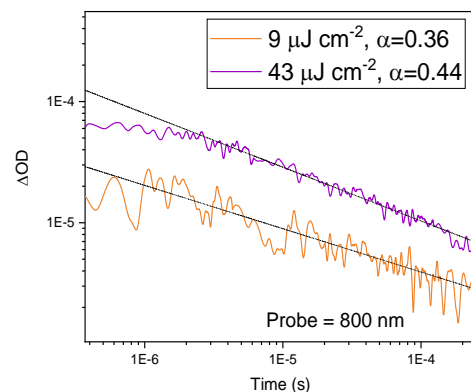


Figure 4.16: Kinetics of TAPP (20.86 mg/mL in anisole spin coated: 10,000 rps; 800 rpm; 2 min). Excited with a pump wavelength of 450 nm and probed at 800 nm. The black lines are the power law fitting ($\Delta OD \propto t^{-\alpha}$) to each decay.

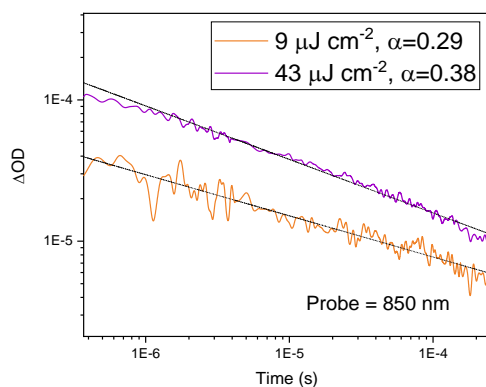


Figure 4.17: Kinetics of TAPP (20.86 mg/mL in anisole spin coated: 10,000 rps; 800 rpm; 2 min). Excited with a pump wavelength of 450 nm and probed at 850 nm. The black lines are the power law fitting ($\Delta OD \propto t^{-\alpha}$) to each decay.

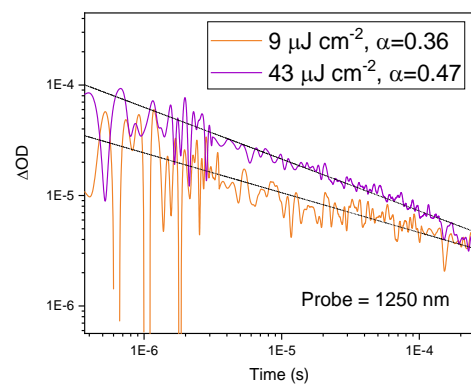


Figure 4.18: Kinetics of TAPP (20.86 mg/mL in anisole spin coated: 10,000 rps; 800 rpm; 2 min). Excited with a pump wavelength of 450 nm and probed at 1250 nm. The black lines are the power law fitting ($\Delta OD \propto t^{-\alpha}$) to each decay.

4.2.1 TAPP Film and Solution Comparison

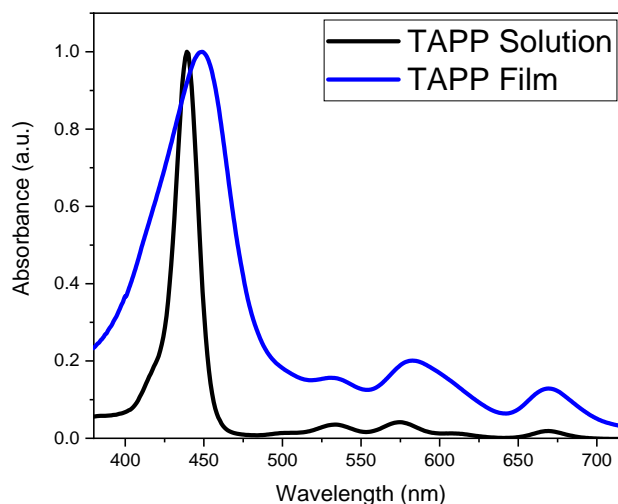


Figure 4.19: Normalised ground state absorption spectrum of a solution of TAPP (0.006575 mg/mL in chlorobenzene), and a TAPP film (8.06mg/mL spin coated: 12,000 rps; 800 rpm; 2 mins).

Figure 4.19 is the normalised ground state absorbance spectrum comparing a TAPP solution and film. The full width half maximum (FWHM) is the width of a spectrum peak measured between points on the y-axis which are half the maximum amplitude. The FWHM can be used to compare the broadening of the Soret band between TAPP solution and films. With respect to the Soret band, the FWHM of the solution is 19 ± 0.6 nm and for the film the FWHM is 64 ± 1.6 nm. The reason the film shows a broader Soret and Q-bands is because of the crystallinity of the film and light is diffracted to a greater extent.^{21,22} There is a broadening of the UV-vis spectrum with increased conjugation.²³ Figure 4.19 also shows a shift in the Soret band peak of 11 nm which could indicate a change in the degree of structural order of the materials.^{21,24} Even though in a solution the porphyrin molecules can aggregate, it will never be to an ordered extent as a film, hence the description of crystallinity for the film but a possible structural order in solution.

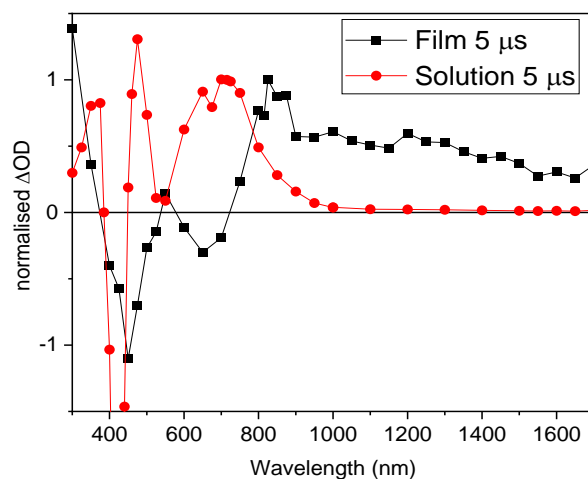


Figure 4.20: Normalised microsecond transient absorption spectrum of TAPP film (8.06mg/mL spin coated: 12,000 rps; 800 rpm; 2 mins), excited with a pump wavelength of 450 nm and excitation density of $40 \mu\text{J cm}^{-2}$, compared to a solution of TAPP (0.006575 mg/mL in chlorobenzene), 2mm path length quartz cuvette, excited with a pump wavelength of 427 nm and excitation density of $45 \mu\text{J cm}^{-2}$.

Figure 4.20 shows the comparison of transient absorption spectra between a TAPP film and solution. The solution shows a broad peak $\sim 600\text{-}800$ nm which decreases as the probe wavelength moves into the IR region where no signal is observed, in contrast to the film which exhibits a sharp peak at 825 nm and a steady broad peak in the IR wavelength probe region. Moreover, the oxygen-dependent kinetics of the TAPP solution and film show two different species. Essentially, under an oxygen atmosphere the TAPP film continues to show a signal at the probe wavelength, whereas, the signal all but disappears for the TAPP solution under an oxygen atmosphere. This indicates charges being formed when measuring the film and a triplet species being formed when measuring the solution. Tran-Thi *et al.* have also seen the same trend when comparing porphyrin-phthalocyanine assemblies in solution and in Langmuir-Blodgett films.²⁵ They postulate that the energy of the CT state is higher than that of the triplet when the porphyrin assemblies are in solution, while it is inverted in the film, because this makes the overall system in the lowest energy configuration. This theory can be lent to what is seen when comparing the oxygen-dependent kinetics of the TAPP film and solution: triplets in solution and charges in the film. Chang *et al.* have studied the effects of thin

film morphology, including crystallinity and orientation, and conclude that the morphology of conjugated polymers is a critical factor that significantly affects intrinsic charge transport characteristics.²⁶ The probability is that the TAPP film will have a degree of crystallinity whereas the solution will not, and so charge transport will be more possible in a solid state rather than in solution. As previously mentioned, neither a charge or a triplet is better, it is about how the material can be used and the efficacy of the application. Even though the synthesis of the films may not lead to identical films in each case, the films are safer and easier to transport compared to solutions which can leak into the surrounding environment and be hazardous to animals. The synthesis technique used to make COFs in this thesis has mainly revolved around films, because of the ideal that they can be used in applications that require ease of transportation. This concludes any results for TAPP in solution and will now focus on TAPP and COF films.

4.3 COF Film

The following sections explore the properties of COF films and comparisons to TAPP films.

Figure 4.21 shows a ground state absorption spectrum of a TAPP film and then a COF sample made from the same TAPP film. The synthesis procedure is detailed in Chapter 2. Even though the ground state absorbances of both films are similar, there is a distinctive blueshift of the Soret and Q-bands for the COF film of 10 nm (0.06 eV). The Soret bands largely overlap but the Q-bands show different distinctive peaks for the TAPP and COF respectively, especially when differentiating between two COF peaks at 570 and 600 nm where the TAPP shows a broader band across this range. The average blue shift in nm across the peaks is 12 nm, which is outside of the error margins and hence more significant. Due to defects in the crystallinity of materials, the materials UV-Visible data can show a blue shift.²⁷ This implies that the COF formation has not led to ordered frameworks but many disordered domains. Although there has been a shift in Soret bands, the FWHM of the Soret bands are near the same; the FWHM for the TAPP film is 42 ± 1.1 nm whereas the FWHM for the COF film is 40 ± 1.1 nm. Broadening of the peaks

can also be used to distinguish the crystallinity of the films but the FWHM does not indicate a change in the crystallinity even though the blue shift does indicate a change in crystallinity.^{21,23} Nüesch *et al.* studied the one-dimensional arrangement of strongly coupled monomers, specifically H-aggregation of porphyrins and correlated absorption and emission of a dye in solution, at the surface and in the solid state; showing a link between crystal structure and photophysical properties.²⁸ H-aggregates are when the transition moments of the monomers are perpendicular to the line of centre, so the arrangement in H-aggregates is face-to-face. The dipolar coupling between monomers, as a cause of the aggregation geometry, leads to a blue shift of the absorption band because the dipole is oriented parallel to the transition dipole moment of the dye. H-aggregates in general have short singlet and triplet excited state lifetimes.^{29,30} Herein, the change in aggregation and bonding from COF formation may have an affect on the excited state delocalisation, which has been shown in previous analysis if COF films that have been exfoliated by addition of metal centres.³¹

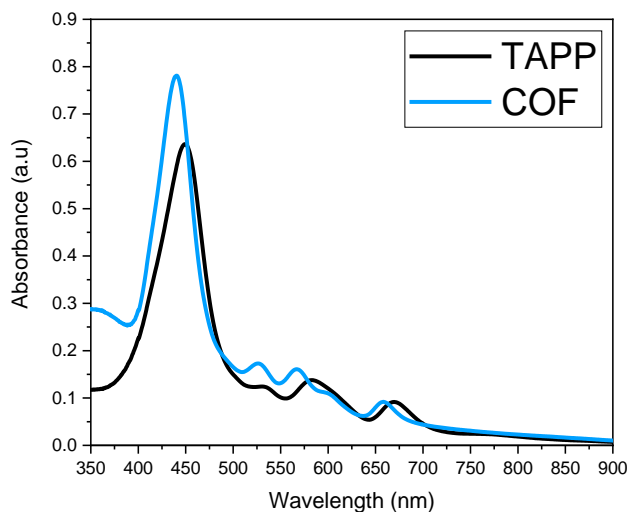


Figure 4.21: Ground state absorption of TAPP film (9.56 mg/mL in anisole spin coated: 10, 000 rps; 800 rpm; 2 min) and COF synthesised from mentioned TAPP film.

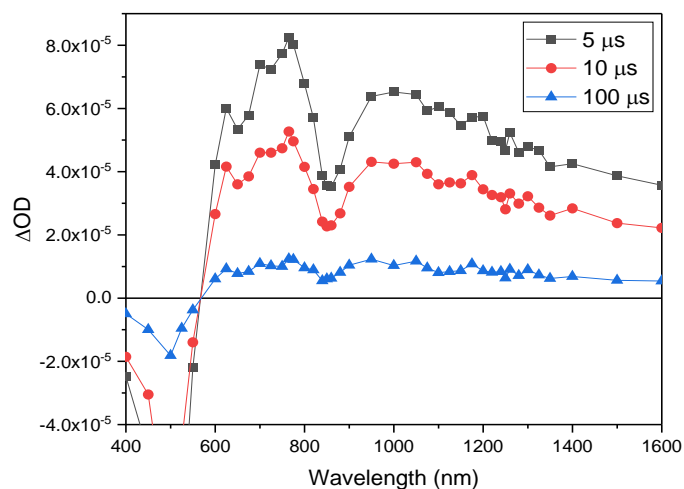


Figure 4.22: Microsecond transient absorption spectrum of a COF film made from TAPP film (9.56 mg/mL in anisole spin coated: 10, 000 rps; 800 rpm; 2 min). Excited with a pump wavelength of 450 nm and excitation density of $53 \mu\text{J cm}^{-2}$.

Figure 4.22 shows the microsecond transient absorption spectrum of a COF film. The negative signal $\sim 400\text{-}600$ nm shows the ground state bleach. However, there is no negative signal to indicate the ground state bleach of the Q-bands. The transient species is more prominent, and the signal outweighs that of the ground state bleach. The peak at 765 nm, and the broad peak in the IR region ~ 1250 nm show the transient species of the COF film. As the peaks showing the transient species for the TAPP film were investigated to be charges, measuring the oxygen dependency and kinetic decays at the two COF peaks will help to understand what kind of excited state is forming, be it a triplet state or charged state etc. Oxygen dependence measurements are taken to determine the presence or lack of triplet states. Figure 4.23 shows the oxygen dependence measurements at a pump wavelength of 450 nm and probe wavelength of 765 nm.

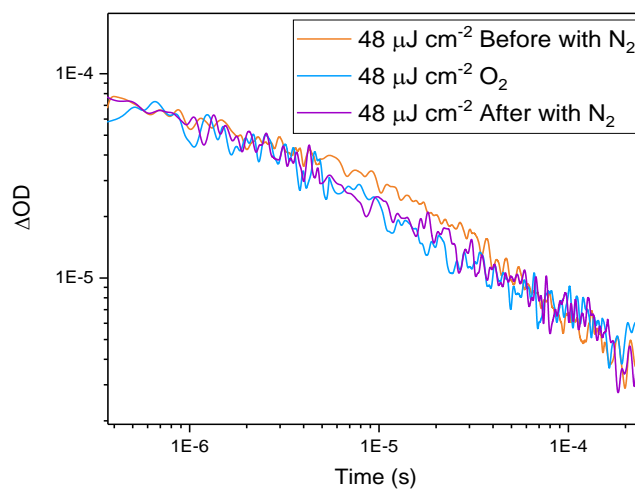


Figure 4.23: Oxygen dependent kinetics of COF film. Excited with a pump wavelength of 450 nm, probe wavelength of 765 nm and excitation density of $48 \mu\text{J cm}^{-2}$.

Figure 4.23 shows that the kinetic decay remains the same when in an inert atmosphere as well as when the film is purged with oxygen. Measurements were also taken at a pump wavelength of 450 nm and probe wavelength of 650, 800 and 1250 nm and these can be seen in Appendix 1. All the oxygen dependence measurements could eliminate the presence of triplet states and suggest charges. This will further be investigated by the excitation energy dependence kinetic measurements and the power law fitting.

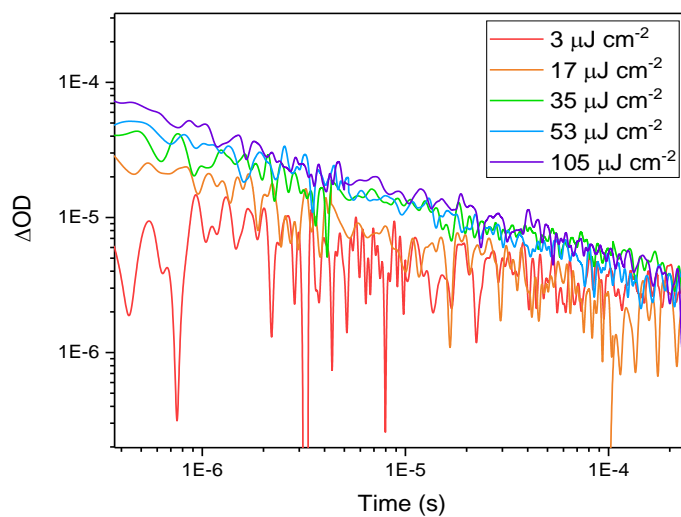


Figure 4.24: Kinetics of a COF film. Excited with a pump wavelength of 450 nm and probe wavelength of 765 nm.

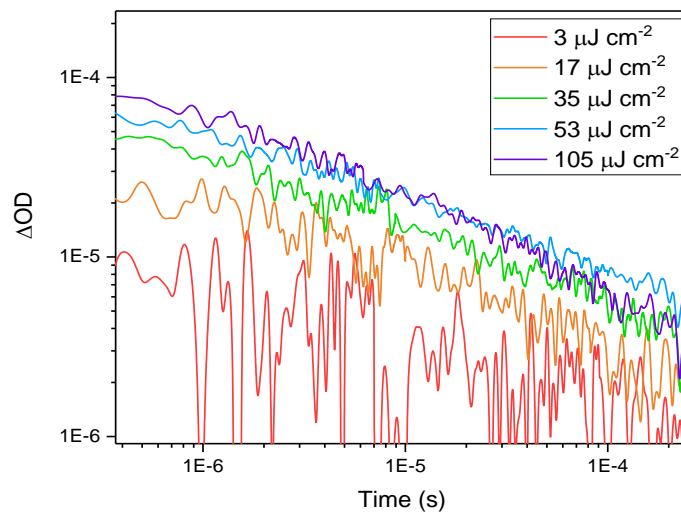


Figure 4.25: Kinetics of a COF film. Excited with a pump wavelength of 450 nm and probe wavelength of 800 nm.

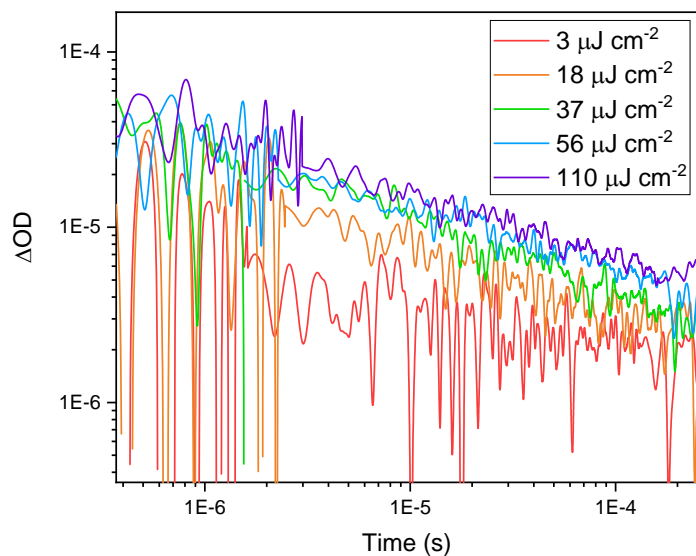


Figure 4.26: Kinetics of COF. Excited with a pump wavelength of 450 nm and probe wavelength of 1250 nm

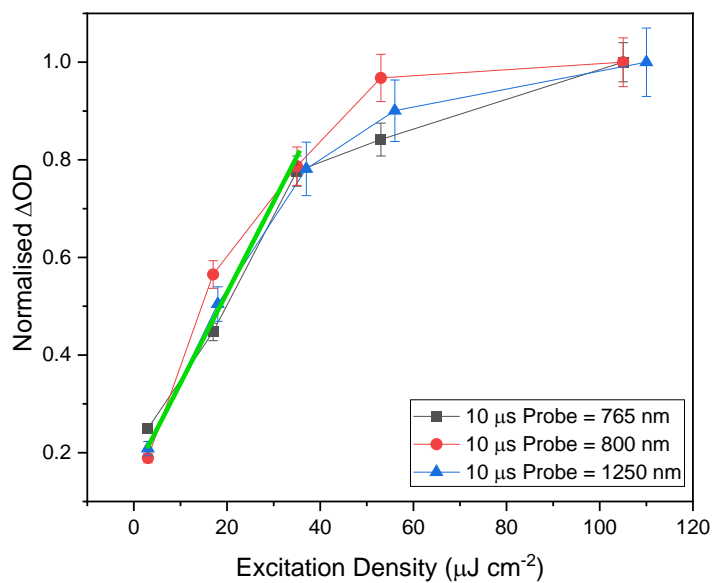


Figure 4.27: Normalised ΔOD measured at $10 \mu s$ as a function of laser excitation density. The slope to the plateau, which is averaged amongst the different probe wavelengths, is plotted as a green line with a gradient, x , of 0.016.

Figures 4.24-4.26 are the kinetic measurements taken of the COF film at probe 765, 800 and 1250 nm. It can be seen that the ΔOD plateaus from $\sim 53 \mu\text{J cm}^{-2}$ excitation density. This has been seen from other kinetic measurements using the same TAPP molecule, even with energies nearing $160 \mu\text{J cm}^{-2}$, the trace is no different to those measured around $50 \mu\text{J cm}^{-2}$. The purpose of Figure 4.27 is to show the dependence of excitation density, which is consistent with bimolecular recombination rather than geminate recombination. As the excitation density increases, the ΔOD plateaus. The slope of the plateau is 0.016, which is less steep than the TAPP film the COF was made from by 6%. The 6% change is calculated using the gradients with two significant figures because the gradients are very similar, so using only one significant will not show a difference but using more than two significant figures is not realistic in reporting data. The 6% reduction in slope implies that reaching the plateau will be at a higher excitation density and charge extraction will be delayed (if ramping from $0 \mu\text{J cm}^{-2}$). By predetermining the energy needed for efficient charge extraction then it would not be efficient to excite at lower excitation densities however, in real world situations the levels of light reaching a solar cell will not always be at the most intense and at different times of the day charge extraction will have different rates. Ryu *et al.* studied the light intensity-dependent variation in defect contributions to charge transport and recombination in a perovskite solar cell.¹⁶ When there are defects in the solar cell with a discernible distribution, the defects contribute to distinct effects on the transport and recombination of charge carriers.¹⁶ One defect contributed as charge traps that alter charge-carrier transport but only occurs at low levels of light intensity, and becomes inconsequential at high intensity, for example, high energy in the plateau region of an excitation energy dependence graph where more charge carriers are being generated. Another defect contributes as recombination centres, but these points are less understood and Ryu *et al.* have insufficient information to form a conclusion on recombination centre defects. The changes in film morphology are discussed in this thesis but specific defects are difficult to assign. It is interesting to further investigate specific defects and how these have an impact on overall performance because maybe

no synthetic technique will be perfect, but finding the technique that results in fewer of a certain defect will be desirable.

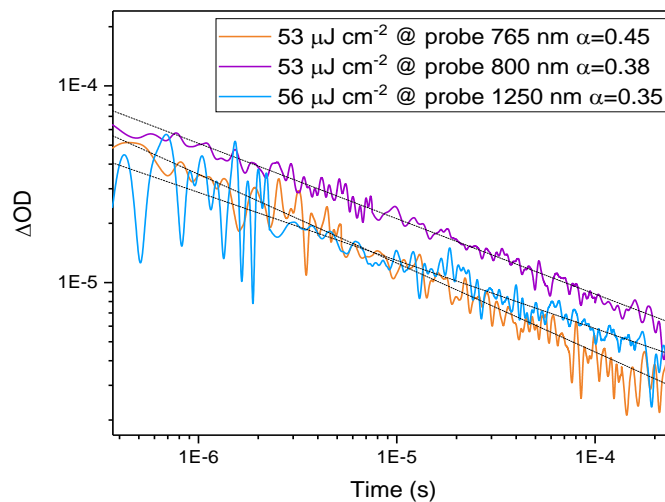


Figure 4.28: Comparison of COF kinetics at probe wavelengths of 765, 800 and 1250 nm. Excited with a pump wavelength of 450 nm. Excitation density is 53–56 $\mu\text{J cm}^{-2}$. The black lines are the power law fitting ($\Delta\text{OD} \propto t^{-\alpha}$) to each decay.

765 nm is the wavelength with the highest amplitude peak in the TA spectrum. The faster saturation could be a result of a preferential energy pathway compared to the other wavelengths. Jakowetz *et al.* have reported that at certain wavelengths there is a greater probability of singlet-singlet annihilation which contributes to the number of charges.¹ This could be one explanation as to why at different probe wavelengths, the behaviour of the transient species changes.

Figure 4.28 is a comparison of the kinetic decays of a COF film at different probe wavelengths but at the same excitation density. The purpose is to compare the charges at different probe wavelengths. The α values listed in the legend in Figure 4.28 show that there is a difference of 0.1 between the charges at probe wavelengths 765 and 1250 nm. Each probe wavelength has different trap distribution energies with the probe wavelength of 800 nm lying in between. The results indicate that as the probe

wavelength moves towards the IR there are deeper trap states, and this facilitates slower detrapping of charges.

Research by Jin *et al.* has postulated that shallow traps may only restrict the efficient movement of charges through trapping and detrapping processes, while deep traps hinder detrapping and could enable non-radiative recombination pathways.³²

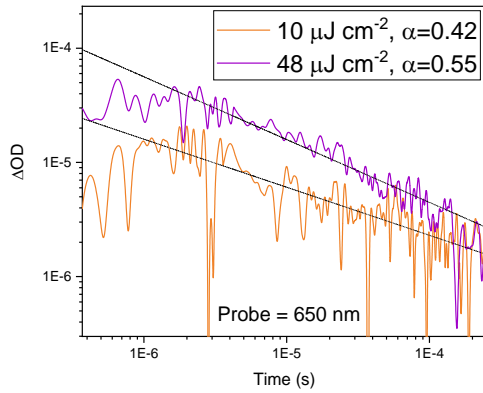


Figure 4.29: Kinetics of COF film. Excited with a pump wavelength of 450 nm and probed at 650 nm. The black lines are the power law fitting ($\Delta OD \propto t^{-\alpha}$) to each decay.

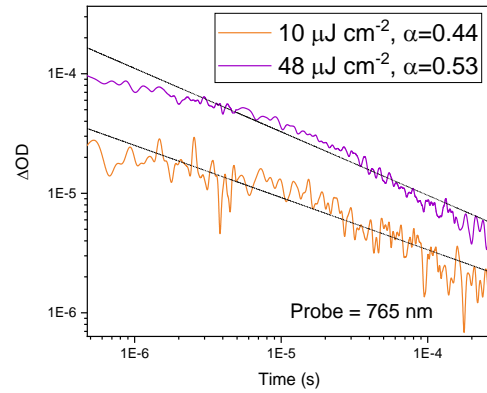


Figure 4.30: Kinetics of COF film. Excited with a pump wavelength of 450 nm and probed at 765 nm. The black lines are the power law fitting ($\Delta OD \propto t^{-\alpha}$) to each decay.

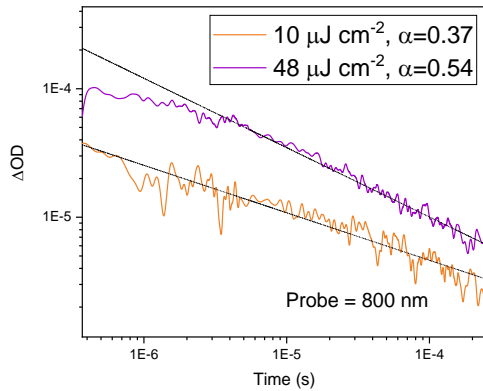


Figure 4.31: Kinetics of COF film. Excited with a pump wavelength of 450 nm and probed at 800 nm. The black lines are the power law fitting ($\Delta OD \propto t^{-\alpha}$) to each decay.

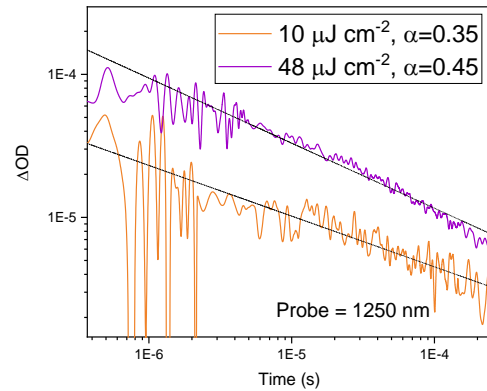


Figure 4.32: Kinetics of COF film. Excited with a pump wavelength of 450 nm and probed at 1250 nm. The black lines are the power law fitting ($\Delta OD \propto t^{-\alpha}$) to each decay.

Figures 4.29-4.32 show the kinetic decays of a COF film. Each figure displays the kinetic decays which have the same pump and probe wavelength but a comparison of excitation density. Kinetic decays have been measured at 765 and 1250 nm which are the peaks in the transient absorption spectrum as well as 800 and 650 nm. Kinetics have been measured at 800 nm because it is where the TAPP and COF transient absorption spectra intersect (Figure 4.33). The kinetic decay at probe 650 nm was taken to compare the ground state bleach in the TAPP spectrum to the positive ΔOD in the COF spectrum, this is elaborated on in Section 4.1. The results draw the same conclusions that the TAPP kinetics provided; which is that the α value is inconsistent. On average across Figures 4.29-4.32 there is a change in α of 0.12 which mimics the change over the many repeats that were carried out. As previously mentioned, there is scope for future work which leads back to the synthesis and preparation of the films. Even though all TAPP films in this study were prepared using a spin coater and then the COF synthesis method was the same, the changes in TAS data and inconsistencies in the kinetic results show that the sample preparation is not ideal. Potential solutions include making films using the TAPP in different ways, i.e. Langmuir-Blodgett films. Future work is detailed in Chapter 6.

4.3.1 TAPP and COF Film Comparison

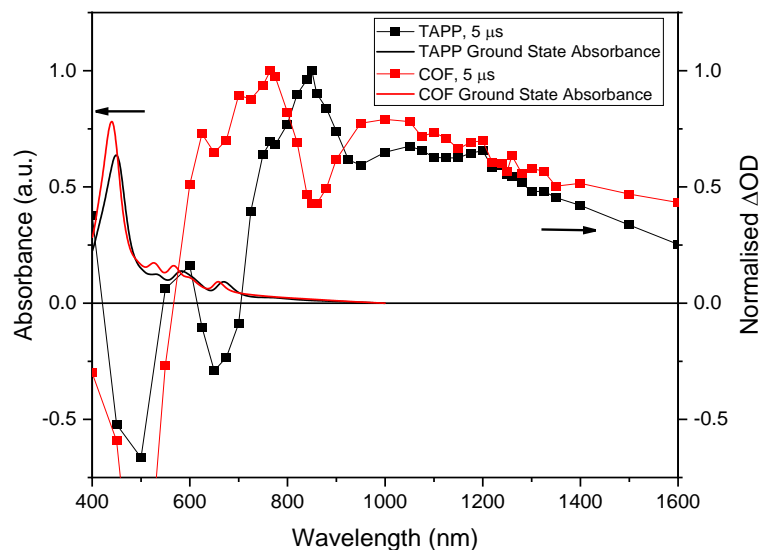


Figure 4.33: Normalised microsecond transient absorption spectrum of TAPP film (9.56 mg/mL in anisole spin coated: 10, 000 rps; 800 rpm; 2 min), excited with a pump wavelength of 450 nm and excitation density of $42 \mu\text{J cm}^{-2}$, compared to a COF made from the aforementioned TAPP film, excited with a pump wavelength of 450 nm and excitation density of $53 \mu\text{J cm}^{-2}$. Ground state absorbance overlaid.

Figure 4.33 is the comparison between the TAPP and COF film transient absorption spectra. The results are not normalised to ‘per photon absorbed’ because the excitation density used was the same and the ground state absorption peaks are too alike to make the normalisation any different. So, the results have been normalised to 1. The similarities are the ground state bleach at 400-600 nm and the broad peak in the IR region. The first difference is that the ground state bleach at ~ 650 nm for the TAPP film is not present for the COF film. It has been mentioned previously that the transient species at this wavelength is more prominent, and the signal outweighs that of the ground state bleach. As this change between TAPP and COF was seen for all 19 repeats, this is suggestive that there has been a change in the film during the synthesis procedure. It could be a positive change, meaning that the COF film exhibits a transient species that has a greater signal in the TA spectrum, or it could mean that the TAPP film has simply

changed in morphology. However, as the change was seen for all repeats, it is more likely that it is as a result of a framework forming. This is because there was some success when imaging the COFs using the STM (on HOPG), and as the same synthesis technique was carried out on the TAS samples then this success will be mirrored. The second difference is a shift in the prominent peaks for each film; the prominent peak occurs at 850 nm for the TAPP film but at 765 nm for the COF film which is a shift of 85 nm (14.6 eV). Wang *et al.* have studied femtosecond TAS of perovskite films, and saw that the grain size (size of the clumps of perovskite) has an effect on the blue shift in a TA spectrum.³³ Wang *et al.* report that as the perovskite grain size increases (comparable to an increase in layers and domains of the COF structure), there is a broadening of the absorption spectra.^{33,34} Specifically, there is a blue-shift of the transient peak if the structure becomes more porous by the grain size increasing. The grain size was confirmed by XRD. This blue shift can be applied to the shift seen in Figure 4.38 (and across other samples) to explain that as the COF is being formed, there is a greater extent of layers and domains added on the surface through the Schiff-base condensation reaction with the BDA linker, and so the pseudo-grain sizes are increasing. As previously explained, the extent of the shift seen in Figure 4.38 is different, this could be indicative of different extents of synthesis and clumping within the films with a greater blue shift representing larger domains and more layers of COF.

The oxygen dependence measurements have already eliminated the presence of triplets so the peaks are assigned to charges. To compare the charges being formed the kinetic decays at both points will be compared in the following section.

4.3.2 TAPP and COF Comparison of Kinetics

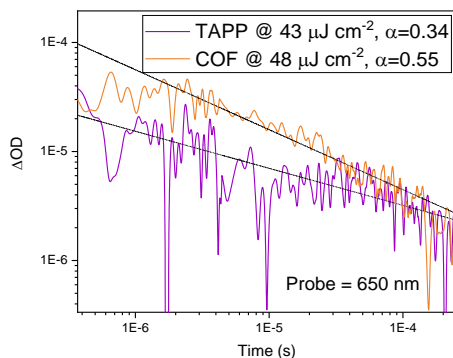


Figure 4.34: Kinetics of TAPP (20.86 mg/mL in anisole spin coated: 10, 000 rps; 800 rpm; 2 min) and COF film. Both films excited with a pump wavelength of 450 nm and probed at 650 nm. TAPP film at an excitation density of $43 \mu\text{J cm}^{-2}$ and COF film at $48 \mu\text{J cm}^{-2}$. The black lines are the power law fitting ($\Delta\text{OD} \propto t^\alpha$) to each decay.

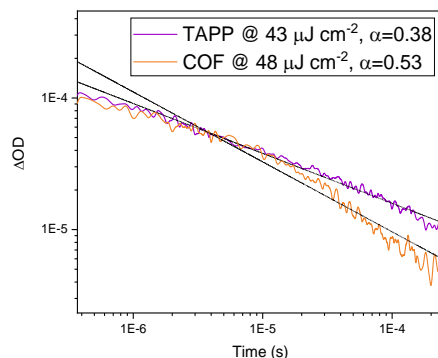


Figure 4.35: Kinetics of TAPP (20.86 mg/mL in anisole spin coated: 10, 000 rps; 800 rpm; 2 min) and COF film. Both films excited with a pump wavelength of 450 nm. TAPP film probed at 850 nm and at an excitation density of $43 \mu\text{J cm}^{-2}$ and COF film probed at 765 nm and at an excitation density of $48 \mu\text{J cm}^{-2}$. The black lines are the power law fitting ($\Delta\text{OD} \propto t^\alpha$) to each decay.

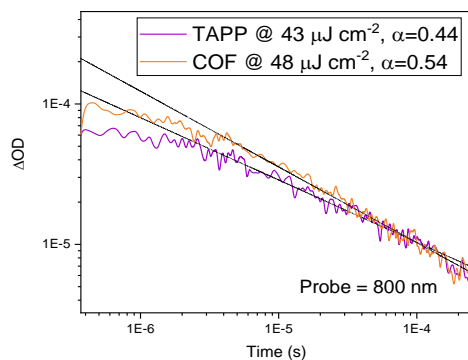


Figure 4.36: Kinetics of TAPP (20.86 mg/mL in anisole spin coated: 10, 000 rps; 800 rpm; 2 min) and COF film. Both films excited with a pump wavelength of 450 nm and probed at 800 nm. TAPP film measured at an excitation density of $43 \mu\text{J cm}^{-2}$ and COF film measured at an excitation density of $48 \mu\text{J cm}^{-2}$. The black lines are the power law fitting ($\Delta\text{OD} \propto t^\alpha$) to each decay.

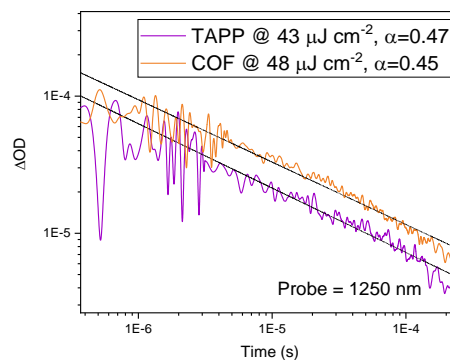


Figure 4.37: Kinetics of TAPP (20.86 mg/mL in anisole spin coated: 10, 000 rps; 800 rpm; 2 min) and COF film. Both films excited with a pump wavelength of 450 nm and probed at 1250 nm. TAPP film measured at an excitation density of $43 \mu\text{J cm}^{-2}$ and COF film measured at an excitation density of $48 \mu\text{J cm}^{-2}$. The black lines are the power law fitting ($\Delta\text{OD} \propto t^\alpha$) to each decay.

All the kinetics for both the TAPP and COF film follow a power law decay therefore, it is clear to see that it is because of a charged state (Figures 4.34-4.37). When comparing the kinetic decays between the TAPP and COF film at the same probe wavelength and roughly the same laser energy, there is no clear pattern regarding the gradient α . In general, as the probe wavelength increases from 650 to 1250 nm, the TAPP α value increases, but the COF α value stays the same until 1250 nm and then it decreases significantly. It is difficult to attribute a reason for this as all samples showed different kinetics when comparing the TAPP and COF films. It is not this thesis' aim to be vague or inconclusive but, to find trends where there are none will hamper future experiments that might use these results as a basis. The kinetic results in Figures 4.34-4.37 should be overhauled with a new synthesis and verification technique to determine the percentage of COF in the studied film. Unfortunately, this is beyond the timeline of this thesis, and future work should endeavour to focus on accuracy of the synthesis and results rather than hope that by increasing the number of repeats then a pattern would emerge.

The results reported in this thesis are an overview from 19 sample repeats. The shift in the prominent peaks for TAPP and COF films (the prominent peak occurs at 850 nm for the TAPP film but at 765 nm for the COF film as seen in Figure 4.33) has been reliably reproduced across all samples. The shift in the prominent peaks and the change in the ground state bleach at ~ 650 nm are two results which have remained constant amongst all the experiments. Again, a key problem has been reproducibility with respect to the α value derived from the power law. Even though, each film was prepared in exactly the same manner possible, each film would give a different kinetic decay, this has made it very difficult to find a pattern as to the behaviour of the charges.

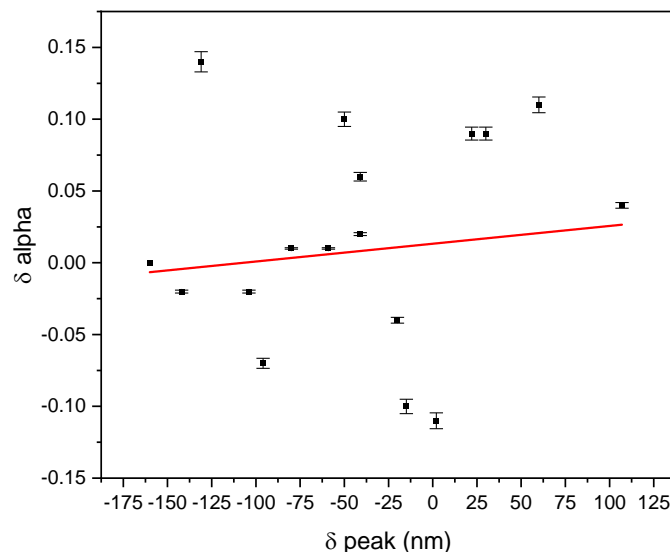


Figure 4.38: A plot of the change in α value against the change in transient peak between TAPP and COF films (nm). All films were made in exactly the same way, as detailed in Chapter 2.

To compare the number of films that were investigated, especially the change in the α values across the films, a plot of the shift in main transient peak from TAPP to COF versus change in α value of the kinetics at each peak was used. Every sample was prepared in exactly the same way however, if all the films investigated were the “same”, then all the points in the plot should cluster as the peak shift would be the same and the change in α would be the same. However, as seen in Figure 4.38, there is no strong trend and the peak shift and α change is different each time. The standard deviation for the peak shift is 73 nm, and the standard deviation for the change in α is 0.074 which are respectively high as the data points are spread out over a large range of values. One reason, as studied by Ostroverkhova *et al.*, is that transient photoconductive properties are dependent on the film morphology, especially thin films.³⁵ So, for many studies where bimolecular recombination is assigned as the energetic pathway, there could be a consistent α value for different excitation densities if the sample being investigated is in the bulk or solution and it is assumed that an energetically homogeneous system at each transient species wavelength is present. Even though Ostroverkhova *et al.* studied

pentacene films at picosecond timescales, the same conclusion applies for the TAPP and COF films which are thin films and so not energetically homogeneous system at each transient species wavelength. Dyer-Smith *et al.* and Lenes *et al.* have looked further into the effect of film morphology on bimolecular recombination, but with regards to fullerene organic solar cells, and so there has not been a power law analysis.^{36,37} However, both groups still support the conclusions that the bimolecular pathway is sensitive to film morphology and disorder in the film will hamper the charge generation and carrier mobility.^{36,37} Häusermann *et al.* state that disorder, which will impede movement of charge carriers, is always present in organic semiconductors, independent of the material being a single crystal or polycrystalline/amorphous thin-films.³⁸ As this thesis supports the occurrence of bimolecular recombination in TAPP and COF films, the results that show an inconsistent α value can be reasoned with the fact that the morphology of the film is not consistent. It would be interesting to make a range of films, with the intention of introducing disorder to some films to then analyse the TA kinetic decays from most to least ordered. One way in which to introduce disorder would be to purposefully let some of the linker or water in the vapour phase condensate on the substrate, this is can damage the film. To ensure which films are the most ordered, a large scaled STM analysis can be used to ascertain how ordered the film is (if conducted on a conductive substrate). Comparing Pump Wavelengths

So far, all the TAS measurements have been taken when pumping the Soret band. Figure 4.39 is the ground state absorption spectrum of a TAPP and COF film with higher amplitude peaks at a wavelength greater than 600 nm compared to the films used to produce Figure 4.21. When comparing the Q band in the region 650–680 nm, it is possible to excite at a wavelength that does not show a strong absorbance for the TAPP or COF and *vice versa*. This can be seen in Figure 4.40: at 652 nm this is a peak of a Q band for the COF film but a reduced amplitude for the TAPP film. Therefore, using a pump wavelength of 652 nm, it is possible to study the COF film with little effect from the TAPP that has not reacted in the film. The TAPP film was excited at a pump wavelength of 680 nm for the same reason; it is a Q band peak for the TAPP but not for the COF film. The

purpose is to compare the transient absorption spectra of the TAPP and COF excited with a pump wavelength of 450 nm, to transient absorption spectra of TAPP and COF excited with a pump wavelength in a Q-band region. This will enable the possibility to isolate more strongly the transients coming from one material rather than the other and then to determine whether there is any effect from residual TAPP in the film after an unsuccessful synthesis.

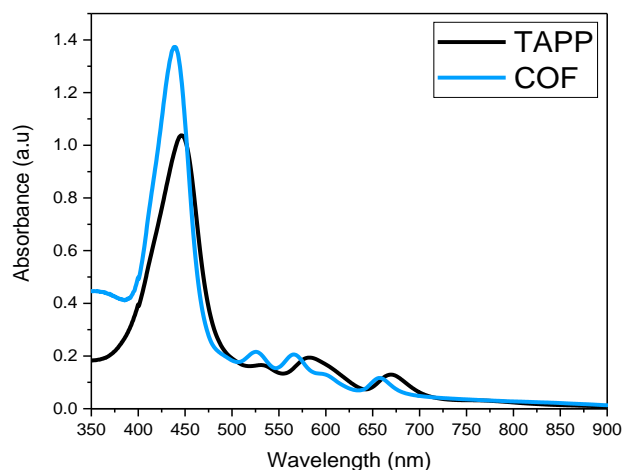


Figure 4.39: Ground state absorption of TAPP film (9.56 mg/mL in anisole spin coated: 10, 000 rps; 800 rpm; 2 min) and COF synthesised from mentioned TAPP film.

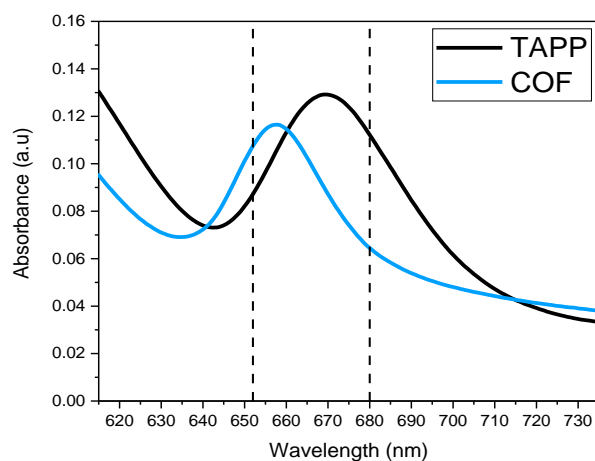


Figure 4.40: Ground state absorption of TAPP film (9.56 mg/mL in anisole spin coated: 10, 000 rps; 800 rpm; 2 min) and COF synthesised from mentioned TAPP film. Straight dashed lines at 652 and 680 nm showing different pump wavelengths that will be used.

4.3.3 TAPP Film, Pump Wavelength = 680 nm

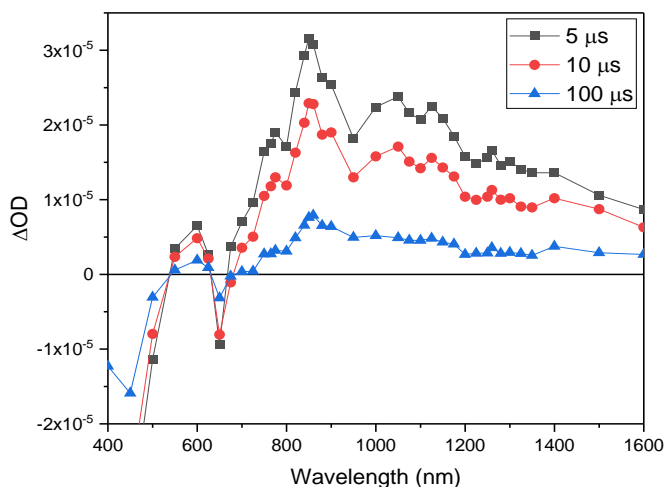


Figure 4.41: Microsecond transient absorption spectrum of TAPP film (9.56 mg/mL in anisole spin coated: 10, 000 rps; 800 rpm; 2 min). Excited with a pump wavelength of 680 nm and excitation density of $48 \mu\text{J cm}^{-2}$.

Figure 4.41 is the transient absorption spectrum of a TAPP film excited with a pump wavelength of 680 nm. The spectrum is near identical to the TAPP film excited with a pump wavelength of 450 nm shown in Figure 4.9. (A comparison spectrum is shown in Figures 4.47 and 4.48.) The two negative signals at 450 and 650 nm show the ground state bleach of the TAPP film. The peak at 850 nm and the broad peak moving into the IR show the transient species of the film. Oxygen dependence measurements were taken at a pump wavelength of 680 nm to determine the presence or lack of triplet states and are collected in Appendix 2. As with the TAPP films measured at a pump wavelength of 450 nm, the oxygen dependence results do not provide evidence of triplets but rather charges.

4.3.4 COF Film, Pump Wavelength = 652 nm

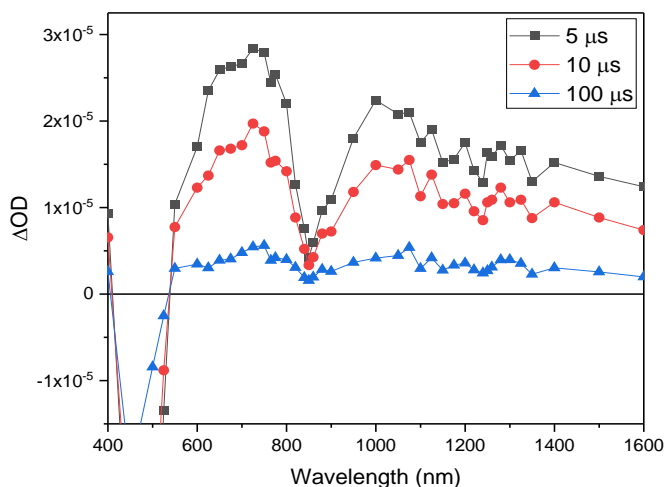


Figure 4.42: Microsecond transient absorption spectrum of a COF film made from TAPP film (9.56 mg/mL in anisole spin coated: 10, 000 rps; 800 rpm; 2 min). Excited with a pump wavelength of 652 nm and excitation density of $45 \mu\text{J cm}^{-2}$.

Figure 4.42 shows the microsecond transient absorption spectrum of a COF film excited with a pump wavelength of 652 nm. The spectrum is extremely similar to the COF film excited with a pump wavelength of 450 nm shown in Figure 4.22. (A comparison spectrum is shown in Figures 4.58 and 4.59.) The negative signal $\sim 400\text{-}600$ nm shows the ground state bleach. However, there is no negative signal to indicate the ground state bleach of the Q-bands but this was also seen for the COF film excited with a pump wavelength of 450 nm. The transient species is more prominent, and the signal outweighs that of the ground state bleach. The peak at 765 nm, and the broad peak in the IR region ~ 1250 nm show the charges of the COF film which were identified using the oxygen-dependence measurements (Appendix 2). The kinetics will be expanded upon after describing the comparison TA spectrum in Figure 4.43.

4.3.5 5 μ s Comparison of TAPP and COF films

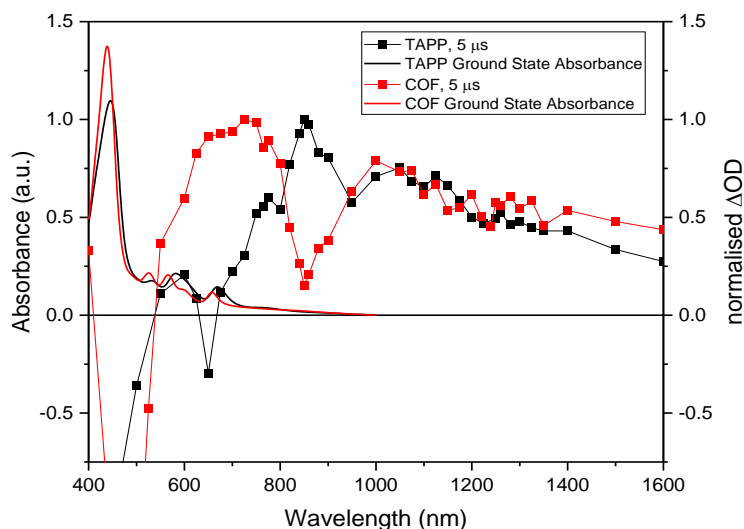


Figure 4.43: Normalised microsecond transient absorption spectrum of TAPP film (9.56 mg/mL in anisole spin coated: 10,000 rps; 800 rpm; 2 min), excited with a pump wavelength of 680 nm and excitation density of $48 \mu\text{J cm}^{-2}$, compared to COF made from aforementioned film, excited with a pump wavelength of 652 nm and excitation density of $45 \mu\text{J cm}^{-2}$. Ground state absorbance overlaid.

Figure 4.43 is the comparison between the TAPP and COF film transient absorption spectra at a pump wavelength of 680 and 652 nm respectively. The spectrum matches the comparison between the TAPP and COF film measured at a pump wavelength of 450 nm because; (1) the similarities are the ground state bleach at 400-600 nm and the broad peak in the IR region; (2) the differences are the ground state bleach at ~ 650 nm for the TAPP film which is not present for the COF film; and (3) there is a shift in the prominent peaks for each film, the prominent peak occurs at 850 nm for the TAPP film but at 765 nm for the COF film. It was not expected that there would be a difference in the TA spectra when using different pump wavelengths. Using different pump wavelengths was to try and understand better the effects of the unreacted TAPP in a COF film. The fact that the TA spectra remain the same at different pump wavelengths for the TAPP and COF respectively is positive as it can be claimed that at a pump wavelength of 450 nm, the COF is being largely studied rather than the TAPP.

There is no comparison of the kinetics between the TAPP and COF films measured at different excitation energies because it is not possible to compare the α of TA kinetics for which there are different exciton densities photogenerated in the films. The charge densities will be massively different and normally, high densities lead to faster charge recombination, therefore the α values are not analogous. Still, the oxygen dependence measurements have already eliminated the presence of triplets so the peaks are assigned to charges.

To conclude the results regarding the films pumped at 680 and 652 nm: there is no difference between transient absorption spectra between TAPP and COF films measured at different pump wavelengths. This is a significant and a very positive result because it can be concluded that when exciting the COF film at 450 nm, the main component analysed is the COF rather than any residual TAPP from an unsuccessful synthesis. This is shown in the spectra in Figures 4.44-4.47 which have been normalised to 1 and normalised per photon absorbed and there is no difference in the transient absorption spectra. The purpose of normalising per photon absorbed is to account for the difference in measuring at a pump wavelength of 680 and 652 nm as well as minor changes in excitation density.³⁹ The shape of the trace of the ΔOD in each spectrum is near identical and regarding Figures 4.45 and 4.47, the amplitude is also near-identical.

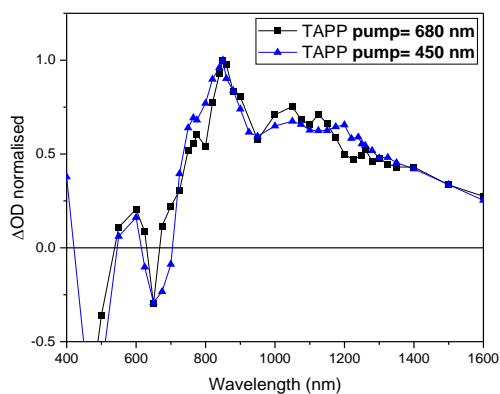


Figure 4.44: Normalised to 1, microsecond transient absorption spectrum of TAPP film, excited with a pump wavelength of 450 nm and excitation density of $43 \mu\text{J cm}^{-2}$, compared to a TAPP film excited with a pump wavelength of 680 nm and excitation density of $43 \mu\text{J cm}^{-2}$.

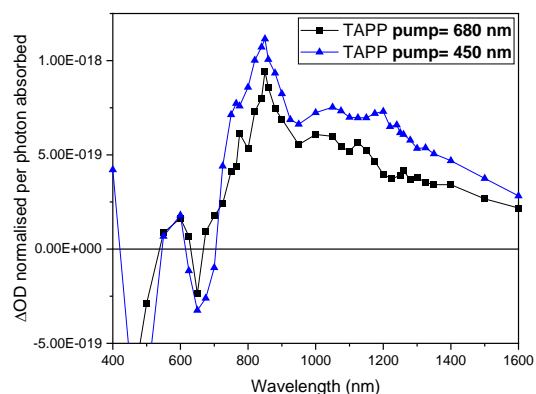


Figure 4.45: Normalised microsecond transient absorption spectrum of TAPP film, excited with a pump wavelength of 450 nm and excitation density of $43 \mu\text{J cm}^{-2}$, compared to a TAPP film excited with a pump wavelength of 680 nm and excitation density of $43 \mu\text{J cm}^{-2}$.

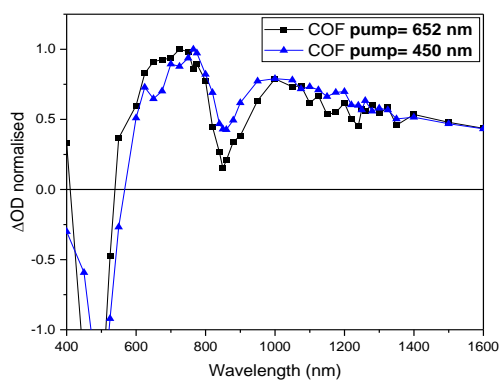


Figure 4.46: Normalised to 1 microsecond transient absorption spectrum of a COF made from a TAPP film excited with a pump wavelength of 652 nm and excitation density of $45 \mu\text{J cm}^{-2}$, compared to a COF film excited with a pump wavelength of 450 nm and excitation density of $52 \mu\text{J cm}^{-2}$.

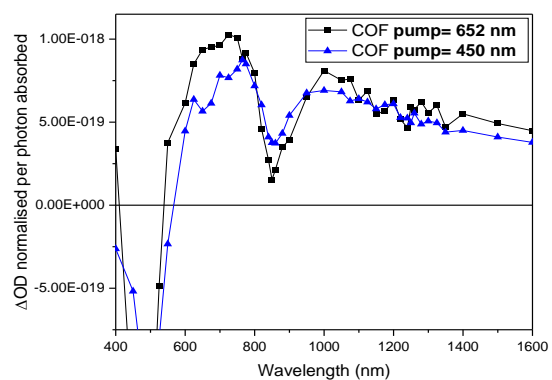


Figure 4.47: Normalised microsecond transient absorption spectrum of a COF made from a TAPP film excited with a pump wavelength of 652 nm and excitation density of $45 \mu\text{J cm}^{-2}$, compared to a COF film excited with a pump wavelength of 450 nm and excitation density of $52 \mu\text{J cm}^{-2}$.

4.4 Conclusion

To begin with, it was decided to study the photophysical properties of TAPP in solution using TAS. There have been many studies of porphyrins in solution and due to the high Soret band in the ground state absorbance (Figure 4.1), this would give a greater signal during the TAS measurements. Figure 4.4 indicates the presence of triplets in solution which is in accordance with literature of studies on porphyrins in solution.²⁵ As the aim of this thesis is to study the photophysical properties of COFs, a COF solution was made but, because of the unsuccessful reaction in solution and the likelihood that the majority of the solution is unreacted TAPP, it was not possible to measure the TAS of a COF solution. The transient absorption spectrum comparing TAPP and COF solution was near-identical (Figure 4.7).

TAS studies were then carried out on TAPP and COF films. Firstly, the focus was on TAPP films and the results show that charges were present over triplets, this is clear to see from the oxygen dependence measurements and kinetic decay studies (Section 4.2.1). The excitation density dependence measurements showed evidence for bimolecular recombination which was further supported by fitting a power law to the kinetic decays. Unfortunately, there was no definitive relationship between the kinetic decays at the same pump wavelength but different probe wavelengths, for example Figures 4.14-4.18. The change in α is small (~ 0.1) which suggests that bimolecular recombination is facilitated at higher excitation density, but this is not conclusive because of the repeatability of the samples, as shown in Figure 4.38. So, even though the UV-vis results showed different aggregation in the blue shifts, the alpha values did not draw such a direct conclusion.

The COF TAS studies showed evidence for charges and bimolecular recombination too and like the TAPP films there was no definitive relationship between the kinetic decays at the same pump wavelength but different probe wavelengths. However, when comparing the transient absorption spectra (Figure 4.33) there is a distinct shift in the prominent peak at 850 nm for the TAPP film to 765 nm for the COF

film. This was seen across all samples. The peaks were already assigned to charges but in order to compare the charge formation the kinetic decays were compared (Figures 4.34-4.37). Unfortunately, the same lack of pattern in the change of α arises when comparing the charge formation between TAPP and COF films.

Chapter 3 describes the COF synthesis and the unreliable nature of the synthesis. Therefore, it was important to ascertain whether when pumping both the TAPP and COF films in the broad Soret band, there is no overriding effect from unreacted TAPP in the COF film. By changing the pump wavelength to the Q-band to selectively pump TAPP and then COF (which blue shifts), it was possible to conclude that when pumping the COF at 450 nm, the COF was the predominant species. This can be seen in Figures 4.44-4.47 which show the same transient absorption spectra at different pump wavelengths.

The photophysical properties of COF films have been studied and show the presence of charges in the visible and IR spectrum. Further work can elucidate more information about the rate of bimolecular recombination and the depth of traps across the energetic distribution of trap states which is the rate limiting process. Future work should focus on the effect charges have over triplets in applications which aim to harness solar energy. Needless to say, this thesis has just scratched the surface of the behavior of COFs made from TAPP. Considering the numerous precursors that can be used to make COFs, it is likely that further research will also uncover properties about COFs that will lead to exciting new applications and help understand photophysical behaviors.

4.5 Bibliography

- 1 A. C. Jakowetz, T. F. Hinrichsen, L. Ascherl, T. Sick, M. Calik, F. Auras, D. D. Medina, R. H. Friend, A. Rao and T. Bein, *J. Am. Chem. Soc.*, 2019, **141**, 11565–11571.
- 2 D. Nettels, D. Haenni, S. Maillot, M. Gueye, A. Barth, V. Hirschfeld, C. G. Hübner, J. Léonard and B. Schuler, *Phys. Chem. Chem. Phys.*, 2015, **17**, 32304–32315.
- 3 L. Stryer and R. P. Haugland, *Proc. Natl. Acad. Sci. U. S. A.*, 1967, **58**, 719–726.
- 4 M. Calik, F. Auras, L. M. Salonen, K. Bader, I. Grill, M. Handloser, D. D. Medina, M. Dogru, F. Löbermann, D. Trauner, A. Hartschuh and T. Bein, *J. Am. Chem. Soc.*, 2014, **136**, 17802–17807.
- 5 S. M. Andrade, R. Teixeira, S. M. B. Costa and A. J. F. N. Sobral, *Biophys. Chem.*, 2008, **133**, 1–10.
- 6 R. Berera, R. van Grondelle and J. T. M. Kennis, *Photosynth. Res.*, 2009, **101**, 105–118.
- 7 S. Karuthedath, J. Gorenflot, Y. Firdaus, W. Y. Sit, F. Eisner, A. Seitkhan, M. K. Ravva, T. D. Anthopoulos and F. Laquai, *Adv. Energy Mater.*, 2019, **9**, 1802476.
- 8 R. N. Griffin, *Photochem. Photobiol.*, 1968, **7**, 175–187.
- 9 M. Scholz, R. Džedić, T. Breitenbach and J. Hála, *Photochem. Photobiol. Sci.*, 2013, **12**, 1873–1884.
- 10 M. B. Ericson, S. Grapengiesser, F. Gudmundson, A. M. Wennberg, O. Larkö, J. Moan and A. Rosén, *Lasers Med. Sci.*, 2003, **18**, 56–62.
- 11 S. Kim and H. C. Choi, *Commun. Chem.*, 2019, **2**, 1–8.
- 12 S. Wan, F. Gándara, A. Asano, H. Furukawa, A. Saeki, S. K. Dey, L. Liao, M. W. Ambrogio, Y. Y. Botros, X. Duan, S. Seki, J. F. Stoddart and O. M. Yaghi, *Chem. Mater.*, 2011, **23**, 4094–4097.
- 13 J. D. Servaites, M. A. Ratner and T. J. Marks, *Energy Environ. Sci.*, 2011, **4**, 4410–

4422.

- 14 F. Laquai, D. Andrienko, C. Deibel and D. Neher, in *Advances in Polymer Science*, 2017, vol. 272, pp. 267–291.
- 15 S. Albrecht, J. R. Tumbleston, S. Janietz, I. Dumsch, S. Allard, U. Scherf, H. Ade and D. Neher, *J. Phys. Chem. Lett.*, 2014, **5**, 1131–1138.
- 16 S. Ryu, D. C. Nguyen, N. Y. Ha, H. J. Park, Y. H. Ahn, J.-Y. Park and S. Lee, *Sci. Rep.*, 2019, **9**, 19846.
- 17 T. M. Clarke, F. C. Jamieson and J. R. Durrant, *J. Phys. Chem. C*, 2009, **113**, 20934–20941.
- 18 O. Ostroverkhova, *Handbook of Organic Materials for Electronic and Photonic Devices*, Elsevier, 2019.
- 19 I. Montanari, A. F. Nogueira, J. Nelson, J. R. Durrant, C. Winder, M. A. Loi, N. S. Sariciftci and C. Brabec, *Appl. Phys. Lett.*, 2002, **81**, 3001–3003.
- 20 J. E. Dominguez, L. Fu and X. Q. Pan, *Appl. Phys. Lett.*, 2002, **81**, 5168–5170.
- 21 G. Kalyuzhny, A. Vaskevich, G. Ashkenasy, A. Shanzer and I. Rubinstein, *J. Phys. Chem. B*, 2000, **104**, 8238–8244.
- 22 H. Abudukeremu, N. Kari, Y. Zhang, J. Wang, P. Nizamidin, S. Abliz and A. Yimit, *J. Mater. Sci.*, 2018, **53**, 10822–10834.
- 23 W.-F. Su, in *Characterization of Polymer*, 2013, pp. 89–110.
- 24 J. L. Humphrey and D. Kuciauskas, *J. Phys. Chem. C*, 2008, **112**, 1700–1704.
- 25 T.-H. Tran-Thi, T. Fournier, A. Y. Sharonov, N. Tkachenko, H. Lemmetyinen, P. Grenier, K.-D. Truong and D. Houde, *Thin Solid Films*, 1996, **273**, 8–13.
- 26 M. Chang, G. Lim, B. Park and E. Reichmanis, *Polymers (Basel)*, 2017, **9**, 212.
- 27 D. Zhang, Y. Guo and Z. Zhao, *Appl. Catal. B Environ.*, 2018, **226**, 1–9.

- 28 F. Nüesch and M. Grätzel, *Chem. Phys.*, 1995, **193**, 1–17.
- 29 S. Das and P. V Kamat, *J. Phys. Chem. B*, 1999, **103**, 209–215.
- 30 C. Nasr and S. Hotchandani, *Chem. Mater.*, 2000, **12**, 1529–1535.
- 31 Z. Fu, X. Wang, A. M. Gardner, X. Wang, S. Y. Chong, G. Neri, A. J. Cowan, L. Liu, X. Li, A. Vogel, R. Clowes, M. Bilton, L. Chen, R. S. Sprick and A. I. Cooper, *Chem. Sci.*, 2020, **11**, 543–550.
- 32 H. Jin, E. Debroye, M. Keshavarz, I. G. Scheblykin, M. B. J. Roeffaers, J. Hofkens and J. A. Steele, *Mater. Horizons*, 2020, **7**, 397–410.
- 33 L. Wang, C. McCleese, A. Kovalsky, Y. Zhao and C. Burda, *J. Am. Chem. Soc.*, 2014, **136**, 12205–12208.
- 34 C. R. Kagan, C. B. Murray, M. Nirmal and M. G. Bawendi, *Phys. Rev. Lett.*, 1996, **76**, 1517–1520.
- 35 O. Ostroverkhova, S. Shcherbyna, D. G. Cooke, R. F. Egerton, F. A. Hegmann, R. R. Tykwinski, S. R. Parkin and J. E. Anthony, *J. Appl. Phys.*, 2005, **98**, 033701.
- 36 C. Dyer-Smith, J. Nelson and Y. Li, in *McEvoy's Handbook of Photovoltaics: Fundamentals and Applications*, Elsevier Inc., 2018, pp. 567–597.
- 37 M. Lenes, S. W. Shelton, A. B. Sieval, D. F. Kronholm, J. C. Hummelen and P. W. M. Blom, *Adv. Funct. Mater.*, 2009, **19**, 3002–3007.
- 38 R. Häusermann, K. Willa, B. Blülle, T. Morf, A. Facchetti, Z. Chen, J. Lee and B. Batlogg, *Org. Electron.*, 2016, **28**, 306–313.
- 39 C. Cantrell, *Multiple-Photon Excitation and Dissociation of Polyatomic Molecules - Google Books*, Springer Science & Business Media, 1st Editio., 2013, vol. 35.

5 Photophysical Properties of Zinc and Copper Metalloporphyrins

5.1 Introduction

Previously discussed in Chapter 1, porphyrins are large macrocycles with an 18-electron π system and are a class of molecules containing a flat ring of four linked heterocyclic pyrrole subunits, connected at their α -carbon atoms via methane bridges. The four nitrogen atoms in the porphyrin core can coordinate to a range of different metal atoms. Different coordinated metal atoms can modify the porphyrins' optical and chemical properties.

Metalloporphyrins can be divided into two groups based on their UV-vis and fluorescence properties. Regular metalloporphyrins contain closed-shell metal ions (d^0 or d^{10}); for example Zn^{II} , in which the $d\pi$ (d_{xz} , d_{yz}) metal-based orbitals are relatively low in energy.¹ These have very little effect on the porphyrin π to π^* energy gap in porphyrin electronic spectra (Figure 5.1). Irregular porphyrins are metalloporphyrins in which the metals are of d^m , $m = 6-9$, having filled $d\pi$ orbitals. In hypso porphyrins there is significant metal $d\pi$ to porphyrin π^* orbital interaction (metal to ligand π -backbonding, Figure 5.2). This results in an increased porphyrin π to π^* energy separation causing the electronic absorptions to undergo hypsochromic (blue) shifts.^{2,3}

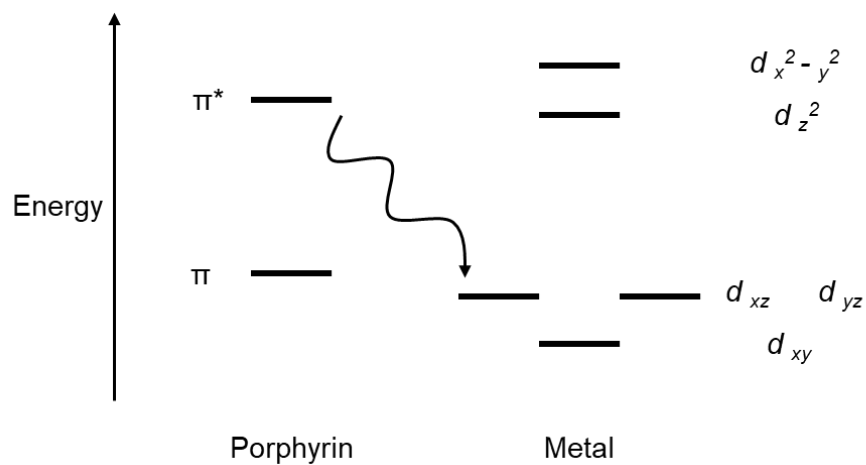


Figure 5.1: Molecular orbital diagram for metalloporphyrins showing orbital mixing between the π^* and metal d-orbitals.

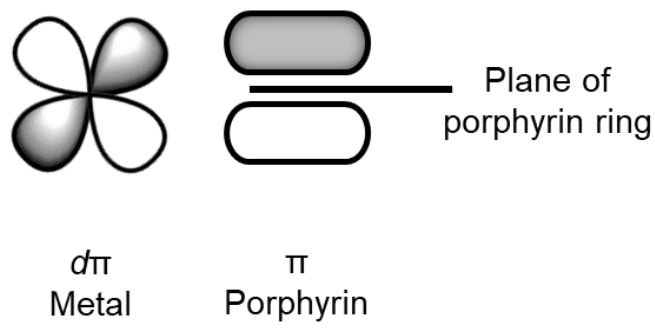


Figure 5.2: The d_{xy} metal orbital overlap with the π system of the porphyrin ring.

The results from Chapter 4 focused on the photophysical pathways of a freebase TAPP molecule, concluding that the charge states match the kinetics of the transient species rather than triplet states; even though both relaxation pathways are reported in literature.

This chapter focusses on the effect of coordinating a metal atom into the centre of TAPP molecules. The presence of a transition metal atom at the centre of the porphyrin enhances spin-orbit coupling, leading to a noticeable activation of intersystem crossing to triplet states.^{4,5} This would suggest that triplet species would be more

probable in metalloporphyrins. However, like freebase porphyrins, the literature shows evidence for the potential of charge states and triplet states, under various conditions.^{6,7}

5.1.1 Triplet or Charge State

Shediac *et al.* have studied the singlet and triplet excited states of emissive, conjugated Zn-porphyrin compounds probed by optical and electron paramagnetic resonance (EPR) spectroscopic methods.⁸ They state that the lowest excited singlet and triplet states of porphyrin-metal complexes are generally higher in energy than the analogous excited states of their respective free base porphyrin macrocycles. However, they also conclude that transient triplet-triplet TAS data show that the lifetime of T_1 excited states are similar for porphyrin arrays when all are metallated, when only partly metallated as well as all freebase porphyrins. So, they conclude that there are no low-lying charge resonance states that serve to efficiently deactivate the T_1 state.

However, research by Patchkovskii *et al.* and, Linschitz and Pekkarinen who studied metallated porphyrins, and in general, favour deactivation of excited states by low lying charge transfer states.^{4,9}

Hernández-Fernández *et al.* have studied the effect of metallation on electron couplings for hole transport in stacked porphyrin dyads.¹⁰ One porphyrin they studied, *meso*-tetraphenylporphyrin, is analogous to the TAPP and Zn-TAPP used in this thesis. Using a computational method, they considered porphyrins with different metallic centres as this is a common approach to tune the properties of a porphyrin-containing material. The simulations show that the choice of the metal can be crucial for the hole-transfer properties of the molecule. For Zn-porphyrin a small increase (~10%) of the value of electron coupling compared to the unsubstituted porphyrin is observed at all intermolecular distances. Hernández-Fernández *et al.* explain that the cause is due to the d^{10} configuration of Zn^{2+} preventing the mixing, making the HOMO of the Zn-porphyrin only slightly different from that of porphyrin. The small increase of electronic coupling can be understood as the HOMO of the metallated system is more localised on the nitrogen and *meso*-carbon than that of porphyrin, giving rise to a more efficient overlap

between orbitals of adjacent molecules. The highest transfer rates may be expected from those metals which leave the HOMO of the porphyrin intact.

Research by Bahr *et al.* have shown that a small increase in electron coupling can achieve longer-lived charge separation in Zn-porphyrin triads.¹¹ Bahr *et al.* studied the driving force and electron coupling effects on photoinduced electron transfer in a fullerene and porphyrin-based triad.¹¹ Excitation of the porphyrin moiety leads to photoinduced electron transfer from the porphyrin S_1 to the fullerene and subsequent electron transfer leads to a charge separated state with a lifetime of 170 ns. Their results go on to show that tailoring the electron transfer properties of such molecules have potential applications in non-homogeneous media such as monolayer films. Also, that high-yield photoinduced electron transfer in such conditions is a prerequisite for possible applications in solar energy conversion and opto-electronic devices.

Wijesinghe *et al.* have also studied the photoinduced electron transfer in a linked *meso*-triphenylamine Zn-porphyrin-quinone dyad.¹² A multimodular donor-acceptor system composed of three triphenylamine moieties at the *meso*-positions of a Zn-porphyrin macrocycle and a quinone at the fourth *meso*-position was newly synthesised and characterised. The triphenylamine moieties improved the electron donor ability of the Zn-porphyrin. Appreciable electronic interactions of the triphenylamine and quinone moieties with the porphyrin π -system were observed. Using time-resolved pump probe techniques the electron transfer reaction path was explored. When the Zn-porphyrin was predominantly excited, a rapid charge separation followed by equally fast charge recombination was observed.

The results in this chapter look at Zn-TAPP, Cu-TAPP and then the COFs made from the mentioned porphyrins to determine the deactivation pathway preferred by metallated porphyrin systems.

5.2 Studies on ZnTAPP: Results and Discussion

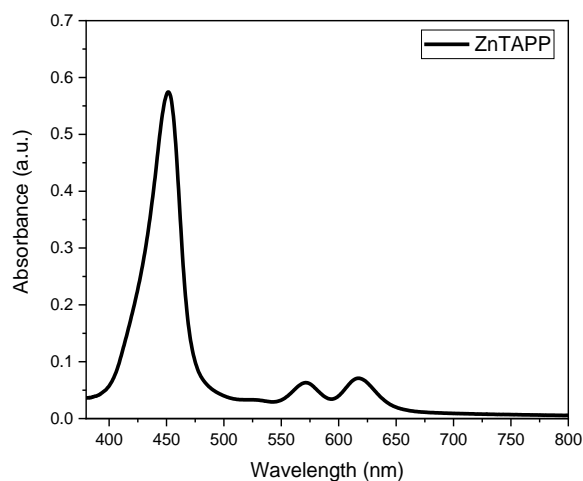


Figure 5.3: Ground state absorption of ZnTAPP film (ZnTAPP in THF spin coated: 10, 000 rps; 800 rpm; 2 min).

Figure 5.3 shows a ground state absorption spectrum of a ZnTAPP film. The porphyrin macrocycle is metallated so two Q bands instead of four are observed.¹³ The Soret band is found at 450 nm and the Q-bands are found at ~640 and ~575 nm.

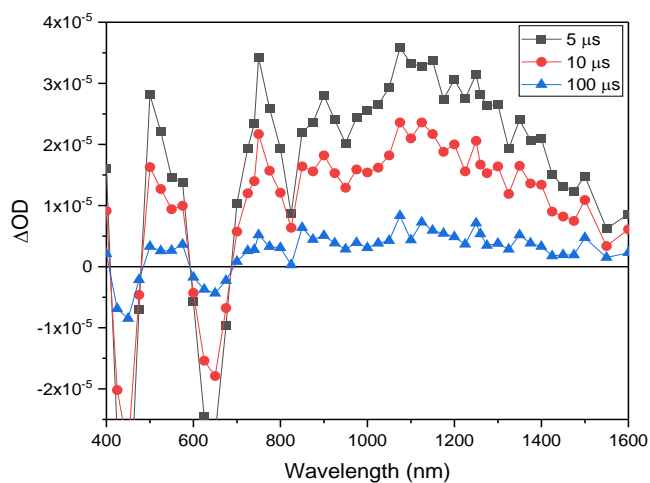


Figure 5.4: Microsecond transient absorption spectrum of ZnTAPP film (ZnTAPP in THF spin coated: 10, 000 rps; 800 rpm; 2 min). Excited with a pump wavelength of 450 nm and excitation density of $32 \mu J cm^{-2}$.

Figure 5.4 is the TA spectrum of a ZnTAPP film. The two negative signals at 450 and 650 nm show the ground state bleach of the ZnTAPP film. The peaks at 750, 875 nm and broad peak at 1125 nm show the transient species of the film. The peak at 1125 nm in the IR region of the spectrum is very broad and gradually declines as the wavelength increases to 1600 nm. In comparison to freebase TAPP, there is a greater distribution of excited states in the NIR in ZnTAPP as the spectrum is broader.

Figure 5.5 shows the oxygen dependence measurements at a pump wavelength of 450 nm and probe wavelength of 750 and 1125 nm. When measuring the kinetics under an oxygen atmosphere the trace remains near-identical. Measurements were also taken at a pump wavelength of 450 nm and probe wavelength of 875 nm (Appendix 3). All the oxygen dependence measurements do not support the presence of triplet states and could suggest charges. The kinetic decays look like a power law decay so this will be investigated by fitting to the excitation energy dependence kinetic measurements.

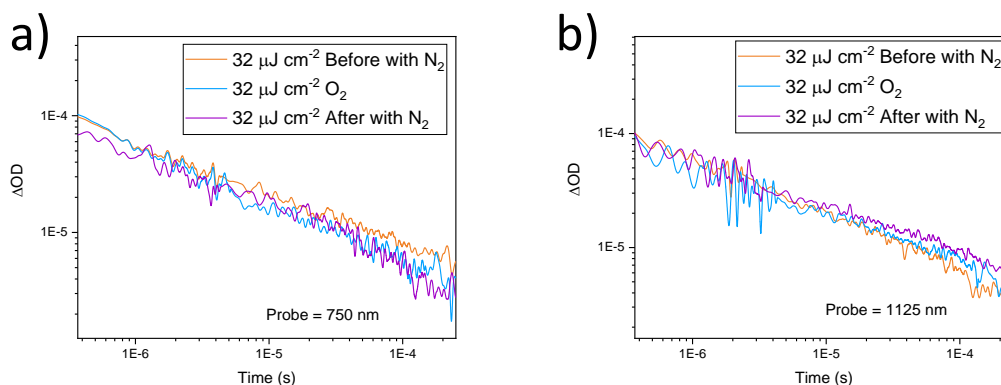


Figure 5.5: Oxygen dependent kinetics of ZnTAPP film (2.95 mg/mL in THF spin coated: 10, 000 rps; 800 rpm; 2 min). Excited with a pump wavelength of 450 nm, probe wavelength of a) 750 nm, b) 1125 nm, and excitation density of $32 \mu\text{J cm}^{-2}$.

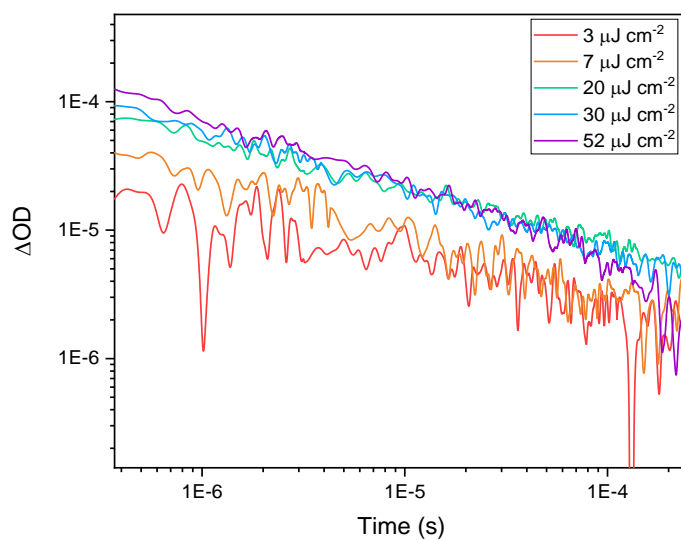


Figure 5.6: Kinetics of ZnTAPP film (ZnTAPP in THF spin coated: 10, 000 rps; 800 rpm; 2 min). Excited with a pump wavelength of 450 nm and probed at 750 nm.

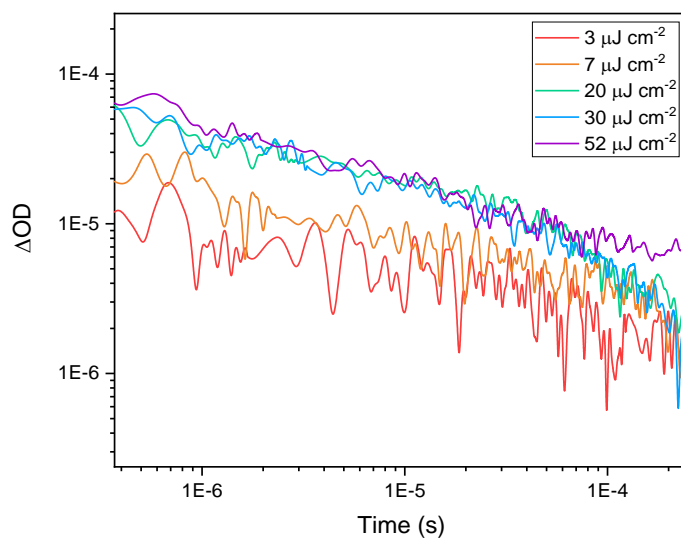


Figure 5.7: Kinetics of ZnTAPP film (ZnTAPP in THF spin coated: 10, 000 rps; 800 rpm; 2 min). Excited with a pump wavelength of 450 nm and probed at 875 nm.

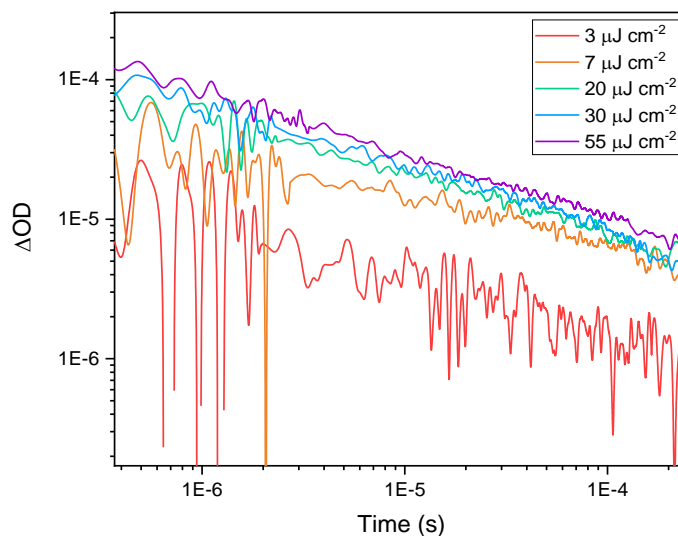


Figure 5.8: Kinetics of ZnTAPP film (ZnTAPP in THF spin coated: 10, 000 rps; 800 rpm; 2 min). Excited with a pump wavelength of 450 nm and probed at 1125 nm.

Figures 5.6-5.8 are the kinetic measurements taken of the same ZnTAPP film at 750, 875 and 1125 nm. The results follow the same trend as the excitation density measurements for the freebase TAPP and COF films presented in Chapter 4. The traces measured at different laser energies show a power law decay and that the ΔOD plateaus from $\sim 50 \mu\text{J cm}^{-2}$ for ZnTAPP. Figure 5.9 shows the dependence of excitation density and shows a trend for bimolecular recombination because as the excitation density has increased, the ΔOD plateaus.

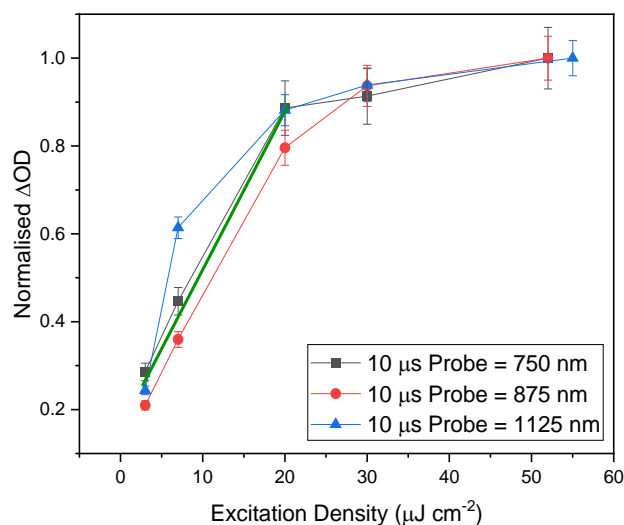


Figure 5.9: Normalised ΔOD measured at $10 \mu s$ as a function of laser excitation density. The slope to the plateau is averaged amongst the three data plots and is a green line with a gradient, x , of 0.032.

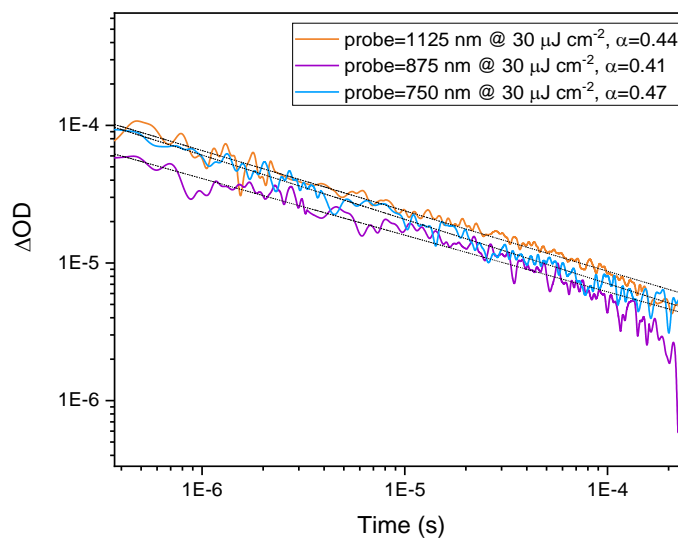


Figure 5.10: Kinetics of ZnTAPP film (ZnTAPP in THF spin coated: 10, 000 rps; 800 rpm; 2 min). Excited with a pump wavelength of 450 nm and excitation density of $30 \mu J cm^{-2}$, with varying probe wavelengths. The black lines are the power law fitting ($\Delta OD \propto t^{-\alpha}$) to each decay.

Figure 5.10 is a comparison of the kinetic decays of the same ZnTAPP film and at the same pump energy and excitation density but at different probe wavelengths: 750,

875 and 1125 nm. The magnitude of the power law's exponent α is similar for all probe wavelengths at the same laser energy so all points have similar trap distribution energies. This means that the charges at these "depths" will require the same amount of energy to leave the trap and then recombine. Similar insignificant variations were seen for the freebase TAPP and COF films. Unfortunately, the reproducibility and reliability of the kinetic decay data was a major stumbling block during this study. Other runs of the same sample would give different α values, so it is not possible to conclude that there is any change in the films at different probe wavelengths. The reasons for the variation could be due to the synthesis procedure; the extent of the framework synthesised could be different each time, or changes in the laser set-up. Every effort was made to ensure the laser energy, background, filters etc. were exactly the same but the results were still different after 5 repeats. Figure 5.11 shows the variation in α values at the three probe wavelengths for ZnTAPP. Samples 1 and 3 show a similar trend; and then 4 and 5 are similar but the couplets are different to each other, and then sample 2 stands out as an irregularity. The overlaps of the error bars indicate that no two samples are within the error to be considered similar, so samples 2, 1 and 5 overlap at 1125 nm but samples 4 and 5 overlap at 750 nm etc.

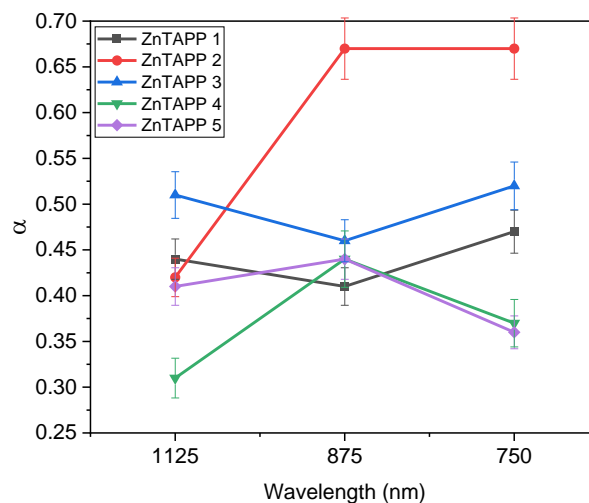


Figure 5.11 Comparison of alpha values at the three sampling wavelengths for ZnTAPP with error bars showing standard deviation.

5.2.1 ZnCOF

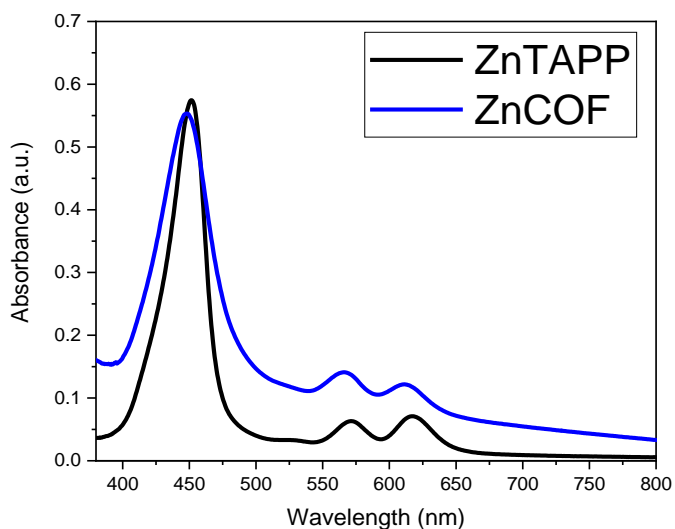


Figure 5.12: Ground state absorption of ZnTAPP film (ZnTAPP in THF spin coated: 10, 000 rps; 800 rpm; 2 min) and ZnCOF made from said ZnTAPP film.

Figure 5.12 shows a ground state absorption spectrum of a ZnTAPP film and then a COF sample made from the same ZnTAPP film. The COF was synthesised with the standard set-up described in Chapter 2. Even though the ground state absorbances of both films are similar, there is a slight broadening of the Soret band for the ZnCOF film. With respect to the Soret band, the FWHM of the ZnTAPP is 42.6 nm and for the COF the FWHM is 33.5 nm. There is a difference of 9.1 of the FWHM, however, both the Soret and Q-bands largely overlap. There is a very small possibility that it may be an indication of a lack of success of the synthetic procedure, so the “ZnCOF” film is still mainly composed of ZnTAPP. Otherwise, they just characteristically overlap. There appears to be a blue shift in the Q bands of the ZnCOF as well, but the shift is less than 5 nm for both peaks. Table 5.1 lists the shifts in the Soret and Q-bands for four of the five ZnTAPP and ZnCOF samples measured. The shifts are so minimal the errors in the Soret band shifts overlap for samples 2, 3 and 5. Minor change could be a result of variations of the film from spin-coating or minor changes in sample loading in the UV-vis spectrometer.

ZnTAPP > ZnCOF	Sample 1	Sample 2	Sample 3	Sample 5
Change in Soret band (nm)	8 ± 1.9	3 ± 1.9	4 ± 1.9	4 ± 1.9
Change in Q-bands (nm)	5 ± 0.5	5 ± 0.5	4 ± 0.5	4 ± 0.5

Table 5.1: A list of peak shifts between ZnTAPP films and the resultant ZnCOF film for the Soret and Q-bands in the UV-vis spectra. The error reported is the population standard deviation.

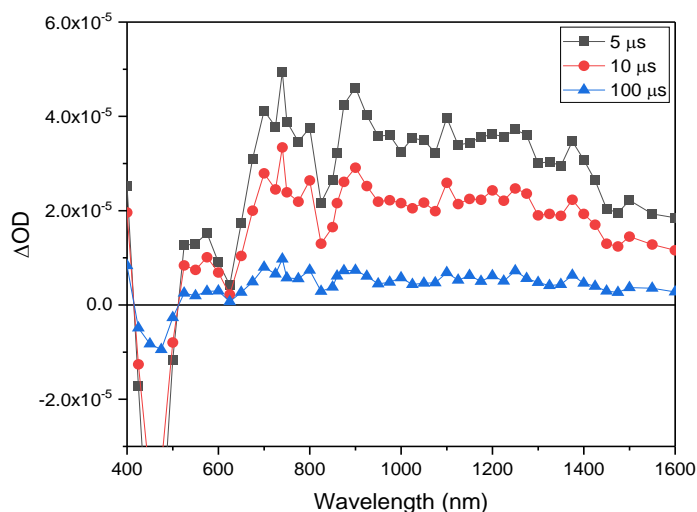


Figure 5.13: Microsecond transient absorption spectrum of ZnCOF film. Excited with a pump wavelength of 450 nm and excitation density of $32 \mu\text{J cm}^{-2}$.

Figure 5.13 shows the microsecond transient absorption spectrum of a ZnCOF film. The negative feature at ~ 450 nm shows the ground state bleach, which corresponds to the Soret band in the ground state absorption spectrum. However, there are no negative peaks to indicate the ground state bleach of the Q-bands because the signal from the transient species outweighs that of the ground state bleach. The peaks at 750 and 875 nm, and the broad peak in the IR region ~ 1125 nm show the transient species of the COF film. Again, measuring the kinetic properties at these points will help to understand what kind of excited state is forming, and the time it takes for the species to decay.

Figure 5.14 shows the oxygen dependence measurements at a pump wavelength of 450 nm and probe wavelength of 750 and 1125 nm. As with all the oxygen dependence

measurements for the porphyrin and COF films, there is no change in the trace when in an inert atmosphere or purged with oxygen. Measurements were also taken at a pump wavelength of 450 nm and probe wavelength of 875 nm (Appendix 3). The oxygen dependence measurements purport the presence of charges rather than triplets and with previous results, there is a strong indication of a power law decay which is analysed by the excitation energy dependence kinetic measurements.

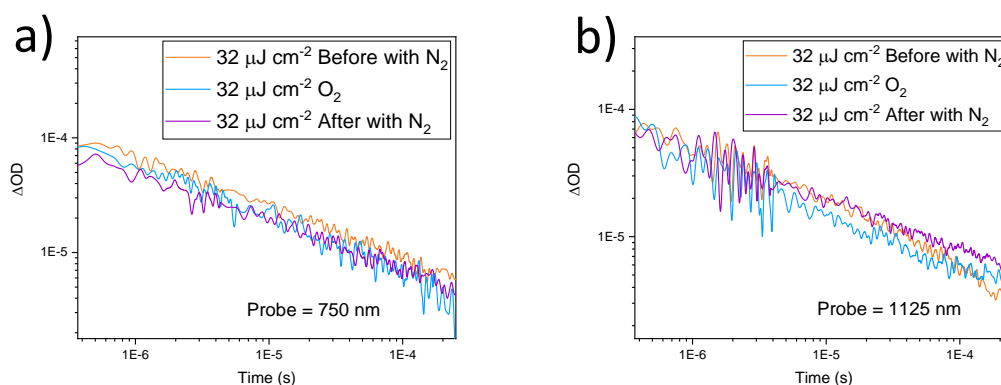


Figure 5.14: Oxygen dependent kinetics of ZnCOF film. Excited with a pump wavelength of 450 nm and probe wavelength of a) 750 nm and b) 1125 nm.

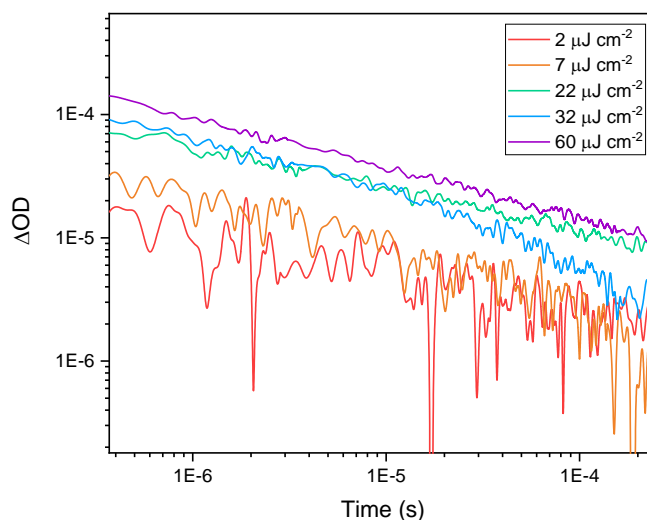


Figure 5.15: Kinetics of ZnCOF film. Excited with a pump wavelength of 450 nm and probed at 750 nm.

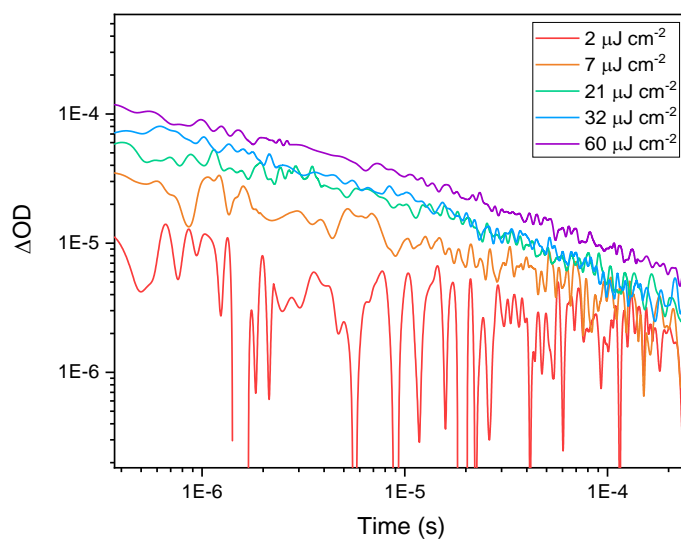


Figure 5.16: Kinetics of ZnCOF film. Excited with a pump wavelength of 450 nm and probed at 875 nm.

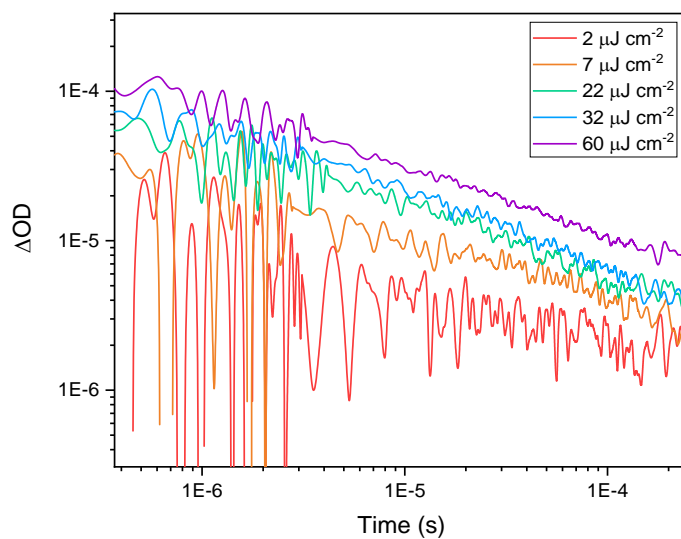


Figure 5.17: Kinetics of ZnCOF film. Excited with a pump wavelength of 450 nm and probed at 1125 nm.

Figures 5.15-5.17 are the kinetic measurements taken of the COF film at 750, 875 and 1125 nm. The traces measured at different laser energies show a power law decay,

whereas for the ZnTAPP film (and freebase TAPP) there was a point when the ΔOD began to plateau. This does not mean that the ΔOD for the ZnCOF will not plateau but potentially at a much higher excitation density. This may be because there are more charges forming as well as there being a higher saturation barrier; and indicates that there is a change in the density of states (DOS) between the ZnTAPP film and the ZnCOF. The reason for the change in DOS could be a cause of the effective mass of the charge carriers changing.^{14,15} Holes and electrons have different effective masses.¹⁶ In ZnTAPP films, there is no extended conjugation so the charge transport is intrinsic and there will be the same number of electrons and holes. For ZnCOF films, there are extended domains because of the incorporation of the BDA linker molecule and then the charge transport can occur across molecules and is referred to as extrinsic charge transport. With respect to extrinsic charge transport the number of electrons and holes does not have to be equal, so this supports the reasoning that there has been a successful synthesis of ZnCOF domains and the photophysical behaviour has changed.¹⁶ Nevertheless, for the ZnCOF, in order not to damage the film, the laser energy was not increased beyond $60 \mu\text{J cm}^{-2}$. Hence, in Figure 5.18, a plateau is not seen which is the trend being seen for bimolecular recombination but this is an experimental error as a higher excitation density was not attempted to fully complete the graph. The increased number of defects has led to an increase in the depth of the DOS as the data implies that much higher excitation densities are required to saturate the kinetics but this was not realised due to sample degradation. Unfortunately, this makes Figure 5.18 moot but is included in this chapter to show the complete data manipulation carried out.

The slope of the approach to the plateau has been included with the ZnTAPP showing $x = 0.032$ (Figure 5.9) and the ZnCOF showing $x = 0.025$. As seen with the comparison between the freebase TAPP and COF, there is a decrease in the approach to the plateau and for the zinc analogues it's a decrease of 22%. As explained in Chapter 4, the approach of the plateau can help to understand how efficient charge extraction can be. However, as discussed in the previous paragraph the plateau in Figure 5.18 is not reached and the percentage decrease is not accurate, nonetheless, it follows the same

trend as the freebase analogues and the decrease in gradient will remain as the slope in Figure 5.18 looks like it is tending towards a plateau, but the exact percentage will change.

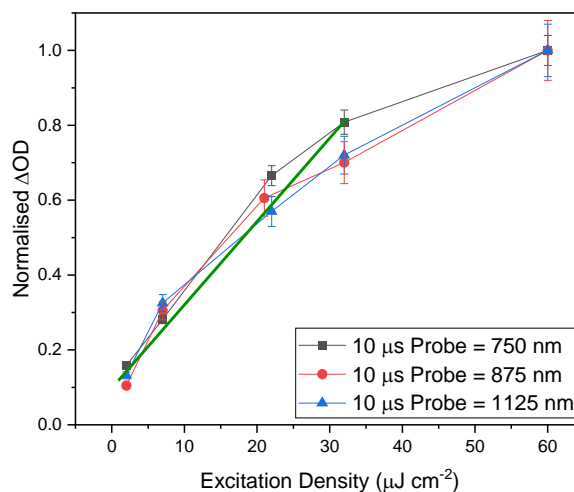


Figure 5.18: Normalised ZnCOF ΔOD measured at 10 μs as a function of laser excitation density. The slope to the plateau is an average of the three probe plot and is shown as a green line with a gradient, x , of 0.025.

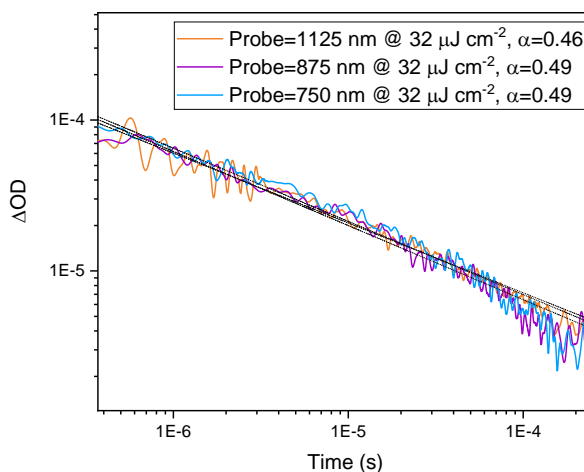


Figure 5.19: Kinetics of ZnCOF film. Excited with a pump wavelength of 450 nm and excitation density of 32 $\mu\text{J cm}^{-2}$, with varying probe wavelengths. The black lines are the power law fitting ($\Delta\text{OD} \propto t^{-\alpha}$) to each decay.

Figure 5.19 compares the kinetic decays of the ZnCOF film at different probe wavelengths but the same excitation density and pump wavelength. The α is alike for all probe wavelengths so all points have similar trap distribution energies. This means the species generated at each wavelength is similar in its properties and lifetime decays; which was also observed for ZnTAPP sample 1, shown in this thesis.

5.2.2 ZnTAPP and ZnCOF Comparison

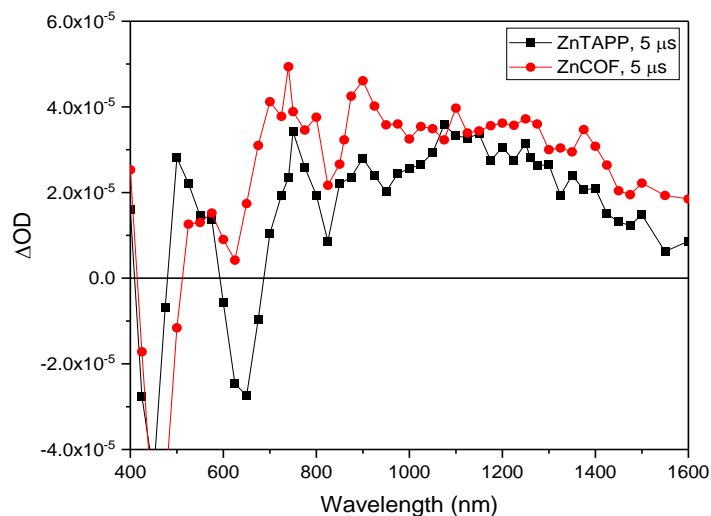


Figure 5.20: Microsecond transient absorption spectrum of ZnTAPP film (ZnTAPP in THF spin coated: 10, 000 rps; 800 rpm; 2 min) and ZnCOF film made from said ZnTAPP film. Excited with a pump wavelength of 450 nm and excitation density of $32 \mu\text{J cm}^{-2}$.

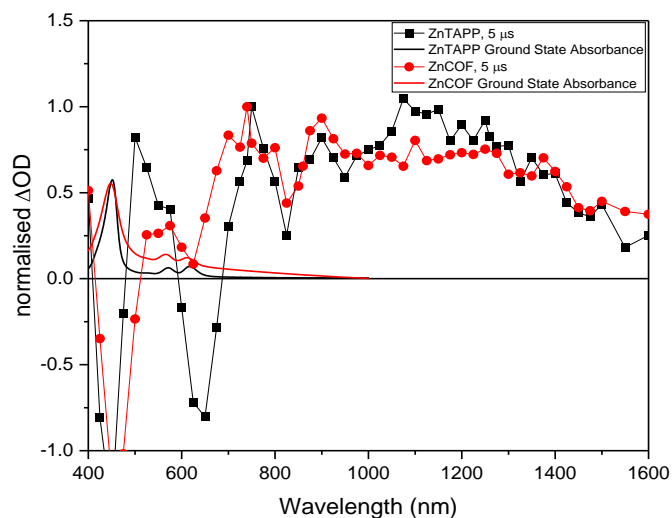


Figure 5.21: Normalised microsecond transient absorption spectrum of ZnTAPP film (ZnTAPP in THF spin coated: 10, 000 rps; 800 rpm; 2 min) and ZnCOF film made from said ZnTAPP film. Excited with a pump wavelength of 450 nm and excitation density of $32 \mu\text{J cm}^{-2}$. Ground state absorbance overlaid.

Figures 5.20 and 5.21 are the comparison between the ZnTAPP and ZnCOF film transient absorption spectra. Figure 5.21 has been normalised and includes the ground state absorption spectra. Focussing on the normalised transient absorption spectra, the only significant difference is that the ground state bleach is visible in the ZnTAPP spectrum but not in the ZnCOF spectrum at around 600 nm. This is dependent on the strength of the signal of the transient species at a certain wavelength and at 650 nm the transient species of the ZnCOF film has a higher optical absorbance. As the ground state absorbance has only slightly changed then it is an indication of a lack of change of the morphology of the ZnCOF film, so the IR region most likely reflects the same transient species for both the ZnTAPP and ZnCOF films. The same results as seen in Figures 5.19 and 5.20 reflects all the results collected for repeat ZnTAPP and ZnCOF films. Thus the results are repeatable but the reliability needs to be ascertained alongside the success of synthesis using data in Chapter 3 from the FTIR and XPS results of the ZnTAPP and ZnCOF films.

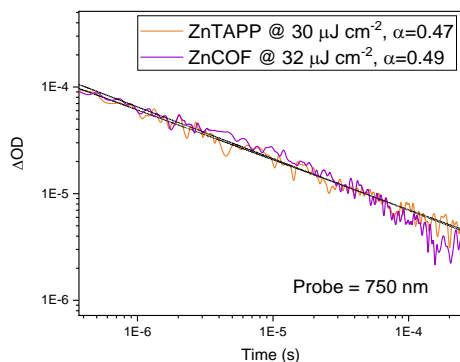


Figure 5.22: Kinetics of ZnTAPP film (ZnTAPP in THF spin coated: 10, 000 rps; 800 rpm; 2 min) and ZnCOF film made from said ZnTAPP film. Excited with a pump wavelength of 450 nm, probe wavelength of 750 nm and excitation density of 30 and 32 $\mu\text{J cm}^{-2}$ respectively. The black lines are the power law fitting ($\Delta\text{OD} \propto t^{-\alpha}$) to each decay.

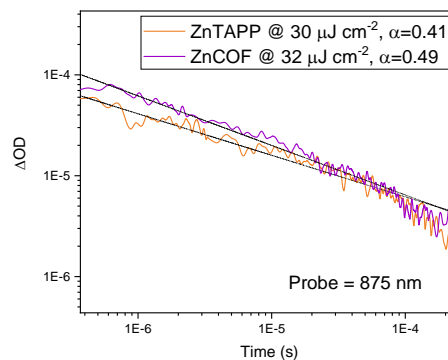


Figure 5.23: Kinetics of ZnTAPP film (ZnTAPP in THF spin coated: 10, 000 rps; 800 rpm; 2 min) and ZnCOF film made from said ZnTAPP film. Excited with a pump wavelength of 450 nm, probe wavelength of 875 nm and excitation density of 30 and 32 $\mu\text{J cm}^{-2}$ respectively. The black lines are the power law fitting ($\Delta\text{OD} \propto t^{-\alpha}$) to each decay.

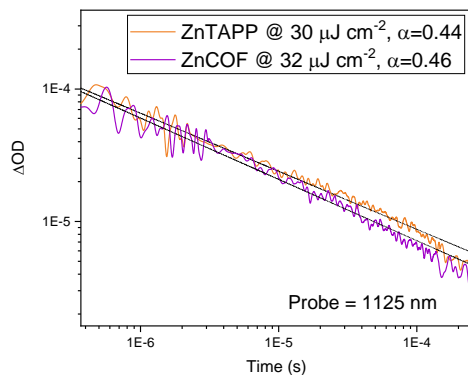


Figure 5.24: Kinetics of ZnTAPP film (ZnTAPP in THF spin coated: 10, 000 rps; 800 rpm; 2 min) and ZnCOF film made from said ZnTAPP film. Excited with a pump wavelength of 450 nm, probe wavelength of 1125 nm and excitation density of 30 and 32 $\mu\text{J cm}^{-2}$ respectively. The black lines are the power law fitting ($\Delta\text{OD} \propto t^{-\alpha}$) to each decay.

When comparing the kinetic decays (Figures 5.22 – 5.24) between the ZnTAPP and ZnCOF film at the same probe wavelength and roughly the same laser energy, the gradient α is near identical. This may be more due to the lack of success of the reaction rather than there being similarities in the decay kinetics of both the transient species in the ZnTAPP and ZnCOF films. However, the transient absorption spectra show that there has been some change in morphology as the ground state bleach has changed (the negative to positive peak at 650 nm in the TA spectrum). It is important to note that all the kinetics for both the ZnTAPP and ZnCOF film follow a power law decay therefore, it is probable to assign this to a charged state.

A comparison of the change in α and peak shift, as seen in Figures 4.39 and 5.46, cannot be carried out for ZnTAPP and ZnCOF as there was no shift in peaks. This is another indication of a lack of success of reaction as a peak shift is seen for the freebase and copper analogues of the porphyrin.

5.3 Studies on CuTAPP: Results and Discussion

Figure 5.25 shows a ground state absorption spectrum of a CuTAPP film and the Soret band is found at 450 nm and the Q-bands are found at 550 and 600 nm.

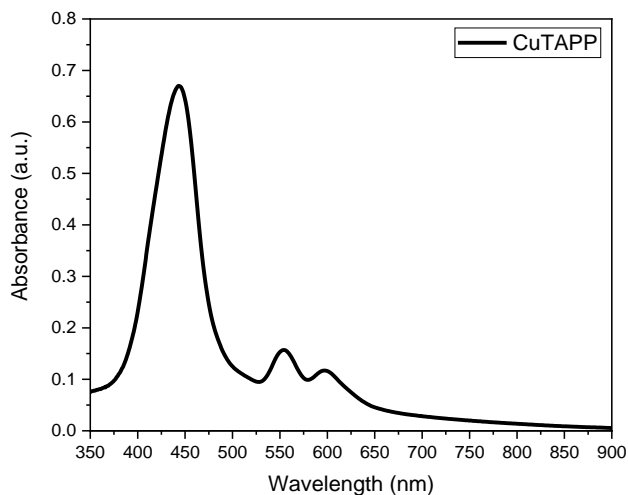


Figure 5.25: Ground state absorption of CuTAPP film (10.01 mg/mL in anisole spin coated: 10, 000 rps; 800 rpm; 2 min).

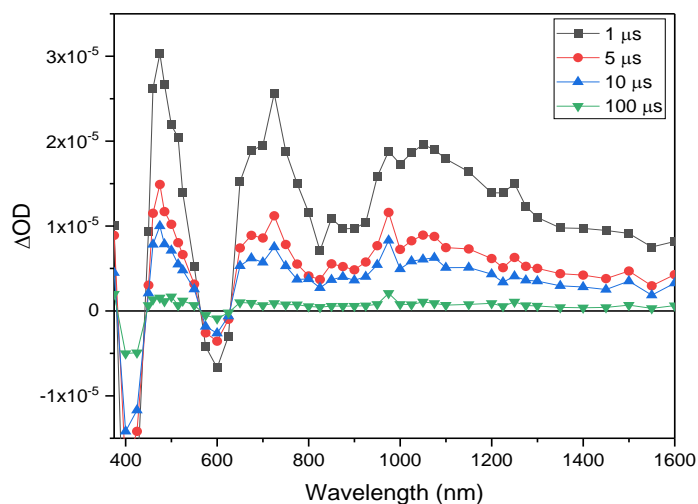


Figure 5.26: Microsecond transient absorption spectrum of CuTAPP film (10.01 mg/mL in anisole spin coated: 10,000 rps; 800 rpm; 2 min) excited with a pump wavelength of 450 nm and excitation density of $67 \mu\text{J cm}^{-2}$.

Figure 5.26 is the transient absorption spectrum of a CuTAPP film. Common features with TAPP and ZnTAPP are the two negative signals at 450 and 600 nm showing the ground state bleach. Other commonalities with TAPP and ZnTAPP include a peak in the 750 nm region and a broad peak in the IR. Common features are expected as the molecules are all analogous except the change in the metal centre. A significant difference in comparison to the TAPP and ZnTAPP films is the lifetime of the CuTAPP excited species was longer, so it was possible to collect a transient absorption spectrum at 1 μs as well as 5, 10 and 100 μs . Kim *et al.* have studied the photophysical pathways of copper porphyrins and suggest that they are more thermally dependent than a freebase analogue, and therefore charge states deactivate faster in room temperature.¹⁷ The evidence from Figure 5.26 compared to TAPP and ZnTAPP supports this theory, because of the shortening of the lifetime of the charge species.

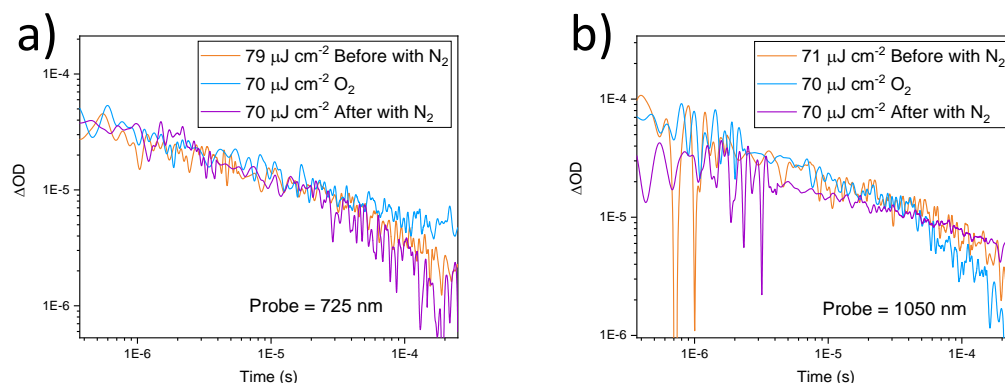


Figure 5.27: Oxygen dependent kinetics of CuTAPP film (10.01 mg/mL in anisole spin coated: 10,000 rps; 800 rpm; 2 min). Excited with a pump wavelength of 450 nm and probe wavelength of a) 725 nm and b) 1050 nm.

Figure 5.27 are the oxygen dependence kinetics measured at the same excitation density and pump wavelength but different probe wavelengths. In Appendix 4, another measurement at a probe wavelength of 475 nm can be found which shows the same result as Figure 5.27. The result is that the film is not oxygen sensitive and the transient species is not likely to be a triplet.

The following excitation energy dependent studies were carried out at an increase in energy compared to TAPP and ZnTAPP. Figures 5.28 – 5.31 show the excitation energy dependence of the CuTAPP films. At an excitation density below $19 \mu\text{J cm}^{-2}$ the signal to noise ratio was outweighed by noise and a kinetic decay was not possible to record. Also, there is not an increase and then plateau of ΔOD versus excitation density which has been used to compare bimolecular recombination to geminate recombination. With a few more measurements at a higher excitation density then maybe a plateau could be distinguished but these experiments were not carried out so not to damage the film or have other higher energy annihilation mechanism occurring.

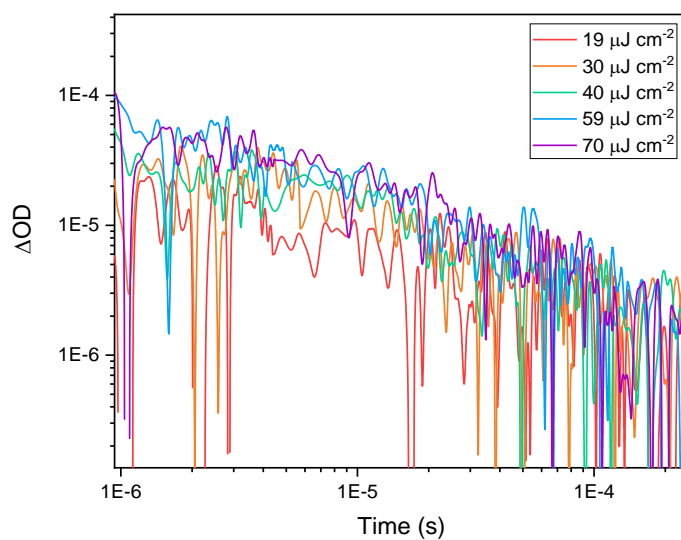


Figure 5.28: Kinetics of CuTAPP film (10.01 mg/mL in anisole spin coated: 10, 000 rps; 800 rpm; 2 min). Excited with a pump wavelength of 450 nm and probe wavelength of 475 nm.

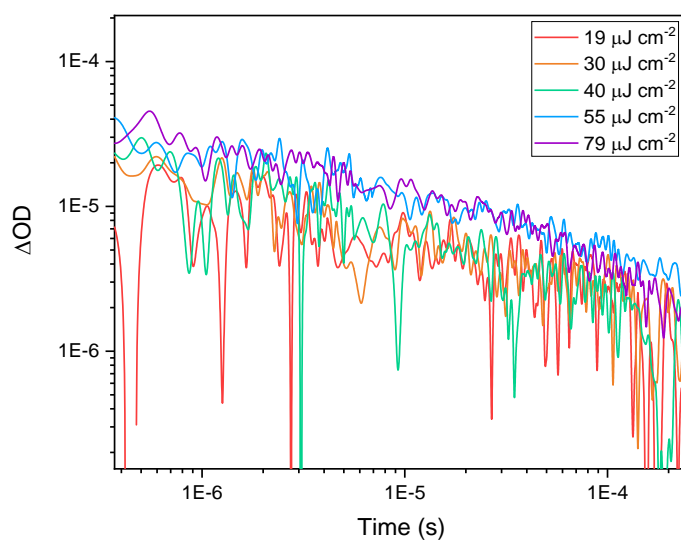


Figure 5.29: Kinetics of CuTAPP film (10.01 mg/mL in anisole spin coated: 10, 000 rps; 800 rpm; 2 min). Excited with a pump wavelength of 450 nm and probe wavelength of 725 nm.

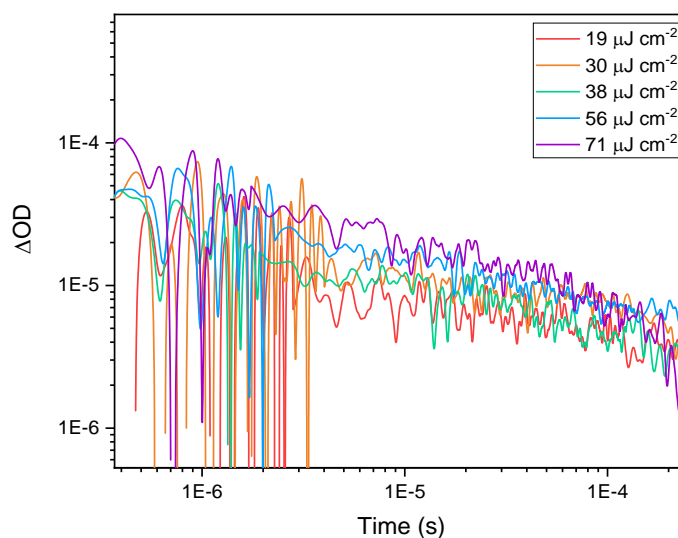


Figure 5.30: Kinetics of CuTAPP film (10.01 mg/mL in anisole spin coated: 10, 000 rps; 800 rpm; 2 min). Excited with a pump wavelength of 450 nm and probe wavelength of 1050 nm.

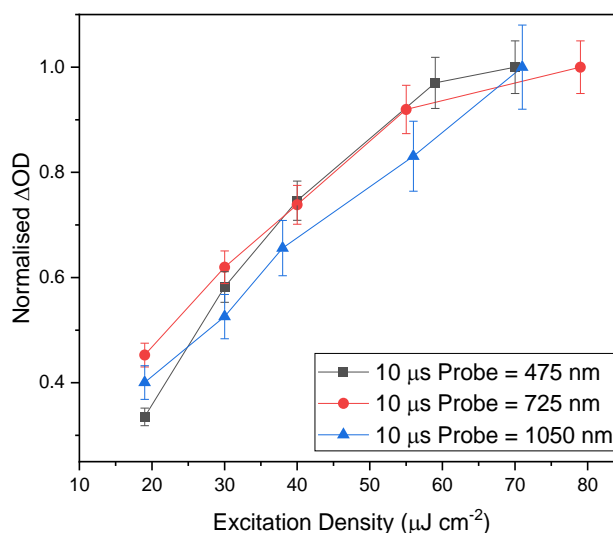


Figure 5.31: Normalised CuTAPP ΔOD measured at 10 μs as a function of laser excitation density.

As mentioned, a much higher laser energy was needed to measure the kinetic decays compared to the TAPP and ZnTAPP films and still it is difficult to see a significant difference in ΔOD from different laser energies. This could be because of a lower charge

population or extinction coefficients. Figure 5.31 shows the ΔOD as a function of excitation density. It is difficult to discern whether there is a linear relationship or if the ΔOD plateaus at higher energy. At higher energies there is a risk of damaging the porphyrin films or risk of other energetic pathways such as exciton annihilation processes which will affect the results of the transient decay kinetics. Further study needs to be carried out with the CuTAPP in order to determine if the results collected above are reliable and reproducible or if there are ways to improve the signal to noise ratio, for example, increasing the film thickness. For this reason, a comparison of the gradient before reaching a plateau has not been plotted or compared between CuTAPP and CuCOF because both films showed a questionable linear relationship that needs further investigation.

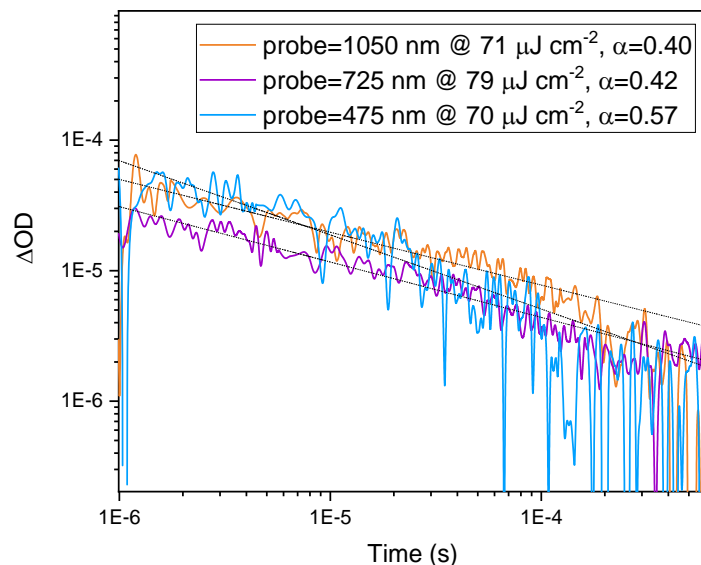


Figure 5.32: Kinetics of CuTAPP film (10.01 mg/mL in anisole spin coated: 10, 000 rps; 800 rpm; 2 min). Excited with a pump wavelength of 450 nm and varying probe wavelengths. The black lines are the power law fitting ($\Delta OD \propto t^{-\alpha}$) to each decay.

Figure 5.32 is a collection of the kinetic decays of the CuTAPP film at the same excitation density and pump wavelength but at different probe wavelengths. The power law fit in Figure 5.32 provides an α value of 0.57 when measuring the kinetics at a probe

wavelength of 475 nm but an α value of 0.42 at 725 nm, and 0.40 at 1050 nm. The value of α is different for the kinetic decays in the NIR (725 and 1050 nm) compared to a lower wavelength (475 nm) so the probe wavelengths have different trap distribution energies depending on whether it is in the NIR or near the UV wavelengths. This could be because the charge species generated are different or that with enough repeats the error and uncertainty are determined to fix a more reliable α value.

5.3.1 CuCOF

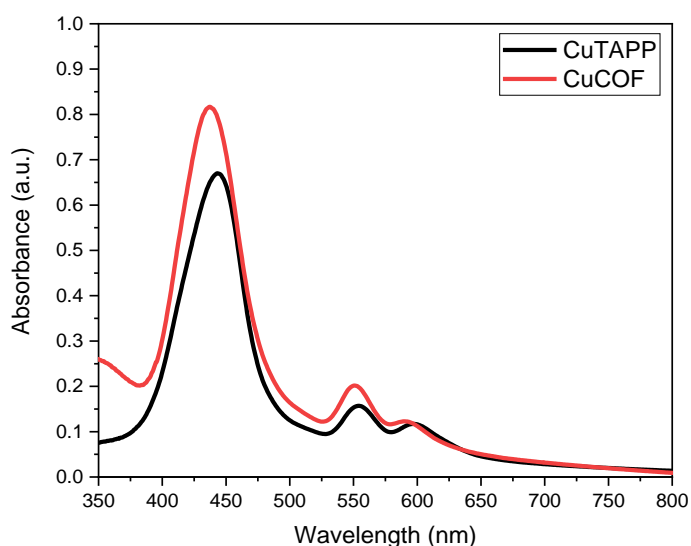


Figure 5.33: Ground state absorption of CuTAPP film (10.01 mg/mL in anisole spin coated: 10,000 rps; 800 rpm; 2 min) and CuCOF made from said CuTAPP film.

Figure 5.33 shows a ground state absorption spectrum of a CuTAPP film and then a COF sample made from the same CuTAPP film. The ground state absorbances of both films are similar, although there is an increase in absorbance for the CuCOF film and the relative intensity of the Q bands is slightly different. However, both the Soret and Q-bands largely overlap. This may be an indication of a lack of success of the synthetic procedure, so the “CuCOF” film is still mainly composed of CuTAPP as for freebase TAPP and COF there is a change in the ground state absorbance.

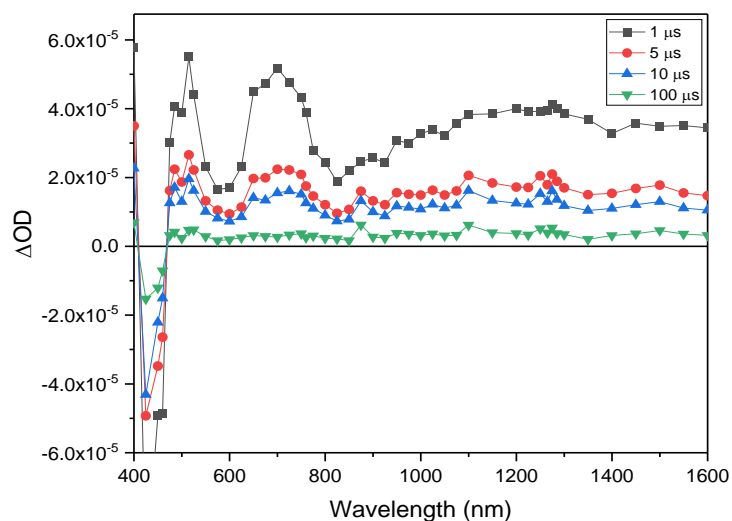


Figure 5.34: Microsecond transient absorption spectrum of CuCOF film. Excited with a pump wavelength of 450 nm and excitation density of $70 \mu\text{J cm}^{-2}$.

Figure 5.34 is a transient absorption spectrum of a CuCOF film. The trough at 450 nm shows the ground state bleach of the CuTAPP film. As previously seen with COF made from freebase TAPP and ZnTAPP, the ground state bleach 600-650 nm is not visible as a negative signal but a positive signal. The peaks at 515 and 725 nm and broad peak at 1050 nm show the transient species of the film. The 475 nm peak for the CuTAPP film has shifted to 515 nm for all the samples measured as the ground state absorption onset has shifted slightly. This change in feature can be used to indicate a change in the morphology of the film, for example, the formation of extended domains in which transient species like charges can move around in. It is likely that a reaction has occurred to the CuTAPP film and that the measured transient absorption is of the CuCOF film which can be seen in the STM images in Chapter 3. There is a high likelihood that there will be areas where no reaction has taken place, but this cannot be quantified. As with the CuTAPP film, the excitation density used to measure the transient absorption spectrum of the CuCOF film is greater by $\sim 40 \mu\text{J cm}^{-2}$ and the kinetic decays could be measured on a shorter timescale, which in the case of CuTAPP and CuCOF is 1 μs . It has been mentioned that the charge states for copper analogues of porphyrins deactivate

faster, and so the parameters to measure the transient absorption spectrum, like the shorter timescale at 1 μs , have been adjusted. Sakuma *et al.* studied copper(II)-assisted charge transfer quenching of the excited state of zinc(II) porphyrins and when conducting individual studies on a pyridine functionalised copper porphyrin they confirm that the lifetime of the charge-separated state is around 2 μs which supports the results in Figure 5.34 as after 5 μs the signal drastically decreases.¹⁸ Sakuma *et al.* state that there should be a relatively long lifetime of the charge-separated state because of the slow electron exchange reaction of the Cu(II)/Cu(I) couple. However, in the scenario in this thesis there is no Cu(I) coupling and hence the charge state can deactivate faster via singlet excited states that Sakuma *et al.* say are common pathways in copper porphyrins. Asano *et al.* studied copper porphyrin solutions and also state that there is prompt intersystem crossing to the lowest excited triplet state caused by the interactions of an unpaired electron in the highest copper $d\sigma$ orbital and the (π,π^*) excited configurations in individual, unbonded copper porphyrins.¹⁹

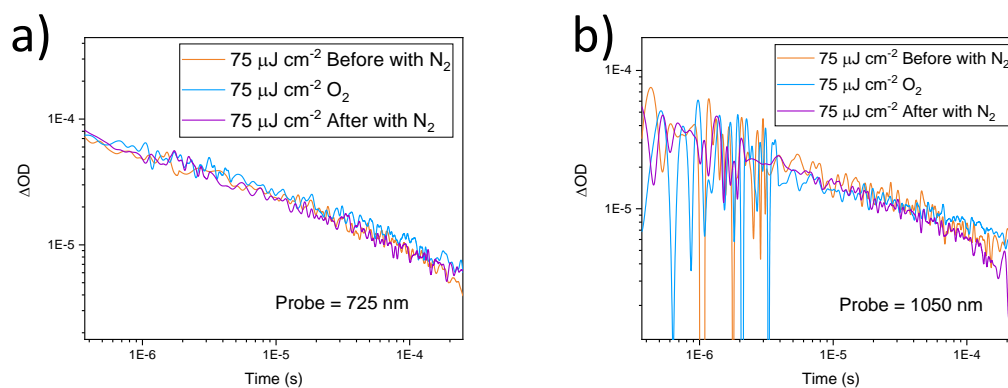


Figure 5.35: Oxygen dependent kinetics of CuCOF film. Excited with a pump wavelength of 450 nm and probe wavelength of a) 725 nm and b) 1050 nm.

The oxygen dependence kinetics in Figure 5.35 show that the transient species of the CuCOF is not likely to be a triplet as the kinetic decay remains the same in the presence of an inert atmosphere and in the presence of an oxygen atmosphere.

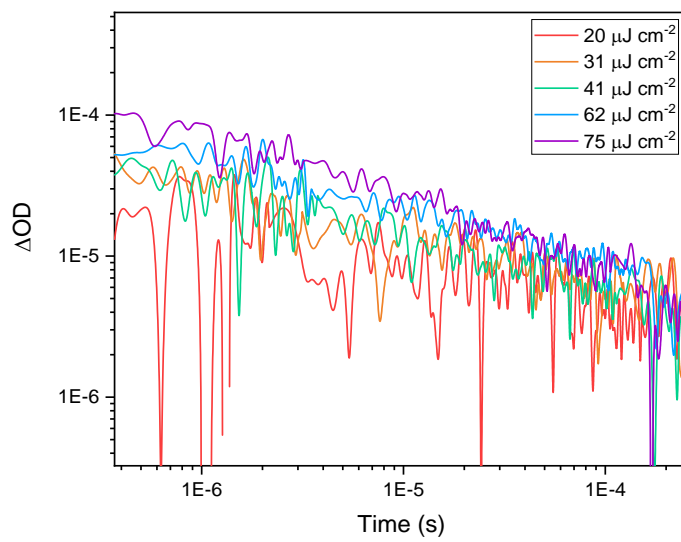


Figure 5.36: Kinetics of CuCOF film. Excited with a pump wavelength of 450 nm and probed at 515 nm.

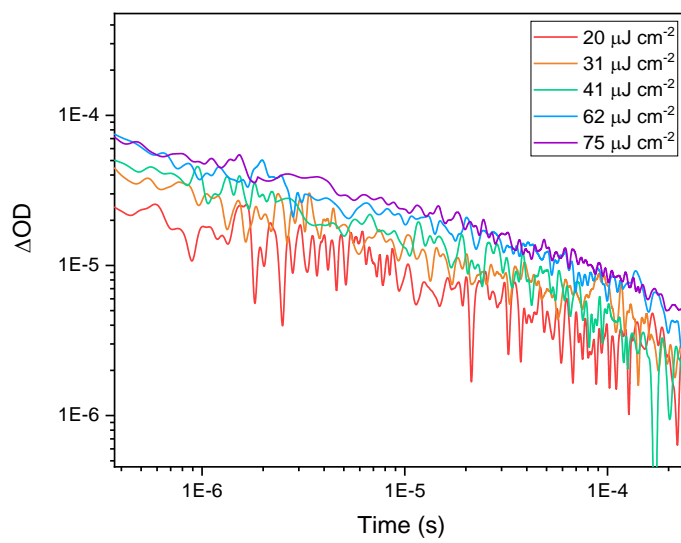


Figure 5.37: Kinetics of CuCOF film. Excited with a pump wavelength of 450 nm and probed at 725 nm.

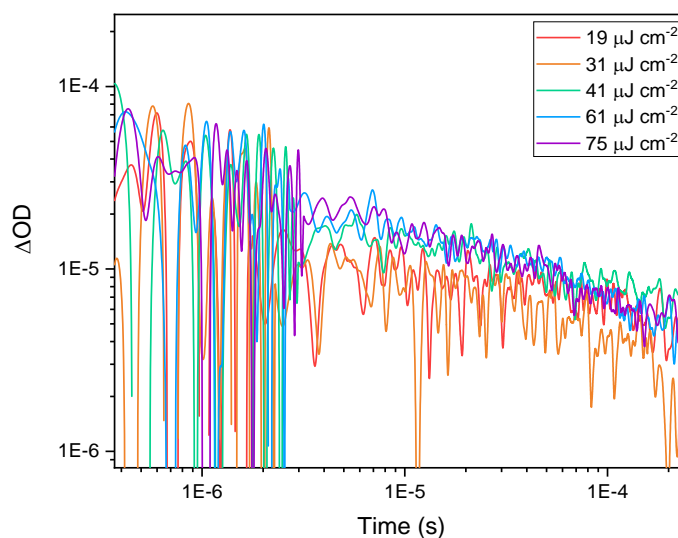


Figure 5.38: Kinetics of CuCOF film. Excited with a pump wavelength of 450 nm and probed at 1050 nm.

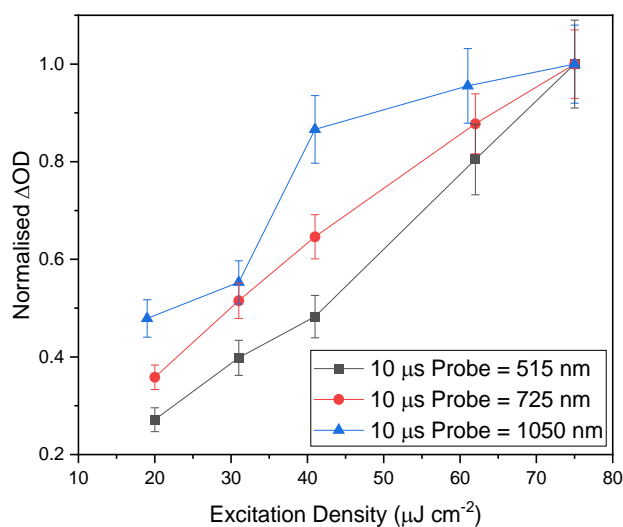


Figure 5.39: Normalised CuCOF ΔOD measured at 10 μs as a function of laser excitation density.

Figures 5.36 – 5.39 study the excitation density dependence of the CuCOF films. As with the CuTAPP films, more points are needed on the graph in Figure 5.39 to determine if the ΔOD will plateau at higher excitation densities. However, this can lead

to unwanted higher activation pathways that will affect the results and are not suitable for this study of porphyrin/COF thin films. The trend at 1050 nm does not support the likelihood of a geminate recombination because there is not a strong linear relationship seen in Figure 5.39, but there could be a linear relationship at 515 and 725 nm but it is not conclusive to determine without more points at higher excitation density.

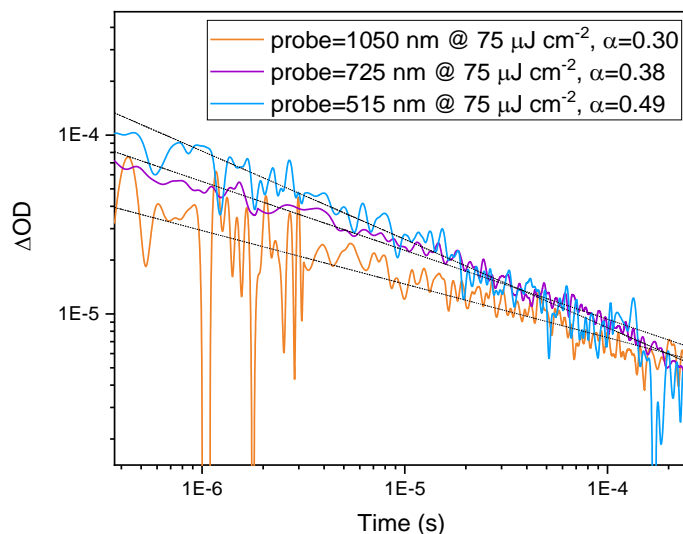


Figure 5.40: Kinetics of CuCOF film. Excited with a pump wavelength of 450 nm and excitation density of $75 \mu\text{J cm}^{-2}$, with varying probe wavelengths. The black lines are the power law fitting ($\Delta\text{OD} \propto t^{-\alpha}$) to each decay.

Figure 5.40 is a collection of the kinetic decays of the CuTAPP film at the same excitation density and pump wavelength but at different probe wavelengths. The same trend is seen as the CuTAPP kinetic comparison in Figure 5.32 because at lower wavelengths the α gradient is larger. Figure 5.40 shows an α value of 0.49 when measuring the kinetics at a probe wavelength of 515 nm but an α value of 0.38 at 725 nm, and 0.30 at 1050 nm. So, the probe wavelengths detect different trap distribution energies depending on whether it is in the NIR or near the UV wavelengths. Therefore, the charge species at different wavelengths are different as the properties of recombination and lifetimes can be different.

5.3.2 CuTAPP and CuCOF Comparison

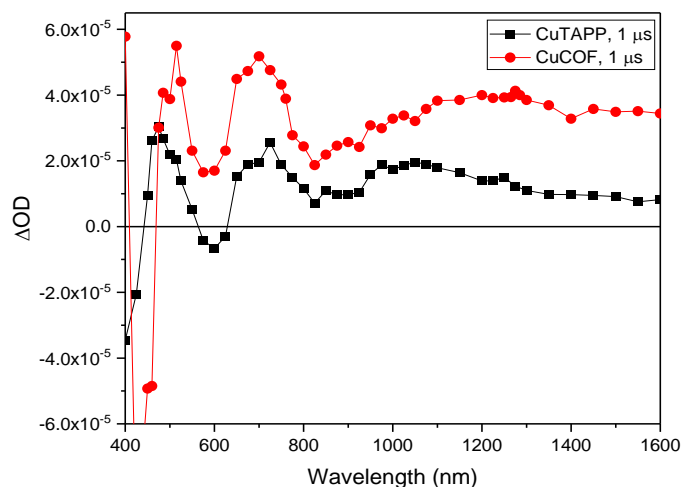


Figure 5.41: Microsecond transient absorption spectrum of CuTAPP film (10.01 mg/mL in anisole spin coated: 10, 000 rps; 800 rpm; 2 min) and CuCOF film made from said CuTAPP film. Excited with a pump wavelength of 450 nm and excitation density of $67 \mu\text{J cm}^{-2}$ and $70 \mu\text{J cm}^{-2}$ respectively.

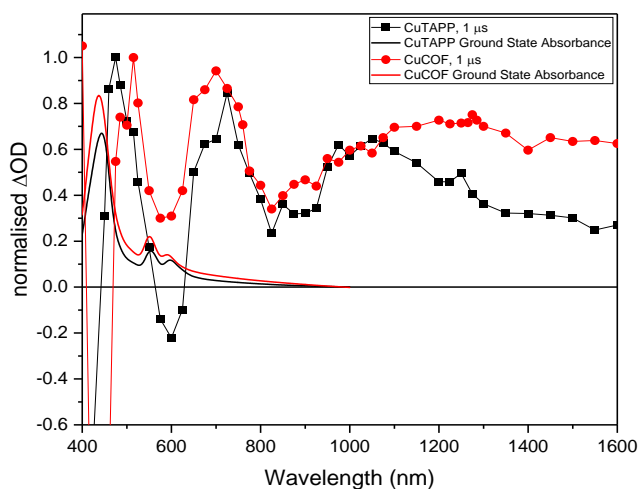


Figure 5.42: Normalised microsecond transient absorption spectrum of CuTAPP film (10.01 mg/mL in anisole spin coated: 10, 000 rps; 800 rpm; 2 min) and CuCOF film made from said CuTAPP film. Excited with a pump wavelength of 450 nm and excitation density of $67 \mu\text{J cm}^{-2}$ and $70 \mu\text{J cm}^{-2}$ respectively. Ground state absorption overlaid.

Figures 5.41 and 5.42 are the comparison between the CuTAPP and CuCOF film transient absorption spectra. Figure 5.42 has been normalised and includes the ground state absorption spectra. Focussing on the normalised transient absorption spectra, one significant difference is that the ground state bleach is visible in the CuTAPP spectrum but not in the CuCOF spectrum at around 600 nm which follows the same trend with freebase TAPP and ZnTAPP. The significant difference is the ΔOD in the IR region above 1100nm. The CuTAPP shows a ΔOD that is steadily decreasing towards 1600 nm. The CuCOF ΔOD remains steady towards 1600 nm. It would be interesting to see how the ΔOD changes after 1600 nm. From all 3 CuTAPP/CuCOF samples analysed the trend was the same in the IR region. It is possible that the CuCOF film has a greater absorbance of transient species, i.e. charges, in the IR region compared to the visible.

Figures 5.43 – 5.45 compare the kinetics between the CuTAPP and CuCOF films at the same probe and pump wavelength, and with similar laser energies the gradient α decreases only slightly for the CuCOF film but not in a common way for each probe wavelength. A decreasing α value implies that the charges could recombine slower. However, for the separate measurements of the CuTAPP to the CuCOF, the kinetic decays were vastly different which makes any comparisons made unreliable and inaccurate. With more samples then a better view of a trend could be analysed.

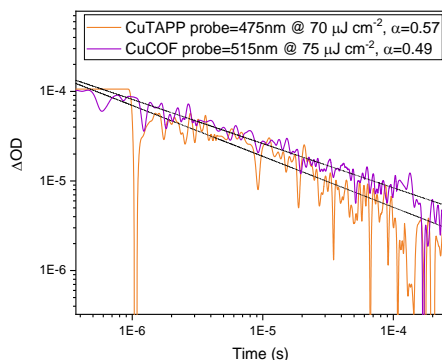


Figure 5.43: Kinetics of CuTAPP film (10.01 mg/mL in anisole spin coated: 10, 000 rps; 800 rpm; 2 min) and CuCOF film made from said CuTAPP film. Excited with a pump wavelength of 450 nm, probe wavelength of 475 and 515 nm, and excitation density of $70 \mu\text{J cm}^{-2}$ and $75 \mu\text{J cm}^{-2}$ respectively. The black lines are the power law fitting ($\Delta\text{OD} \propto t^{-\alpha}$) to each decay.

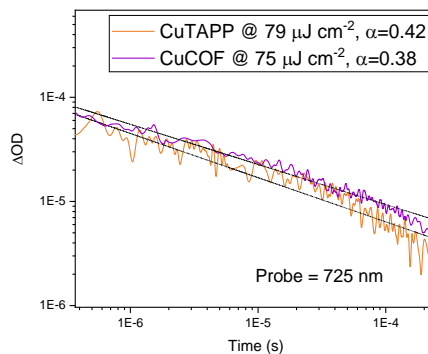


Figure 5.44: Kinetics of CuTAPP film (10.01 mg/mL in anisole spin coated: 10, 000 rps; 800 rpm; 2 min) and CuCOF film made from said CuTAPP film. Excited with a pump wavelength of 450 nm, probe wavelength of 725 nm, and excitation density of $79 \mu\text{J cm}^{-2}$ and $75 \mu\text{J cm}^{-2}$ respectively. The black lines are the power law fitting ($\Delta\text{OD} \propto t^{-\alpha}$) to each decay.

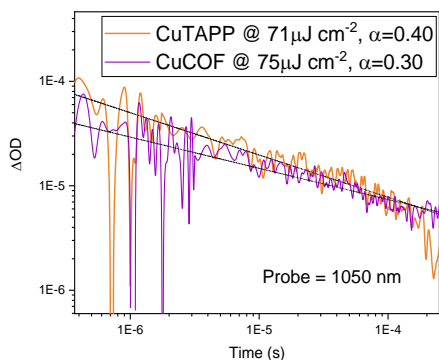


Figure 5.45: Kinetics of CuTAPP film (10.01 mg/mL in anisole spin coated: 10, 000 rps; 800 rpm; 2 min) and CuCOF film made from said CuTAPP film. Excited with a pump wavelength of 450 nm, probe wavelength of 1050 nm, and excitation density of $71 \mu\text{J cm}^{-2}$ and $75 \mu\text{J cm}^{-2}$ respectively. The black lines are the power law fitting ($\Delta\text{OD} \propto t^{-\alpha}$) to each decay.

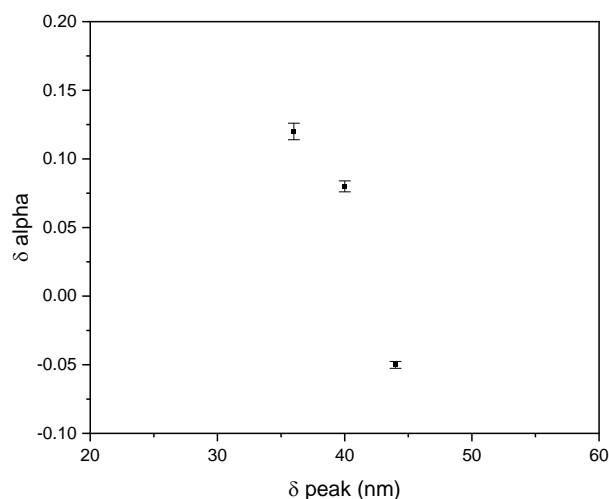


Figure 5.46: A plot of the change in α value against the change in transient peak between CuTAPP and CuCOF films (nm).

Figure 5.46 is analogous to Figure 4.39 which is used to compare the number of films that were investigated of the copper analogues. To study the change in the α values across the 3 films, a plot of the shift in main transient peak from CuTAPP to CuCOF versus change in α value of the kinetics at each peak was used. If all the films investigated were the same, then all the points in the plot should cluster as the peak shift would be the same and the change in α would be the same. However, as seen in Figure 5.46, there is no strong trend and the peak shift and α change is different each time. This is because only 3 repeats were carried out and so trying to find a deeper meaning in the changes between CuTAPP and CuCOF will require more samples to be repeated.

5.4 Metal-TAPP comparison

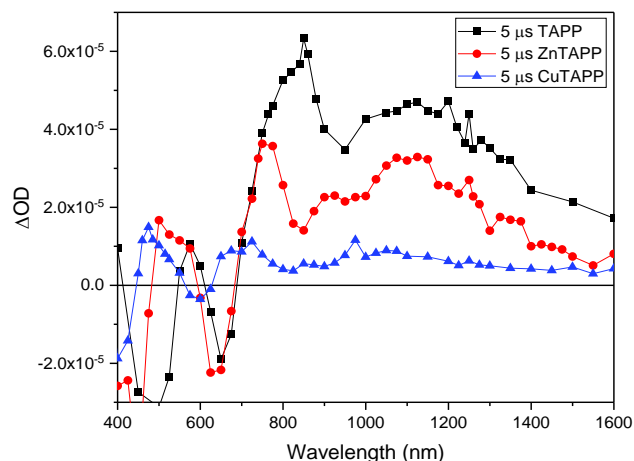


Figure 5.47: Microsecond transient absorption spectrum of TAPP film (7.67 mg/mL in anisole spin coated: 10, 000 rps; 800 rpm; 2 min) excited with a pump wavelength of 450 nm and excitation density of $42 \mu\text{J cm}^{-2}$; compared to a ZnTAPP film (2.95 mg/mL in THF spin coated: 10, 000 rps; 800 rpm; 2 min) excited with a pump wavelength of 450 nm and excitation density of $32 \mu\text{J cm}^{-2}$; and CuTAPP film (10.01 mg/mL in anisole spin coated: 10, 000 rps; 800 rpm; 2 min) excited with a pump wavelength of 450 nm and excitation density of $67 \mu\text{J cm}^{-2}$.

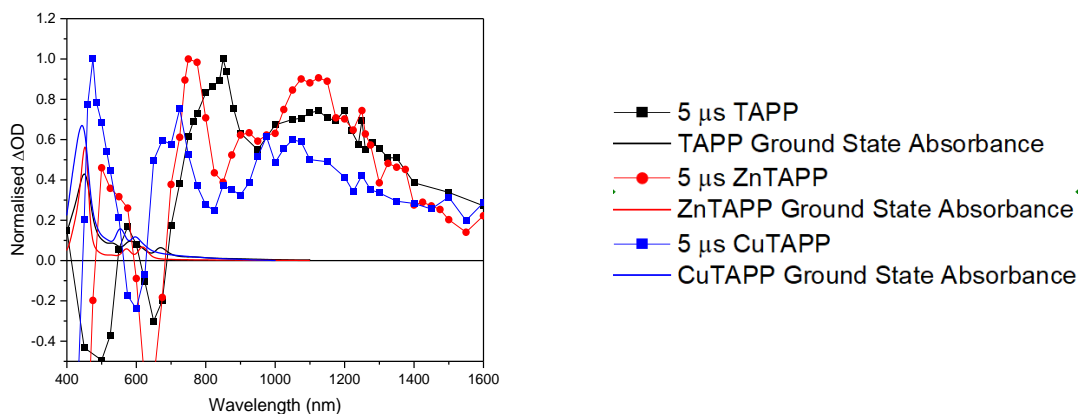


Figure 5.48: Normalised microsecond transient absorption spectrum of TAPP film (7.67 mg/mL in anisole spin coated: 10, 000 rps; 800 rpm; 2 min) excited with a pump wavelength of 450 nm and excitation density of $42 \mu\text{J cm}^{-2}$; compared to a ZnTAPP film (2.95 mg/mL in THF spin coated: 10, 000 rps; 800 rpm; 2 min) excited with a pump wavelength of 450 nm and excitation density of $32 \mu\text{J cm}^{-2}$; and CuTAPP film (10.01 mg/mL in anisole spin coated: 10, 000 rps; 800 rpm; 2 min) excited with a pump wavelength of 450 nm and excitation density of $67 \mu\text{J cm}^{-2}$. Ground state absorbance overlaid.

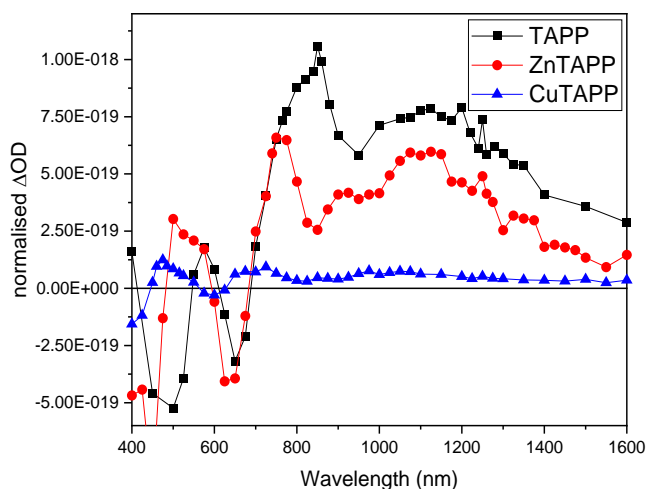


Figure 5.49: Normalised to per photon absorbed, microsecond transient absorption spectrum of TAPP film (7.67 mg/mL in anisole spin coated: 10, 000 rps; 800 rpm; 2 min) excited with a pump wavelength of 450 nm and excitation density of $42 \mu\text{J cm}^{-2}$; compared to a ZnTAPP film (2.95 mg/mL in THF spin coated: 10, 000 rps; 800 rpm; 2 min) excited with a pump wavelength of 450 nm and excitation density of $32 \mu\text{J cm}^{-2}$; and CuTAPP film (10.01 mg/mL in anisole spin coated: 10, 000 rps; 800 rpm; 2 min) excited with a pump wavelength of 450 nm and excitation density of $67 \mu\text{J cm}^{-2}$. All traces are normalised from the $5 \mu\text{s}$ original traces from Figure 5.45.

Figures 5.47 – 5.49 are various transient absorption spectra to compare the freebase TAPP to its metal analogues. Figure 5.47 compares the raw transient absorption data at a $5 \mu\text{s}$ timescale. Figure 5.48 is a normalisation to 1 of Figure 5.47 with the ground state absorbance overlaid. Figure 5.49 is normalised to per photon absorbed as the excitation density for each porphyrin was different so to compare the ΔOD more accurately, the excitation density has been normalised. It is clear to see that as the TAPP becomes metallated the amplitude of the absorbance of the transient species decreases. It is difficult to explain the decrease in absorbance as copper and zinc are in the same period of the periodic table and only separated by 2 mass units. In literature, the hydration properties have been studied and compared for copper and zinc porphyrins which can be used to compare the interactions of the molecules in this scenario. The zinc porphyrins show a stronger association with water molecules and tend to stack more closely together compared to copper porphyrins.²⁰ Therefore, charge dissociation is over

a larger distance for zinc porphyrins and the absorbance is greater.²¹ This hydration property suggests that the metals can have very different properties and such properties are affecting the charge lifetimes. There are a number of characteristics that could be studied to relate to the charge lifetimes to explain the decrease in charge lifetimes. But these characteristics will also be different once formed into a COF and as yet, there have not been extensive studies carried out.

5.5 Conclusion

This chapter focussed on comparing two metallated analogues of freebase TAPP and then the COF films synthesised from the different porphyrins. The two metals focused on were zinc and copper. The ZnTAPP and CuTAPP both were spin coated on the substrates for the COF synthesis, and resulted in COF structures that could be imaged using the STM. Therefore, it was decided to continue the photophysical studies on these two metallated porphyrins as a comprehensive set of data can be collected; from synthesis to TAS studies.

In relation to freebase TAPP there is a change between the metallated porphyrin film and subsequent metallated COF. Focussing on the normalised transient absorption spectra, one difference is that the ground state bleach is visible in the porphyrin spectra at around 600 nm but not in the COF film. This trend was seen for freebase and metallated porphyrins. However, where there is a shift in the transient peak in the NIR for the freebase porphyrin film, there is no such shift for the metallated porphyrins. The reason for this may be that there was no or lack of success of synthesis of a COF framework and therefore, a difference in signal from the TAS was not distinguishable. If there was any success from the synthesis procedure, the stronger signal from the porphyrin outweighed the COF signal. However, it could be that there is no significant change between the TAS spectra between the metallated porphyrins and the COFs.

A fascinating result is seen of the kinetic decays plotted at different excitation densities, which can be seen in Figures 5.15-5.17. For all other kinetic decays plotted at different excitation densities (including freebase TAPP), there was a point when the ΔOD

began to plateau. The ZnCOF could still plateau but at a much higher excitation density. This indicates that there is a change in the DOS between the ZnTAPP film and the ZnCOF. The reason for the change in DOS could be a cause of the effective mass of the charge carriers changing.^{14,15} For ZnCOF films, there are extended domains and then the charge transport can occur across molecules and is referred to as extrinsic charge transport. With respect to extrinsic charge transport the number of electrons and holes does not have to be equal, so this supports the reasoning that there has been a successful synthesis of ZnCOF domains and the photophysical behaviour has changed.¹⁶

After the extensive studies on the freebase TAPP and COF which showed the presence of charges rather than triplets, it became evident quickly that there were charges generated for the metallated analogues. This was supported by the oxygen dependent studies. The lifetime of said charges was the most obvious difference between the porphyrins. From the freebase TAPP to ZnTAPP to CuTAPP the lifetime of the charges diminished significantly. This suggests that there is a core change in the porphyrins that affects the photophysical properties, for example, the conjugation with the π -orbitals of the porphyrin ring. To investigate this further, a collection of results from different metals will help to build a trend of the effect the metal has on the porphyrin core. The direct effect in this thesis was that when analysing the CuTAPP and CuCOF a higher excitation density was used to have a higher signal to noise ratio, and the kinetic decays were measured at shorter timescales because at longer timescales (i.e. 100 μ s) that have normally been used, the charge had already decayed and no signal was observed. When investigating a wider range of metallated porphyrins, the lifetimes of the charges can build a picture of which will have greater impact for applications of energy harvesting.

5.6 Bibliography

- 1 D. M. Roundhill, in *Photochemistry and Photophysics of Metal Complexes*, Springer US, Boston, MA, 1994, pp. 321–340.
- 2 D. Marsh and L. Mink, *J. Chem. Educ.*, 1996, **73**, 1188.
- 3 J. P. Strachan, S. Gentemann, J. Seth, W. A. Kalsbeck, J. S. Lindsey, D. Holten and D. F. Bocian, *J. Am. Chem. Soc.*, 1997, **119**, 11191–11201.
- 4 S. Patchkovskii, P. M. Kozlowski and M. Z. Zgierski, *J. Chem. Phys.*, 2004, **121**, 1317–1324.
- 5 M. John Plater, S. Aiken and G. Bourhill, *Tetrahedron*, 2002, **58**, 2415–2422.
- 6 T.-H. Tran-Thi, T. Fournier, A. Y. Sharonov, N. Tkachenko, H. Lemmetyinen, P. Grenier, K.-D. Truong and D. Houde, *Thin Solid Films*, 1996, **273**, 8–13.
- 7 N. M. Barbosa Neto, D. S. Correa, L. De Boni, G. G. Parra, L. Misoguti, C. R. Mendonça, I. E. Borissevitch, S. C. Zílio and P. J. Gonçalves, *Chem. Phys. Lett.*, 2013, **587**, 118–123.
- 8 R. Shediach, M. H. B. Gray, H. Tetsuo Uyeda, R. C. Johnson, J. T. Hupp, P. J. Angiolillo and M. J. Therien, *J. Am. Chem. Soc.*, 2000, **122**, 7017–7033.
- 9 H. Linschitz and L. Pekkarinen, *J. Am. Chem. Soc.*, 1960, **82**, 2411–2416.
- 10 F. Hernández-Fernández, M. Pavanello and L. Visscher, *Phys. Chem. Chem. Phys.*, 2016, **18**, 21122–21132.
- 11 Bahr, Kuciauskas, Liddell, Moore, Moore and Gust, *Photochem. Photobiol.*, 2000, **72**, 598–611.
- 12 C. A. Wijesinghe, M. Niemi, N. V. Tkachenko, N. K. Subbaiyan, M. E. Zandler, H. Lemmetyinen and F. D'Souza, *J. Porphyr. Phthalocyanines*, 2011, **15**, 391–400.
- 13 M. Gouterman, *J. Mol. Spectrosc.*, 1961, **6**, 138–163.

- 14 J. Singh, in *Journal of Non-Crystalline Solids*, North-Holland, 2002, vol. 299–302, pp. 444–448.
- 15 S. Rangan, C. Ruggieri, R. Bartynski, J. I. Martínez, F. Flores and J. Ortega, *J. Phys. Chem. C*, 2016, **120**, 4430–4437.
- 16 Z. M. Gibbs, F. Ricci, G. Li, H. Zhu, K. Persson, G. Ceder, G. Hautier, A. Jain and G. J. Snyder, *npj Comput. Mater.*, 2017, **3**, 1–7.
- 17 D. Kim, D. Holten and M. Gouterman, *J. Am. Chem. Soc.*, 1984, **106**, 2793–2798.
- 18 T. Sakuma, T. Ohta, T. Yagyu, H. D. Takagi and M. Inamo, *Inorg. Chem. Commun.*, 2013, **38**, 108–111.
- 19 M. Asano, O. Ohno, Y. Kaizu and H. Kobayashi, in *Photochemistry and Photophysics of Coordination Compounds*, Springer Berlin Heidelberg, 1987, pp. 291–294.
- 20 S. T. Moin and T. S. Hofer, *Mol. Biosyst.*, 2016, **12**, 2288–2295.
- 21 T. Da Ros, M. Prato, D. Guldi, E. Alessio, M. Ruzzi and L. Pasimeni, *Chem. Commun.*, 1999, 635–636.

6 Conclusion and Future Work

The research in this thesis has investigated further the photophysical applications of porphyrin 2D-COFs using microsecond-TAS which, unlike ultrafast spectroscopy, can study longer lived excited states.

To begin with, the synthesis of the COF, even though unreliable, was a success across the freebase TAPP and the zinc and copper analogues. The ZnCOF showed very good monolayer coverage. Khayum *et al.* have focused on zinc ion interactions in 2D-COFs, and conclude that the zinc ion enables efficient inter-layer interaction because of the divalent Zn^{2+} ions with adjacent C=O and N-H provide a rigid structure and even an excellent discharge capacity.¹

The STM was a well-chosen technique to study the COF films. Many researchers who synthesise COF monolayer films, and analogous 2D films, use STM because it's a powerful tool to carefully scrutinise the films on a small scale with a high resolution to see defects.²⁻⁴ The STM images shown in Chapter 3 were all collected on the same instrument at ambient conditions. Using ambient STM was the reason so many films could be synthesised and analysed because of the ease of changing the samples, scanning parameters and scanning tips. For future investigations, it is highly recommended to use ambient STM for the aforementioned reasons.

Unfortunately, throughout the duration of this research, it has become evident that the reproducibility and reliability of results has been a large stumbling block in the collected results. Every effort was made to collect reproducible results through care in the synthesis and subsequent analytical techniques. It became evident that during the synthesis process there are changing variables that cannot be controlled, for example, number of nucleation sites during the vapour phase reaction or the cooling down of the steel autoclaves in which the experiments were carried out. To address this in the future, an altered technique can be designed to monitor the reaction more closely and reduce any human error. One method would be to change the original deposition of the porphyrin solution on the substrate by making

a Langmuir–Blodgett film. A detailed description has been published by D. Schwartz in 1997.⁵ A Langmuir–Blodgett film is reported to be a promising method for preparation of thin films because it enables precise control of the monolayer thickness and homogeneous deposition of the monolayer over large areas. Sakamoto *et al.* used a Langmuir–Blodgett technique to initiate a multilayer synthesis but each individual layer was added in a Langmuir–Blodgett method.⁶ Sakamoto *et al.* report a successful synthesis using this method as the result was highly crystalline multilayer polymeric frameworks.

Additionally, the cooling down of the steel autoclaves needs to be regulated to improve the crystallisation process of the COF films. However, as the autoclave cools, the water and linker molecule in the vapour phase can condense on the substrate, thus destroying the film synthesised. One solution can be to incorporate a valve in the autoclave to release the vapour once the cool down step has begun. Then, the film can be cooled slowly without risk of the water or linker destroying the film. This improved design of the autoclave is shown in Section 3.5, Figure 3.18.

Another technique that can be explored is to initiate the reaction on the surface by spin coating not only the porphyrin on the substrate, but also a small amount of linker molecule in solution, as well as having an excess amount of linker in the vapour phase. Having the linker only in the vapour phase relies on the fact that there will be successful collisions with the surface to initiate nucleation sites. The drawback is that by adding the linker into a solution with the porphyrin then the reaction can commence immediately and lead to clumping or lack of extended networks because the linker can react with all reaction sites on the porphyrin blocking the synthesis of the framework.

As the results show in Chapter 3, there was success in making some COF films but there is a lot of room for improvement and many variables that can be adjusted. Once a standardised and successful technique is established, there is the opportunity to change the precursors. For example, using different linker molecules can change the properties of the COF network depending on the application, be it for catalytic processes or photophysical applications. However, using a vapour phase technique may not be possible because if the linker molecule has a higher mass then its boiling

point will increase and by increasing the temperature of the COF synthesis can affect the porphyrin molecules on the substrate and the process will become less environmentally friendly. When using a larger linker molecule, one possible solution can be to deposit the linker as a layer on top of the porphyrin layer and continue the reaction in the same manner as described in this thesis.

Aside from tackling the difficulties in finding a reliable and successful synthetic technique, it is important to find other ways to confirm the success of the reaction aside from STM. This thesis also used FTIR and XPS and both techniques were able to show a positive COF synthesis. FTIR showed the reaction of the amine to an imine and XPS was able to show the formation of imine bonds but also the formation of hemiaminal bonds which are intermediate bonds. Other techniques may be more comprehensive in determining the success of the synthesis across the whole substrate rather than on small areas on the substrate. Atomic force microscopy (AFM) is another microscopic technique but has the capabilities of scanning larger surface areas than an STM. X-ray diffraction (XRD) is used to analyse crystal structures and can be extrapolated to COF films if they are multi-layered. The information on the crystal structure can be used to understand the regularity of the layers of film and determine the chemical species present.

Many interesting results came from the TAS studies in this thesis. Firstly, when comparing the TA spectra between freebase TAPP and then the COF, there was a distinctive shift in the transient peak from around 850 to around 765 nm (Figure 4.33). The varied extents of this shift are shown in Figure 4.38, nonetheless there was always a shift. Wang *et al.* have studied femtosecond TAS and saw that the grain size has an effect on the blue shift in a TA spectrum.⁷ The grain size is comparable to an increase in layers and domains of the COF structure. Specifically, there is a blue-shift of the transient peak if the grain size increases by the molecular structure growing or becoming more porous.^{7,8} This blue shift can be applied to the shift seen in Figure 4.33 (and across other samples) to explain that as the COF is being formed, there is a greater extent of layers and domains added on the surface, and so the pseudo-grain sizes are increasing. As previously explained, the extent of the shift seen in Figure 4.38 is different, this could be indicative of different extents of synthesis and

clumping within the films with a greater blue shift representing larger domains and more layers of COF.

It is positive to see that a clear change was seen in the TA spectra between the porphyrin precursor and then the synthesised COF. This was also seen with a change in the ground state bleach between the porphyrin and then the COF. Busby *et al.* studied excited-state self-trapping and ground-state relaxation dynamics in poly(3-hexylthiophene) and propose that a reduction in the ground state bleach could be linked to how amorphous the material is but this is only a hypothesis and not confirmed.⁹ The same hypothesis can be applied to the change in ground state bleach seen in this thesis, so the extent of how amorphous the film is is changing but further investigations will need to confirm this change.

As with the change in ground state bleach showing a change in the films, the ground state UV-vis has also shown a change in the films from the synthesis procedure. Figure 4.21 shows a ground state absorption spectrum of a TAPP film and then a COF sample and there is a distinctive blueshift of the Soret and Q-bands for the COF film of 10 nm. The Q-bands especially show different distinctive peaks for the TAPP and COF film. The average blue shift in nm across the peaks is 12 nm. Due to defects in the crystallinity of materials, the materials UV-Visible data can show a blue shift.¹⁰ This implies that the COF formation has not led to ordered frameworks but many disordered domains which is also supported by the aforementioned blue shift in the TA spectrum by Wang *et al.* and even the change of the amorphous properties exhibited by a change in ground state bleach by Busby *et al.*^{7,9}

Another consistency seen from the TAS measurements is the support of the presence of charges from the oxygen dependence measurements. All kinetic measurements of films taken in the presence of oxygen did not stray from the measurements taken in an inert atmosphere, which gives a strong support for the lack of triplets, and hence assigning charges to the transients formed in the porphyrin and COF films (including metal analogues).¹¹

As well as the oxygen dependence measurements, another positive consistency were the experiments carried out at different pump wavelengths; this

was in order to isolate TAS measurements of the COF sample from the TAPP measurements. The ground state absorbance in Figure 4.40 demonstrates well why measuring at two different pump wavelengths for the same sample will ensure the measurement of the TAPP and then the COF sample. At 680 nm, the ground state absorbance shows that the only part of the sample that is showing an absorbance is the TAPP. Whereas, the opposite is true at 652 nm, only the COF is showing absorbance in the ground state absorbance spectrum. The hypothesis is that when comparing the TA absorbance for both TAPP and COF at 680 and 652 nm respectively with the TA absorbance at pump 450 nm, then the TA absorbance spectra should overlap. If there is an overlap then it can be concluded that when measuring at pump 450 nm, it is still at TA measurement of the TAPP and COF individually rather than residual TAPP in the COF sample. The TA spectra showing the overlaps between the TAPP and COF samples are shown in Figures 4.44-4.47, which have been normalised to 1 and normalised to per photon absorbed. Normalising to per photon absorbed is important when comparing different pump wavelengths and excitation density energies so that both these parameters are scaled.¹² Albeit large parts of this thesis struggled with poor reproducibility, the fact that the TA spectrums collected were those of TAPP and COF respectively is a positive result because the transient species excitation wavelengths have been identified and further research can focus on kinetic studies.

With respect to the kinetic measurements, even though many repeat analyses were carried out using the same synthesis process and TAS parameters, the TAS kinetic results were different nearly each time. As the synthesis process was the same in each case, the reason may be due to the small variances in thickness of the films or the extent of the success of the reaction across wide areas on the surface. Efforts were made to investigate the thickness of the films using a profilometer and an AFM but the results were doubtful and difficult to repeat. When further investigating the kinetic decays at the peaks of the transient absorption spectrum, the results were different each time. The measurement of different kinetic decays is shown in Figure 4.38 which displays the changing α value.

One way in which to begin to improve the kinetic measurements could be to see whether a changing α value is caused by the laser setup or the porphyrin/COF films changing, even over small amounts of time. A single sample needs to be made and the kinetics have to be measured at the same pump and probe wavelength and laser excitation density repeatedly, even leaving the sample in the same position whilst being purged with nitrogen. Then measure the kinetics three times a day for one week for example, to collect the α value. It would be hoped that the α value would be exactly the same but maybe there are intrinsic changes of the film over time that occur that effect the α value. After determining the aforementioned change, another way to improve the kinetics would be to improve the sample setup, as described in Section 4.1 relating to the TAPP solution. The TAPP solution was incredibly sensitive to oxygen quenching and the TAPP or COF films could be affected by small amounts of oxygen. Described in Section 4.1 is a technique in which the cuvette containing the sample is placed inside another cuvette which undergoes a freeze-pump-thaw process to ensure a hermetic seal in an inert atmosphere.

Focussing on the photophysical properties of ZnTAPP and ZnCOF films, an interesting result is seen of the kinetic decays plotted at different excitation densities, which can be seen in Figures 5.14-5.16 which are measured at probe wavelengths of 750, 875 and 1125 nm. For all other kinetic decays plotted at different excitation densities (including freebase TAPP), there was a point when the ΔOD began to plateau. This does not mean that the ΔOD for the ZnCOF will not plateau but potentially at a much higher excitation density. This indicates that there is a change in the DOS between the ZnTAPP film and the ZnCOF. The reason for the change in DOS could be a cause of the effective mass of the charge carriers changing.^{13,14} In ZnTAPP films, there is no extended conjugation so the charge transport is intrinsic and there will be the same number of electrons and holes. For ZnCOF films, there are extended domains because of the incorporation of the BDA linker molecule and then the charge transport can occur across molecules and is referred to as extrinsic charge transport. With respect to extrinsic charge transport the number of electrons and holes does not have to be equal, so this supports the reasoning that there has been

a successful synthesis of ZnCOF domains and the photophysical behaviour has changed.¹⁵

There is a lot of potential in future work regarding the photophysical properties of the COF films. The variety in the results collected is interesting within itself by showing how sensitive the films are when there are slight changes in the overall system. Going forward, the changes in the morphology of the frameworks should be determined between each sample before a photophysical investigation.

As the initial aim of this project was to investigate thin films, moving towards TAS studies of monolayer porphyrins and COFs. (A thin film was arbitrarily considered a film that has a Soret peak in the ground state absorption spectrum equal to or less than 0.1 abs.) There is a large potential for future work in adapting the TAS setup to have multiple transmissions through a sample to increase the signal of the thinner sample films.¹⁶ The study of thin films can produce interesting properties of the porphyrin and COF films if the case is the same as graphene. Monolayer films like graphene and materials analogous to graphene show remarkable properties in the monolayer region with increased strength and electrical properties.¹⁷⁻¹⁹

6.1 Bibliography

- 1 A. M. Khayum, M. Ghosh, V. Vijayakumar, A. Halder, M. Nurhuda, S. Kumar, M. Addicoat, S. Kurungot and R. Banerjee, *Chem. Sci.*, 2019, **10**, 8889–8894.
- 2 S.-Y. Ding and W. Wang, *Chem. Soc. Rev.*, 2013, **42**, 548–568.
- 3 M. X. Wu and Y. W. Yang, *Chinese Chem. Lett.*, 2017, **28**, 1135–1143.
- 4 N. Bilbao, D. Waghray, T. Janssen and S. De Feyter, *Microsc. Microanal.*, 2019, **25**, 1478–1479.
- 5 D. K. Schwartz, *Surf. Sci. Rep.*, 1997, **27**, 245–334.
- 6 R. Sakamoto, K. Hoshiko, Q. Liu, T. Yagi, T. Nagayama, S. Kusaka, M. Tsuchiya, Y. Kitagawa, W. Y. Wong and H. Nishihara, *Nat. Commun.*, 2015, **6**, 1–9.
- 7 L. Wang, C. McCleese, A. Kovalsky, Y. Zhao and C. Burda, *J. Am. Chem. Soc.*, 2014, **136**, 12205–12208.
- 8 C. R. Kagan, C. B. Murray, M. Nirmal and M. G. Bawendi, *Phys. Rev. Lett.*, 1996, **76**, 1517–1520.
- 9 E. Busby, E. C. Carroll, E. M. Chinn, L. Chang, A. J. Moulé and D. S. Larsen, *J. Phys. Chem. Lett.*, 2011, **2**, 2764–2769.
- 10 D. Zhang, Y. Guo and Z. Zhao, *Appl. Catal. B Environ.*, 2018, **226**, 1–9.
- 11 F. Wilkinson and A. A. Abdel-Shafi, *J. Phys. Chem. A*, 1999, **103**, 5425–5435.
- 12 C. Cantrell, *Multiple-Photon Excitation and Dissociation of Polyatomic Molecules - Google Books*, Springer Science & Business Media, 1st Editio., 2013, vol. 35.
- 13 J. Singh, in *Journal of Non-Crystalline Solids*, North-Holland, 2002, vol. 299–302, pp. 444–448.
- 14 S. Rangan, C. Ruggieri, R. Bartynski, J. I. Martínez, F. Flores and J. Ortega, *J. Phys. Chem. C*, 2016, **120**, 4430–4437.
- 15 Z. M. Gibbs, F. Ricci, G. Li, H. Zhu, K. Persson, G. Ceder, G. Hautier, A. Jain and G. J. Snyder, *npj Comput. Mater.*, 2017, **3**, 1–7.
- 16 A. R. S. Kandada, G. Grancini, A. Petrozza, S. Perissinotto, D. Fazzi, S. S. K. Raavi and G. Lanzani, *Sci. Rep.*, 2013, **3**, 2073.

- 17 N. R. Wilson, P. A. Pandey, R. Beanland, R. J. Young, I. A. Kinloch, L. Gong, Z. Liu, K. Suenaga, J. P. Rourke, S. J. York and J. Sloan, *ACS Nano*, 2009, **3**, 2547–2556.
- 18 Y. Zhu, S. Murali, W. Cai, X. Li, J. W. Suk, J. R. Potts and R. S. Ruoff, *Adv. Mater.*, 2010, **22**, 3906–3924.
- 19 R. Mas-Ballesté, C. Gómez-Navarro, J. Gómez-Herrero and F. Zamora, *Nanoscale*, 2011, **3**, 20–30.

Appendix 1

TAPP and COF oxygen dependence, excited with a pump wavelength of 450 nm.

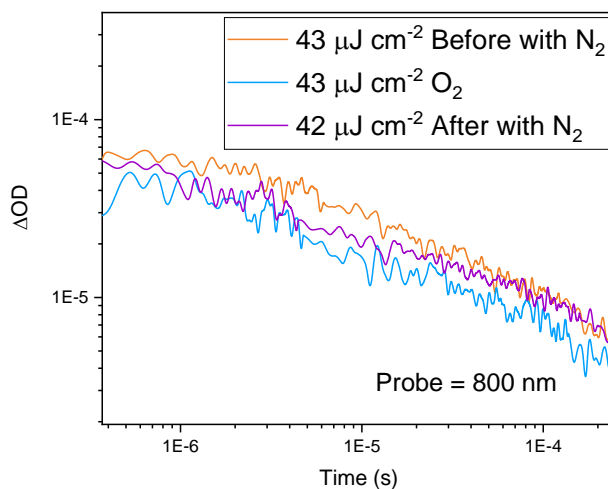


Figure A.1: Oxygen dependent kinetics of TAPP (20.86 mg/mL in anisole spin coated: 10, 000 rps; 800 rpm; 2 min). Excited with a pump wavelength of 450 nm, probe wavelength of 800 nm and excitation density of 42-43 $\mu J cm^{-2}$.

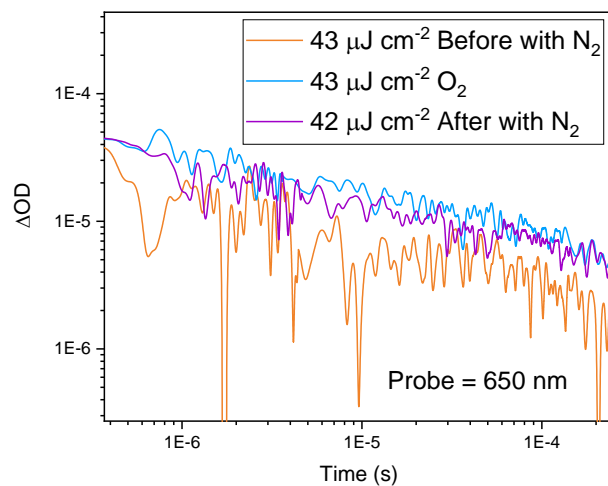


Figure A.2: Oxygen dependent kinetics of TAPP (20.86 mg/mL in anisole spin coated: 10, 000 rps; 800 rpm; 2 min). Excited with a pump wavelength of 450 nm, probe wavelength of 650 nm and excitation density of 42-43 $\mu J cm^{-2}$.

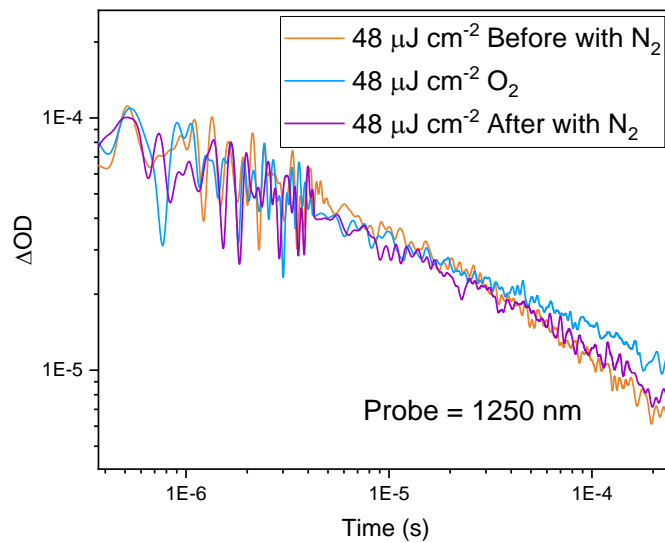


Figure A.3: Oxygen dependent kinetics of COF film. Excited with a pump wavelength of 450 nm, probe wavelength of 1250 nm and excitation density of $48 \mu\text{J cm}^{-2}$.

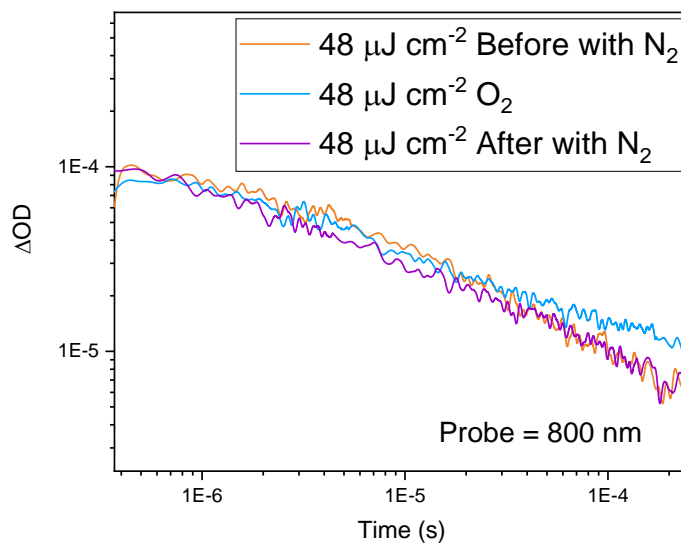


Figure A.4: Oxygen dependent kinetics of COF film. Excited with a pump wavelength of 450 nm, probe wavelength of 800 nm and excitation density of $48 \mu\text{J cm}^{-2}$.

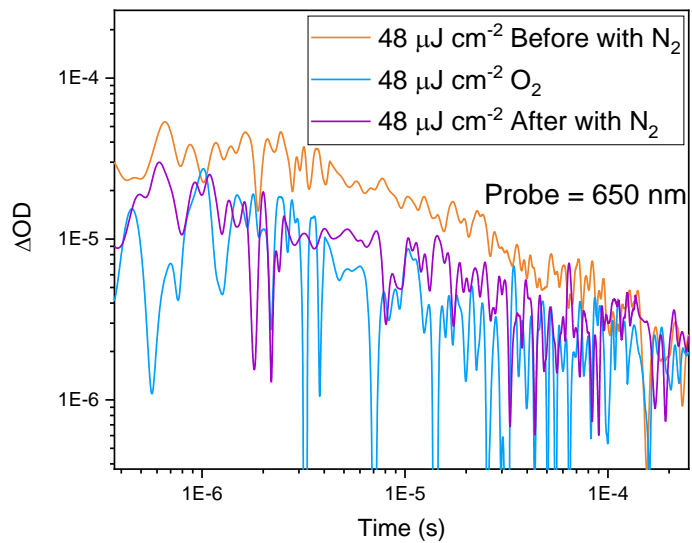


Figure A.5: Oxygen dependent kinetics of COF film. Excited with a pump wavelength of 450 nm, probe wavelength of 650 nm and excitation density of $48 \mu J cm^{-2}$.

Appendix 2

TAPP and COF oxygen dependence, excited with a pump wavelength of 680 and 652 nm respectively.

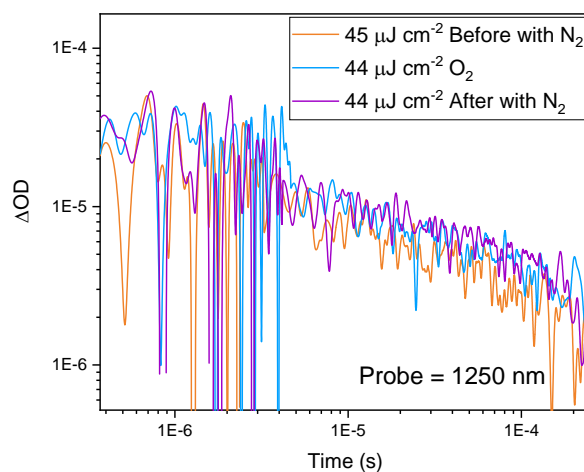


Figure A.6: Oxygen dependent kinetics of TAPP (20.86 mg/mL in anisole spin coated: 10, 000 rps; 800 rpm; 2 min). Excited with a pump wavelength of 680 nm, probe wavelength of 1250 nm and excitation density of 44-45 $\mu\text{J cm}^{-2}$.

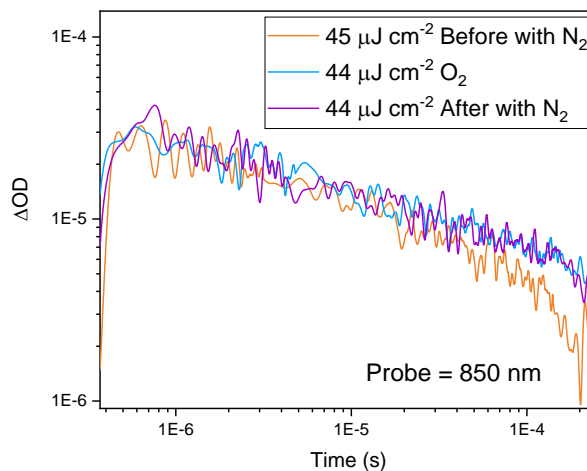


Figure A.7: Oxygen dependent kinetics of TAPP (20.86 mg/mL in anisole spin coated: 10, 000 rps; 800 rpm; 2 min). Excited with a pump wavelength of 680 nm, probe wavelength of 850 nm and excitation density of 44-45 $\mu\text{J cm}^{-2}$.

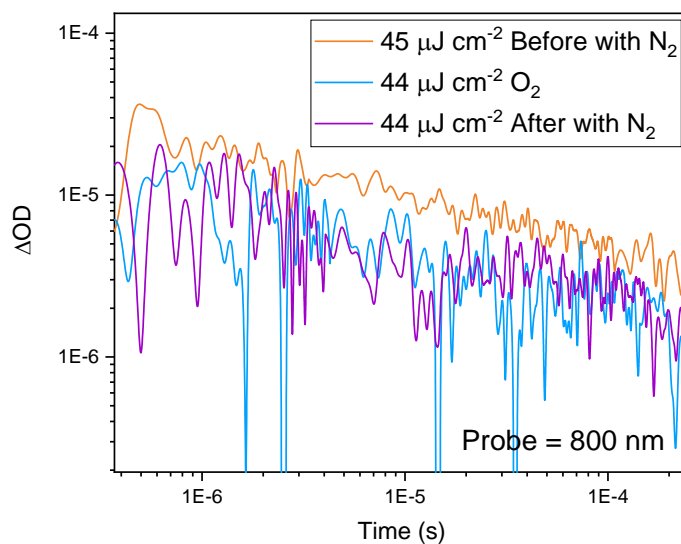


Figure A.8: Oxygen dependent kinetics of TAPP (20.86 mg/mL in anisole spin coated: 10, 000 rps; 800 rpm; 2 min). Excited with a pump wavelength of 680 nm, probe wavelength of 800 nm and excitation density of 44-45 $\mu\text{J cm}^{-2}$.

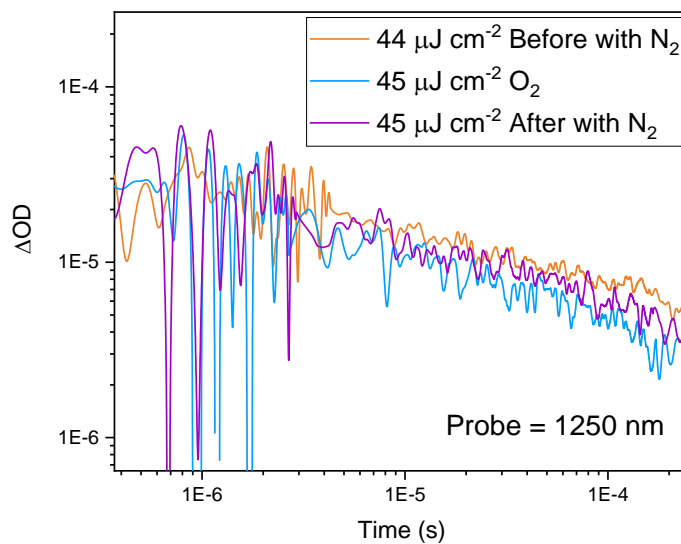


Figure A.9: Oxygen dependent kinetics of COF film. Excited with a pump wavelength of 652 nm, probe wavelength of 1250 nm and excitation density of 44-45 $\mu\text{J cm}^{-2}$.

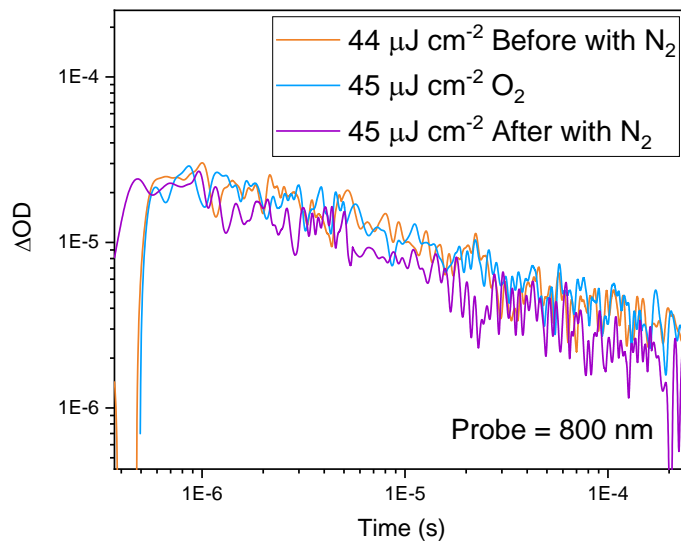


Figure A.10: Oxygen dependent kinetics of COF film. Excited with a pump wavelength of 652 nm, probe wavelength of 800 nm and excitation density of 44-45 $\mu\text{J cm}^{-2}$.

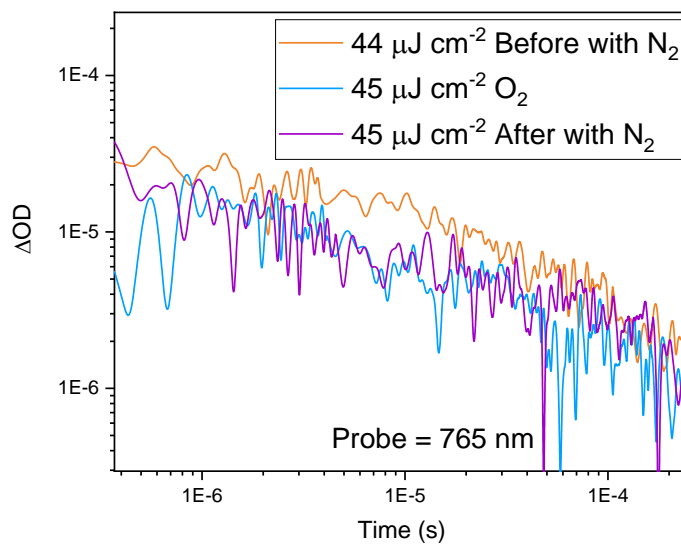


Figure A.11: Oxygen dependent kinetics of COF film. Excited with a pump wavelength of 652 nm, probe wavelength of 765 nm and excitation density of 44-45 $\mu\text{J cm}^{-2}$.

Appendix 3

Zn-TAPP and Zn-COF oxygen dependence, excited with a pump wavelength of 450 nm.

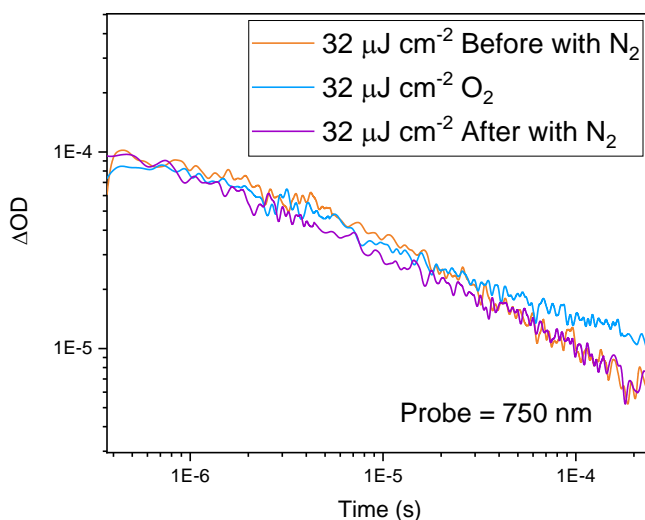


Figure A.12: Oxygen dependent kinetics of ZnTAPP film (2.95 mg/mL in THF spin coated: 10, 000 rps; 800 rpm; 2 min). Excited with a pump wavelength of 450 nm and probe wavelength of 750 nm.

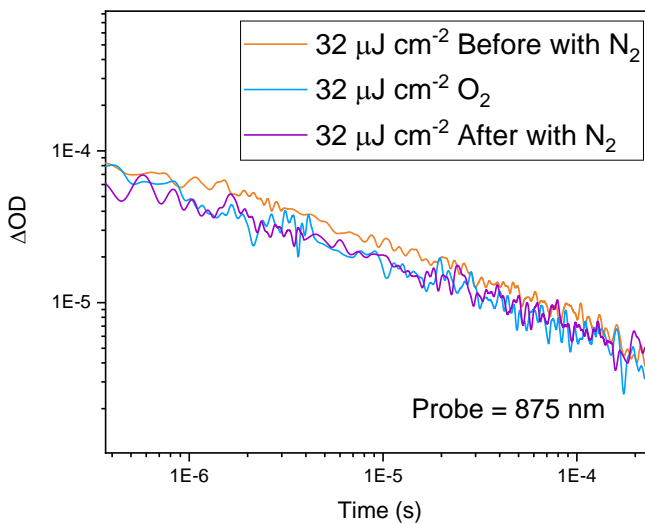


Figure A.13: Oxygen dependent kinetics of ZnCOF film. Excited with a pump wavelength of 450 nm and probe wavelength of 875 nm.

Appendix 4

Cu-TAPP and Cu-COF oxygen dependence, excited with a pump wavelength of 450 nm.

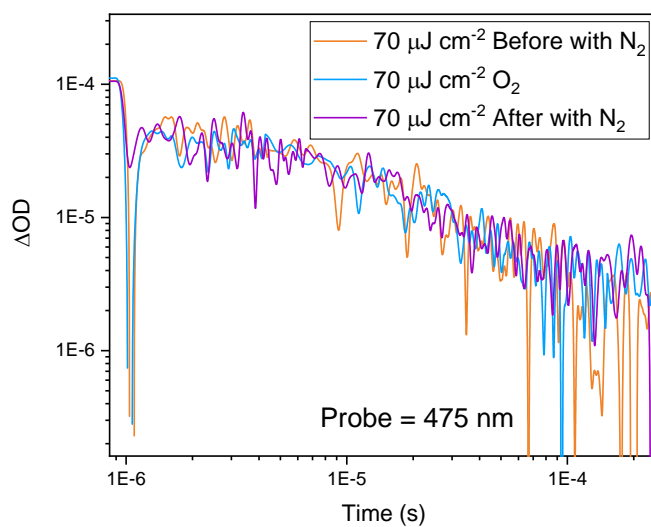


Figure A.14: Oxygen dependent kinetics of CuTAPP film (10.01 mg/mL in anisole spin coated: 10,000 rps; 800 rpm; 2 min). Excited with a pump wavelength of 450 nm and probe wavelength of 475 nm.

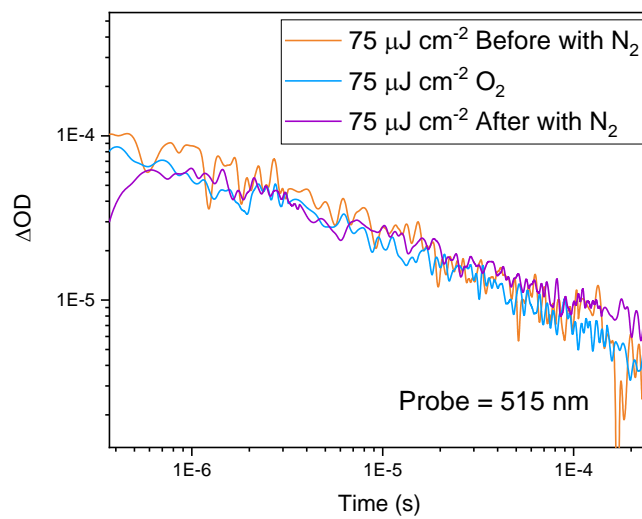


Figure A.15: Oxygen dependent kinetics of CuCOF film. Excited with a pump wavelength of 450 nm and probe wavelength of 515 nm.